

# **Biomaterial-based transdermal and implantable vaccine delivery systems for cancer immunotherapy**



**Swansea University**  
**Prifysgol Abertawe**

PhD thesis by **Saul Michue Seijas BSc, MChem**

**Swansea University, 2022**

*Submitted to Swansea University in fulfilment of the requirements for  
the Degree of Doctor of Philosophy*

PhD supervisor: **Prof. Juan C. Mareque-Rivas**

## Summary

Activating the immune system to target cancer cells is one of the most promising and novel therapeutic approaches for cancer treatment. It offers the potential for long-term protection and limiting off-target cytotoxicity in healthy tissue, which are some of the major drawbacks in chemotherapy. However, limited patient response and autoimmune adverse effects remain current challenges in cancer immunotherapy. The administration of immunotherapies and combination therapies into the immune cell-rich dermal skin region using biodegradable microneedles or into the tumour resection site using implants could overcome these limitations by stimulating a local and controlled therapeutic response.

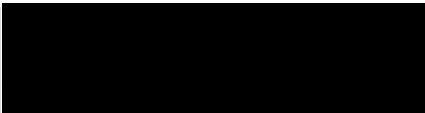
This thesis presents the development and functionalisation of biomaterial-based microneedles and implantable devices to promote the sustained delivery of a variety of immunomodulatory drugs and anticancer agents into the microenvironment of the tumour aiming to locally modulate the immune response. Specifically, the covalent functionalisation of hyaluronic acid to a clinically investigated IDO inhibitor, 1-methyltryptophan, was explored as well as the development of a variety of immunomodulatory nano- and microparticle systems including: (i) self-assembled hyaluronic acid nanoparticles incorporating the clinically used immune checkpoint inhibitor, anti-PD-L1; (ii) immunostimulatory vaccine functionalised iron oxide nanoparticles, (iii) a Pt(IV) prodrug decorated iron oxide nanoparticle system for immunochemotherapy; and (iv) multimodal biosilica-based constructs showing intrinsic peroxidase-like activity and biosensor applications.

The incorporation of some of these systems into microneedles and implantable devices demonstrated gradual drug release under physiological conditions and retention of functional activity *in vitro* using different murine and human cancer cell models. The experimental results highlight the potential of these microneedles and implants as sustained delivery platforms for enhanced cancer immunotherapy and combination therapy.

# Declarations and Statements

## DECLARATION

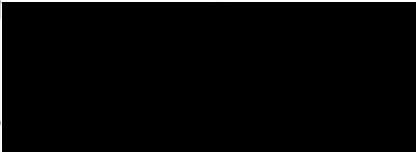
This work has not previously been accepted in substance for any degree and is not being concurrently submitted in candidature for any degree.

Signed  (candidate)

Date ..... 27/02/2022 .....

## STATEMENT 1

This thesis is the result of my own investigations, except where otherwise stated. Where correction services have been used, the extent and nature of the correction is clearly marked in a footnote(s).

Other sources are acknowledged by footnotes giving explicit references. A bibliography is appended 

Signed ..... (candidate)

Date ..... 27/02/2022 .....

## STATEMENT 2

I hereby give consent for my thesis, if accepted, to be available for photocopying and for inter-library loans after expiry of a bar on access approved by the Swansea University.

Signed ..... (candidate)

Date ..... 27/02/2022 .....

# Contents

Summary .....	ii
Declarations and Statements.....	iii
Contents .....	iv
Acknowledgements.....	vii
List of Figures.....	viii
List of Tables.....	xi
List of Equations.....	xi
Abbreviations .....	xii
<b>1 Chapter 1 Introduction.....</b>	<b>1</b>
<b>1.1 Defence mechanisms of the adaptive and innate immune system.....</b>	<b>2</b>
<b>1.2 Immune evasive mechanisms of tumour cells.....</b>	<b>6</b>
<b>1.3 Cancer immunotherapy .....</b>	<b>12</b>
1.3.1 Immune checkpoint inhibitors and co-stimulators.....	13
1.3.2 Adjuvants .....	18
<b>1.4 Nanomedicine in anticancer therapy.....</b>	<b>19</b>
1.4.1 Active tumour targeting.....	20
1.4.2 Stimuli responsive nanosystems.....	21
1.4.3 Drug delivery systems .....	23
1.4.3.1 Inorganic NPs systems .....	23
1.4.3.2 Polymeric NP systems.....	29
<b>1.5 Microneedles (MNs) for transdermal drug delivery.....</b>	<b>33</b>
1.5.1 Solid MNs .....	35
1.5.2 Polymeric and carbohydrate MNs .....	36
1.5.2.1 Dissolvable and biodegradable MNs.....	37
1.5.3 Comprehensive MN-based drug delivery systems for cancer immunotherapy	41
<b>1.6 Polymeric implants for cancer therapy .....</b>	<b>44</b>
1.6.1 Types and fabrication of polymeric implants.....	44
1.6.2 Casted implant developments in cancer immunotherapy .....	48
<b>1.7 Overview and objectives of this research .....</b>	<b>49</b>
<b>2 Chapter 2 Materials and methods .....</b>	<b>52</b>
<b>2.1 Materials.....</b>	<b>53</b>
<b>2.2 Instrumentation .....</b>	<b>55</b>
<b>2.3 Methods .....</b>	<b>57</b>

<b>3</b>	<b>Chapter 3 Development of a hyaluronic acid-based biomaterial functionalised with an IDO inhibitor for cancer immunomodulation .....</b>	<b>71</b>
<b>3.1</b>	<b>Introduction .....</b>	<b>72</b>
3.1.1	Hyaluronic acid (HA) for anti-cancer drug formulations.....	72
3.1.2	HA modification methods .....	72
3.1.3	HA functionalisation with anti-cancer agents.....	74
3.1.4	HA hydrolysis and enzymatic degradation.....	75
3.1.5	Clinical investigation of small molecule inhibitors of the tryptophan catabolism pathway.....	78
3.1.6	Aims and objectives .....	79
<b>3.2</b>	<b>Results .....</b>	<b>80</b>
3.2.1	Synthesis and characterisation of the 1MT functionalised HA biomaterial ..	80
3.2.2	Purification of the 1MT-HA biomaterial.....	83
3.2.3	Release of 1MT from 1MT-HA at different pH conditions .....	86
<b>3.3</b>	<b>Discussion .....</b>	<b>91</b>
<b>4</b>	<b>Chapter 4 Design and synthesis of immunomodulatory nanoparticle systems and biosilica-based theranostic constructs .....</b>	<b>94</b>
<b>4.1</b>	<b>Introduction .....</b>	<b>95</b>
4.1.1	Design of a HA-based NP system for cancer immunotherapy.....	95
4.1.2	Functionalisation of SPIONs with platinum-based anti-cancer agents.....	96
4.1.3	Biosilica-based materials for cancer therapy.....	98
4.1.4	Design of a biosilica-based theranostic system for combination cancer therapy and as biosensor device .....	100
4.1.5	Aims and objectives .....	103
<b>4.2</b>	<b>Results .....</b>	<b>104</b>
4.2.1	Synthesis and characterisation of anti-PD-L1 loaded 1MT-HA NPs (1MT-HA@anti-PD-L1 NPs).....	104
4.2.2	Release studies of immunomodulatory agents from HA NPs.....	107
4.2.3	Development of immunomodulatory IONP systems.....	109
4.2.3.1	Synthesis and characterisation of IONP-Pt(IV).....	110
4.2.3.2	Synthesis and characterisation of IONP-DOTAP-pIC.....	115
4.2.4	Development of an immunomodulatory biosilica-based scaffold.....	116
4.2.4.1	Intrinsic peroxidase-like activity of commercial diatoms .....	116
4.2.4.2	Diatom functionalisation with glucose oxidase .....	118
4.2.4.3	Diatom functionalisation with IONPs.....	119
4.2.5	Development of a diatom-based biosensor.....	123
4.2.5.1	Synthesis and characterisation of anti-PD-L1 functionalised diatoms ....	123

4.2.5.2	Synthesis and functional activity of anti-PD-L1 modified IONPs .....	126
4.2.5.3	Methodology and functional evaluation of D-antiPD-L1 biosensor .....	129
<b>4.3</b>	<b>Discussion .....</b>	<b>133</b>
<b>5</b>	<b>Chapter 5 Synthesis, functionalisation and characterisation of biodegradable hyaluronic acid-based MNs and implantable devices for cancer immunotherapy .....</b>	<b>138</b>
<b>5.1</b>	<b>Introduction .....</b>	<b>139</b>
5.1.1	Biodegradable microneedles (MNs) for cancer immunotherapy .....	139
5.1.2	Dissolvable biomaterial-based implantable devices for cancer immunotherapy .....	141
5.1.3	Design of the immunotherapeutic MN and implantable devices.....	142
5.1.4	Aims and objectives .....	144
<b>5.2</b>	<b>Results .....</b>	<b>145</b>
5.2.1	HA MN fabrication, optimisation, and characterisation .....	145
5.2.2	MN skin penetration efficiency experiments.....	146
5.2.3	MN biocompatibility studies .....	153
5.2.4	Fluorescent QD incorporated HA MNs .....	154
5.2.5	Theranostic IONP loaded HA MNs .....	155
5.2.5.1	Fabrication and characterisation of IONP MNs .....	155
5.2.5.2	IONP MN release and functional activity assays.....	158
5.2.6	Immunomodulatory 1MT-HA MN fabrication and release study .....	160
5.2.7	Fabrication, functionalisation, and characterisation of HA-based implants	161
5.2.8	IONP micelle loaded HA implant.....	162
5.2.9	IONP-DOTAP-pIC-R837 loaded HA implant.....	165
5.2.10	1MT-HA loaded implant.....	167
5.2.11	Functional assays with an immunomodulatory 1MT-HA implant .....	168
5.2.11.1	Non-cell based IDO inhibition assay with 1MT-HA implant.....	168
5.2.11.2	IDO inhibition assay with 1MT-HA implant using HeLa cells .....	170
5.2.11.3	Screening of IDO inhibition of 1MT-HA implant on different cancer cell lines	173
5.2.11.4	IDO inhibition assay with 1MT-HA implant using OVCAR8 and MC38 cells	175
<b>5.3</b>	<b>Discussion .....</b>	<b>178</b>
<b>6</b>	<b>Final discussion and outlook.....</b>	<b>181</b>
<b>7</b>	<b>Appendix.....</b>	<b>185</b>
<b>8</b>	<b>Bibliography .....</b>	<b>191</b>

# Acknowledgements

First and foremost, I would like to thank my supervisor Prof. Juan C. Mareque-Rivas for giving me the opportunity to undertake this exciting research project and for the active support, advice, and guidance throughout my PhD. It has not only enabled me to contribute to the development of innovative anti-cancer therapeutics, but also helped me broaden my knowledge and skill sets and has motivated me to specialise in this field.

I would also like to give my gratitude to my second supervisor Prof. Owen Guy and Dr. Raha Rahbari for introducing me to the world of microneedles and providing me with the tools, materials, and knowledge to perform various microneedle-based assays featured in this thesis. A special thanks goes to my research group colleague Marc Bilbao-Asensio for performing some of the bioassays and his support in the tissue culture laboratories until I could work independently.

Additionally, I thank our internal collaborators Dr. Nick Jones and Dr. James Cronin for their support and kindly providing many of the cell lines. My gratitude also goes to the RBGO group for kindly providing other cell lines used in this research. I hereby thank our industrial collaborator, Bloomage Freda Biopharm Co. LTD, for kindly supplying the hyaluronic acid materials used in this project.

Dr. James McGettrick, Dr. Sally James, Dr. David Howard, Dr. Anitha Devadoss, Dr. Jon Evans, Dr. Jezabel Garcia Parra and Dr. Jacob Mitchell have all made an equally valuable contribution to my training of different equipment that has aided to my formation and to the progress of this research.

Finally, I would like to thank all my colleagues and friends that I made throughout my PhD. Marc ha sido un gran placer compartir laboratorio contigo, aquí nuestros caminos se separan, pero nuestra amistad permanecerá. Joel, it was a pleasure working with you and I wish you all the best for the remainder of your PhD and future career. To Chiara, Michael, Edward, and Natasha who joined my PhD journey from the start and all the other amazing people that joined afterwards.

To Kadie, mi amor, and my parents, Pilar y Ricardo, you have been by my side throughout all the ups and downs and always believed in my ability to complete this long journey with success, which has filled me with strength and motivation to help me turn my personal and career ambitions into reality.

# List of Figures

<i>Figure 1.1 Schematic representation of the adaptive immune mechanisms acting on tumour cells..</i>	6
<i>Figure 1.2 Hallmarks of cancer.</i>	9
<i>Figure 1.3 Schematic illustration of the mechanisms involved in cancer immunoediting..</i>	11
<i>Figure 1.4 Immune checkpoint inhibition mechanisms of anti-PD-1 and anti-CTLA-4.....</i>	14
<i>Figure 1.5 Structure and function of the tumour overexpressed IDO1 immune checkpoint. .</i>	15
<i>Figure 1.6 Mechanism of tryptophan metabolism. ....</i>	16
<i>Figure 1.7 Examples of clinically investigated immune checkpoints.....</i>	18
<i>Figure 1.8 APC interaction with clinically investigated and FDA-approved TLR agonists..</i>	19
<i>Figure 1.9 Design and mechanism of action of inherently therapeutic IONVs. ....</i>	26
<i>Figure 1.10 Illustration of inorganic nanoparticle types and potential mechanisms for active tumour targeting. ....</i>	29
<i>Figure 1.11 Illustration of polymeric nanoparticle systems as well as their potential for active targeting and stimuli-responsive mechanisms for triggered vaccine release.....</i>	32
<i>Figure 1.12 Schematic representation of different types of MNs for transdermal drug delivery.....</i>	35
<i>Figure 1.13 Polymeric MN source materials and fabrication methods. ....</i>	40
<i>Figure 1.14 Examples of dissolvable MN drug delivery systems for cancer immunotherapy applications. ....</i>	42
<i>Figure 1.15 Examples of solid MN systems for cancer immunotherapy. ....</i>	44
<i>Figure 1.16 Overview of different types of polymeric implants for application in cancer therapy.....</i>	45
<i>Figure 1.17 Examples of dissolvable implantable devices for cancer immunotherapy. ....</i>	48
<i>Figure 1.18 Overview schematic of aims and objectives.....</i>	51
<i>Figure 3.1 Schematic representation of different HA covalent and non-covalent functionalisation strategies for cancer therapeutic applications. ....</i>	73
<i>Figure 3.2 Crystal structure of Hyal1 complexed to HA disaccharide unit at the substrate binding cleft.....</i>	76
<i>Figure 3.3 The HA degradation mechanism as proposed by Zhang et al.....</i>	77
<i>Figure 3.4 Chemical structure of the IDO1 inhibitor indoximod (D-1MT) currently under clinical investigation for the treatment of different cancers. ....</i>	79
<i>Figure 3.5 Schematic overview of thesis Chapter 3. ....</i>	79
<i>Figure 3.6 Reaction scheme for the synthesis of the 1MT-HA biomaterial.....</i>	80
<i>Figure 3.7 NMR characterisation of 1MT-HA biomaterial.....</i>	82
<i>Figure 3.8 Stacked (A) <sup>1</sup>H NMR and (B) <sup>13</sup>C NMR spectra of 1MT, HA and 1MT-HA (from top to bottom). ....</i>	83
<i>Figure 3.9 <sup>1</sup>H NMR of 1MT-HA after purification by dialysis in D<sub>2</sub>O with proton labelling. ....</i>	84
<i>Figure 3.10 <sup>1</sup>H NMR of 1MT-HA after purification by centrifugal filtration in D<sub>2</sub>O with proton labelling. ....</i>	85
<i>Figure 3.11 Reaction scheme for ion-exchange purification of 1MT-HA using a sulfonic acid-based resin. ....</i>	86
<i>Figure 3.12 1MT calibration curve by RP-HPLC and UV detection at 223 nm with a concentration range of 0-100 μM. ....</i>	87



<b>Figure 3.13 Release of 1MT from 1MT-HA over 48 h at 37°C at pH 5, 6.5 and 8.....</b>	<b>88</b>
<b>Figure 3.14 RP-HPLC characterisation of 1MT-HA 48 h release study at different pH conditions.....</b>	<b>89</b>
<b>Figure 4.1 Design of self-assembled HA-based NP system for combination immunotherapy.....</b>	<b>96</b>
<b>Figure 4.2 Illustration of a Pt(IV) prodrug functionalised IONP system and its potential combination therapeutic anticancer mechanism.....</b>	<b>98</b>
<b>Figure 4.3 Examples of different diatom species with varied frustule shapes.....</b>	<b>99</b>
<b>Figure 4.4 Proposed design of biosilica-based systems.....</b>	<b>102</b>
<b>Figure 4.5 Overview schematic of chapter 4.....</b>	<b>103</b>
<b>Figure 4.6 1MT-HA@anti-PD-L1 NP characterisation.....</b>	<b>105</b>
<b>Figure 4.7 BCA protein assay for the quantification of anti-PD-L1 incorporated 1MT-HA NPs.....</b>	<b>106</b>
<b>Figure 4.8 FPLC characterisation of 1MT-HA@anti-PD-L1 NPs.....</b>	<b>107</b>
<b>Figure 4.9 1MT-HA@anti-PD-L1 NP degradation experiment.....</b>	<b>108</b>
<b>Figure 4.10 Overlaid FPLC chromatograms of anti-PD-L1 released from 1MT-HA@anti-PD-L1 NPs in the presence of HAase.....</b>	<b>109</b>
<b>Figure 4.11 Reaction scheme for IONP-Pt(IV) synthesis.....</b>	<b>110</b>
<b>Figure 4.12 <sup>1</sup>H-NMR spectra of (A) c,c,t-[Pt(NH<sub>3</sub>)<sub>2</sub>Cl<sub>2</sub>(OH)<sub>2</sub>] in DMSO-d<sub>6</sub> and (B) c,c,t-[Pt(NH<sub>3</sub>)<sub>2</sub>Cl<sub>2</sub>(O<sub>2</sub>CCH<sub>2</sub>CH<sub>2</sub>CO<sub>2</sub>H)<sub>2</sub>] in D<sub>2</sub>O.....</b>	<b>111</b>
<b>Figure 4.13 <sup>1</sup>H-NMR stacked spectra of PEG-Pt(IV) (top) and the unmodified PEG-NH<sub>2</sub> phospholipid (bottom) in D<sub>2</sub>O.....</b>	<b>112</b>
<b>Figure 4.14 Characterisation of IONP and IONP-Pt(IV)..</b>	<b>113</b>
<b>Figure 4.15 Characterisation of IONP-Pt(IV) using an OPD assay.....</b>	<b>114</b>
<b>Figure 4.16 Reaction scheme for IONP-pIC synthesis.....</b>	<b>115</b>
<b>Figure 4.17 Characterisation of IONP-DOTAP and IONP-DOTAP-pIC by DLS.....</b>	<b>116</b>
<b>Figure 4.18 SEM of purified commercial diatoms showing micron-sized elliptical structures and fragments with nano-sized pores.....</b>	<b>117</b>
<b>Figure 4.19 Peroxidase-like activity assay of commercial diatoms at different H<sub>2</sub>O<sub>2</sub> concentrations.....</b>	<b>118</b>
<b>Figure 4.20 Tandem catalysis-based peroxidase-like activity assay of diatoms in the presence of Glu and GOx and controls.....</b>	<b>119</b>
<b>Figure 4.21 Characterisation of IONP-citrate micelles by DLS and zeta potential.....</b>	<b>120</b>
<b>Figure 4.22 Characterisation of IONP functionalised diatoms by SEM-EDX.....</b>	<b>121</b>
<b>Figure 4.23 Peroxidase-like activity assay of diatoms modified with IONPs and GOx (D-IONP-GOx) and control samples.....</b>	<b>122</b>
<b>Figure 4.24 Reaction scheme for the multistep synthesis of Diatom-anti-PD-L1 (D-aPDL1) as a sensing device for PD-L1.....</b>	<b>123</b>
<b>Figure 4.25 Overlay of XPS spectra of at D-amine and D-unmodified comparing the N 1s binding energy.....</b>	<b>124</b>
<b>Figure 4.26 XPS spectra of D-maleimide (top) and D-amine (bottom) comparing the C 1s binding energy.....</b>	<b>125</b>
<b>Figure 4.27 XPS spectrum of D-aPD-L1 analysing the C 1s binding energy.....</b>	<b>126</b>
<b>Figure 4.28 Reaction scheme for the covalent functionalisation of IONP with anti-PD-L1.....</b>	<b>127</b>
<b>Figure 4.29 Characterisation of IONP-Mal and IONP-aPDL1. (A) DLS by number distribution and (B) zeta potential in MilliQ water (average of 3 measurements).....</b>	<b>128</b>
<b>Figure 4.30 Functional PD-L1 ELISA of IONP-aPDL1.....</b>	<b>129</b>

<i>Figure 4.31 Developed method for biosilica-based PD-L1 sensor.</i>	130
<i>Figure 4.32 Peroxidase-like activity assay of the biosilica-based PD-L1 sensor. (A) Peroxidase-like activity assay of the control sample in the absence of PD-L1 and (B) D-PD-L1 biosensor.</i>	131
<i>Figure 5.1 Micromolding by casting for polymeric MN fabrication.</i>	140
<i>Figure 5.2 Design of HA-based biodegradable MNs and implantable devices for cancer immunotherapy.</i>	143
<i>Figure 5.3 Overview of NP systems and immunomodulatory agent incorporated into HA MNs and HA implants.</i>	144
<i>Figure 5.4 Photograph and SEM imaging of blank HA MNs.</i>	146
<i>Figure 5.5 Schematic of MN skin penetration experiment method.</i>	147
<i>Figure 5.6 MN porcine skin penetration experiment for 1h.</i>	148
<i>Figure 5.7 SEM of MN porcine skin penetration experiment for 1 h.</i>	149
<i>Figure 5.8 HAase incorporated MN porcine skin penetration for 1 h.</i>	150
<i>Figure 5.9 HA MN porcine skin penetration experiment for 24 h.</i>	151
<i>Figure 5.10 Images of HA MN porcine skin penetration experiment for 24 h.</i>	152
<i>Figure 5.11 Analysis of MN porcine skin penetration depth.</i>	152
<i>Figure 5.12 Co-culture cell viability assay of HA MNs.</i>	153
<i>Figure 5.13 QD MN loading characterisation by fluorescence microscopy.</i>	155
<i>Figure 5.14 Characterisation of IONP MNs.</i>	157
<i>Figure 5.15 IONP release study from IONP MNs over 24 h characterised by UV-vis spectroscopy.</i>	158
<i>Figure 5.16 DLS characterisation of IONPs released from IONP MN.</i>	159
<i>Figure 5.17 Peroxidase-like activity assay of IONPs after release from HA MN.</i>	160
<i>Figure 5.18 RP-HPLC characterisation of 1MT released from 1MT-HA MNs.</i>	161
<i>Figure 5.19 Images of a blank HA implantable disc as a biodegradable drug administration device.</i>	162
<i>Figure 5.20 IONP implant degradation experiment UV-vis characterisation.</i>	163
<i>Figure 5.21 DLS characterisation of IONP micelle released from IONP implant.</i>	164
<i>Figure 5.22 Peroxidase-like activity assay of IONP released from HA implant.</i>	165
<i>Figure 5.23 Transwell co-culture assay of IONP-DOTAP-pIC implant.</i>	166
<i>Figure 5.24 Characterisation of 1MT-HA implant degradation experiment by RP-HPLC.</i>	168
<i>Figure 5.25 Representative non-cell based IDO inhibition assay with the 1MT-HA implant. (A) Kynurenine calibration curve from 0-100 <math>\mu</math>M based on peak area at 360 nm (N = 1). (B) HPLC chromatograms of positive controls without the inhibitor (+Trp/-1MT) and with the inhibitor (+Trp/+1MT), negative control (-Trp/-1MT) and 1MT-HA implant sample (+Trp/+1MT-HA implant (0.5 mM 1MT)) (N = 1).</i>	169
<i>Figure 5.26 L-kynurenine calibration by RP-HPLC at UV absorbance detection of 360 nm (N = 3).</i>	170
<i>Figure 5.27 HeLa cell IDO inhibition screening at different concentrations of 1MT. (A) RP-HPLC characterisation of L-kynurenine produced by HeLa cells treated with 1MT at concentrations from 0 to 500 <math>\mu</math>M. (B) Graph representation of 1MT concentration to % IDO inhibition relationship. (C) MTT cell viability assay following HeLa cell incubation with 1MT samples for 20 h. % Cell viability presented in relation to -IFN-<math>\gamma</math>/-1MT control (N = 1).</i>	171
<i>Figure 5.28 Representative IDO inhibition assay with 1MT-HA implant using HeLa cells.</i>	172
<i>Figure 5.29 Representative IDO inhibition assay of different human cancer cell lines.</i>	174

<i>Figure 5.30 IDO inhibition assay of different murine cancer cell lines..</i>	175
<i>Figure 5.31 Representative IDO inhibition assay with 1MT-HA implant and controls using OVCAR8 cells.....</i>	176
<i>Figure 5.32 Representative IDO inhibition assay with 1MT-HA implant and controls using MC38 cells.....</i>	177

## List of Tables

<i>Table 1.1 Examples of PRRs association to PAMPs and their origin. ....</i>	3
<i>Table 3.1 Summary of the % 1MT released at the different pH conditions and timepoints based on the % 1MT modification yield by NMR.....</i>	90
<i>Table 5.1 Experimental conditions used for the analysis of IDO expression in different cancer cell lines. ....</i>	173

## List of Equations

<i>Equation 1.1 Fenton chemistry mediated IONP induced tumour cell ferroptosis. Fe(II)/Fe(III) undergo redox reactions in the presence of H<sub>2</sub>O<sub>2</sub> in the TME resulting in ROS generation. ....</i>	25
---	----

# Abbreviations

<b>APC</b> Antigen presenting cells	<b>IL</b> Interleukin
<b>BCC</b> Basal cell carcinoma	<b>IONP</b> Iron oxide nanoparticle
<b>BOC</b> Tert-butyloxycarbonyl	<b>LN</b> Lymph nodes
<b>CDI</b> Carbonyldiimidazole	<b>LRR</b> Leucine rich repeats
<b>CD</b> Cluster differentiation	<b>MAb</b> Monoclonal antibody
<b>CLSM</b> Confocal laser scanning microscopy	<b>MDSC</b> myeloid-derived suppressor cells
<b>CMC</b> Carboxymethyl cellulose	<b>MHC</b> Major histocompatibility complex
<b>Cy5.5</b> Cyanine 5.5	<b>MN</b> Microneedle
<b>DC</b> Dendritic cells	<b>MRI</b> magnetic resonance imaging
<b>DLS</b> Dynamic light scattering	<b>MTT</b> 3-(4,5-Dimethylthiazol-2-yl)-2,5-diphenyltetrazolium bromide
<b>DMAP</b> Dimethylaminopyridine	<b>MWCO</b> Molecular weight cut-off
<b>DMSO</b> Dimethylsulfoxide	<b>NF-<math>\kappa</math>B</b> Nuclear factor kappa B
<b>DSPE-PEG</b> 1,2-Distearoyl-sn-glycero-3-phosphoethanolamine-poly(ethylene glycol)	<b>NIR</b> Near infra-red
<b>EDTA</b> Ethylenediaminetetraacetic acid	<b>NK</b> Natural killer cells
<b>ELISA</b> Enzyme-linked immunosorbent assay	<b>NMR</b> Nuclear magnetic resonance
<b>FDA</b> Food and drug administration	<b>NP</b> Nanoparticle
<b>FITC</b> Fluorescein isocyanate	<b>OVA</b> Ovalbumin
<b>HA</b> Hyaluronic acid	<b>PBL</b> Peripheral blood lymphocytes
<b>HAase</b> Hyalunoidase	<b>PBS</b> Phosphate buffer saline
<b>IDO</b> Indoleamine-2,3-dioxygenase	<b>PCL</b> Polycaprolactone
<b>IFN</b> Interferon	<b>PDA</b> Photodiode array
	<b>PDI</b> Polydispersity index

<b>PDMS</b> Polydimethylsiloxane	<b>TBA-OH</b> Tetrabutylammonium hydroxide
<b>PEG</b> Polyethylene glycol	<b>TCR</b> T cell receptor
<b>PES</b> Polyethersulfone	<b>T<sub>eff</sub></b> T effector cell
<b>PHA</b> Phytohemagglutinin	<b>TEM</b> Transmission electron microscopy
<b>PLGA</b> Poly(lactic-co-glycolic acid)	<b>T<sub>g</sub></b> Glass transition temperature
<b>PMMA</b> Polymethyl methacrylate	<b>T<sub>h</sub></b> T helper cell
<b>Poly I:C</b> Polyinosinic:polycytidylic acid	<b>TIR</b> Toll interleukin receptor
<b>PSPD</b> Position sensitive photo-detector	<b>TLC</b> Thin layer chromatography
<b>PVA</b> Polyvinyl alcohol	<b>TLR</b> Toll-like receptor
<b>PVP</b> Polyvinylpyrrolidone	<b>TMB</b> 3,3',5,5'-Tetramethylbenzidine
<b>QD</b> Quantum dot	<b>T<sub>reg</sub></b> T regulatory cell
<b>SEM</b> Scanning electron microscopy	<b>1MT</b> 1-Methyl-DL-tryptophan
<b>SPION</b> Superparamagnetic iron oxide nanoparticle	

# **Chapter 1**

# **Introduction**

## 1.1 Defence mechanisms of the adaptive and innate immune system

The human immune system is a complex defence apparatus designed for the deterrence of foreign antigens such as those found on cancer cells and pathogens including bacteria, viruses, fungi, and parasitic organisms that compromise our health and essential biological functions.<sup>1</sup> The two main defence mechanisms in humans are the innate and adaptive immunity. The innate immune system is the first and the most rapidly acting form of defence comprising from a series of immune cells derived from stem cells found in bone marrow.<sup>2</sup> These cells contain germline-encoded receptors that recognise proteins, nucleic acids and glycans, which are frequently expressed on pathogenic organisms, known as pathogen-associated molecular patterns (PAMPs) including lipopolysaccharides (LPS), nucleic acids and other proteins found either on the cell membrane or intracellularly.<sup>3,4</sup> The main pattern recognition receptors (PRRs) include toll-like-receptors (TLR), nucleotide-binding oligomerization domain-like receptors (NLR), C-type lectin receptors (CLR) and RIG-1 like receptors (RLR).<sup>5,6</sup>

TLRs are the most thoroughly studied family of PRRs and defined as type I integral membrane glycoproteins consisting of an extracellular N-terminal ectodomain and intracellular toll-interleukin-1 receptor (TIR) domains. The ectodomain contains 19-25 leucine rich repeat (LRR) motifs made up from amino acid chains and is responsible for ligand binding, whereas the TIR domains direct the signalling response, which is typically triggered by ligand-mediated dimerization of TLRs and adaptor protein recruitment.<sup>7,8</sup> PRRs are also capable of recognising damage associated molecular patterns (DAMPs), defined as inflammatory signals expressed on damaged cells (**Table 1.1**).<sup>9</sup> Amongst the vigilantes of the innate immune system are macrophages, granulocytes, natural killer cells, mast cells, complement proteins and dendritic cells.<sup>1</sup> When a pathogen is identified, a signalling cascade is initiated that leads to the activation of inflammatory responses through typical inflammatory transcription factors, such as NF- $\kappa$ B, mitogen-activated protein kinase (MAPK) and AP-1.<sup>10,11</sup> An abundance of different types of proinflammatory cytokines and chemokines are released that either directly induce apoptosis in the pathogenic cells or alerts other immune cells for support.<sup>12,13</sup> Macrophages, dendritic cells, mast cells and granulocytes, including neutrophils, basophils and eosinophils, have a more extensive arsenal of defence mechanisms involving the digestion of pathogens by phagocytosis or macropinocytosis and orchestrate pathogen

targeted attacks involving nicotinamide adenine dinucleotide phosphate (NADPH) oxidase (NOX2) mediated reactive-oxygen-species (ROS) generation or the release of enzymes such as proteases, cathepsin G, cationic proteins, elastases, lysosome and defensins.<sup>1,14,15</sup> However, some pathogens do not express common PAMPs or have evolved to conceal them in order to blend in with healthy cells allowing them to proliferate and infiltrate the host without initial resistance.<sup>16</sup>

**Table 1.1 Examples of PRRs association to PAMPs and their origin.** The innate immune response towards foreign pathogens is mediated by PRR recognition of pathogenic proteins and damage signals.<sup>4,6,9,10</sup>

Group	PRR	Location	PAMP/DAMP	Organism
TLRs	TLR1/TLR2	Cell surface	Triacyl lipopeptides	Bacteria
		Cell surface	Diacyl lipopeptides	<i>Mycoplasma</i>
	TLR2	Cell surface	Lipoteichoic acid	Gram-positive bacteria
			Zymosan	Fungi
	TLR3	Cell surface	Envelope glycoproteins	Viruses
		Cell surface/ Endosome	dsRNA	Viruses
	TLR4	Cell surface	LPS	Gram-negative bacteria
			Envelope glycoproteins	Viruses
			Mannan	Fungi
			Glycoinositolphospholipids	Protozoans
TLR5	Cell surface	Flagellin	Flagellated bacteria	
TLR7/8	Endosome	ssRNA	Viruses	
TLR9	Endosome	CpG DNA	Bacteria, Viruses, Protozoans	
NLRs	NOD1	Cytoplasm	Peptidoglycan	Gram-negative bacteria
	NOD2	Cytoplasm	Peptidoglycan	Gram-positive bacteria
	NALP3	Endosome	Adenosine triphosphate, uric acid crystals, muramyl dipeptide	Bacteria, Viruses
RLRs	RIG-I	Cytoplasm	dsRNA	Viruses
	MDA5	Cytoplasm	dsRNA	Viruses
CLRs	Dectin-1	Cell surface	B-Glucans	Fungi



DC-SIGN	Cell surface	Glycoprotein	Viruses
---------	--------------	--------------	---------

The adaptive immune response, which is developed only in vertebrates, steps into action when the innate immunity has been outmanoeuvred and is no longer able to combat the disease on its own. The adaptive immune system acts by identifying pathogen-expressed antigens and producing immunomodulatory molecules that specifically seek out and destroy molecules expressing those antigens.<sup>17</sup> The clonal selection theory proposed by Sir Macfarlane Burnet in 1957, which now is a widely accepted principle of immunology, postulates that only those lymphocytes that are actively stimulated by antigens survive and proliferate, whereas lymphocytes that remain inactive or self-react with each other are eliminated from the vast lymphocyte repertoire.<sup>18</sup> His theories paved the way for the understanding of the complexity of cells and mechanisms of the adaptive immunity.

Additional to their inflammatory innate immune responses, macrophages and dendritic cells function as mediators of the adaptive immune system by digesting pathogens and expressing their protein fragments via the major histocompatibility complex (MHC) class I or II membrane proteins.<sup>19,20</sup> Once exposed to a foreign antigen, they mature to become antigen presenting cells (APCs) with the mission of travelling through the lymphatic system to the draining lymphoid tissue including lymph nodes, spleen, Peyer's patches and mucosal tissues, where the pathogen-associated antigens are presented to receptors of naïve T cells that mature into antigen-specific T cell (**Figure 1.1 A**).<sup>21</sup> Effector T cells are classified into helper T cells (e.g. CD4<sup>+</sup> T cells), cytotoxic T cells (e.g. CD8<sup>+</sup> T cells and NK T cells) and regulatory T cells (Treg). Some immune cells including  $\gamma\delta$  T cells and NK T cells can carry out both innate and adaptive immune responses via a MHC-independent antigen presentation pathway.<sup>22,23</sup> CD4<sup>+</sup> T cells are activated via MHC class II-mediated antigen presentation and can be subcategorised into T helper (Th) cells, Th1, Th2, and Th17, each dominated by their unique set of immunostimulatory pathways. Th1 cells specialise in activating macrophages through the release of cytokines, interferon-gamma (IFN- $\gamma$ ) and tumour necrosis factor-beta (TNF- $\beta$ ), while Th2 cells preferentially induce B cell activation with the secretion of interleukins.<sup>24</sup> Th17 cells were discovered more recently and have been found to promote inflammatory responses and neutrophil development accompanied by the upregulation of several interleukins and TNF- $\alpha$ .<sup>25</sup> Regulatory T cells (Tregs) are an immune inhibiting phenotype of CD4<sup>+</sup> T cells, characterised by the expression of forkhead box P3 (FoxP3) transcription factor, and are responsible for the control of effector T cell production.<sup>26</sup> Tregs are known to adopt an important role against autoimmune diseases but can also have negative effects when they are used to the advantage of the disease, for instance, in the context of cancer

development.<sup>27</sup> Mature cytotoxic CD8<sup>+</sup> T cells recognise and eliminate infected cells expressing antigens presented through MHC class I specific to the antigens that the T cells were primed against.<sup>28</sup>

Another vital lymphocyte group of the adaptive immune system are B cells that release antibodies upon antigen presentation. Antibodies or immunoglobins consist of a constant and variable region made up by light and heavy chains. The light and heavy chains of the variable region complement each other to form the antigen-binding-site and determine its specificity.<sup>29</sup> B cells that encounter a foreign antigen engulf and degrade the pathogen and present that specific antigen to Th cells via MHC class II. This interaction, typically accompanied by co-stimulatory CD40 ligand-receptor binding, results in the activation of B cells and differentiation into plasma cells enabling the release of antigen-specific immunoglobins (**Figure 1.1 B**).<sup>30</sup> B cell activation is also possible without Th cell-mediated stimulation by producing antibodies directly in response to interaction with microbial constituents. This is known as the thymus-independent pathway and occurs predominantly in individuals exhibiting a deficiency of T cells.<sup>31</sup> Similar to innate immune cells, lymphocytes of the adaptive immune system are generated and develop from stem cells in the primary lymphoid organs including the bone marrow and thymus with the latter being prevalent for the development of T-cells.<sup>32</sup>

Pathogens that are targeted by cytotoxic lymphocytes via an antigen-specific pathway are subjected to a cascade of cytolytic proteins such as granzymes and perforins that induce apoptotic cell death.<sup>33</sup> Alternatively, cell lysis can also be activated by cytokine mediated ROS generation or through the FasL and TNF-related apoptosis-inducing ligand (TRAIL) receptor transduction pathway (**Figure 1.1 C**).<sup>34,35</sup> Lymphocytes that remain after the foreign antigen has been eliminated are known as memory cells that guarantee a more rapid and effective response if the pathogen is encountered again by lowering the activation threshold for antigen-specific T cell and B cell development and proliferation.<sup>36</sup> Cytotoxic lymphocytes development and activity is not immediate and usually transpires with a delay of several days after initial pathogen recognition, prior to which the host relies solely on the innate immune response.<sup>37</sup> This accentuates the importance of both the adaptive and innate immunity collaborating to identify and abolish foreign antigens from the system. Our fundamental and constantly evolving knowledge of human immunology has been one of the most important steppingstones in the design of novel vaccines, therapies, and diagnostic tools for a variety of diseases including cancer and will undoubtedly continue to be pivotal for the future developments.

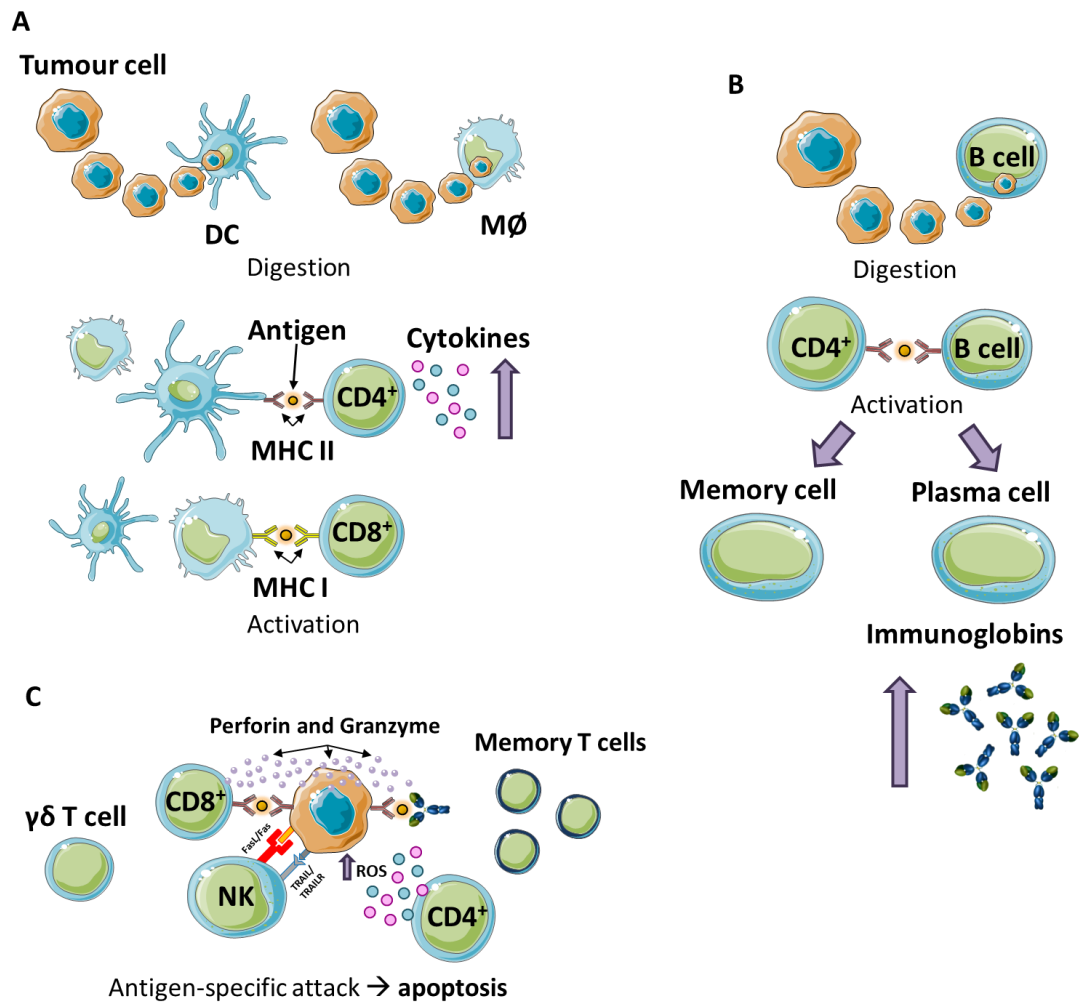


**Figure 1.1 Schematic representation of the adaptive immune mechanisms acting on tumour cells.** (A) The digestion of cancer cells by dendritic cells and macrophages leads to their maturation into APCs that present the tumour-associated antigens to naïve T-cells in the lymph nodes. (B) B-cells develop into plasma cells that produce tumour antigen-specific antibodies. (C) Following antigen presentation, T-cells develop into effector T cells that seek out and eliminate the cancer cells through various signalling pathways. Memory T cells and memory B cells are recruited to ensure a prolonged antigen-specific response against recurrence. DC-Dendritic cell; Mφ-Macrophage.

## 1.2 Immune evasive mechanisms of tumour cells

Human cancers are known to manifest themselves in response to internal or external risk factors. While certain recreational drug consumptions, diets, prolonged exposure to carcinogens and some health conditions have been shown to enhance the probability of cancer development, carcinogenesis can often be correlated to errors in DNA replication during cell repair, in the absence of external triggers.<sup>38,39</sup> Some of the known external stimuli are associated with cigarette smoking, alcohol, red meat consumption, UV exposure, bacteria and viruses.<sup>40-45</sup>

Cancers are also known to arise in the absence of exogenous stimulation due to old age or through non-sporadic inheritance of cancer predisposition genes. Due to the constant cell division during the lifetime of any individual, cell mutations are not uncommon, but are usually harmless and corrected by the DNA repair system.<sup>46</sup> As an individual ages, long-lived cells, including stem cells, accumulate DNA damage due to repeated exposure to oxidative stress correlated to the natural cell metabolism. Consequently, the risk of genomic instability increases leading to a higher incidence of somatic cell mutations that result in modifications of DNA protein sequencing and the cell cycle regulatory system.<sup>47</sup> However, cancer development is not limited to defects in DNA sequencing but is also correlated to epigenetic alterations such as chromatin remodelling, a compromised proteostasis, related to the maintenance of intracellular and extracellular protein homeostasis, and telomere shortening.<sup>48</sup> Chromatin alterations, including DNA methylation, phosphorylation, acetylation, citrullination and ubiquitination, are processes that have been associated with cancer development.<sup>49</sup>

The exact series of biological events leading up to the initiation of mutagenesis and to what extent they are preventable is up to this day not fully understood, but significant progress has been made in the identification of genes that are involved in cancer susceptibility due to their high likelihood to undergo anomalous somatic mutation, which is often provoked by a damaged DNA repair network.<sup>38,50</sup> There are two groups of genes directly associated with cancer susceptibility, namely, proto-oncogenes and tumour suppressor genes.<sup>51</sup> Proto-oncogenes include a variety of genes that are prone to turn cancerous upon mutation and are mainly engaged in cell proliferation signalling, whereas tumour suppressor genes are responsible for the surveillance of DNA repair, apoptosis signalling and inhibition of cell division processes.<sup>51,52</sup> Examples of oncogenes include human epidermal growth factor receptors (HER-2 and EGFR), vascular endothelial growth factor receptors (VEGFR) and the BCR-ABL fusion gene, all of which exhibit a functional role in the tyrosine kinase enzyme activity that mediates cell proliferation, apoptosis and other cell metabolic processes.<sup>53,54</sup> Oncogenes have been shown to not only be involved in the initiation of neoplasia, but also in its progression and maintenance. However, some studies have revealed that the upregulation of certain oncogenes does not inherently favour tumour development and, in certain cases, has been shown to promote cell apoptosis or senescence, a phenomenon in which the cell terminates proliferation activity but does not undergo cell death.<sup>55,56</sup> One of the most critical tumour suppressor genes is p53, which is inactivated in approximately 50% of human cancers.<sup>57</sup> It regulates the activation of oncogenes and DNA damage by

upregulating the transcription of pro-apoptotic proteins, PUMA and NOXA.<sup>57,58</sup> Other common tumour suppressor genes include RB1 and BRCA1, which are mutated in a variety of cancers, but predominantly in retinoblastoma and breast cancers, respectively.<sup>59,60</sup> A portion of these cancer-associated genes are relevant predisposition genes inherited from a previous generation of ancestors. The inherited allele of a mutated predisposition gene is usually not harmful, because the second allele of that gene is able to rectify its functionality. However, if the second allele is subjected to mutation instigated by one of the many possible mechanisms described above, the gene can no longer carry out its function and emerges as carcinogenic. Hence, the higher risk of cancer development in individuals with predisposition genes is due to the induction of carcinogenesis after a single somatic mutation, unlike sporadic cancers that require two mutations of a gene.<sup>61</sup>

In order to consolidate the diversity of mechanistic processes that enable human tumour growth and survival within an inherently rigorous and intelligent immune system, Weinberg *et al.* proposed six core hallmark capabilities with two additional emerging hallmarks and a pair of enabling characteristics (**Figure 1.2**).<sup>62</sup>



**Figure 1.2 Hallmarks of cancer.** Core hallmarks (dark blue), emerging hallmarks (light blue) and enabling characteristics (grey). Reproduced from Weinberg et al.<sup>62</sup>

The cancer initiation mechanisms have been discussed above, but tumour progression implicates a series of additional strategies that are developed at a later stage, in which malignant cells acquire certain features that enable them to grow, metastasise whilst evading immune detection and attack.<sup>63</sup> The human immune system is constituted by an innate and adaptive immune response to foreign pathogens as discussed in the previous section. However, cancer cells are highly adaptive to the mechanisms of our defence system and evolve to avoid its detection in a process known as immunoediting that consists of three stages: elimination, equilibrium and escape (**Figure 1.3**).<sup>64,65</sup> In the first stage, immune cells are initially able to identify tumour-associated antigens (TAAs) and tumour-specific mutant antigens (TSMAs) and prime antigen-specific lymphocytes, including CD4<sup>+</sup> T helper cells, CD8<sup>+</sup> T cells, NK T cells, B cells and memory cells, towards tumour cells and effectively eliminate them.<sup>66</sup>

At this stage, tumour cells enter an equilibrium phase in which immune cells are actively constraining tumour development by eliminating immunogenic tumour cells, while the less immunogenic cells remain dormant until they are eventually eradicated or undergo epigenetic alterations that enables anti-tumour immune evasion.<sup>67</sup> Memory T and B cells ensure that

tumour dormancy is retained for years before the balance between anti-tumour immunity and tumour immune evasion is disrupted and progression in either direction incurs.<sup>68</sup> The third stage of immunoediting involves immune escape and this is commonly enacted by the downregulation or complete inactivation of the MHC class I protein, which is essential for antigen presentation to adaptive immune cells and recognition by CTL.<sup>69</sup> MHC class I expression can be inhibited through mutation of transport molecules to the cell membrane such as  $\beta$ 2-microglobulin, downregulation of transporter associated with antigen processing (TAP), loss of transcription factors and DNA methylation.<sup>70,71</sup> T cell anergy is also induced by cancer cell secretion of immunosuppressive agents including transforming growth factor beta (TGF- $\beta$ ), indoleamine 2,3-dioxygenase (IDO), prostaglandin-E2 (PGE2), arginase and extracellular adenosine.<sup>72,73</sup> Hypoxia and certain oncogenes can activate angiogenic signalling proteins such as vascular endothelial growth factor (VEGF) that promotes tumour growth and is also known to inhibit DC maturation.<sup>74</sup> NK cells recognise and induce apoptosis in cancer cells overexpressing the MICA/MICB surface proteins through the distinctive NKG2D receptor stimulation pathway.<sup>75</sup>

In the immune evasion stage, tumour cells can undergo epigenetic silencing that allows them to shed these surface proteins in order to avoid NK detection and destruction.<sup>76</sup> The recruitment of inflammation-mediated Tregs, myeloid-derived suppressor cells (MDSCs) and tumour-associated macrophages (TAMs) aid in the creation of an immunosuppressive tumour microenvironment.<sup>77</sup> Activated macrophages can either polarise towards a proinflammatory M1 phenotype or an anti-inflammatory and immunosuppressive M2 phenotype. TAMs are associated with the M2 phenotype, which promote tumour progression through angiogenesis signalling, aiding metastasis and the upregulation of immunosuppressive growth factors (e.g. TGF- $\beta$  and VEGF), cytokines (e.g. IL-10 and IL-6) and enzymes (e.g. IDO and arginase), further establishing a favourable microenvironment in which the cancer is enabled to thrive.<sup>78</sup> IDO and arginase exhibit the functions of catabolising L-tryptophan and L-arginine, respectively, which consequently results in upregulation of Tregs that downregulate the generation and proliferation of immunostimulatory effector T cells.<sup>79</sup>

Inhibitory T cell receptors, such as cytotoxic T lymphocyte antigen-4 (CTLA-4) and programmed death-1 (PD-1), found on the tumour cell surface are another important composite of the immune evasion network that inactivates antigen receptor recognition of tumour cells by antigen-specific CTLs.<sup>80</sup> The ability of tumours to alter their metabolisms is one of the emerging hallmarks and cancer cells achieve this by reprogramming their glucose

metabolism via a glycolysis-favoured pathway. This energy producing pathway is beneficial, as it is not hindered by the hypoxic environment frequently found in tumours. The considerably lower ATP production compared to the traditional oxidative phosphorylation process is compensated by increasing the glucose influx into the tumour cells through upregulation of glycolytic enzymes and glucose transporters, such as GLUT1. The oncoprotein, K-Ras, and the hypoxia both induce hypoxia regulating transcription factors that upregulate glycolysis in order to sustain tumour cell survival.<sup>81</sup> In some cases, cancers have further adapted by utilising lactate, a glycolysis waste product, as an energy source for a subpopulation of tumour cells and, thereby, enable their growth.<sup>82</sup>

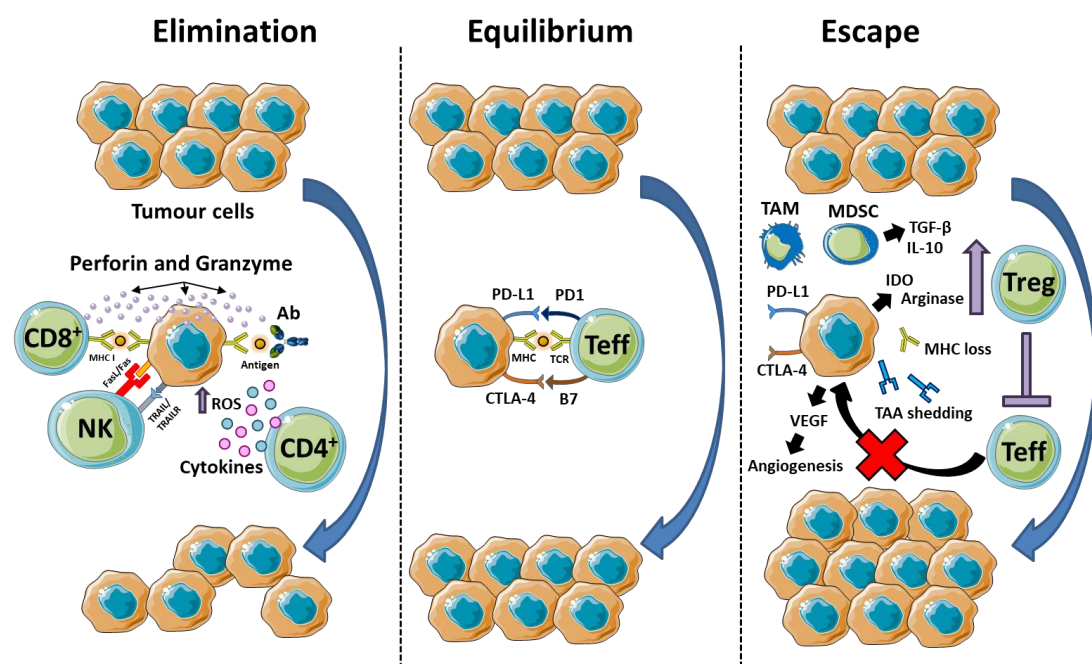


**Figure 1.3 Schematic illustration of the mechanisms involved in cancer immunoediting.** The 3 stages of cancer immunoediting are: Elimination in which cancer cells are recognised and effectively abolished by the adaptive immune system. Equilibration occurs when some cancer cells are eliminated, but other less immunogenic tumour cells avoid immune recognition. In the Escape stage, cancer cells develop an immunosuppressive microenvironment by surrounding themselves with cells that release immunosuppressive signals and shed antigens to avoid immune detection.

With such a vast display of immunosuppressive and immune stimulating signalling occurring simultaneously and persistently, the outcome of the disease, ultimately, comes down to an imbalance in the conflict between the anti-tumour immune responses and the tumour escape forces that leads to either cancer suppression or cancer progression and metastasis. The multitude of tumour-associated immune evasive mechanisms that are currently known are potentially only a small fraction of all the viable pathways yet to be discovered.<sup>83</sup> Many of the tumour-specific or tumour-overexpressed targets have already been exploited for the



development of novel cancer immunotherapies and combination therapies with some clinical success.<sup>84</sup> Our increasing knowledge of tumour evasive strategies and progress in developing vaccines that can reverse or inhibit them, forecasts a promising future for immunomodulatory cancer therapeutics.

### 1.3 Cancer immunotherapy

In 1891, William B. Coley, who is widely accepted as the founding father of cancer immunotherapy, was the first to attempt to therapeutically harness the immune system in patients with bone sarcoma that developed erysipelas by injecting the patients with mixtures of activated and inactivated *Streptococcus pyogenes* and *Serratia marcescens* bacteria, termed 'Coley's toxin'.<sup>85,86</sup> It achieved complete tumour remission in some patients with different cancer types including sarcoma, testicular carcinoma and lymphoma, but the unknown underlying immunological mechanisms and the high risks of infecting patients with pathogenic bacteria led to scepticism amongst oncologist worldwide.<sup>87</sup> Thereafter, the opportunities of immunotherapy were elucidated with advances in immunology such as the discovery of cancer immunosurveillance,<sup>88</sup> followed by the discovery of T cells, B cells, and dendritic cells.<sup>89,90</sup> The attention of oncological research towards immunotherapies began to escalate with the clinical approval of the lymphocyte-activating cytokines, recombinant human IFN- $\alpha$ -2b for the treatment of hairy cell leukaemia and high-dose IL-2 in patients with metastatic melanoma and renal cell carcinoma.<sup>91,92</sup>

Despite high clinical success in a small group of patients, the response rate of these treatments was mostly moderate, cancer type specific and associated with a high risk of developing autoimmune-related adverse effects.<sup>93</sup> The breakthrough came with the discovery of the immune checkpoints, cytotoxic T-lymphocyte-associated protein (CTLA-4) and programmed cell death protein 1 (PD-1) by James P. Allison and Tasuku Honjo, respectively, who were both awarded the 2018 Nobel prize in Physiology or Medicine for their pioneering work.<sup>94</sup> The discovery and clinical success of the immune checkpoint inhibitor therapies paved the way for a rapidly increasing interest in the field and novel developments in cancer immunotherapies and combination therapies. Current immunotherapies can be categorised into immune checkpoint inhibitors, monoclonal antibodies, adoptive T cell therapies, cytokines, cancer vaccines, oncolytic viruses, and adjuvants. The following sections describe some of these immunotherapeutic approaches and discuss the mechanism of action and clinical impact of these treatments.

### 1.3.1 Immune checkpoint inhibitors and co-stimulators

Immune checkpoints are cell surface proteins that are expressed on a variety of immune cells, but also overexpressed on cancer cells and have an immunosuppressive function involving the inhibition of cytotoxic T cells activation via TCR-mediated tumour-associated antigen recognition.<sup>95</sup> The discovery of the checkpoints CTLA-4 and PD-1 was a breakthrough in immunotherapy as it showed exceptionally high clinical success in some cancers that had failed to be eradicated by conventional chemotherapies and radiotherapies.<sup>96</sup> CTLA-4-targeted therapies were first FDA-approved in 2011 and branded ipilimumab, while nivolumab became the first FDA-approved PD-1 inhibitor, for the treatment of melanoma.<sup>97</sup> CTLA-4 expressed on T cells compete with the costimulatory receptor CD28 for ligand binding to the molecules, B7-1 and B7-2, on tumour cells.<sup>98</sup> The costimulatory effect from CD28-B7 interaction results in T cell activation and proliferation, while CTLA-4 aims to inhibit this interaction and it known to have more affinity for the competing ligands. Its other immunosuppressive pathways are mediated by preventing the release of T cell stimulatory cytokines and recruitment of signalling proteins that inhibit transcription factors affiliated with T cell activation.<sup>98</sup> PD-1 is mostly expressed on T and B lymphocytes and upregulated by signalling via the PI3K-Akt protein kinase pathway and pro-inflammatory cytokine secretion including IFN- $\gamma$ , TNF- $\alpha$  and IL-2 (**Figure 1.4**).<sup>99</sup>

More recently an alternative pathway through STAT3 transcription in combination with IL-6 generation has demonstrated to enhance PD-1 expression.<sup>100</sup> This checkpoint protein is activated upon binding to PD-L1 or PD-L2 receptors on cancer cells, but the latter has less affinity for PD-1 and its immunosuppressive properties are not well established. Upon ligand binding, effector T cell proliferation and cytokine upregulation is inhibited, while Tregs production is increased, which promotes tumour cell growth and immune evasion. In addition to its role in T cell energy, PD-1 promotes the generation of anti-inflammatory IL-10 that helps forge an immunosuppressive microenvironment.<sup>99</sup> Tregs, abundantly found in the tumour microenvironment, are known to express PD-1 and can differentiate naïve CD4<sup>+</sup> T cells into Tregs in the presence of the co-receptor CD3 and TGF- $\beta$ .<sup>101</sup> The mechanism by which B cell activation is inhibited by PD-1 has not been fully elucidated, but studies have shown correlation between mature B cell-mediated antigen-specific antibody activity and PD-1 inhibition.<sup>102</sup> Clinical studies on cancer patients co-administered with PD-1 and CTLA-4 inhibitors have shown enhanced therapeutic benefit compared to the response observed with individual treatments but was correlated with an elevated risk of developing autoimmune diseases (**Figure 1.4**).<sup>103</sup>

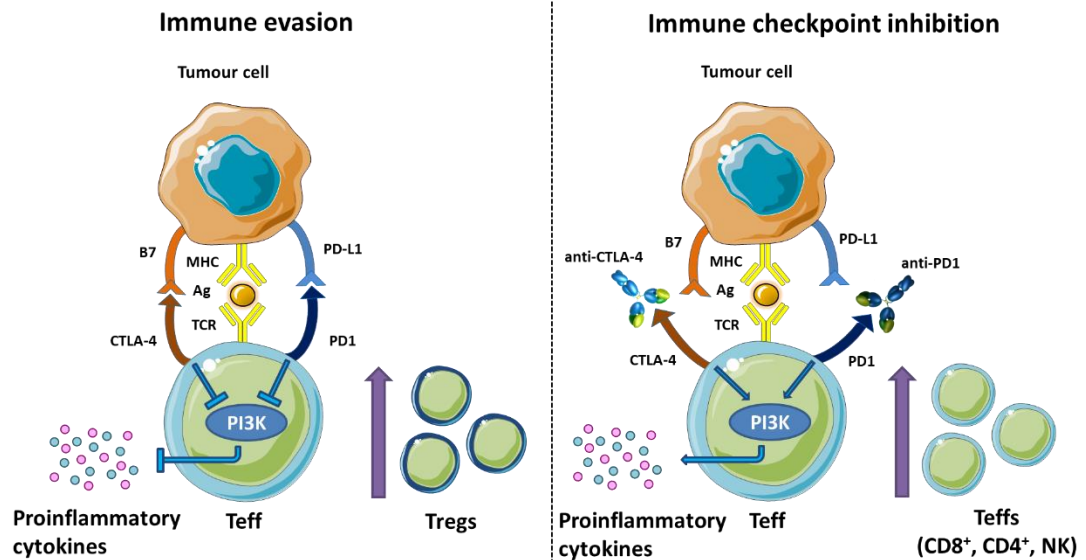


**Figure 1.4 Immune checkpoint inhibition mechanisms of anti-PD-1 and anti-CTLA-4.** Tumour cells avoid adaptive immune recognition via the expression immune checkpoints that are found on tumour cell and  $T_{eff}$  cell surfaces. Immune checkpoint inhibitors such as anti-PD-1 and anti-CTLA-4 blocks the interaction of the checkpoint proteins with their respective ligands on tumour cells leading to the recovery of cancer immunosurveillance. Ag -Antigen; TCR - T cell receptor;  $T_{eff}$  - effector T cell; Tregs - regulatory T cells.

Currently, several other inhibitors of PD-1 and its ligands have been approved worldwide for the treatment of a multitude of cancers, such as atezolizumab for the treatment of bladder cancer and avelumab for Merkel cell carcinoma therapy.<sup>104</sup> The motivation to discover the next generation of immune checkpoint targets has led to the investigation of novel candidates, some of which showed promising results in clinical trials. Immune checkpoint-targeted drugs are categorised into inhibitors and co-stimulatory molecules. Due to their relatively low therapeutic response compared to PD-1 inhibitors, these drugs are mostly studied in combination with other immune checkpoint inhibitors in clinical and pre-clinical settings.<sup>105</sup>

IDO is an immunosuppressive heme-bearing enzyme overexpressed on tumour cells including melanoma, ovarian cancer, colorectal cancer, sarcoma, and chronic lymphocytic leukaemia. It's structure and composition were presented by Sugimoto *et al.* and consists of a large and small domain connected by a long loop, of which the  $\alpha$  and  $3_{10}$  helices of the large domain created the hydrophobic pockets containing the ferrous Fe-heme groups (**Figure 1.5 A**).<sup>106</sup> It is responsible for L-tryptophan metabolism via the kynurenine pathway. The reaction is initiated by the incorporation of oxygen that leads to cleavage of the double bond at the 2,3 position of the indole group that results in the formation of N-formylkynurenine before it is enzymatically reduced to L-kynurenine (**Figure 1.5 B**).

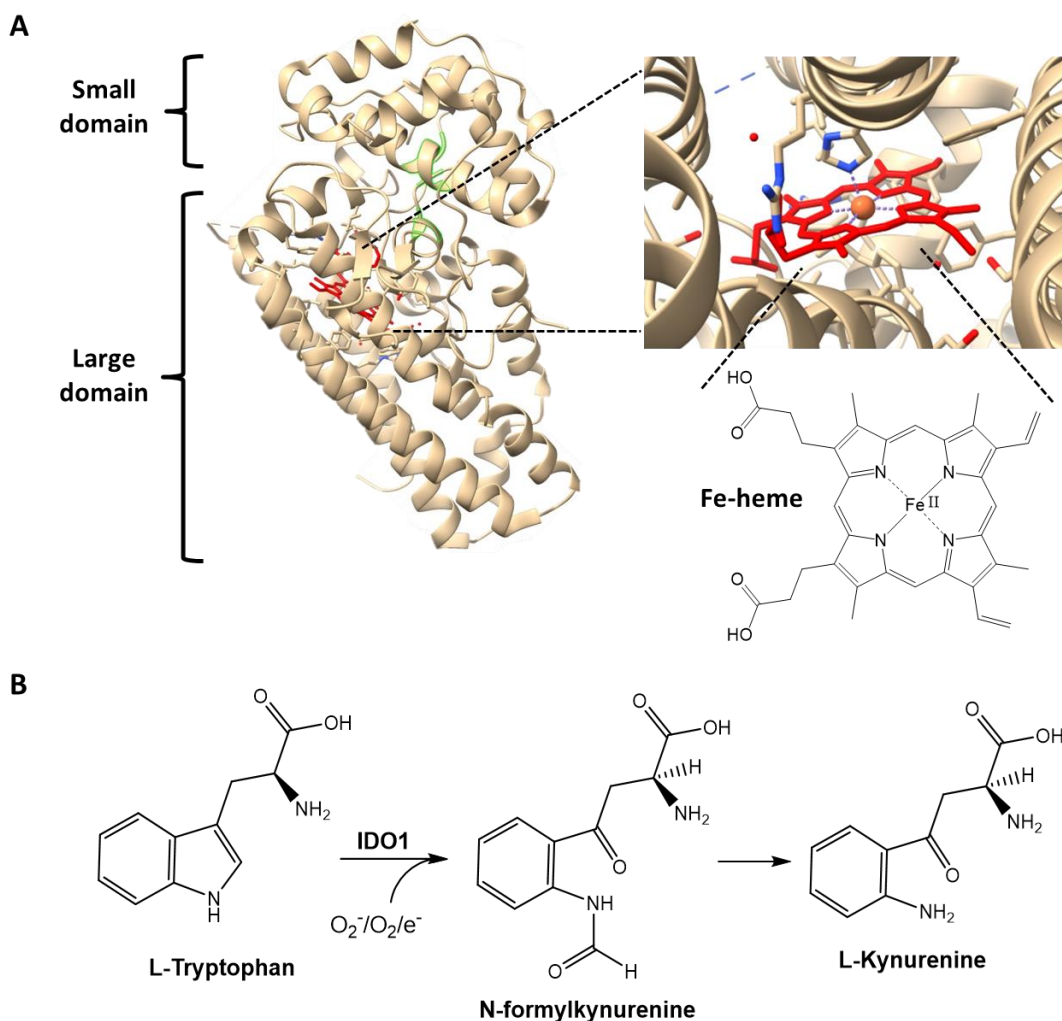


**Figure 1.5 Structure and function of the tumour overexpressed IDO1 immune checkpoint.** (A) IDO1 crystal structure with illustration of the Fe-heme moiety residing in the hydrophobic pockets. (B) Reaction scheme of IDO1 metabolism of L-tryptophan via the incorporation of oxygen into the N-formylkynurenine intermediate, which is then enzymatically reduced to L-kynurenine.

The same research group also proposed a mechanistic route for the tryptophan metabolism involving the oxygen transfer from the Fe-heme group to the substrate. The first step of the reaction involves the proton transfer from the HN-indole group of tryptophan, followed by an electrophilic addition reaction to form a dioxetane intermediate species. The oxidation of this molecule to N-formylkynurenine precedes the formation of kynurenine in the presence of  $H_2O$  and kynurenine formamidase, releasing formic acid as the by-product (**Figure 1.6**).

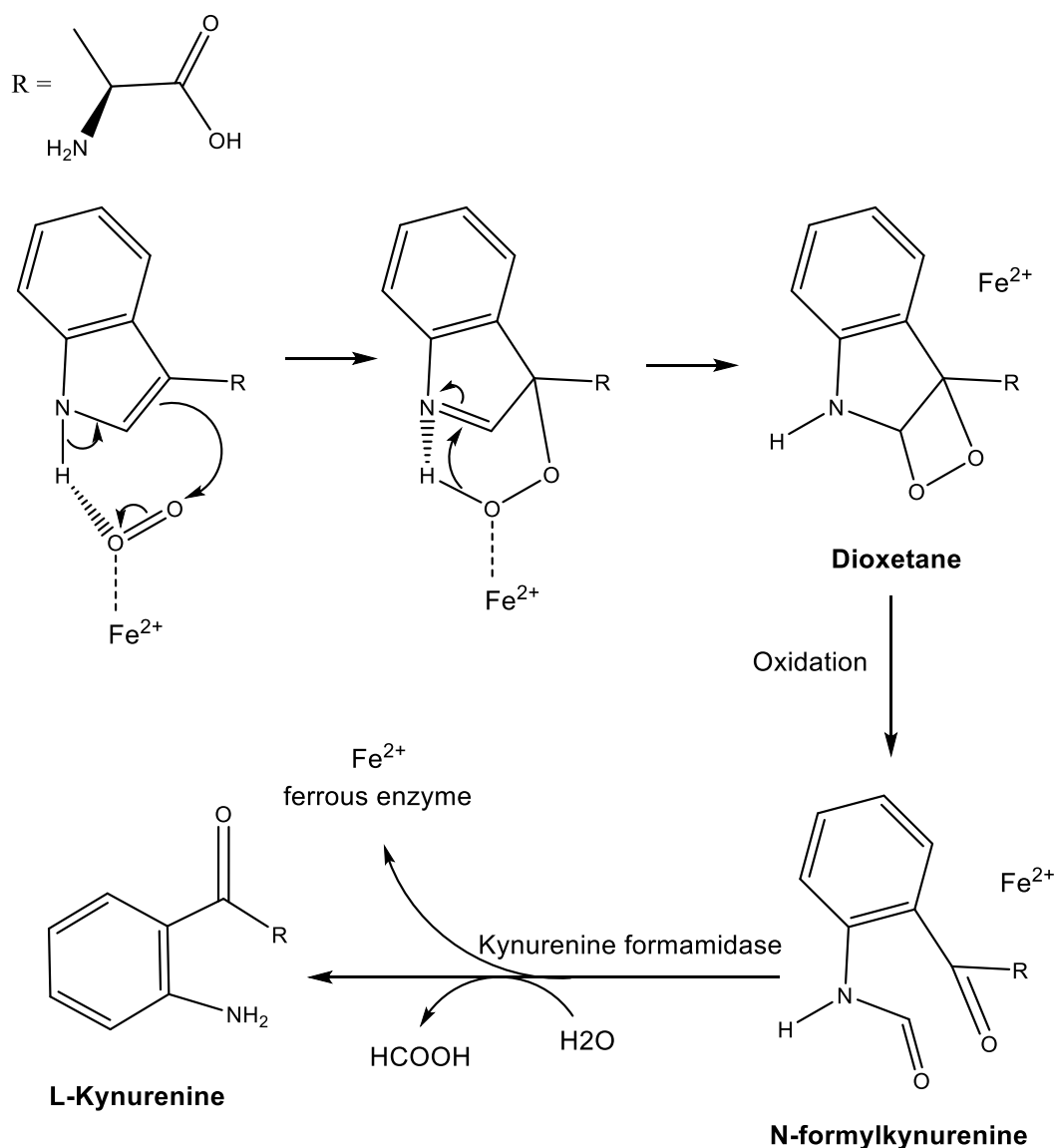


**Figure 1.6 Mechanism of tryptophan metabolism.** The mechanism is initiated by the interaction of NH proton of the indole group with the dioxygen species of  $\text{Fe}^{2+}$  from the heme group in its ferrous state. The Kynurenine formation proceeds via a dioxetane intermediate that oxidises to N-formylkynurenine followed by kynurenine formamidase-mediated L-kynurenine formation.<sup>106</sup>

As mentioned earlier, IDO yields T cell energy by metabolising tryptophan that terminates with the production of kynurenine resulting in the upregulation of Tregs. IDO expression is dependent on proinflammatory  $\text{IFN-}\gamma$  activity in the tumour microenvironment. 1-methyl-tryptophan, also known as indoximod, is currently undergoing phase II clinical trials with a promising objective response rate of 52% in melanoma patients by oral administration in combination with CTLA-4 or PD-1 inhibitors.<sup>107</sup> In another phase I/II trial, the IDO inhibitor epacadostat is being investigated with a 75% objective response rate in melanoma patients, while barely any response was observed for other cancer types such as colorectal cancer.<sup>108</sup>

However, some patients in this trial abandoned the treatment due to severe adverse effects. Other noteworthy checkpoint inhibitor targets in advanced clinical trials are T cell immunoglobulin and mucin-domain containing-3 (TIM-3), expressed mostly on NK cells, T cell immunoglobulin and ITIM domain (TIGIT), lymphocyte activation gene-3 (LAG-3), which is found on both T cells and NK cells, and V-domain Ig-containing suppressor of T-cell activation (VISTA).<sup>109</sup>

OX40 is a co-stimulatory glycoprotein and a member of the tumour necrosis factor receptor family that is mostly expressed on T cells and NK cells potentiating their survival and proliferation through NF- $\kappa$ B and nuclear factor of activated T-cells (NFAT) signalling pathways.<sup>110</sup> Its activation is enabled by binding to the OX40L ligand, also referred as CD252, on APC and leads to the downregulation of Tregs and other immunosuppressive cytokines, possibly by direct inhibition of the Treg-associated gene, FoxP3.<sup>110</sup> The OX40L-Fc fusion protein has shown promising results in preclinical studies in combination with anti-OX40 antibodies and demonstrated activation of T cells, DCs and vascular endothelial cells within the TME.<sup>111</sup> Schreiber *et al.* derived that OX40L-Fc binds to PD-1 and OX40 simultaneously, thus, enhancing the immunostimulatory effects of both target treatments using a single agent.<sup>112</sup> 9B12 is a murine-based monoclonal antibody that stimulates OX40 expression and was studied in a phase I clinical trial on solid metastatic cancer with partial tumour regression in 12 out of 30 patients and no severe toxicity.<sup>113</sup> Glucocorticoid-induced TNF receptor family-related protein (GITR), inducible co-stimulator (ICOS), and CD40 are amongst other co-stimulatory immune checkpoint targets currently under investigation in human clinical trials for immunotherapy of various cancer types (**Figure 1.7**).<sup>114</sup> Since the discovery of PD-1 and CTLA-4 inhibitors, the development of novel immune checkpoints inhibitors and co-stimulators has made rapid progress with many agents being approved for clinical testing either as monotherapies or combination therapies. Given the relatively early age of immune checkpoint research, it seems promising that the full potential of these immunotherapeutic agents is yet to be unveiled in the coming years.

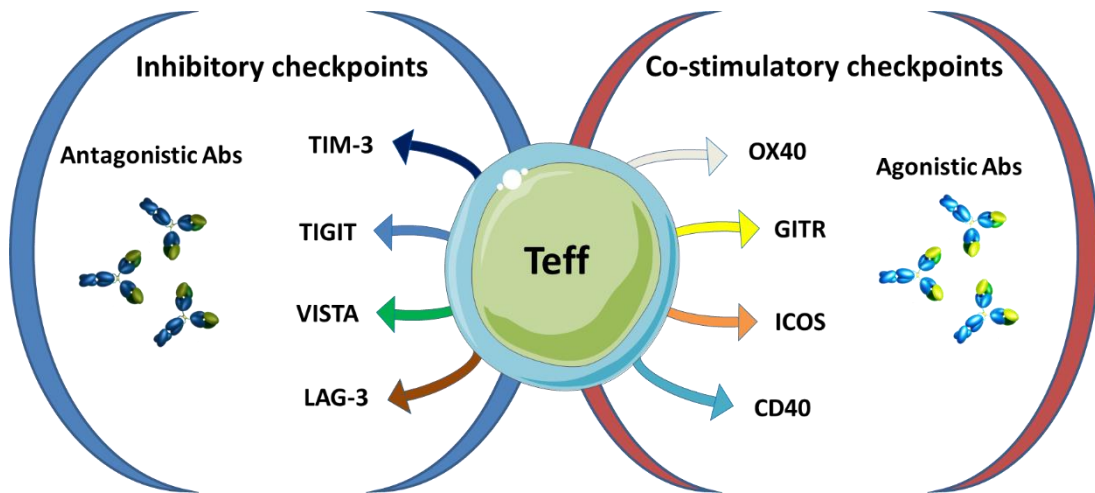


**Figure 1.7 Examples of clinically investigated immune checkpoints.** Immune checkpoints are classed into inhibitory checkpoints that favour tumour progression via immunosuppressive signalling, and co-stimulatory checkpoints that activate the adaptive immune system and promote an immunostimulatory response.

### 1.3.2 Adjuvants

Cancer vaccines and other immunotherapies are often co-administered with immunostimulatory molecules, termed adjuvants, that enhance the overall therapeutic efficiency and stimulate an immune response against tumour cells. Adjuvants do not elicit directly anti-tumour activity, but instead promote cytokine production and maturation of dendritic cells and other immune cells leading to antigen presentation and activation of effector T cells.<sup>115</sup> TLR agonists are a type of adjuvant commonly investigated for immunotherapy and currently there are three TLR agonists approved for clinical use against cancer in the US, namely Imiquimod, monophosphoryl lipid A (MPLA) and Bacillus Calmette-Guérin (BCG).<sup>116</sup> Imiquimod has been approved for the treatment of basal cell carcinoma and is an imidazoquinoline-like molecule that binds to the intracellular TLR7 resulting in APC maturation and Th cell activation through the release of cytokines, prominently IFN- $\gamma$ , TNF- $\alpha$  and IL-12.<sup>117</sup> The TLR4 agonist MPLA is derived from lipopolysaccharide (LPS) and in clinical use for the treatment of human papilloma virus (HPV)-induced cervical cancer. It functions as an adjuvant by activating APCs through TRIF and MyD88 dependent pathways that induce pro-inflammatory cytokine stimulation.<sup>118</sup> BCG, a TLR2/4 heterodimer agonist, is derived from a weakened bacterial strain of *mycobacterium bovis* and FDA approved for bladder cancer therapy, but despite its clinical success, the precise immunomodulatory mechanisms remain under investigation.<sup>119</sup> The TLR9 agonist, CpG ODN, TLR7/8 agonist, resiquimod, and TLR3 agonist poly-IC are further adjuvant examples that are currently investigated in clinical trials for the treatment of several cancer types (**Figure 1.8**).<sup>120,121</sup> Some studies have also

shown tumour-stimulating effects in response to TLR stimulation, such as LPS-based TLR4 agonist derived from *helicobacter pylori* promoting tumour cell proliferation and anti-inflammatory cytokine release.<sup>122,123</sup> Some TLR agonists can be beneficial as monotherapies but due to their moderate therapeutic effect they are typically used in combination with other immunostimulatory agents such as anti-PD-1.<sup>124</sup> Therefore, adjuvants are a powerful tool for enhancing the anti-tumour immune response in combination with established immunotherapies and promoting long-lasting immunity against different cancer types.

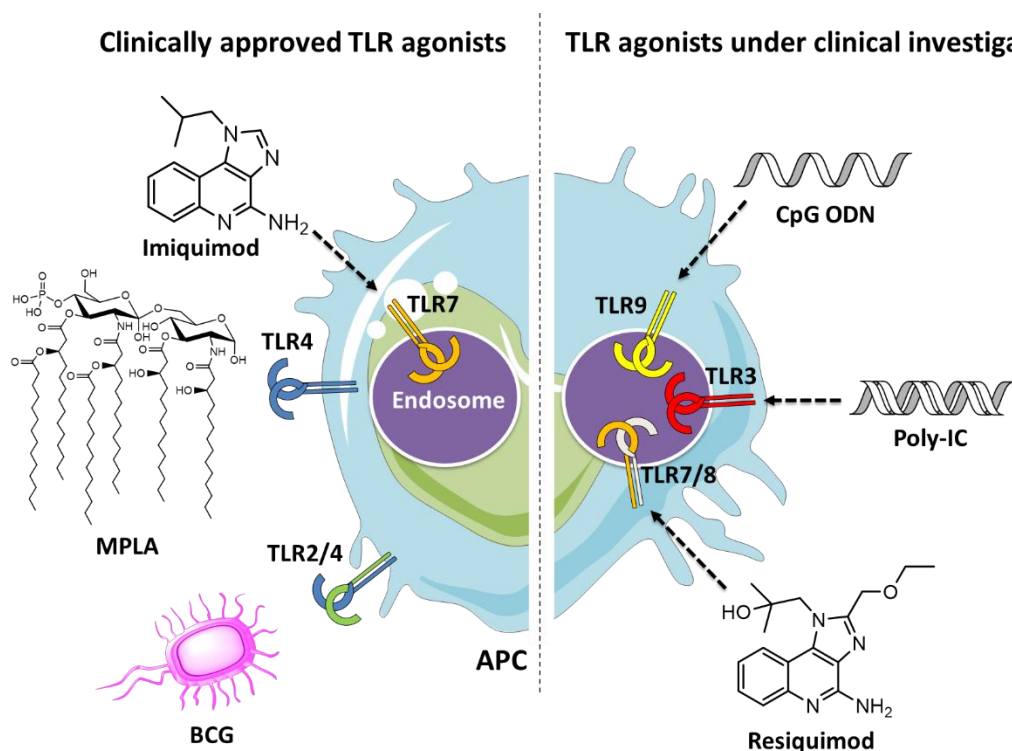


**Figure 1.8 APC interaction with clinically investigated and FDA-approved TLR agonists.** Several TLR agonists have been clinically approved or undergoing clinical investigation and include small molecules (imiquimid and resiquimod), a glycolipid (MPLA), a bacteria-derived vaccine (BCG), synthetic single stranded DNA (CpG ODN), and double stranded RNA molecules (poly-IC).<sup>118,120,121</sup>

## 1.4 Nanomedicine in anticancer therapy

Nanomedicine refers to the application of nanotechnology for medicinal practices and has been a prolific field of scientific research forging monumental developments in disease therapeutics, diagnostics, and regenerative medicine.<sup>125</sup> The design, synthesis, and modification of different nanoparticle (NP) systems as therapeutic, diagnostic or theranostic drug carriers have revolutionised oncology research by overcoming previous issues such as the delivery and chemical stability of hydrophobic drugs and unsuitable pharmacokinetic and



pharmacodynamic profiles. NPs offer several therapeutic advantages including improved vaccine circulation time, enhanced tumour targeting specificity, reduced off-target cytotoxicity, gradual drug release kinetics and the possibility of combination therapies using a single delivery platform.<sup>126</sup> One of the consequences of tumour angiogenesis is the enhanced pore size in the neovasculature due to the overexpression of vascular growth factors, lack of lymphatic drainage and high interstitial fluid pressure. The blood vessel pore cut-off diameter ranges from 380-780 nm, which enables passive tumour targeting by preferential convection and diffusion into the TME of solid tumours using NPs with a smaller hydrodynamic size than the pores.<sup>127</sup> This phenomenon is known as the enhanced permeability and retention (EPR) effect, discovered by Maeda and Matsumura in 1986, but it remains a controversial theory in oncology due to the moderate clinical outcome of passive tumour targeting systems and the more recent elucidation of the high heterogeneity of the EPR effect between different tumours, within metastatic tumours of the same individual and the variability during the period of tumour progression.<sup>128</sup> It is also known that the high interstitial fluid pressure within the blood vessels in the vicinity of the solid tumour and solid-phase stress arising from tumour growth prevent nanovector convection into the TME.<sup>129</sup> The size of the NPs is vital for successful drug delivery not only to enter the TME through the leaky neovasculature, but also to avoid rapid systemic clearance. Particles with a diameter below 6 nm are removed by renal excretion, while a diameter above 200 nm and without a suitable hydrophilic coating to prevent opsonization leads to clearance via the reticuloendothelial system.<sup>130,131</sup>

#### **1.4.1 Active tumour targeting**

The modification of a nanocarrier with tumour targeting agents to improve tumour-specificity and reduce adverse effects due to off-target cytotoxicity is defined as active tumour targeting. NPs benefit from a high surface-to-volume ratio enabling surface modification with combination of tumour targeting molecules and anticancer agents to achieve an enhanced therapeutic effect. While passive tumour targeting is gratified by delivery of drugs into the TME, some active targeting agents require tumour cell internalisation in order to reduce off-target adverse effects and trigger a desired therapeutic response as is the case for chemotherapeutic drugs, oncolytic viruses, some TLR agonists and other gene therapies.<sup>132</sup> Typical tumour cell overexpressed targets are HER2, CD20, CD19, luteinizing hormone-releasing hormone (LHRH) receptor, integrin  $\alpha\beta$  heterodimers, transferrin receptor and folate receptor. One route involves the targeting of the tumour vasculature with anti-angiogenic agents that reduce the blood supply to the tumour and

thereby oust the nutrients and oxygen required for tumour growth. Clinically investigated targets of the neovasculature are VEGFR, integrins  $\alpha\beta3$  and  $\alpha\beta5$ , matrix metalloproteinases 2 and 9 (MMP2 and MMP9) and aminopeptidase N.<sup>133–135</sup> The process of drug encapsulation and expression of tumour cell targeting moieties also prevents the procurement of multi-drug resistance, which is a process in which tumour cells selectively remove cells that respond to treatment and maintain cells that evade it through the expression of transporter proteins, known as adenine triphosphate-binding cassette transporters.<sup>136</sup> P-glycoprotein, MRP1 and BCRP are examples of transporter proteins that detect a wide range of anticancer drugs and eject them from the cell through efflux pump.<sup>137</sup>

### 1.4.2 Stimuli responsive nanosystems

Stimuli responsive drug delivery systems are an advanced approach of active tumour targeting in which the nanocarriers are designed to activated in response to an intrinsic tumour-based or externally induced chemical, thermal, light, electronic, or magnetic stimulus.<sup>138</sup> The TME tends to be more acidic (pH 6.5-7) than the healthy regions of body (pH 7.4) due to the elevated lactic acid production through the aerobic glycolysis process that takes preference over oxidative phosphorylation in the tumour tissue as defined by the Warburg effect.<sup>139</sup> Nanocarriers have been designed to exploit the acidic environment by conjugation of the therapeutic drug via an acid-labile bond such as an ester, hydrazine, acetal, orthoester, imine and cis-aconityl that are conditioned to release the drug exclusively in the acidic TME.<sup>140</sup> Many chemotherapeutic drugs, favour tumour cell internalisation by endocytosis to maximise their therapeutic effect and reduce unspecific damage to healthy tissue, while other anticancer agents such as oncolytic viruses are targeted towards the genetic material in the cell nucleus. Endocytosis can proceed via different pathways including clathrin-mediated endocytosis, caveolae-mediated endocytosis, lipid raft endocytosis, macro-pinocytosis, and phagocytosis. Clathrin-mediated endocytosis, commonly known as receptor-mediated endocytosis, can be conveyed via expression of targeting ligands including transferrin, riboflavin and mannose-6- phosphate, and is the most efficient route of cell internalisation as it ensures cell specificity and the possibility of manipulation of the intracellular signalling pathways.<sup>141</sup> Interactions with intracellular endosomal vesicle membrane can then determine how the drug is metabolised by the cell with the potential to localise in the lysosome, which is an acidic cell compartment (pH 4-5) containing a plethora of enzymes responsible for breaking down biomolecules. Endosomal maturation comprises different stages from early to late endosome exemplified by a gradually reducing pH gradient

and an increased production of digestive enzymes within the intracellular vesicle until the endosome eventually fuses with the lysosome.<sup>142</sup>

Some stimuli responsive nanosystems benefit from the acidic lysosome environment enabling the selective release of therapeutic drugs through acid-labile bonds. However, lysosomal accumulation of hydrophobic anticancer drugs is often associated with drug resistance as the drug becomes trapped by electrostatic interactions and broken down before it can reach its intracellular target. Cell internalisation of NPs through the caveolae-mediated endocytosis and lipid raft endocytosis pathways generally avoid lysosomal degradation and can be forced with targeting molecules including cholera toxin B, folic acid, albumin, and low-density lipoproteins through receptor-specific binding to caveolae membrane protein domains followed by phosphorylation processes that promote caveolae vesicle formation.<sup>143</sup> Cationic polymer coating of the NP is a frequently utilised technique to facilitate the passage through the net negatively charged phospholipid bilayer of the cell membrane. Natural and semi-synthetic cationic polymers used for NP surface coating include cationic dextran, cationic cellulose, cationic chitosan and cationic gelatin while typical synthetic cationic polymers are polyethyleneimine (PEI), poly(2-N,N-dimethylaminoethylmethacrylate), poly-L-lysine and polyamidoamines, which tend to have improved batch-to-batch structural consistency compared to natural polymer and allow facile modification with tumour targeting biomolecules.<sup>144</sup> An alternative route is the coating with amphiphilic molecules with the hydrophobic section favourably interacting with the phospholipid tails that constitute the cell membrane, thereby, encouraging cell internalisation.<sup>145</sup>

Once the nanocarrier is internalised into the cell, one of the subsequent challenges is the prevention of lysosomal degradation of the therapeutic payload. Many of the cationic polymers can escape the endosome-lysosome and take the nanocarrier to its intended target within the cell in a process known as the proton sponge effect.<sup>146</sup> The characteristic amine groups of these weakly basic molecules act as a buffer by absorbing protons in the endosome due to the pKa exceeding the pH of the endosomal compartment. The absorbed protons can no longer leave the endosome through membrane diffusion, which raises the pH and disrupts the equilibrium potential across the membrane, which leads to an influx of chloride anions in an effort to re-establish the equilibrium potential. This raises the osmotic pressure within the vesicle that leads to swelling and eventually bursting of the endosome allowing its contents to disperse into the cytosol. An alternative route by which these amine group-

bearing polymers can escape the endosome is through anchoring to the net anionic membrane through electrostatic interactions followed by fusion and release of the therapeutic drug load beyond the endosomal membrane boundaries.<sup>147</sup>

Chemotherapies and gene therapies that target DNA require internalisation into the cell nucleus. The nucleus is composed of an outer and inner membrane with protein channels of approximately 10-15 nm in diameter, defined as the nuclear pore complex, which connects both membranes and responsible for the transport of macromolecules in and out of the nucleus.<sup>148</sup> NPs functionalised with certain basic amino acid residues have shown to favourably accumulate in the nucleus as the peptide binds the nuclear pore complex and allows the nanocarrier contents to accumulate within the nuclear compartment.<sup>149</sup> The high affinity of acridine to the nucleus has also led to this molecule being integrated in nanocarrier systems for nuclear targeting as well as the incorporation of EGFR targets which are known to enter the nucleus upon receptor-ligand activation.<sup>150</sup> While nuclear targeting is the most common approach for cancer gene therapy other cell compartments such as the mitochondria and endoplasmic reticulum are potential therapeutic targets due to their essential role in the regulation of many cell functions including apoptotic cell death and protein synthesis and transport.<sup>151,152</sup>

### **1.4.3 Drug delivery systems**

Nanotechnology systems that are used clinically for cancer therapy include inorganic NPs, polymeric micelles, liposomes, dendrimers, and solid lipid NPs in the shape of spheres, rods, tubes, and others. Intrinsic material characteristics such as thermal, optical, electrical, and magnetic properties can improve the delivery performance and trigger a tumour-targeted drug release. A coherent nanoconstruct comprises a suitable nanocarrier, the drug load through encapsulation or covalently modification onto the NP surface and a tumour targeting agent, which allows specific delivery and affinity to tumour cells. Their large surface-to-volume ratio enables high density surface modification with mono- and combination therapies.

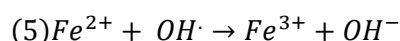
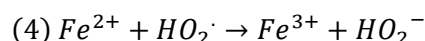
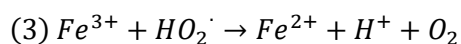
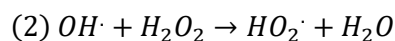
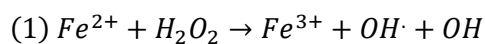
#### **1.4.3.1 Inorganic NPs systems**

Inorganic NPs are widely used in nanomedicine due to their favourable physical and chemical properties. The most common clinically and pre-clinically applied inorganic NP systems are iron oxide, silver, gold, quantum dots, silica, carbon nanotubes and hybrids.<sup>153</sup>

*Iron oxide NPs:* Magnetite ( $\text{Fe}_3\text{O}_4$ ) NPs are widely investigated for cancer therapy and diagnostics due to their magnetic properties, biocompatibility, and versatility for modifications.<sup>154</sup> They are prepared by different methods including thermal decomposition, co-precipitation, hydrothermal method, polyalcohol method, reverse micelle method, bacterial aerobic synthesis and others.<sup>155–159</sup> The hydrothermal method may be favoured due to its low environmental footprint as NPs are obtained without the use of organic solvents, whilst the polyalcohol method is more time-efficient by producing water soluble NPs in a single step. The reverse micelle method was reported as a highly up-scalable procedure using inexpensive and non-toxic reagents. However, the thermal decomposition and co-precipitation are the most common and well-established methods. The thermal decomposition method involves nucleation and growth of iron crystals by high temperature treatment of an organometallic iron complex in an organic solvent and the addition of a fatty acid or fatty amine as a coating layer under inert conditions.<sup>155</sup> In the co-precipitation method, a mixture of  $\text{Fe}^{2+}$  and  $\text{Fe}^{3+}$  salt precursors are typically added to an aqueous alkaline solution under inert conditions followed by addition of a hydrophilic polymer to stabilise the particles.<sup>160</sup> All preparation methods are designed to yield highly crystalline and monodisperse NPs in order to be able to exploit their magnetic properties but often require additional surface coating with an amphiphilic molecule such as phospholipids or surfactants to provide water solubility.

Particles under the size of 20 nm display superparamagnetic characteristics.<sup>161</sup> In essence, this allows them to experience magnetization under an external magnetic field without any remanent magnetic interactions upon removal of the external magnet, which prevents the NPs from aggregating and allows on-demand targeted drug delivery. Their magnetic properties can be applied for NP imaging by MRI and cancer therapeutic properties by hyperthermia, a process in which the electromagnetic waves induced by an alternating magnetic field are converted into thermal energy raising the local temperature to 40–43°C leading to tumour cell apoptosis.<sup>162</sup> The high metabolic rate of tumour cells associated with a high demand of blood supply and nutrients leads to a reduced oxygen availability in the TME. The hypoxic environment and the upregulation of superoxide dismutase in tumour cell mitochondria results in an increased generation of hydrogen peroxide.<sup>163</sup> Iron oxide NPs (IONPs) were discovered to have inherent anti-cancer properties via a process known as ferroptosis in the acidic TME, in which  $\text{Fe}^{2+}$  and  $\text{Fe}^{3+}$  ions drive the conversion of hydrogen peroxide into reactive oxygen species (ROS), such as  $\text{OH}^\cdot$  and  $\text{HO}_2^\cdot$ . The resulting oxidative stress leads to tumour cell death via an Fe-dependent non-apoptotic pathway, promoted by

the inhibition of system xc<sup>-</sup> and GPX4 regulatory molecules.<sup>164</sup> The chemical mechanisms involved in ferroptosis can be described by Fenton chemistry and chain reactions as proposed by Barb *et al.* (**Equation 1.1**).<sup>165</sup>



**Equation 1.1 Fenton chemistry mediated IONP induced tumour cell ferroptosis.** Fe(II)/Fe(III) undergo redox reactions in the presence of H<sub>2</sub>O<sub>2</sub> in the TME resulting in ROS generation. Reproduced from Barb *et al.*<sup>165</sup>

Superparamagnetic iron oxide nanoparticles (SPIONs) have shown high pre-clinical success in combination with immunotherapies. In a recent study by Mareque-Rivas *et al.*, SPIONs were electrostatically attached with TLR9 and TLR3/7 agonist (CpG ODN and poly I:C) and co-administered with the immunostimulatory monoclonal antibodies (anti-PDL1 and OX40) in a murine B16 melanoma model demonstrating complete tumour elimination and no tumour recurrence for 30 days after re-challenge (**Figure 1.9**).<sup>166</sup> This is a prime example of the therapeutic potential *in vivo* and beyond of SPIONs by acidic TME triggered ferroptosis-mediated oxidative damage to cancer cells, versatility of modification through covalent and electrostatic surface functionalisation and the combination with immunotherapeutic agents promoting CTL activation and inhibition of tumour immune evasion.

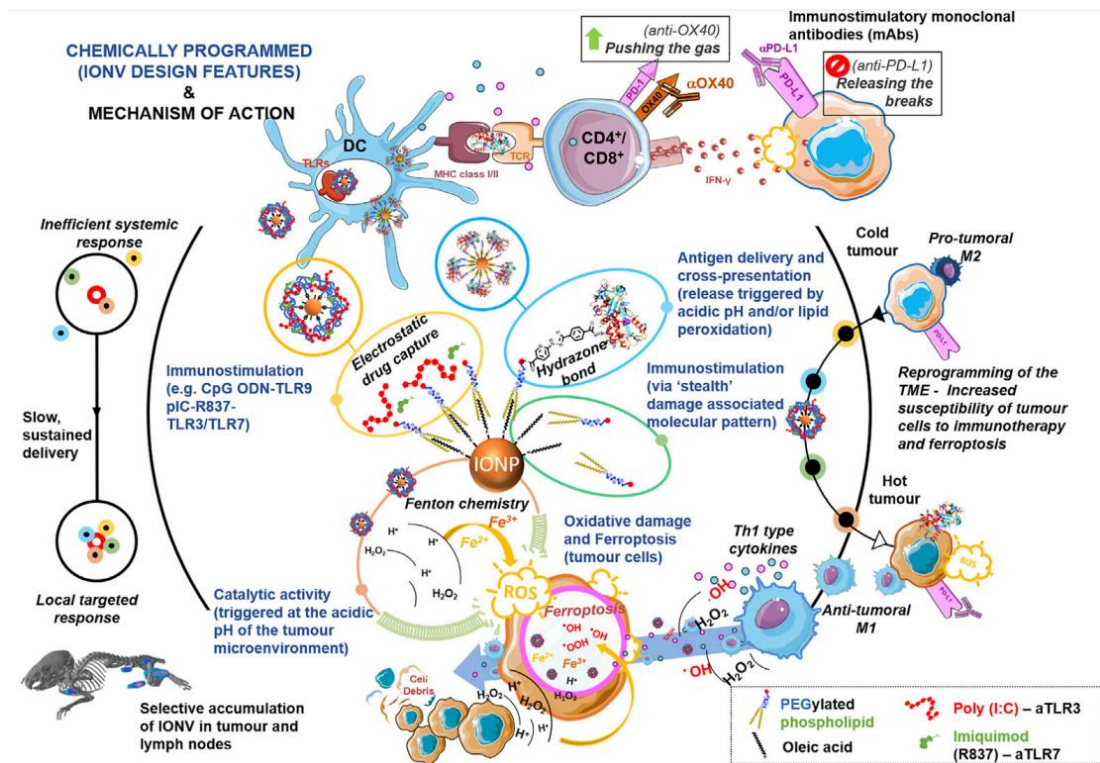


**Figure 1.9 Design and mechanism of action of inherently therapeutic IONVs.** These IONVs have chemically programmed multi-functional elements to activate and reprogram immune cells and cancer cells, harnessing the TME to sensitize tumours for immunotherapy and ferroptosis. Reproduced from Mareque-Rivas et al.<sup>166</sup>

**Quantum dots:** Quantum dots (QDs) are semiconductor NPs with a size of 1.5 to 10 nm and typically have a core shell composition, which reduces photobleaching and chemical resistance.<sup>167</sup> Their high absorption coefficient and quantum yield make them promising candidates for bioimaging applications. They have a broad absorption wavelength and a narrow photoluminescence emission band, but the absorption in the near-infrared region is the most critical for biomedical applications since they can be detected at higher tissue depths and experience less background interference.<sup>168</sup>

QDs are limited by their cytotoxicity *in vivo* as the core atoms can decompose under an oxidative environment or exposure to radiation, despite their shell coating layer and have been found to accumulate in liver, spleen and lymphatic system.<sup>169</sup> QD below 5 nm in size have shown complete systemic clearance by the kidney, which may be of benefit for clinical imaging applications.<sup>170</sup> For improved biocompatibility and stability core-shell QDs can be functionalised with amphiphilic polymers such as PEG, by ligand exchange of the QD surface molecules with bifunctional ligands including cysteine and glutathione, or by phospholipid coating, such as DSPE-PEG, to form micelles.<sup>171–173</sup> The silanization ligand exchange approach with a thiol-terminal silane, which can crosslink with neighbouring silanes around the QD

shell, is known to provide high stability and reduced toxicity.<sup>174</sup> Additional coverage with silanes containing other terminal groups allows control over surface charge for electrostatic or covalent modification with targeting agents and anticancer vaccines.<sup>175</sup> The toxicity can be reduced by doping of the core elements with less toxic ones and some studies have reported no adverse effects *in vivo* after core-shell QD administration, but more thorough investigation is required before translation of QDs drug delivery systems into the clinic.<sup>176,177</sup> Gao *et al.* demonstrated core-shell quantum dot mediated tumour imaging and targeting in mice by *in vivo* fluorescence imaging. The core-shell CdSe-ZnS quantum dots were coated with a hydrophobic coordinating ligand followed by an amphiphilic triblock polymer to render the NPs hydrophilic and was covalently conjugated by EDAC assisted amide-bond formation to tumour targeting ligands such as prostate-specific membrane antigen. The non-toxicity *in vivo* of these QDs may present upcoming opportunities for this system to be explored further as immunotherapeutic biomarkers.<sup>178</sup>

*Gold NPs:* Gold NPs exhibit localised surface plasmon resonance in which delocalised electron oscillations at the interface between the NP and surrounding medium are excited by an incident light beam into resonance at a frequency that is specific to the refractive index that can be analysed for their use as biosensors.<sup>179</sup> Gold NPs may also be used as contrast agents for cancer diagnostics by computed tomography due to their high X-ray attenuation and biocompatibility. This can be exploited by gold surface functionalisation with anti-cancer vaccines and tumour cell targeting moieties to track the delivery and accumulation in the tumour site. Hainfeld *et al.* developed a water-soluble pegylated Au NPs covalently attached to anti-Her2 antibodies that preferentially accumulated in HER2 positive tumour compared to the HER2 silenced control group in a murine breast cancer model.<sup>180</sup>

*Silver NPs:* Silver NPs are known for their inherent cancer therapeutic properties believed to arise from oxidative stress upon the release of silver ions leading to DNA damage and apoptosis, the extent of which is dependent on the NP size, surface charge and shape.<sup>181</sup> They have also been found to have angiogenic effects in cancer by reducing the VEGF and receptor expression.<sup>182</sup> Mouse-serum albumin coated Ag NPs with an average size of 10 nm have shown increased tumour cell internalisation and the inhibition of tumour growth-promoting cytokines including TNF- $\alpha$ , IL-1 $\beta$  and IL-6 in a murine fibrosarcoma model.<sup>183</sup>

*Mesoporous silica NPs:* This type of NPs is widely used in cancer drug delivery due to their unique structural properties and enhanced biocompatibility that sets them apart from other NP systems. They were first proposed by Vallet-Regi *et al.* as drug delivery devices by using



surfactants to control the NP pore sizes and analyse drug incorporation efficiency.<sup>184</sup> Their high pore volume and surface area permits the high modification yields and malleable vaccine release kinetics, while the surface terminal silanol groups are highly susceptible for modification with many types of functional groups.<sup>185–187</sup> Lu *et al.* proposed a mesoporous silica nanoparticle system coated with 1-methyl-D-tryptophan modified phospholipid with incorporation of the chemotherapeutic agent, oxaliplatin, into the phospholipid bilayer.<sup>188</sup> The study showed negligible tumour growth in a pancreatic ductal adenocarcinoma inoculated mice 132 days post-inoculation by exploiting the combined action of the chemo and immunotherapeutic agents.

*Carbon nanotubes:* By definition, these are capped or open-ended tubular shaped graphene and were discovered by Sumio Iijima in 1991.<sup>189</sup> Carbon nanotubes are composed of either a single wall or a stack of multiple graphene sheets with diameters from less than 1 nm to few micrometres with a high aspect ratio.<sup>190</sup> Their outstanding mechanical strength, beyond that of any other known material, low density, chemical resistivity and thermal conductivity make them highly suitable for drug delivery applications. Carbon nanotubes can be cost-efficiently prepared from a fossil fuel-based or plant-based carbon source with high reproducibility in a large scale by chemical vapour deposition using metal NPs as catalysts for nucleation and growth.<sup>191</sup> Due to their hydrophobicity, covalent or non-covalent surface functionalisation is vital for their application in nanomedicine. Several studies have also demonstrated high cell internalisation efficiency with carbon nanotube length of less 1  $\mu\text{m}$  without causing damage to the cell wall, but their precise mechanism of internalisation is to this date not well understood.<sup>192</sup>

The following figure shows the different types of NPs discussed and their potential for active tumour targeting through various mechanisms (**Figure 1.10**).

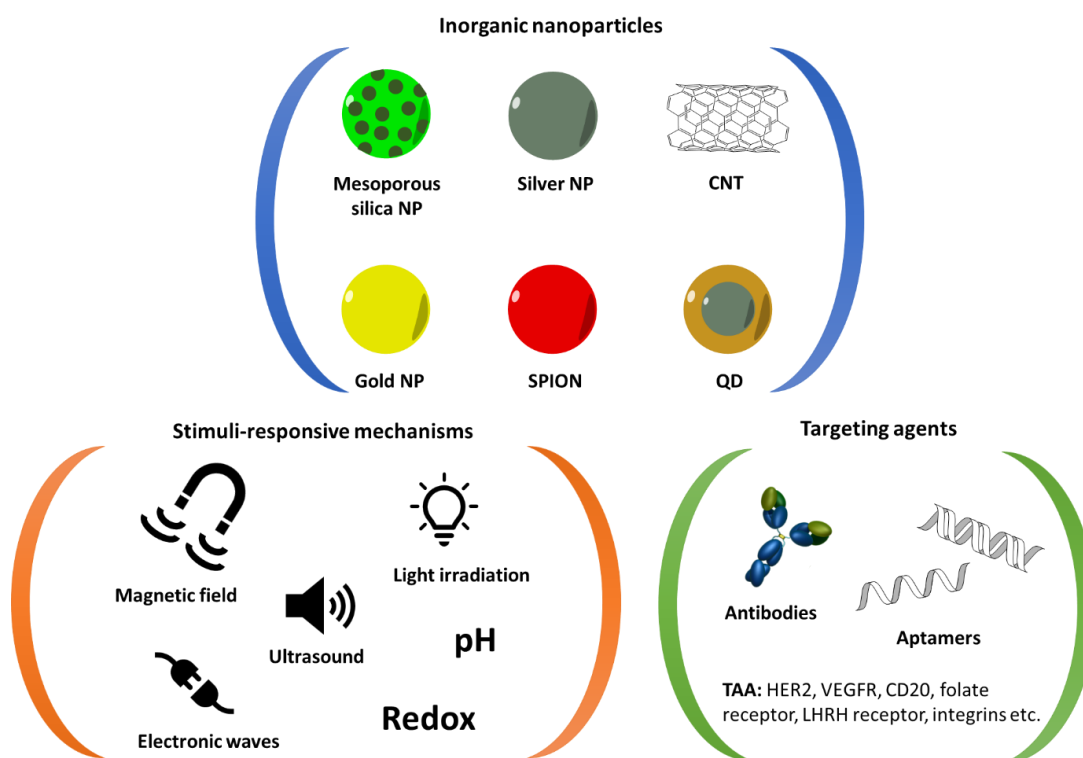


**Figure 1.10 Illustration of inorganic nanoparticle types and potential mechanisms for active tumour targeting.** Different stimuli-responsive mechanisms can ensure controlled drug release. Additionally, the NPs can be modified with tumour targeting agents to enhance site-specific drug delivery.

### 1.4.3.2 Polymeric NP systems

Polymer-based nanovectors benefit from high biocompatibility, biodegradability, ease of fabrication and flexibility for modification.<sup>193</sup> Their enhanced stability and non-toxicity make them excellent NP systems for intravenous and oral drug delivery. Polymer NPs can be subcategorised into micelles, liposomes, polymersome, dendrimers and solid lipid NPs. While external triggers including light, magnetic waves and ultrasound are typically exploited by inorganic NPs, polymeric NPs are more commonly designed to have an environmental stimuli responsive trigger such as pH, enzyme, glucose and redox mediated drug release.<sup>194,195</sup> They are composed of natural and synthetic polymers including hyaluronic acid, chitosan, dextran, polyethylene glycol, poly(lactic-co-glycolic acid), poly(vinyl alcohol), poly(ethylenimine), arginine, dendritic polymers amongst other.<sup>196</sup>

**Polymersomes:** Polymersomes are composed of synthetic amphiphilic polymers and have a spherical shape with an aqueous core enclosed by a bilayer membrane. The membrane diameter is tuneable depending on the choice of the hydrophobic block of the polymer, which is covalently functionalised to the hydrophilic part.<sup>197</sup> A membrane with a larger internal diameter is beneficial to ensure high particle stability and prevent drug leakage

before it can reach its target.<sup>198</sup> The hydrophilic nature of its core allows for encapsulation of anticancer agents including small molecules, proteins, antibodies, and genes. The potential for polymer modification also allows for the expression of tumour targeting agents on the polymersome surface. Intracellular targeted redox responsive systems can take advantage of the high glutathione levels in the cell cytosol and tumour tissue, which is responsible for the reduction of disulfide bonds. Lale *et al.* propose a DOX-loaded PEG and PLA based polymersome interconnected by disulfide bonds and covalently functionalised with breast cancer targeting agents, folic acid and trastuzumab. The polymersome showed increased cell internalisation *in vitro* and enhanced tumour size reduction in a murine breast cancer model.<sup>199</sup>

*Liposomes:* Liposomes are spherical vesicles consisting of a hydrophobic phospholipid bilayer that separates the hydrophilic core from the external aqueous environment. Their size can range from 25 nm to several microns depending on the phospholipid length and the number of bilayers, which are categorised into unilamellar and multilamellar vesicles.<sup>200</sup> The versatility of these particles allows for hydrophobic drug loading into the phospholipid bilayer and hydrophilic vaccine encapsulation into the aqueous core. Furthermore, the liposomes can be surface functionalised with TAA targeting moieties to promote successful drug delivery. Liposomal stability can be optimised by opting for phospholipids with high phase transition temperature, high surface charge and low ionic strength to reduce aggregation and disruption of the phospholipid bilayer.<sup>201,202</sup> In some cases, drug release from liposomes can be induced by hyperthermia to increase the temperature close to the lipid phase transition temperature that results in increased phospholipid bilayer permeability.<sup>203</sup> Allison and Gregoriadis discovered the potential of liposomes as intrinsic adjuvants for the delivery of antigen which were demonstrated to induce higher antibody production in mice compared to the antigen delivery without the nanocarrier.<sup>204</sup>

*Polymeric micelles:* Unlike polymersomes and liposomes, polymeric micelles do not contain a lipidic bilayer that separated the core from the aqueous environment and consists of amphiphilic molecules arranged in a spherical shape with the hydrophobic polymer segment facing the centre and the hydrophilic tail exposed to the surrounding medium. This NP system is of particular interest for the delivery of hydrophobic anticancer drugs that can be solubilised and retain its stability within the micelle core. It also allows the use of reduced drug doses without loss in therapeutic efficiency, which overcomes dose-dependent toxicity and systemic clearance issues often associated with chemotherapeutic treatments.<sup>205</sup> Polymeric micelles have high stability in comparison to low molecular weight surfactant-

based micelles due to their low critical micelle concentration.<sup>206</sup> Crosslinking of the micelle core by radical polymerisation with the aid of a photoinitiator, generation of disulfide bridges or using bifunctional agents can further stabilise the incorporated drug, enhance cell internalisation and improve drug release kinetics.<sup>207</sup> Most preparation methods involve self-assembly of micelles by mixing of the polymer in an organic phase followed by addition of an aqueous phase under specific temperature, solvent ratio, and shear speed conditions, sometimes in the presence of a surfactant molecule that prevents aggregation and aids micelle formation.<sup>208</sup> Several micelle-based anticancer treatments have been clinically approved or are currently under clinical investigation including GenexolPM<sup>®</sup> which is a paclitaxel loaded PEG block copolymer micelle system for the treatment of breast, ovarian and lung cancers.<sup>209</sup>

*Dendrimers:* Dendrimers are polymer structures composed of several layers that are formed by controlled synthesis rather than polymerisation with each layer being termed a generation and can take different shapes. Common cationic polymers used for dendrimer synthesis are poly(amidoamine), poly(phosphorhydrazone) and poly(propyleneimine) which are grown into dendrimers by Michael-addition reactions of acrylates with the polymer terminal amine groups.<sup>210</sup> The use of cationic polymers affords water solubilisation, but simultaneously allows for covalent or electrostatic modification of both hydrophilic and hydrophobic drugs into the dendrimer structure. Dendrimers have also been reported for their suitability for immune cell hybridization. Xu *et al.* demonstrated the covalent attachment of poly(amidoamine) dendrimers to RAW macrophage surface via click-chemistry with minimal injury to the cell membrane or alterations to the cell biology highlighting the opportunity for adoptive cell transfer-based cancer immunotherapy.<sup>211</sup>

*Solid lipid NPs:* Solid lipid NPs differ from liposomes by containing a solid lipid core that is constituted of polymers including glycerides or waxes and surrounded by an amphiphilic surfactant or phospholipid layer exposed to the aqueous environment. As with other polymeric NP systems they can be functionalised with hydrophobic drugs into the core or hydrophilic anticancer agents into the hydrophilic later. An advantage of solid lipid NPs over liposomes is their ease and cost-efficient manufacturing process.<sup>212</sup>

The following figure summarises the different types of polymeric NPs, drug release mechanism and targeting opportunities discussed in the previous sections (**Figure 1.11**).

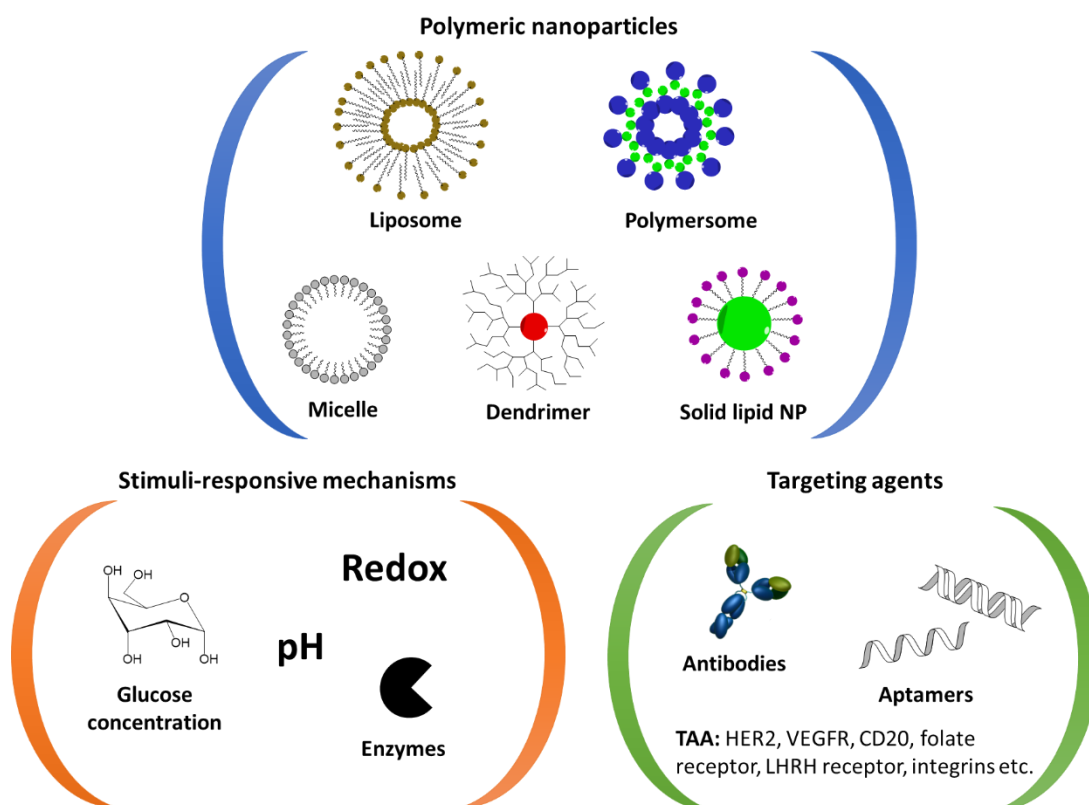


**Figure 1.11 Illustration of polymeric nanoparticle systems as well as their potential for active targeting and stimuli-responsive mechanisms for triggered vaccine release.** Polymeric nanoparticle can be designed to release their payload in response to internal triggers such as enzymes, pH, redox chemistry, or glucose concentration. They can also be covalently or non-covalently functionalised with tumour targeting agents to enhance site-specific drug delivery.

Some of the limitations of nanocarriers include low drug loading efficiency leading to an insufficient response, toxicity arising from an overdose of nanocarrier material, and leaking of the drug load before it can reach its target, which can result in accumulation of the drug in healthy tissues.<sup>213</sup> Nanocarrier migration via the bloodstream to its target often attracts non-specific protein binding onto the surface of the NPs, which is known as opsonization. This can lead to deactivation of tumour targeting molecules, facilitates detection and clearance by the reticuloendothelial system (RES).<sup>214</sup> The degree of protein adsorption leading to protein corona formation depends on electrostatic forces, hydrophobicity and physical properties including size, shape, and topography.

A common strategy to overcome these challenges is the surface coating of the nanocarrier with a hydrophilic polymer such as polyethylene glycol (PEG), which prevents immunogenicity and enhances hydrophilicity enabling longer circulation time and improved targeting efficiency.<sup>215</sup> Saturation of the particle surface with PEG is desired for efficient protein repulsion by steric hindrance but depending on the particle size and the

conformational arrangement of the PEG molecules on the surface, high density PEG adsorption is not always achieved. However, Torchilin *et al.* demonstrated that low density adsorption is not necessarily a drawback as the high mobility of polymer chains due to the larger empty space on the nanocarrier surface could effectively ward off incoming proteins through osmotic repulsion forces.<sup>216</sup> The PEGylation strategy is not flawless as it commonly experiences rapid clearance due to activation of PEG-specific immunoglobins, which further decreases the drug circulation lifetime of subsequent doses of the PEG coated nanocarrier in a phenomenon known as accelerated blood clearance.<sup>217</sup> Polyvinylpyrrolidone has been reported as an alternative to PEG with favourable evasion of the accelerated blood clearance even after repeated administrations in a rat model.<sup>218</sup> Additionally, steric hinderance due to the size increment of the NPs afforded by the PEG layer can also prevent efficient tumour cell internalisation but can be overcome by using low molecular weight PEG or enzymatically cleavable PEG.<sup>215,219</sup>

Overall, nanomedicine is a powerful tool for the functionalisation and targeted delivery of anticancer drugs resulting in reduced toxicity and improved pharmacokinetic and cell internalisation, whilst also posing a suitable platform for modification with tumour targeting agents. NPs are designed to avoid renal and RES clearance by controlling size, shape, and composition. The use of fluorescent and magnetic NP systems is becoming integral for cancer theranostics by significantly enhancing tumour targeting and imaging *in vivo* as well as providing intrinsic anticancer properties through localised hyperthermia or ROS-mediated cell death. Methodical selection of polymer blocks and the ability of cross-polymerisation can further increase NP stability while issues of opsonisation can be overcome by surface coating with hydrophilic polymers.

## 1.5 Microneedles (MNs) for transdermal drug delivery

The origins of drug delivery via the skin for medical applications dates back several thousand years to the ancient Egyptian *Papyrus Ebers* from 1550 BC, which contained several transdermal recipes for the treatment of different lesions and illnesses.<sup>220</sup> Since then, transdermal drug delivery systems have developed by improving dosage control and drug reservoirs enabling on demand release, which has ultimately led to the creation of MNs. The human skin is composed of several layers with the outermost stratum corneum composed of dead skin cells known as corneocytes and dense matrix of lipids that act as a barrier to external pathogens.<sup>221</sup> The following layers in order of increasing depth are epidermis, dermis, and hypodermis. The epidermis is mostly composed of keratinocytes and a relatively

small proportion of melanocytes and Langerhans cells.<sup>222</sup> The dermis is known to have plethora of immune cells and is located at a depth of 150  $\mu\text{m}$  to 2 mm depending on age, gender and area of the body, while nerves, blood vessels, sweat glands, sebaceous glands and hair follicles are resident to the hypodermis.<sup>223,224</sup> MN-based drug delivery systems are gaining a rising interest for investigation for cancer therapeutics and diagnostics due to their non-invasiveness and patient compliance in contrast to conventional hypodermic needle and oral drug delivery.<sup>225</sup> MNs consist of a base with micron scale projections of different shapes including conical, pyramid-shaped and bevelled needles and produced from a range of different materials, such as polymers, carbohydrates, silicon, metals, ceramic and glass. When MNs are applied onto the skin, aqueous microchannels are created in the stratum corneum, through which the drug can diffuse into the underlying layers. The dermis is the target region for MN-based immunotherapy with the potential to elicit an enhanced immune response due to the abundance of immune cells including DC, macrophages, T cells, Langerhans cells NK cells and others.<sup>226</sup> MN drug delivery is non-invasive since dermal skin penetration avoids stimulation of nerves and blood vessels found at increased depths in the hypodermis. This means that MN application is painless and reduce the risk of infection or bruising.<sup>227</sup> Additionally, the use of MNs may not require specialist training and results in reduced hazardous waste production in contrast to hypodermic needles.<sup>228</sup> MNs can be categorised into solid, dissolvable, biodegradable and hydrogel forming microneedles (**Figure 1.12**).

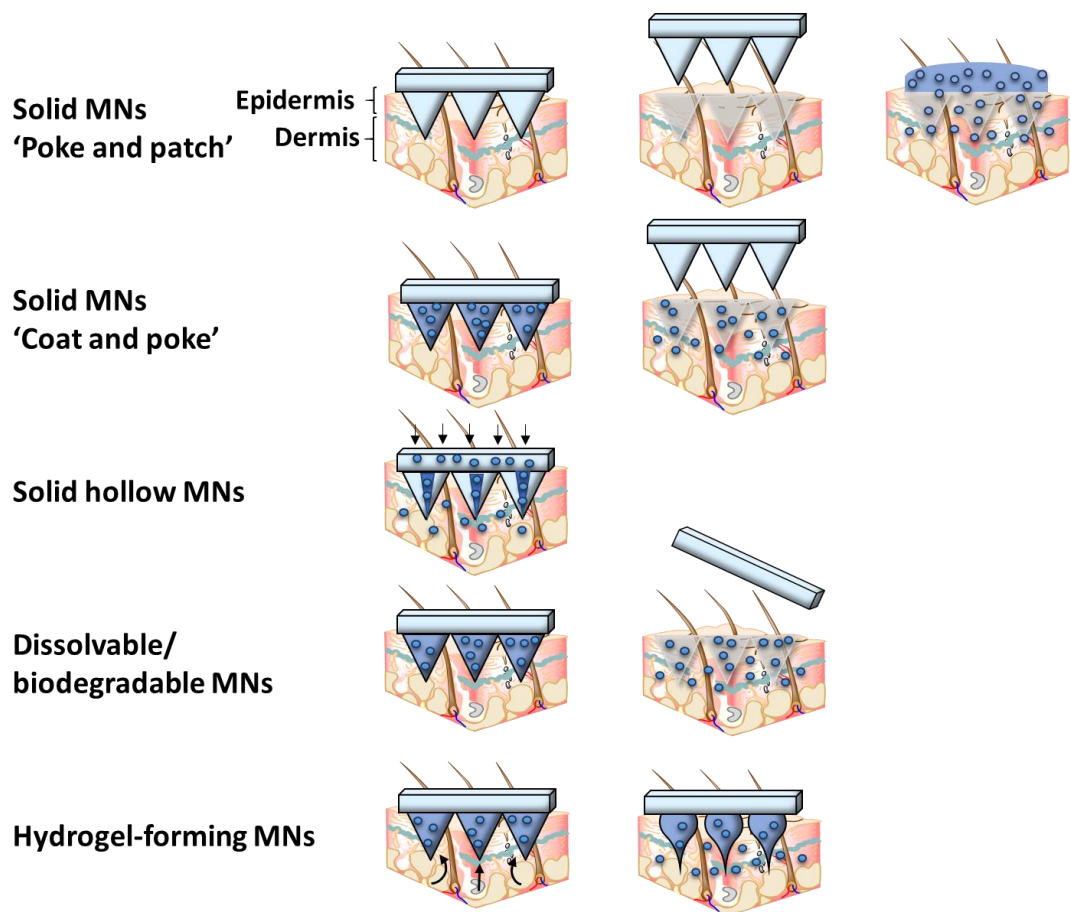


**Figure 1.12 Schematic representation of different types of MNs for transdermal drug delivery.** Solid MNs can either be applied prior to drug administration (poke and patch) or coated with a solution of the drug (coat and poke). Hollow MNs allows the drug to be delivered through the hollow MN channels. Dissolvable/biodegradable MNs remain in the skin after application and gradually dissolve to release the incorporated drug, whilst hydrogel forming MNs swell upon skin application, which allows the drug to be released. Adapted from Larraneta et al.<sup>225</sup>

### 1.5.1 Solid MNs

Solid MNs made from silicon, metal, ceramic, or glass tend to have a higher mechanical strength compared to biodegradable and dissolvable MNs but can suffer from limited biocompatibility and costly fabrication processes. Solid MNs offer 3 common drug delivery approaches:

*Coat and poke:* The ‘coat and poke’ method involves coating the MNs with a solution of the therapeutic agent prior to the MN application into the skin. Coating can be performed by dipping or spraying an aqueous solution of drug onto the MNs. Adherence strength to the MN surface can be enhanced by pre-coating the MNs with a surfactant and increasing the viscosity of the drug solution, while stabilisers can be used to prevent drug degradation during the drying process. Another approach is layer-by-layer coating of oppositely charged



agents to improve adhesion by electrostatic interactions. Saurer *et al.* developed stainless steel MNs precoated with a mixture of linear poly(ethyleneimine) and sodium poly(styrene sulfonate) with a surface negative charge in order to attach cationic plasmid DNA and proteins in a layer-by-layer fashion for up to 16 layers.<sup>229</sup> The fluorescently tagged biomolecules demonstrated successful skin penetration and complete release into porcine skin after 2 h. However, the coating method also has its limitations as it is restricted by the amount of drug that can be deposited onto the surface and can lack efficiency due to weak drug adhesion forces to the microneedles surface that can lead to drug loss during skin penetration.<sup>230</sup>

*Poke and patch:* In the 'poke and patch' approach the skin is first penetrated with the MNs to create microchannels followed by MN removal and the application of the drug in the form of an aqueous solution or gel at the site of penetration, which allows the drug to diffuse through the microchannels into the target skin region. The limitation of this method lies in the difficulty of controlling the drug dosage since a portion of the applied drug solution may remain on the skin surface and the microchannels created by the MNs might heal before the entire drug dose is able to diffuse into the skin.<sup>230</sup>

*Hollow MNs:* With advanced microfabrication techniques, such as deep reactive ion etching, it is possible to generate hollow MNs, capable of delivering the drug through the channels of the needles with an applicator or a drug reservoir incorporated into the MN base. Also referred to as the 'poke and flow' approach, this type of MN allows for more control over the drug dose and is only limited by the capacity of the applicator and can ensure quicker delivery using a syringe-type applicator rather than passive diffusion. Typically, a larger the bore diameter results in a higher flow rate, but it can also compromise the mechanical strength and sharpness of the needles.<sup>231</sup> Guy *et al.* developed a bevel-shaped silicon microneedle array using a novel 3-step dry etch fabrication method. The MNs were attached to a cost-efficiently manufactured syringe applicator and showed efficient skin penetration as well as fluid flow in *ex vivo* human breast samples. The semiconductive MN base could also be exploited for electrochemical sensing applications in combination with non-invasive vaccine delivery.<sup>232</sup> One of the limitations of solid MNs for drug delivery is the possibility of needle fracture upon removal or application leaving non-biodegradable residues in the skin.<sup>233</sup>

## 1.5.2 Polymeric and carbohydrate MNs

Polymeric and carbohydrate based MNs can be classified into solid, dissolving and biodegradable, and hydrogel forming MNs and can be made from natural or synthetic

polymers. Polymeric MNs are generally significantly cheaper to manufacture and more biocompatible than their ceramic, metal, and silicon counterparts, but can lack in mechanical strength as well as the drug loading capacity, which is limited to the volume of the MNs.

*Solid polymeric MNs:* Solid polymeric MNs are typically made from polycarbonate, poly(methyl methacrylate) (PMMA) and polystyrene. These MNs do not dissolve upon skin application and are, therefore, applied using the 'coat and poke' or 'poke and patch' approaches described earlier. The typical fabrication method for PMMA and polystyrene MNs is micromolding and hot embossing using a polydimethylsiloxane (PDMS) mold.<sup>234,235</sup> Hollow tetrahedron-shaped PMMA MNs have been prepared by deep X-ray lithography with good reproducibility and efficient skin penetration *in vivo*.<sup>236</sup>

*Hydrogel-forming MNs:* Some polymers can be exploited for their swelling properties to form hydrogel-forming microneedles. These MNs absorb the interstitial fluid within the skin leading to swelling, upon which, the incorporated drug can diffuse through the micropores created in the polymer matrix into the skin.<sup>237</sup> The drug load can either be stored in a drug reservoir in the MN base or directly incorporated into the MNs tips for gradual or electrically triggered bolus drug release. The polymers used are not always biodegradable, but highly biocompatible and the material is strong enough to prevent residual traces being left behind upon removal of the MNs from the skin. These type of MN systems are produced by physical crosslinking of polymers via a freeze-thawing technique, which strengthens the material and prevents rapid drug release. Polymer formulations used in the literature for hydrogel-forming MNs include PVA-dextran-CMC and poly (methylvinylether)-maleic acid, which are more stable to hydrolytic degradation.<sup>237–239</sup>

*Carbohydrate MNs:* Non-polymeric carbohydrates such as maltose, trehalose, mannitol, xylitol, and galactose have been reported for the synthesis of dissolvable MNs and typically require carbohydrate mixtures to generate sugar glass or carbohydrate-polymer combinations to obtain the desired physical and chemical properties.<sup>225</sup> The casting micromolding method using a PDMS or metal mold is the most popular for the fabrication of carbohydrate MNs. However, high temperature requirements can lead to degradation of thermosensitive drugs such as proteins and genes during the fabrication process.<sup>225</sup>

### **1.5.2.1 Dissolvable and biodegradable MNs**

Dissolvable and biodegradable MNs are increasingly investigated as drug delivery systems for cancer therapeutic applications due to their ease of fabrication, tuneable drug release

kinetics, incorporation of multiple drugs into a single patch, and the possibility of stimuli responsive release. The materials used for these MNs include hyaluronic acid (HA), polylactic-co-glycolic acid (PLGA), polyvinyl alcohol (PVA), carboxymethyl cellulose (CMC), poly(vinylpyrrolidone) (PVP), chitosan, agarose, dextran, alginate amongst others.<sup>240</sup> They can be fabricated using a variety of methods that are suited to different polymers and each displaying their own advantages and limitations as described in the following sections.

*Micromolding method:* Dissolvable and biodegradable MNs are typically prepared by the casting micromolding technique, which involves the deposition of an aqueous polymer solution onto an inert and thermo-stable PDMS mold with an inverted MN pattern.<sup>241</sup> Vacuum application or centrifugation can aid the flow and concentration of the polymer solution into the micromold cavities. Once the solvent has evaporated, the MNs are peeled off from the mold, which can be re-used for subsequent MN fabrications. The molds are typically fabricated by a laser ablation process involving the production of a metal-based master structure, onto which a molten solution of PDMS is deposited and dried to form the inverted MN shape. Micromolding is not limited to casting with other common microfabrication techniques including hot embossing, injection molding and investment molding. However, these methods are more frequently applied for solid MNs that require high temperature treatments.<sup>242–244</sup>

*Drawing lithography:* Another fabrication method is drawing lithography that uses extensional deformation to create high aspect ratio MN patches, but typically requires high temperatures and can suffer from low reproducibility due to the dependency of many factors including thermal control, polymer viscosity, surface tension, drawing acceleration and speed, and uniformity of patterns on contacting pillars.<sup>245</sup> This method involves the deposition of a melted polymer solution, for instance SU-8, between 2 equal plates forming a liquid bridge between them. As the polymer cools down towards its glass transition temperature ( $T_g$ ) the plates are drawn apart forming polymer columns between the 2 plates and necking of the liquid bridge due to differences in surface tension and extensional viscosity until the bridge breaks to form 2 needles structures on the opposing plates.<sup>246</sup> The droplet-born air blowing technique is a low temperature and rapid MN fabrication method in which the polymer droplets are placed between 2 plates which are then separated up to a desired MN length followed by air blowing onto the neck of the liquid bridge to promote drying of the polymer. Once solidified the plates are separated simultaneously to break the polymer bridge and obtain a MN needle patch on each plate.<sup>247</sup>

*Electro-drawing:* Electro-drawing is a non-contact polymer MN fabrication method in which a pyroelectric crystal is placed near a PDMS strip containing polymer droplets and exposed to heat to produce an external magnetic field. The electrohydrodynamic force on the polymer draws the polymer droplet into a MN shape, after which the solvent is evaporated to give a solid MN structure.<sup>248</sup>

*3D printing:* A more recent approach involves 3D printing technology to form MN structures via different methods including ink-jet printing, photopolymerisation-based printing, and fused deposition modelling.<sup>249</sup> Ink-jet printing uses a mechanical printing head operated by a thermal or piezoelectric system that deposits droplets onto a binding surface. Upon drying of the polymer droplet further droplets are deposited on a layer-by-layer basis to form the desired MN shape.<sup>250</sup> Photopolymerisation-based technologies work on the same droplet deposition build-up principle as the ink-jet printing but instead uses photosensitive polymers that are cured upon light irradiation.<sup>251</sup> This method has been applied for the development of polymer MNs for therapeutic and cosmetic applications, for instance, the polymer-based MN patch developed by Innoture Limited, that creates microchannels for the delivery of HA serum into skin and are produced by a photopolymerisation technique developed by Kirby *et al.*<sup>252</sup> Fused-deposition modelling employs an extruder head containing a polymer-based filament heated above its glass transition temperature. The extruder deposits the filament onto a surface in consecutive layers to form the needle structure.<sup>253</sup>

The following figure summarises the different materials and fabrication methods for polymeric and carbohydrate MN (**Figure 1.13 A, B**).

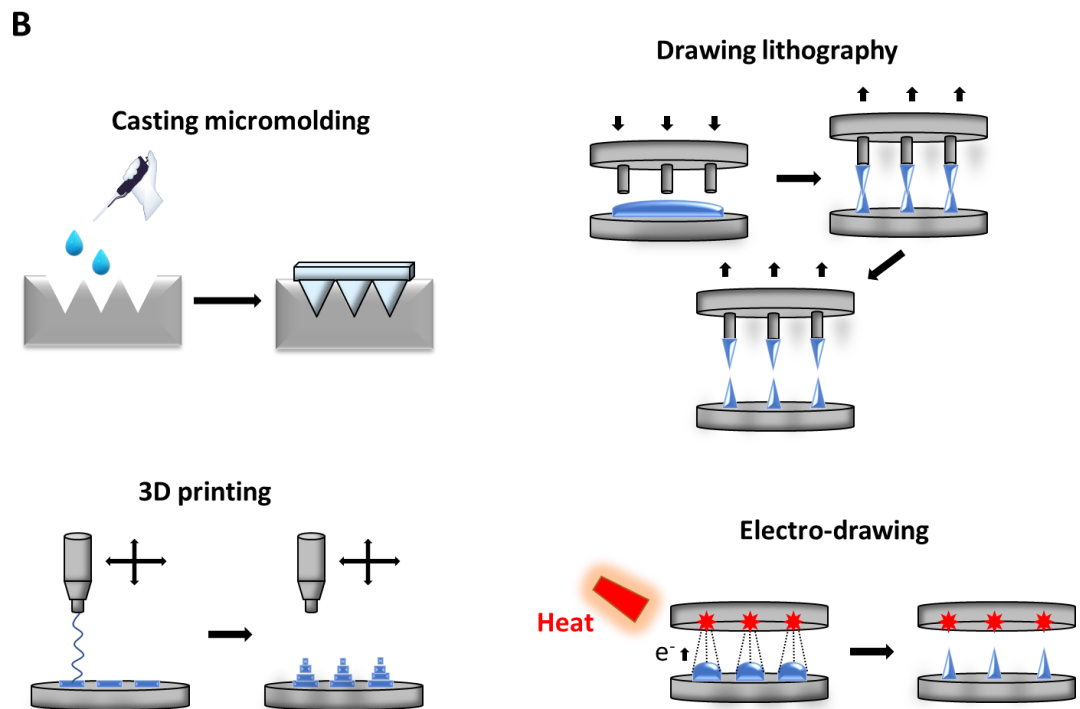
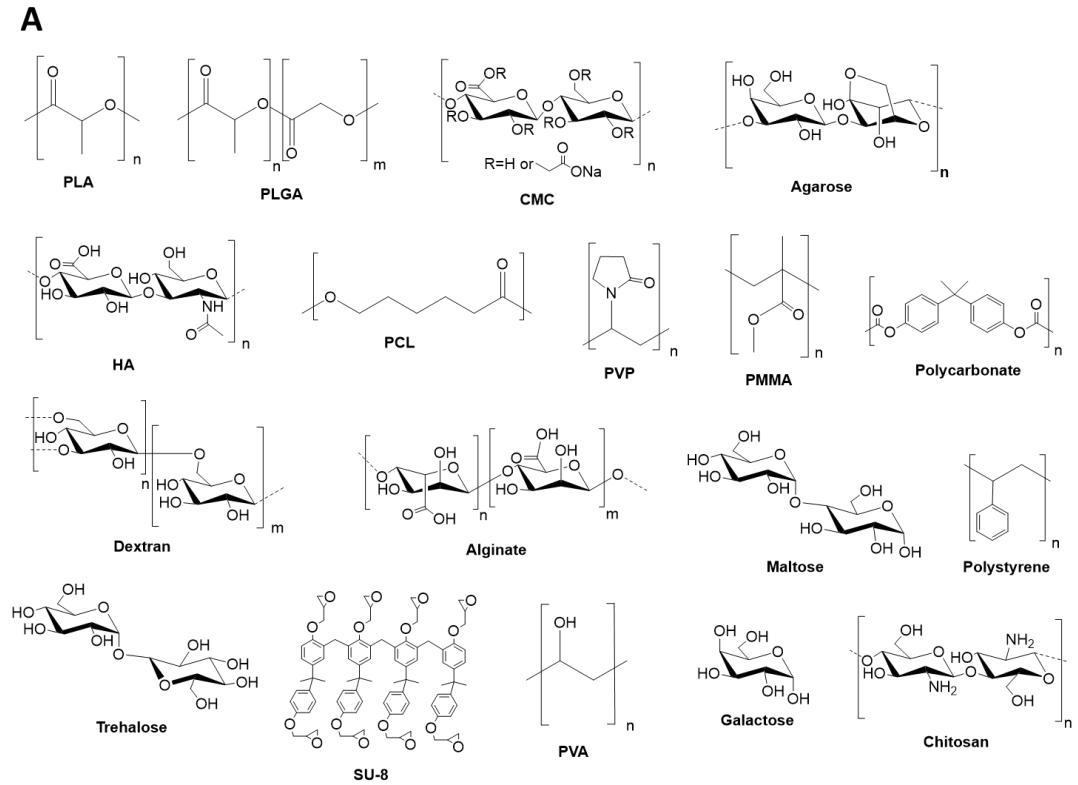


**Figure 1.13 Polymeric MN source materials and fabrication methods.** (A) Synthetic polymers and biomaterials that have been used for polymeric and carbohydrate based MNs; (B) Different polymeric and carbohydrate MN fabrication methods: casting micromolding, drawing lithography, 3D printing and electro-drawing.

### 1.5.3 Comprehensive MN-based drug delivery systems for cancer immunotherapy

The incorporation of immunomodulatory agents and NPs into dissolvable and biodegradable MNs allows for the design of gradually releasing drug administration systems that can locally target the immune cell-rich dermal skin layer in a non-invasive manner, which has awoken great interest for cancer immunotherapy and combination therapies. Ye *et al.* developed a HA-based MN patch incorporating the IDO inhibitor, 1MT, and the immune checkpoint inhibitor, anti-PD-1 (**Figure 1.14 A**).<sup>254</sup> The 1MT was covalently functionalised to HA to enable NP self-assembly with the encapsulation of anti-PD-1 into the core and 1MT integrated into the HA matrix prior to NP incorporation into the MNs. The MNs were fabricated using the casting micromolding method showing tumour growth inhibition in a mouse melanoma model with a 70% survival rate 40 days post-treatment. The same research group developed a similar HA MN system incorporating anti-PD-1 and anti-CTLA-4 into a single patch as a combination immunotherapy.<sup>255</sup> In this system, the immunostimulatory agents were first incorporated into pH-responsive alginate NPs containing catalase and glucose oxidase. Interstitial glucose was oxidised in the presence of glucose oxidase and catalase to generate gluconic acid leading to a pH reduction, which triggered gradual NP degradation and drug release.

Functionalised HA MNs for cancer immunotherapy have also been reported by Kim *et al.* demonstrating enhanced CTL stimulation and reduced tumour volume in B16-OVA melanoma inoculated mice (**Figure 1.14 B**).<sup>256</sup> In this system, low molecular weight HA was covalently bonded to the OVA-derived T cell epitope peptide SIINFEKL via a reductive amination reaction followed by incorporation into MNs by casting micromolding into an inverted bullet-shaped MN mold.

The use of polymer mixtures and cross-polymerisation helps finetuning the mechanical properties of polymeric MNs and ensures efficient skin penetration as well as sustained drug release. Duong *et al.* presented the fabrication of a di-block PEG-polypeptide copolymer MNs for the delivery of immunomodulatory agents.<sup>257</sup> The TLR3 agonist, poly (I:C), and OVA-derived plasmid DNA were loaded onto a cationic amphiphilic nanopolyplex embedded into the copolymer matrix which was then used for the MN fabrication. MN treatment in mice elicited increased OVA antibody expression and delayed tumour progression in a B16-OVA murine model.

Combination therapies using biodegradable MNs can often yield a synergic therapeutic effect. Lan *et al.* developed a dissolvable PVP MN patch loaded with a lipid-based NP system incorporating cisplatin and anti-PD-1, which showed successful cellular uptake *in vitro* and synergistic anticancer response *in vivo* in an oral squamous cell carcinoma murine model (**Figure 1.14 C**).<sup>258</sup> The authors propose that the reduced tumour fibroblast-mediated chemoresistance is due to the immunostimulatory effect of anti-PD-1, promoting the generation of tumour-targeted CD8<sup>+</sup> T cells.

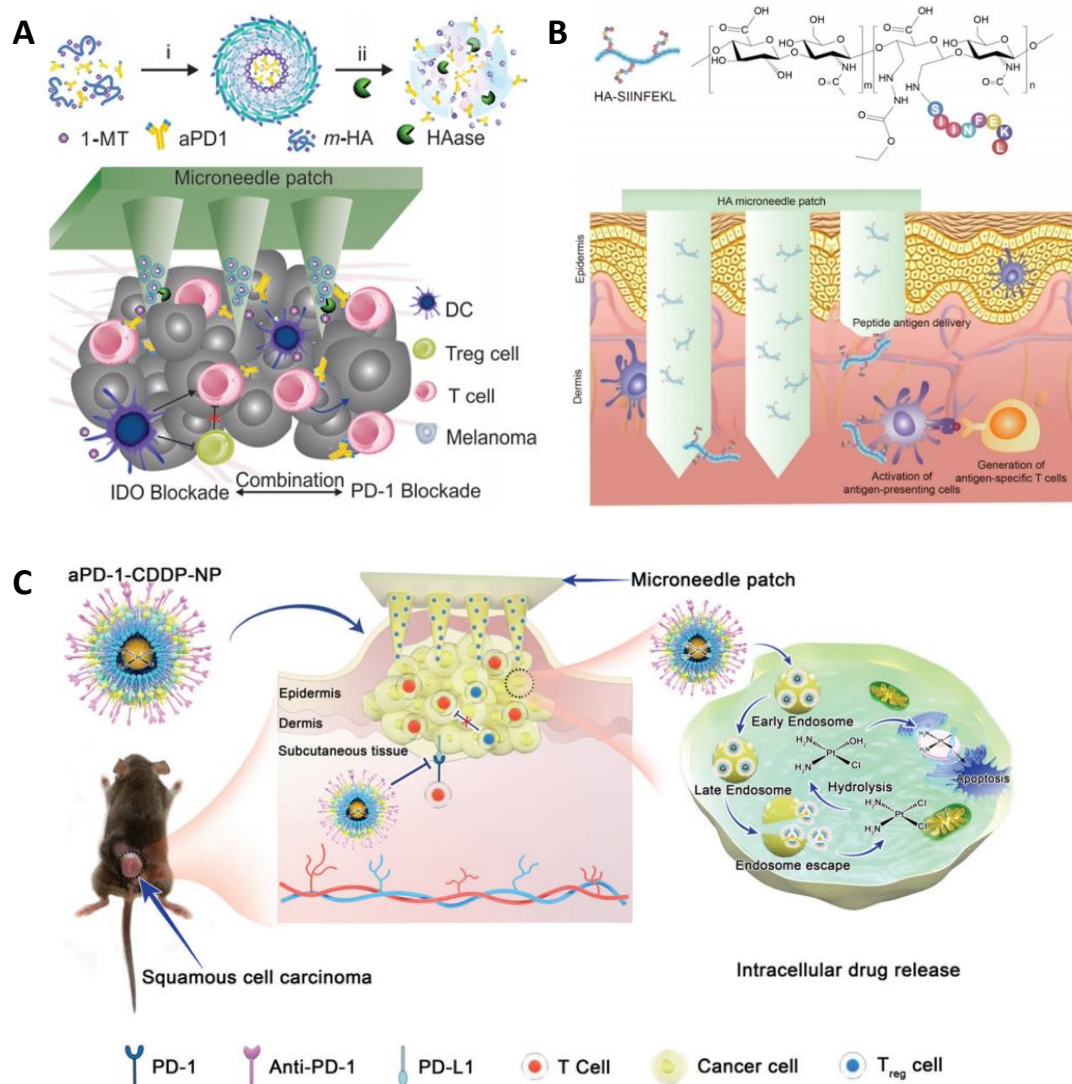


**Figure 1.14** Examples of dissolvable MN drug delivery systems for cancer immunotherapy applications. (A) Schematic illustration of encapsulation and release of IDO inhibitor 1-MT and aPD1 from self-assembled m-HA NPs. Reprinted from Y. Ye *et al.*<sup>254</sup> (B) Schematic illustration for the transdermal immunization using a microneedle patch delivering multivalent hyaluronate (HA)-antigenic peptide (SIINFEKL) conjugates for cancer immunotherapy. Reprinted from Kim *et al.*<sup>256</sup> (C) Schematic illustration of the synergistic effects of immuno-chemotherapy of anti-PD-1 and CDDP delivered through a microneedle. Reprinted from Lan *et al.*<sup>258</sup>

Although solid MNs have been less explored in the context of cancer immunotherapy due to biocompatibility concerns and reduced dosage control, some examples using the 'coat and poke' approach can be found in the literature. Duong *et al.* proposed the use of a layer-by-layer coated polycarbonate MN device for the sustained delivery of a DNA polyplex and poly (I:C) as the immunotherapeutic drug load.<sup>259</sup> The vaccines were adhered to the MN surface with 72 alternating layers of the anionic poly (I:C) and an ultra-pH sensitive cationic polymer with a final layer consisting of a solution of the DNA polyplex. The ultra-pH sensitive polymer transformed into an anionic copolymer upon skin insertion releasing the drug load through electrostatic repulsion. The MN mice *ex vitro* assays demonstrated enhanced antibody and IFN- $\gamma$  expression in response to MN application, while an *in vivo* assay showed promising results with reduced tumour growth and prolonged mice survival in a B16-OVA murine model. Zeng *et al.* also opted for the layer-by-layer approach using insoluble poly(L-lactide) MNs (**Figure 1.15 A**).<sup>260</sup> The MNs were first prepared by the traditional micromolding method followed by up to 128 layers of alternating anionic CpG and cationic tumour antigen layers. The former is a TLR9 agonist, while the latter consisted of the human melanoma antigen, tyrosinase-related protein 2, conjugated to cationic amino acid residue. Vaccine coated MN administration into mice elicited enhanced CD8<sup>+</sup> T cell production and favourable DC cell internalisation *in vitro*. DeMuth *et al.* developed a coherent layer-by-layer MN system by incorporating a NP element (**Figure 1.15 B**).<sup>261</sup> The PLGA-based MN was fabricated by micromolding and the maleimide-crosslinked multilamellar lipid vesicles incorporating the TLR4 agonist, MPLA, and an OVA-derived protein antigen were synthesised. The lipid NPs were attached to the MN surface, which was pre-coated with protamine sulfate and sulfonated poly(styrene), by application of the hydrolytically degradable cationic polymer. Degradation of the polymer upon skin insertion released the lipid vesicles into the system and ensured recognition by APC. The system showed an enhanced anti-OVA immunoglobulin immune response and APC internalisation in mice compared to the controls. The authors also noted that the surface dried vaccine formulation makes storage at room temperature feasible, which would also provide ease of transportation for distribution to the developing world.



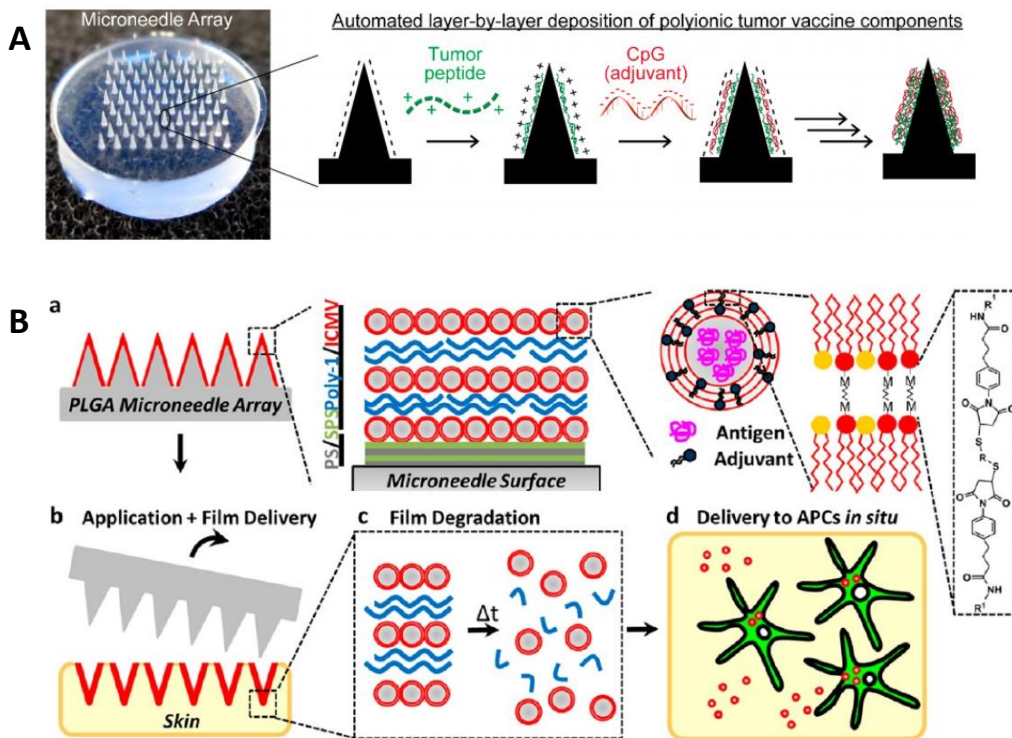


**Figure 1.15 Examples of solid MN systems for cancer immunotherapy.** (A) Approach for Assembling Immune Polyelectrolyte Multilayers on Microneedle Arrays to Enhance Cancer Vaccination. Reprinted from Zeng et al.<sup>260</sup> (B) Schematic illustration of (Poly-1/ICMV) multilayers deposited onto PLGA microneedle surfaces. ICMV lipid nanocapsules are prepared with interbilayer covalent cross-links between maleimide head groups (M) of adjacent phospholipid lamellae in the walls of multilamellar vesicles. (Poly-1/ICMV) PEMs were constructed on microneedles after (PS/SPS) base layer deposition. (b) Microneedles transfer (Poly-1/ICMV) coatings into the skin as cutaneous depots at microneedle insertion points. (c) Hydrolytic degradation of Poly-1 leads to PEM disintegration and ICMV release into the surrounding tissue. (d) ICMV delivery to skin-resident APCs provides coincident antigen exposure and immunostimulation, leading to initiation of adaptive immunity. Reprinted from DeMuth et al.<sup>261</sup>

## 1.6 Polymeric implants for cancer therapy

### 1.6.1 Types and fabrication of polymeric implants

Polymer-based implantable devices can present a highly advantageous approach for solid tumour treatment compared to conventional drug delivery routes by ensuring localised and gradual drug delivery and their potential as scaffolds for combination therapies.<sup>262</sup> Implant administration requires surgical treatment but can beneficially complement tumour resection procedures to prevent tumour recurrence or promote tumour regression in an incomplete tumour resection.<sup>263</sup> Implants can be the preferred choice of vaccine delivery system in cases where solution-based formulations are ineffective or not feasible. Polymeric implants can be classified into cast implants, injectable gels, electro spun nanofibers, 3D

printed implants and microdevices (**Figure 1.16**).<sup>264</sup> As with other drug delivery devices, implants can release their content by passive diffusion or designed for stimuli-responsive drug release through external triggers such as electrical or magnetic waves, ultrasound and light stimulation or environmental changes including pH, enzymes, metabolite concentration and temperature.<sup>264</sup>

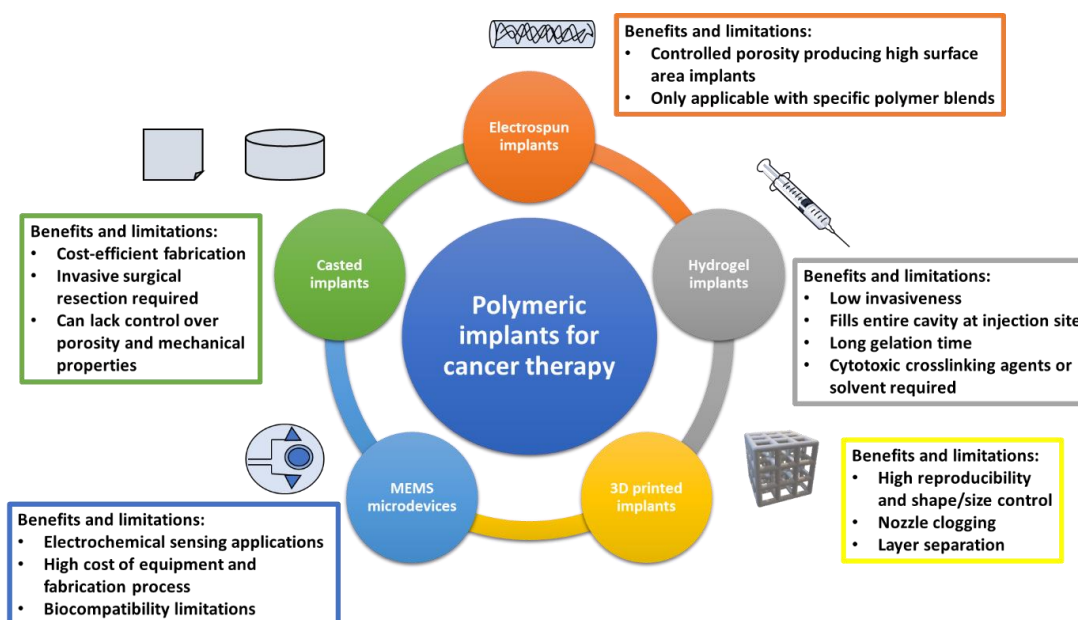


**Figure 1.16 Overview of different types of polymeric implants for application in cancer therapy.** Polymeric implants include solid casted implants, electrospun implants, hydrogel implants, 3D printed implants, and MEMS microdevices. They require specific polymers or polymer-mixtures to achieve desired physical and chemical properties. Adapted from Talebien *et al.*<sup>264</sup>

**Casted implants:** Casted implants are prepared by deposition of a polymer solution into a cast followed by solidification with the aid of heat, crosslinking or recrystallisation.<sup>265</sup> They can come in the form of thin wafers or more complex 3D structures and have been fabricated using a range of polymers including silk, dextran, PAMAM and gelatin. Seib *et al.* developed a silk film loaded with doxorubicin, which was implanted into breast tumour-bearing mice and showed gradual release for over 4 weeks and tumour growth reduction in comparison to the free drug control.<sup>266</sup> The silk film was prepared by casting onto a PDMS mold followed by annealing with water vapour to stabilise the silk film by enhancing the crystallinity and preventing rapid water solubilisation. The poly(1,3-bis-(p-carboxyphenoxy propane)-co-(sebacanhydride)) biodegradable polymer has been used for the development of chemotherapeutic drug incorporated wafers for glioma brain tumour treatment and after clinical success marketed as Gliadel Wafers®.<sup>267</sup> The fabrication involved the combination of the polymer with the chemotherapeutic drug carmustine dissolved in an organic solvent and

spray-dried onto microparticles, which are then deposited into a mold and compressed into a wafer by mechanical pressure. The drug elutes from the wafer over the course of 5 days as the result of hydrolysis of the polymer anhydride bonds, while the complete degradation of the polymer matrix can take up to several months.<sup>268</sup> Several wafers can be implanted at the head tumour resection site achieving a sustained delivery of drug and high bioavailability as there is no requirement to bypass the blood brain barrier. Further research has found that incorporation of different chemotherapeutic agent such as paclitaxel and doxorubin as well as combination with radiotherapy could enhance the therapeutic outcome of these wafers and effectively prevent tumour recurrence.<sup>269–271</sup>

*Injectable implants:* Injectable implants are administered via a hypodermic needle and solidify at the site of injection by phase inversion, crosslinking, temperature, or pH response.<sup>263</sup> Phase inversion occurs when a hydrophobic drug is dissolved in a water-miscible organic solvent and solidified upon injection due to dilution of the solvent in the aqueous environment. Non-polar organic solvents such as ethylbenzoate have shown that phase-inversion occurs more slowly with delayed drug release, while polar organic solvents including DMSO are more water miscible and, therefore, promote faster phase-inversion and drug release.<sup>272</sup> However, this method can often lead to solvent-related cytotoxicity. A preferable method is the use of temperature sensitive hydrogels using polymers that have a low glass transition temperature or melting point, which can be heated up before injection and solidify as they cool down at the site of injection.<sup>273</sup> In some cases, the glass-transition temperature can be controlled by polymer modifications or crosslinking to prevent rapid degradation and drug release from the implant. For instance, the chitosan-glycerophosphate salt hydrogel, better known as BST-Gel<sup>®</sup>, was combined with paclitaxel and showed the same therapeutic efficiency but reduced off-target cytotoxicity compared to 4 intravenous injections of the free drug, due to the gradual release from the hydrogel in a murine breast cancer model.<sup>274</sup> Another common thermosensitive hydrogel used for anticancer therapy is the PLGA-PEG-PLA triblock copolymer, branded OncoGel, which has been used for the incorporation of paclitaxel as standalone treatment and in combination with radiotherapy.<sup>275</sup> A study by Zentner *et al.* showed paclitaxel incorporation into OncoGel demonstrating the same therapeutic efficiency as treatment with paclitaxel in the absence of the hydrogel, but at a 10-fold lower dosing concentration in a murine breast cancer model.<sup>276</sup> Overall, injectable polymer hydrogels are less invasive than casted implants and provide an alternative platform for the local and sustained delivery of anticancer drugs.

*Electrospun implants:* Nanofibrous scaffolds are fabricated by electrospinning, a process in which an electric field is applied onto a solution of polymer drawn out of a syringe to form nano-sized polymer threads that deposit onto a grounded platform to form a porous scaffold consisting of a bed of fibres. Electrospinning for implant fabrication has been investigated with polymers such as PLGA, PLA, gelatin, polycaprolactone and poly(ethylene oxide).<sup>277</sup> The combination of electrospun nanofibers drug delivery systems with photothermal therapy was demonstrated by Chen *et al.*, in which doxorubicin was first incorporated into a core-shell NP system made from Cu<sub>9</sub>S<sub>5</sub> core within a mesoporous silica shell.<sup>278</sup> The nanoparticle induces thermal ablation of tumour cells when irradiated with NIR at 980 nm. The NPs were incorporated into a gelatin and polycaprolactone-based nanofibers. This device showed synergistic therapeutic effects through sustained NIR triggered drug release over 140 hours *in vitro* and significant tumour growth inhibition compared to the controls *in vivo* in a mice hepatoma model.

*3D printed implants:* More recently, 3D printing technology has paved the way for polymer implant fabrication. A porous PLGA and polycaprolactone based 3D-printed patch incorporating the chemotherapeutic drug fluorouracil developed by Yi *et al.* showed gradual drug release kinetics and enhanced tumour growth suppression in a murine pancreatic cancer model.<sup>279</sup> The 3D-printed patch was prepared by extrusion of the polymer mixture in combination with the drug at elevated pressure and temperature to form a paste, which was subsequently loaded onto a 3D printer to form flexible patches with controlled shape, size, pore size and layers.

*MEMS microdevices:* Polymeric implants for cancer therapeutic applications have also been fabricated by MEMS processes such as micromachining and photolithography.<sup>280</sup> These non-degradable devices typically consist of a solid base containing microchannels and micro-reservoirs to transport and store the solution-based drug load. MEMS can incorporate microsensors and micro-actuators that can be designed for electronically controlled drug release.<sup>280</sup> An SU-8 photoresist polymer was used to fabricate a microdevice by photolithography integrated with electrodes and fluidic channels for the sensing of neurological activity and precision drug delivery. The device's potential was analysed *in vivo* by implantation into rat dorsal hippocampus section of the brain and was able to record single-cell activity and local field potential oscillations.<sup>281</sup>

## 1.6.2 Casted implant developments in cancer immunotherapy

Due to limitations of solid implants, specifically regarding the high invasiveness of delivery, there are currently only a few studies in the context of dissolvable or biodegradable disk implants for cancer immunotherapy in the literature and so far, and no such system has been approved for clinical use. However, there are several clinically approved hydrogel-based and implant devices for other types of cancer therapy including Oncogel<sup>®</sup>, Gliadel<sup>®</sup>, and Vantas<sup>®</sup>, amongst others.<sup>282–284</sup> A highly promising study by Stephan *et al.* demonstrated the use of an alginate-based scaffold loaded with tumour targeted T cells for implantation near or at the resection site for enhanced treatment of inoperable or incompletely removed solid tumours and showed increased tumour regression in an ovarian cancer murine model compared to intraperitoneal T-cell injection in the absence of the scaffold (**Figure 1.17 A**).<sup>285</sup> Conde *et al.* developed a solid hydrogel implant from a dextran and poly(amidoamine) G5 dendrimer mixture for the local delivery of a combination therapy that achieved 90% tumour regression in a colon cancer model without resection and no tumour recurrence after resection for 170 days after treatment (**Figure 1.17 B**).<sup>286</sup> This system comprised an immunotherapeutic angiogenesis inhibitor, gold NPs as a heat mediator triggered by NIR irradiation and short interfering RNA-based gene therapy.

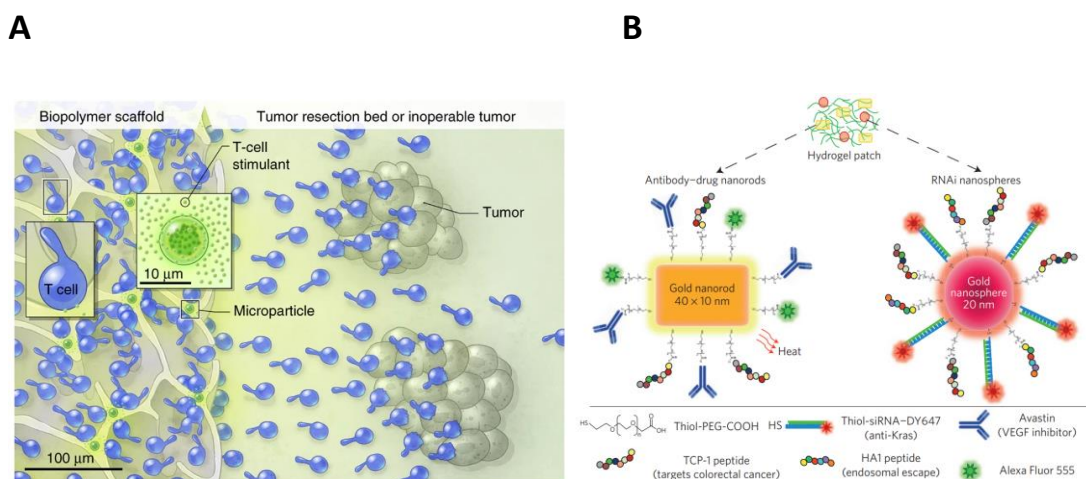


**Figure 1.17 Examples of dissolvable implantable devices for cancer immunotherapy.** (A) Schematic diagram of a T cell-loaded scaffold surgically situated at a tumor site. Stimulatory microspheres incorporated into the device trigger cell expansion and promote their egress into surrounding tissue. Reprinted from Stephan *et al.*<sup>285</sup> (B) Drug-gold nanorods and siRNA-gold nanospheres doped in implantable hydrogels for local drug/gene delivery and local hyperthermia. Reprinted from Conde *et al.*<sup>286</sup>

## 1.7 Overview and objectives of this research

Programming the immune system to recognise and eliminate cancer cells has gained recent interest and recognition due to its clinical success in some cancers. It provides an alternative form of treatment with the potential to overcome some of the main challenges in conventional chemo and radiotherapies such as off-target cytotoxicity and tumour recurrence by navigating the immune system towards a tumour-specific response and developing prolonged protection through the recruitment of memory T cells. Dissolvable and biodegradable transdermal drug delivery systems capable of delivering the drug load into immune cell abundant regions in the skin in a non-invasive manner may reach their full potential in immunotherapy applications, whilst biomaterial-based implantable devices provide an alternative administration route that can be useful when solution-based formulations are not viable. Implantable drug delivery devices can be fabricated at low cost and administered at the tumour resection site to prevent tumour recurrence by ensuring a local and gradual delivery of mono- or combination therapies.

The aim of this thesis is the synthesis and characterisation of an immunomodulatory HA-based biomaterial (1MT-HA) with gradual drug release kinetics that can be used as the base material for the fabrication of NPs and drug administration devices (Chapter 3). The development of different nanoparticle and microparticle systems including anti-PD-L1 incorporated HA NPs, IONPs functionalised with a Pt(IV) prodrug and other immunostimulatory agents, QDs and diatom-based devices with both therapeutic or diagnostic properties (Chapter 4). The incorporation and functional studies *in vitro* of some of these developed NP systems and the 1MT-HA biomaterial into HA-based MNs and implantable devices for cancer immunotherapy applications (Chapter 5). The specific aims and objectives are summarized below:

- Exploring the covalent functionalisation of HA with the clinically relevant IDO inhibitor, 1MT, to achieve a sustained and local release of 1MT in the presence and absence of HAase;
- The synthesis of different immunomodulatory NP and microparticle systems, this includes:

- Synthesis of biodegradable 1MT-HA NPs by a self-assembly process with the aim of obtaining uniformly sized particles and capable of showing gradual drug release kinetics of an immune checkpoint inhibitor (anti-PD-L1);
- Development of IONP-based chemotherapeutic and immunomodulatory constructs including a Pt(IV) prodrug-based IONP system and IONPs functionalised with a combination of immunostimulatory agents (poly-IC and imiquimod) that could achieve a local and synergistic anti-cancer effect;
- Exploring the diagnostic and therapeutic applications of diatoms by a developing tandem catalytic diatom-based device with magnetic properties and the development of a multimodal diatom system by covalent functionalisation with an immune checkpoint inhibitor (anti-PD-L1) and exploring its potential use as a biosensor;
- Fabrication of biodegradable HA-based MNs capable of targeting the immune cell-rich dermal skin layer and implantable devices incorporating the previously developed NP systems and the 1MT-HA biomaterial. The evaluation of the MN skin penetration efficiency and gradual release of the incorporated agents;
- Validation of the retention of functional activity of the incorporated therapeutic agents following the release from a MN or an implantable device *in vitro* using different murine and human cancer cell models.

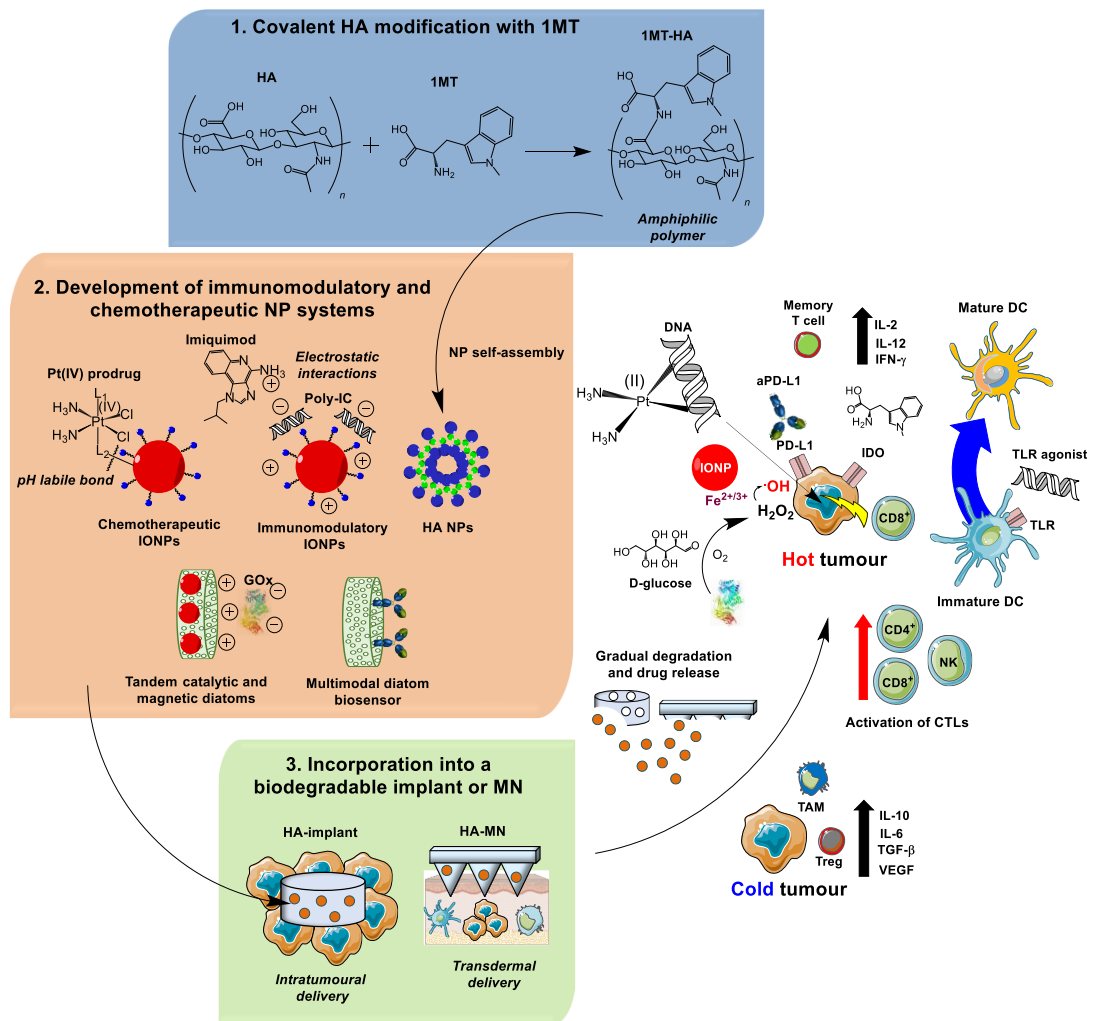


**Figure 1.18 Overview schematic of aims and objectives.** The first stage involves the covalent functionalisation of HA with 1MT to create an amphiphilic biomaterial that can self-assemble into NPs. The second stage of this thesis focuses on the development of immunomodulatory and chemotherapeutic nano- and microparticle systems. The third stage is the incorporation of the systems created in stage 2 into a transdermal or implantable biomaterial-based drug administration device capable of gradual and local drug release turning an immunosuppressive cold tumour into a hot tumour.



# Chapter 2

## Materials and methods

## 2.1 Materials

### 1. Synthesis of 1MT-HA and 1MT-HA@anti-PD-L1 NPs

1-Methyl-DL-tryptophan (1MT) (Sigma-Aldrich), Sodium bicarbonate (VWR International), Di(tert-butyl) decarbonate (Alfa Aesar), tetrahydrofuran (Thermo Fisher Scientific), hydrochloric acid 37% (Thermo Fisher Scientific), ethyl acetate (Thermo Fisher Scientific), ninhydrin (Sigma Aldrich), Dowex™ 50WX8-200 ion-exchange resin, ACROS Organics™ (Thermo Fisher Scientific), tetrabutylammonium hydroxide solution 40% in water (Sigma Aldrich), 1,1'-carbonyldimidazole (Sigma Aldrich), dimethyl sulfoxide (Sigma Aldrich), 4-(Dimethylamino)pyridine (VWR), hyaluronic acid sodium salt (MW: 33kDa and 280kDa) were kindly provided by Bloomage Freda Biopharm Co., Ltd (Jinan, China), SnakeSkin™ dialysis tubing, 10K MWCO, 22 mm (Thermo Fisher Scientific), methanol certified AR for analysis (Thermo Fisher Scientific), anti-PD-L1 (atezolizumab) was kindly provided by CIC bioGUNE (Donostia, Spain), Vivacon 500-PCR grade, 100,000 MWCO (Sartorius), 40 µL disposable plastic cuvette (Malvern Panalytical Ltd.) and folded capillary zeta cell (Malvern Panalytical Ltd.). TLCs were carried out on TLC Silica gel 60 F254 (Sigma-Aldrich).

### 2. 1MT release assays

Hyaluronidase from bovine testes type IV-S 750-3000 U/mg (Sigma Aldrich), PBS Tablets (Phosphate Buffered Saline, Thermo Fisher Scientific), Amicon® Ultra-4 centrifugal filter unit (Sigma-Aldrich), acetonitrile ≥99.5% (AnalaR NORMAPUR® ACS, VWR), potassium phosphate dibasic (Thermo Fisher Scientific), sodium phosphate, monobasic (Thermo Fisher Scientific) and ethylenediaminetetraacetic acid (Thermo Fisher Scientific).

### 3. Non-cellular and cellular IDO inhibition assay

Recombinant human indoleamine-2,3-dioxygenase protein (Abcam), recombinant human IFN-γ, carrier-free (Biolegend), trichloroacetic acid (Sigma-Aldrich), L-tryptophan (Sigma-Aldrich), catalase from bovine liver (Sigma-Aldrich), L-kynurenine (Sigma-Aldrich), methylene blue (Sigma-Aldrich), L(+)-Ascorbic Acid 99% (Thermo Fisher Scientific), 3-(4,5-dimethylthiazol-2-yl)-2,5-diphenyltetrazolium bromide (MTT, Thermo Fisher Scientific), sodium acetate trihydrate (Thermo Fisher Scientific) and acetic acid glacial, extra pure (Thermo Fisher Scientific).

#### **4. Synthesis of IONP and QD micelles**

Hydrophobic IONPs were provided by my PhD colleague Marc Bilbao-Asensio. Hydrophobic CdSe/ZnS core-shell QDs, pIC, anti-PD-L1 (atezolizumab) and R837 (imiquimod) were provided by CIC biomaGUNE. 2-iminothiolane (Traut's reagent) was purchased from Thermo Fisher Scientific. 1,2-distearoyl-sn-glycero-3-phosphoethanolamine-N-[carboxy(polyethylene glycol)-2000] (sodium salt), 1,2-dioleoyl-3-trimethylammonium-propane (chloride salt), 1,2-distearoyl-sn-glycero-3-phosphoethanolamine-N-[methoxy(polyethylene glycol)-2000] (ammonium salt) and 1,2-distearoyl-sn-glycero-3-phosphoethanolamine-N-[amino(polyethylene glycol)-2000] (ammonium salt) were purchased from Avanti Polar Lipids. The purification was performed using 0.45 µm syringe filters (Waters™, Acrodisc, Syringe Filter, PTFE, 4 mm, 0.45 µm, non-polar) and ultracentrifugation on a Beckman Coulter Optima XPN-80 Ultracentrifuge using the Type 45 Fixed-Angle Titanium Rotor with 1.5 mL microcentrifuge tube adapters. The PD-L1 ELSA kit was purchased from Abcam.

#### **5. HA MN fabrication and porcine skin penetration assays**

The MN PDMS molds (15x15 array, cone-shaped, 700 µm and 200 µm height, 600 µm centre-to-centre spacing, 150 µm base radius) were purchased from Blueacre Technology Ltd.. Methylene blue was kindly provided by Prof Owen Guy's research group (CNH).

#### **6. Synthesis of anti-PD-L1 functionalised diatoms**

Commercial diatomaceous earth was purchased from Bulk Powders®. The following materials were used for the antibody conjugation synthesis:

(3-aminopropyl)triethoxysilane 99% (Sigma-Adrich), Sulfo-SMCC (sulfosuccinimidyl 4-(N-maleimidomethyl)cyclohexane-1-carboxylate) (Thermo Fisher Scientific), 2-iminothiolane (Thermo Fisher Scientific), Toluene ACS reagent, ≥99.5% (Sigma-Adrich), sodium hydroxide ACS reagent, ≥97.0%, pellets and anti-PD-L1 (atezolizumab) was kindly provided by CIC bioGUNE (Donostia, Spain). The Pierce Micro BCA Protein Assay Kit was purchased from Thermo Fisher Scientific.

#### **7. Synthesis of Diatom-IONP-GOx and peroxidase-like activity assays**

Polyethyleneimine, branched, M.W. 1,800, 99% (Alfa Aesar), IONP(citrate) micelles were provided by my PhD colleague Marc Bilbao-Asensio, Glucose Oxidase from *Aspergillus niger*, Type X-S, lyophilized powder, 100k-250k U/g (Sigma-Aldrich), D(+)-glucose was kindly

provided by a Dr. Kuehnel's research group, hydrogen peroxide 30% (w/v) (Fisher Scientific), 3,3',5,5'-Tetramethylbenzidine, 98% (Alfa Aesar), dimethyl sulfoxide (Sigma Aldrich), sodium acetate trihydrate (Thermo Fisher Scientific) and acetic acid glacial, extra pure (Thermo Fisher Scientific).

## **8. Cell lines**

Human cervical cancer HeLa cells and human ovarian cancer Skov-3 were kindly provided by the RGO research group (CNH). Murine melanoma B16-F10(OVA) and murine macrophage RAW264.7 cells were kindly provided by Dr. Ane Ruiz de Angulo (CIC biomaGUNE). All other cell lines were kindly provided by Dr. James Cronin's research group (ILS1). The cell culture media, DMEM/phenol red free, high glucose, HEPES (Gibco®) and RPMI-1640 were purchased from Gibco UK. All other cell culture media was kindly provided by Dr. James Cronin's research group (ILS1). Media supplements including L-glutamine (200 mM), fetal bovine serum (FBS) and Penicillin-Streptomycin (Pen-strep, 50 U/mL) were purchased from Gibco UK.

## **2.2 Instrumentation**

### **1. Nuclear magnetic resonance (NMR)**

<sup>1</sup>H-NMR and <sup>13</sup>C-NMR were performed on a Bruker Avance III 500 MHz instrument with frequency resolution of <0.005 Hz and phase resolution of <0.006° running ICON NMR using Topspin 3.2 software. Samples were run in deuterated solvents including CDCl<sub>3</sub>, DMSO-d<sub>6</sub> or D<sub>2</sub>O. For the <sup>13</sup>C-NMR spectra in D<sub>2</sub>O, 5% w/w DMSO was added as a reference.

### **2. High performance liquid chromatography (HPLC)**

RP-HPLC was carried out on a Perkin Elmer Altus HPLC system with an A-10 solvent and sample module, A-10 photodiode array (PDA) detector and operating on the Empower® 3 software. All the samples were run on a Brownlee SPP C-18 Column 150 mm x 4.6 mm ID (Perkin Elmer) using the settings specified in the methods section.

### **3. Fast protein liquid chromatography (FPLC)**

FPLC was performed on a Bio-Rad Laboratories, Inc. NGC chromatography system with an NGC Multi-Wavelength detector II Module, a BioFrac fraction collector and operating on the ChromLab software. Samples in MilliQ were run on a pre-packed Cytiva Lifesciences Superose® 6 Increase 10/30 GL column composed of a cross-linked agarose matrix with a Tricorn™ glass outer casing and a globular protein fractionation range of 5-5000 kDa.

#### **4. Dynamic light scatter (DLS) and zeta potential**

DLS and zeta potential measurements were performed on a Malvern Zetasizer Nano ZS using 175° backscatter detection at 25°C. All samples were dispersed in MilliQ water and zeta potential samples contained 3.4 mM (0.02% w/w) NaCl. Zeta potential was performed at a cell drive voltage of 150 mV using the Smoluchowski approximation.

#### **5. Nanoparticle tracking analysis (NTA)**

NTA was performed on a Particle Metrix Zetaview® instrument (Analytik) with size measurements scanning 11 positions and 2 cycles, while zeta potential analysed 2 positions and 2 cycles. Measurements were taken at 20% camera sensitivity, 30 frames/s and 100 s<sup>-1</sup> shutter settings. All samples were dispersed in MilliQ water and zeta potential samples contained 0.09% NaCl.

#### **6. UV-vis spectroscopy**

UV-vis measurements for IONP and QD micelle quantification and peroxidase-like activity assays were performed on a Thermo Fisher Scientific Nanodrop™ One instrument applying a baseline correction at 750 nm and 2 µL sample volume deposition.

The UV-vis analysis of the bioassays including ELISA, BCA and peroxidase-like activity were carried out on the BMG Labtech FLUOstar® Omega multi-mode microplate reader operating on the MARS Omega software. Sample analysis was performed on Thermo Scientific Nunc™ 96-well microplates.

#### **7. Scanning electron microscopy (SEM) and electron dispersive X-ray spectroscopy (EDX)**

Analysis was performed on a Hitachi S4800 field emission (FE)-SEM instrument using the secondary electron detector and working distance of 8-15 mm, specimen size of 2 inches at probe current: normal and focus mode: UHR. The SEM software was called Hitachi S4800, while the Oxford Instruments EDX module was operated on the INCA Energy software. All samples were mounted onto an aluminium-based 32 mm diameter stub attached either with copper alloy-based clips or leit adhesive carbon tabs 12 mm diameter (Agar Scientific). All photographs of MNs were captured on an iPhone 7 camera.

## 8. Confocal laser scanning microscopy (CSLM)

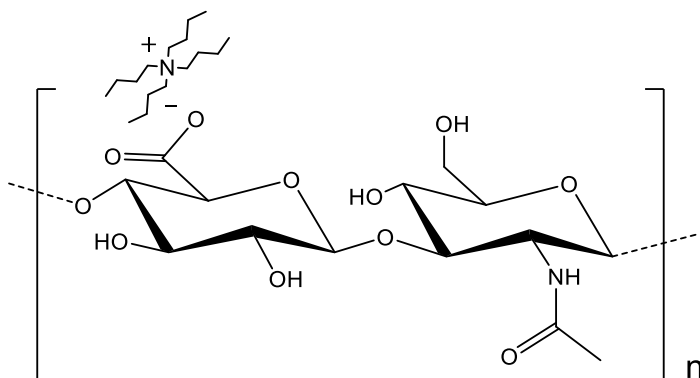
The Carl Zeiss LSM 710 confocal microscope equipped with an HBO 100 mercury vapor short-arc lamp and a QUASAR multichannel detector unit with maximum field resolution of 6144 × 6144 pixels was used for the characterisation of fluorescent MNs.

## 9. X-ray photoelectron spectroscopy (XPS)

XPS was performed on a Kratos Analytical, Ltd. AXIS Supra<sup>+</sup> instrument with a monochromated Al K $\alpha$  X-ray source and 128 channel Delay-Line Detector (DLD). The instrument operates on the ESCape software. All samples were mounted on a combination sample holder and attached with leit adhesive carbon tabs and analysed at 15 mA emission current. Spectra were processed on the CasaXPS software.

## 2.3 Methods

### 1. Synthesis of HA-TBA salt

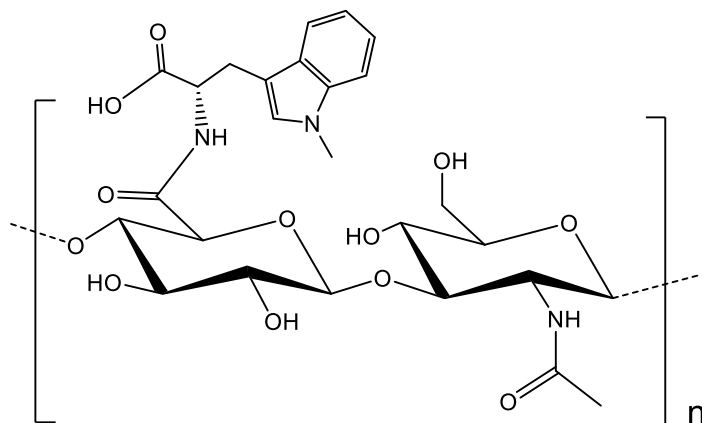


The reaction was carried out as previously reported.<sup>287</sup> HA sodium salt (100.0 mg, 0.264 mmol) was dissolved at 5 mg/mL in MilliQ water and Dowex 50WX 8-200, a sulfonic acid-based exchange resin was added slowly at 4°C until pH 2 was recorded (438 mg) and allowed to stir for 2 h. The resin was filtered off by vacuum filtration and the sulfonated HA was washed 2 times with MilliQ water to remove any resin impurities. Tetrabutylammonium hydroxide (TBA-OH) solution 40% in water was added dropwise to the HA solution until pH 7. Once neutralised, the solution was frozen to -80°C followed by lyophilization. The resulting white solid was stored at -20°C. Yield: 142.7 mg (0.229 mmol), 87.1%.

<sup>1</sup>H-NMR (D<sub>2</sub>O):  $\delta$ 0.95 (t, 3H, TBA -CH<sub>3</sub>),  $\delta$ 1.37 (m, 2H, TBA -CH<sub>2</sub>),  $\delta$ 1.65 (m, 2H, TBA -CH<sub>2</sub>),  $\delta$ 3.20 (t, 2H, TBA -CH<sub>2</sub>),  $\delta$ 2.02 (m, 3H, -NHCOCH<sub>3</sub>),  $\delta$ 3.34-3.84 (m, 15H, sugar anomeric

protons),  $\delta 4.45$  (d, 2H, sugar anomeric protons),  $\delta 7.15$  (s, 1H,  $-\text{CH}_{\text{N-methylindole}}$ ),  $\delta 7.19$  (t, 1H, 1- $\text{MT}_{\text{Ar-H}}$ ),  $\delta 7.30$  (t, 1H, 1- $\text{MT}_{\text{Ar-H}}$ ),  $\delta 7.48$  (d, 1H, 1- $\text{MT}_{\text{Ar-H}}$ ),  $\delta 7.64$  (d, 1H, 1- $\text{MT}_{\text{Ar-H}}$ ).

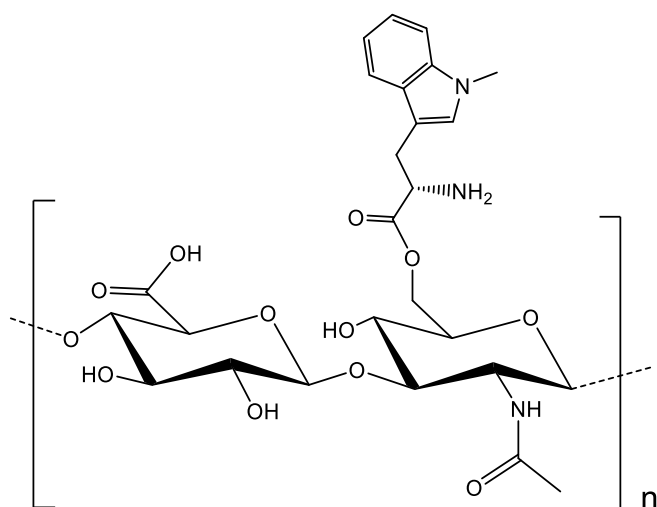
## 2. Synthesis of 1MT-HA



The procedure was adapted from Ye *et al.*<sup>254</sup> 33 kDa MW HA-TBA (293.0 mg, 0.417 mmol) was dissolved in 10 mL anhydrous DMSO and CDI (74 mg, 0.456 mmol) was added. The reaction was stirred at RT under an inert atmosphere overnight (19 h). 1MT (100 mg, 0.458 mmol) and DMAP (10 mg, 0.082 mmol) were added, and the reaction was left stirring for 48 h until esterification was completed. The product was dialysed against 1:1 MilliQ water: methanol using 10 kDa MWCO Snakeskin® dialysis tubing for 24 h followed by an additional dialysis cycle for 48 h in MilliQ water pH 5-6. The product was frozen and lyophilized for 72 h to obtain a white solid. Yield: 139.9 mg (0.241 mmol), 51.2%

$R_f = 0.11$  (silica, ethanol).  $^1\text{H-NMR}$  ( $\text{D}_2\text{O}$ ):  $\delta 2.02$  (m, 3H,  $-\text{NHCOCH}_3$ ),  $\delta 3.54$ - $3.78$  (m, sugar anomeric protons),  $\delta 4.55$  (d, 2H, sugar anomeric protons),  $\delta 7.16$  (s, 1H,  $-\text{CH}_{\text{N-methylindole}}$ ),  $\delta 7.19$  (t, 1H, 1- $\text{MT}_{\text{Ar-H}}$ ),  $\delta 7.31$  (t, 1H, 1- $\text{MT}_{\text{Ar-H}}$ ),  $\delta 7.48$  (d, 1H, 1- $\text{MT}_{\text{Ar-H}}$ ),  $\delta 7.70$  (d, 1H, 1- $\text{MT}_{\text{Ar-H}}$ ).  $^{13}\text{C-NMR}$  ( $\text{D}_2\text{O} + 5\%$  v/v DMSO):  $\delta 24.12$  ( $-\text{NHCOCH}_3$ ),  $\delta 55.89$  ( $-\text{NHCH}_2-$ ),  $\delta 62.13$  ( $-\text{CH}_2\text{OH}$ ),  $\delta 102.13$  and  $\delta 104.76$  ( $-\text{OCHO}$ ),  $\delta 110.92$  (1- $\text{MT}_{\text{Ar-C}}$ ),  $\delta 111.53$  (1- $\text{MT}_{\text{Ar-C}}$ ),  $\delta 120.43$  (1- $\text{MT}_{\text{Ar-C}}$ ),  $\delta 123.31$  (1- $\text{MT}_{\text{Ar-C}}$ ),  $\delta 138.35$  (1- $\text{MT}_{\text{Ar-C}}$ ),  $\delta 175.69$  ( $-\text{NHCOCH}_3$ ),  $\delta 176.49$  ( $-\text{CO-1MT}$ ).

### 3. Synthesis of 1MT-HA ester



The reaction was carried out as previously reported.<sup>254</sup> Briefly, 50 mg (0.228 mmol) of 1MT, NaHCO<sub>3</sub> (72.18 mg, 0.86 mmol) and di(*tert*-butyl) dicarbonate (60 mg, 0.28 mmol) were added to 5 mL of 1:1 THF: MilliQ water and stirred at 0°C for 10 min. The reaction was further stirred at RT for 24 h. THF was evaporated under reduced pressure and the resulting aqueous solution was acidified with 1M HCl dropwise until pH 2. The product was extracted with ethyl acetate and the organic phase evaporated under reduced pressure to give 1MT-BOC as a yellow solid. Yield: 54 mg (0.169 mmol), 73.9%.

The 1MT-BOC product (25 mg, 0.080 mmol) was dissolved in 3 mL anhydrous DMSO at RT and CDI (13 mg, 0.080 mmol) was added. The mixture was stirred for 2 h at RT under inert atmosphere to produce Im-1MT-BOC. 280 kDa MW HA-TBA (30 mg, 0.048 mmol) was dissolved in DMSO at 5% w/w and the Im-BOC-MT solution was added followed by DMAP (5 mg, 0.041 mmol) and the reaction left stirring for 24 h at RT. The product was purified by dialysis against 1:1 water: methanol for 24 h and water with pH 5-6 for 48 h. The dialysed solution was lyophilized to obtain a white solid. Yield: 18.5 mg (0.027 mmol), 57.1%.

$R_f=0.09$  (silica, ethanol). <sup>1</sup>H-NMR (D<sub>2</sub>O):  $\delta$ 1.06 (t, 3H, TBA -CH<sub>3</sub>),  $\delta$ 1.35 (m, 2H, TBA -CH<sub>2</sub>),  $\delta$ 1.65 (m, 2H, TBA -CH<sub>2</sub>),  $\delta$ 3.20 (t, 2H, TBA -CH<sub>2</sub>),  $\delta$ 2.01 (m, 3H, -NHCOCH<sub>3</sub>),  $\delta$ 3.20-3.79 (m, sugar anomeric protons),  $\delta$ 4.48 (d, 2H, sugar anomeric protons),  $\delta$ 7.15 (s, 1H, -CH<sub>Nmethylindole</sub>),  $\delta$ 7.19 (t, 1H, 1-MT<sub>Ar-H</sub>),  $\delta$ 7.30 (t, 1H, 1-MT<sub>Ar-H</sub>),  $\delta$ 7.48 (d, 1H, 1-MT<sub>Ar-H</sub>),  $\delta$ 7.64 (d, 1H, 1-MT<sub>Ar-H</sub>).



#### **4. Synthesis of 1MT-HA@anti-PD-L1 NPs**

The NP self-assembly was carried out as previously reported.<sup>2</sup> 1MT-HA ester (5 mg, 6.1 mmol) and anti-PD-L1 (0.2 mg, 1.38 nmol) were added to a solution of MilliQ water: methanol (2:1 v/v) and the emulsion was stirred at 4°C for 2 h. The methanol was removed by dialysis against MilliQ water using 10 kDa MWCO Snakeskin® dialysis tubing for 72 h and changing of the dialysis solution at 24 h intervals. The free anti-PD-L1 was removed by centrifugal filtration (300 kDa MWCO Nanosep®) and 5 washing cycles with MilliQ water at 2000 g for 10 min. The final 1MT-HA NP suspension was concentrated to 5 mg/mL. Characterisation was performed by DLS, zeta potential, NTA and SEM. For the control NPs the same procedure was followed, but in the absence of the antibody.

#### **5. 1MT-HA and 1MT-HA NP release assays**

1MT-HA or 1MT-HA NPs (5 mg) was added to 500 µL of 1x PBS pH 6.5 at 37°C containing HAase from bovine testes (1 mg, 18.2 nmol, 750-3000 U/mg). For the 1MT-HA biomaterial release assay, different pH conditions (pH 5, pH 6.5, and pH 8) were also analysed in the absence and presence of HAase. 100 µL aliquots were collected after each time point and purified by centrifugal filtration using 3 kDa MWCO spin filters at 12,000 g for 15 min. The filtrate containing the purified 1MT was quantified by RP-HPLC on a C-18 column (4.6 mm x 150 mm) at 223 nm, isocratic elution at 1 mL/min with a mobile phase containing 10 mM potassium phosphate buffer pH 5.0, 0.15 mM EDTA, 20% MeOH and 5% ACN. A 1MT calibration was derived under the same RP-HPLC conditions from 0.0-0.1 mM based on the 1MT UV-vis absorbance peak area at 223 nm.

#### **6. 1MT-HA@anti-PD-L1 NP release assay**

The release study of 1MT-HA@anti-PD-L1 NPs was performed under the same conditions described in experiment 5. The aliquots collected at timepoints 0, 1, 6, 24 and 48 h were purified from intact NPs by centrifugal filtration using 300 kDa MWCO filter at 10,000 g for 20 min. The filtrates were collected and characterised by FPLC. The 1MT-HA@anti-PD-L1 NPs collected timepoint samples were directly injected into the FPLC system on a Superose 6 Increase size-exclusion column at injection volume of 100 µL, flow rate of 0.5 mL/min using isocratic elution in MilliQ water. The UV-vis absorbance was measured at 225 nm and 280 nm.

## **7. Synthesis of HA-MNs**

All the MNs were fabricated by the micromolding technique using 15x15 array inverted MN PDMS molds. A HA solution in MilliQ water (33 kDa MW, 3.79 mM) was sonicated in a water bath at RT for 5 min to remove air bubbles and deposited onto the MN mold ensuring that all the cavities are covered. The mold was exposed to vacuum conditions for 10 min followed by centrifugation at 3000 g for 1 h to force and compact the HA solution into the mold cavities. The supernatant was removed by pipetting and residual HA on the mold was scraped off using a piece of aluminium foil. A piece of 1.5 cm x 8.0 cm silver adhesive tape was attached along the sides of the mold and 1.5 mL HA solution (3.03 mM) was added onto the mold reservoir to form the MN base plate. The MN was allowed to dry at RT and atmospheric pressure for 10 days until all the water is evaporated. The MN was carefully removed from the mold, cut in the desired shape and stored at 4°C until further use. The mold was cleaned by sonication in 50 mL of warm MilliQ water (50°C) for 48 h. For the fabrication of modified MNs the loading agent was added at the desired concentration to the HA solution (3.79 mM) prior to deposition onto the MN mold. The MN morphology was characterised by SEM (SE detector, 1 kV accelerating voltage).

## **8. Synthesis of HA implants**

A HA solution in MilliQ water (33 kDa MW, 100 mg, 3.03 mM) in 1 mL was deposited into a well of a 48-well cell culture plate and dried for 3 days at RT under reduced pressure. The implantable disc was removed from the plate with a clean scalpel and stored at 4°C. For the functionalised implants, the loading agent was added to the HA solution in MilliQ water and homogenised by sonication for 5 min or gentle pipetting before deposition into the well. For the 1MT-HA implants, 30 mg of 1MT-HA was added to the HA solution (70 mg, 2.12 mM) and mixed until homogeneous before addition to the well.

## **9. HA MN and HA implant release assays**

The MN and implant degradation was carried out as outlined for the 1MT-HA release assay (see experiment 5), but in a release volume of 1.5 mL to account for the higher concentration of HA and viscosity of the solution. Sample collection timepoints and characterisation were specific to the experiments. For the 1MT-HA implants, the 1MT released after 48 h was purified by centrifugal filtration using 3 kDa MWCO filters and characterised by RP-HPLC as previously described. The remaining sample was lyophilised for 48 h and concentrated to 38.33 mM in 1x PBS.

## 10. Non-cellular IDO activity and inhibition assay

The IDO inhibition assay was performed as previously described.<sup>288</sup> For the IDO activity assay, a solution of 5 µg/mL of recombinant human IDO (rhIDO) was prepared in a standard assay medium containing 50 mM potassium phosphate buffer at pH 6.5, neutralised ascorbic acid at a working concentration of 20 mM, methylene blue at 10 µM, 100 µg/mL catalase and 200 µM L-tryptophan. The reaction was incubated for 1 h at 37°C to ensure complete metabolism of tryptophan into N-formylkynurenine followed by addition of 30% (v/v) trichloroacetic acid (TCA). The sample was incubated for a further 15 min at 60°C to hydrolyse the intermediate product into L-kynurenine. The solution was centrifuged at 11,500 rpm for 15 min at 4°C and the supernatant characterised by RP-HPLC on a C-18 column at 0.5 mL/min and gradient elution. Solvent A (10 mM sodium acetate buffer at pH 6.5 containing 10% methanol) was reduced from 100% to 50% over 16 min, while solvent B (100% methanol) was increased from 0% to 50% over the same time period. From 16-20 min the mobile phase returned to the initial conditions (100% solvent A) and UV-vis detection of L-kynurenine at 360 nm.

For the inhibition assay a solution of the 1MT released from the 1MT-HA implant at working concentration of 0.5 mM was added to the assay medium containing the enzyme and substrate before the incubation step. The positive control sample was performed in the absence of 1MT. As a negative control a fresh sample of 1MT was added at the same concentration as the 1MT released from the 1MT-HA implant and the amount of L-kynurenine generated quantified by RP-HPLC based on a calibration curve.

## 11. Cell-based IDO inhibition assays

The experimental method was adapted from Yue *et al.*<sup>289</sup> Unless otherwise stated, human and murine tumour cells were seeded at  $2 \times 10^4$  cells per well in a 96-well plate in DMEM/phenol red free or RPMI-1640 media containing 80 µM L-tryptophan, 10% FBS and pen-strep and incubated for 24 h at 37°C and 5% CO<sub>2</sub>. The following day, IFN-γ at 0.4 µg/mL and the 1MT released from the 1MT-HA implant at 0.5 mM in culture media were added to the cells in triplicate at 100 µL/well. As the controls, the cells were incubated without IFN-γ and 1MT (-- control), only IFN-γ (+ control), and IFN-γ with 1MT (- control) at the same concentration as the sample. The cells were incubated for 20 h, after which the supernatants were removed, and the repeats of each sample/control combined followed by treatment with 30 µL TCA (3.05 M) and incubated at 50°C for 30 min in order to precipitate large biomolecules and residual cells as well as to ensure complete hydrolysis of N-

formylkynurenine into L-kynurenine. The samples were purified by centrifugation at 2000 g for 5 min and the supernatants were analysed by RP-HPLC on a C-18 column using the conditions described in experiment 10. Since the experimental conditions have changed with respect to the non-cell-based assay, a new L-kynurenine calibration curve was produced from 0.0 to 0.2 mM used for quantification in all the *in vitro* studies.

### **12. MTT cell viability assay**

After removal of the supernatants for the IDO inhibition assay (experiment 11), to the cells were added 50  $\mu$ L of 0.5 mg/mL MTT in culture media and the cells were incubated at 37°C for 2 h. The supernatants were discarded, and 100  $\mu$ L DMSO was added to the wells to dissolve the generated formazan crystals. After gentle mixing for 30 s the 96-well plate was analysed by at an absorbance of 550 nm on a microplate reader.

### **13. MN porcine skin penetration**

To evaluate the MN penetration efficiency a square porcine skin sample larger than the area of the MN was cut to shape with a clean scalpel. The skin sample was applied with 300  $\mu$ L of HAase (18.2 nmol) in MilliQ water and the solution evaporate at 50°C for 2 h. The dry HAase-treated skin was attached with drawing pins onto a flat piece of cork sheet and the MN applied onto the skin for 1 min with firm pressure, after which medical tape was applied to fix the MN onto the skin and allowed to release the drug load for 24 h. The MN base was removed from the skin and 300  $\mu$ L of 2% wt/wt methylene blue dye was deposited onto the penetrated skin area and allowed to enter the cavities for 15 min. The remaining methylene blue was removed with dry medical wipes, followed by MilliQ water and ethanol moistened wipes. Photographs of porcine skin were captured on an iPhone 7 camera and % area penetration analysed using ImageJ.

### **14. Synthesis of IONP and CdSe/ZnS QD micelles**

The hydrophobic IONPs were prepared by my PhD colleague, Marc Bilbao-Asensio following a previously described procedure.<sup>155</sup> Hydrophobic CdSe/ZnS core-shell QDs were provided by a collaborative group in CIC biomaGUNE. IONP and QD micelle synthesis was carried out as previously described.<sup>290</sup> Hydrophobic IONPs or QDs and DSPE-PEG (2000)-carboxylic acid were suspended in 500  $\mu$ L of chloroform at a 1:2 (wt/wt) ratio and allowed to evaporate overnight at RT and any remaining solvent was removed under vacuum for 1 h. The resulting thin film was heated to 80°C for 30 s and rehydrated in 1 mL of MillQ water whilst gently mixing until the thin film was completely dissolved. The solution was transferred to a 1.5 mL

centrifugation tube and centrifuged at 9700 g for 5 min. The pellet was discarded, and the supernatant was passed through a 0.45  $\mu\text{m}$  syringe filter. This solution was ultracentrifuged at 369,000 g for 1 h and 3 cycles to remove the empty micelles. The pellet was dissolved in MilliQ water and stored at 4°C. The Fe concentration of the micelles was calculated based on a calibration curve by UV-vis spectroscopy, performed by my PhD colleague, Marc Bilbao-Asensio, using an IONP sample of known Fe concentration determined by ICP-OES in CIC biomaGUNE.

*Calculation of IONP concentration:* The IONPs in this thesis have an average diameter of approximately 7.0 nm. The [IONP] in the micelle samples was determined from the [Fe] using the following calculation:

$$V(\text{IONP}) = \frac{4}{3} \times \pi \times r^3 = \frac{4}{3} \times \pi \times (3.5 \times 10^{-7})^3 = 1.8 \times 10^{-19} \text{ cm}^3$$

$$\rho(\text{magnetite}) = 5.17 \text{ g cm}^{-3}; m = \rho(\text{magnetite}) \times V(\text{IONP}) = 9.29 \times 10^{-19} \text{ g}$$

$$\text{moles of Fe}_3\text{O}_4 = m / \text{MW}(\text{Fe}_3\text{O}_4) = 9.25 \times 10^{-19} / 231.5 = 4.01 \times 10^{-21} \text{ mol}$$

$$\text{moles of Fe} = 3 \times \text{moles of Fe}_3\text{O}_4 = 3 \times 4.01 \times 10^{-21} = 1.20 \times 10^{-20} \text{ mol}$$

$$\text{atoms of Fe per IONP} = \text{moles Fe in IONP} \times N_A = 1.20 \times 10^{-20} \times 6.022 \times 10^{23} = 7244 \text{ atoms}$$

### **15. Synthesis of anti-PD-L1 functionalised IONPs (IONP-aPDL1)**

The IONP-maleimide micelle synthesis was carried out as described previously (experiment 14) using the DSPE-PEG (2000)-maleimide phospholipid. The antibody was activated via lysine group modification using Traut's reagent (2-iminothiolane). To Traut's reagent (0.738  $\mu\text{g}$ , 5.38 nmol) in 68.7  $\mu\text{L}$  of degassed 1x PBS pH 8 supplemented with 2 mM EDTA was added anti-PD-L1 (1.3  $\mu\text{L}$ , 0.538 nmol) at Traut's reagent: anti-PD-L1 mol ratio of 10:1 and incubated for 1 h at RT at 800 rpm on a Thermoshaker. The thiol-modified antibody was purified from residual Traut's reagent by centrifugal filtration using 100 kDa MWCO spin filter devices at 4000 g for 3 min and washed 2x with PBS. The thiol-modified anti-PD-L1 at concentration of 1000  $\mu\text{g}/\text{mL}$  (6.90  $\mu\text{M}$ ) was added IONP-maleimide ([Fe]=2 mM) in batches of 70  $\mu\text{L}$  of 1x PBS pH 7 containing 5 mM EDTA. The reaction was incubated overnight (19 h) at RT at 600 rpm on a Thermoshaker. The product was purified by centrifugal filtration using 300 kDa MWCO spin filters at 500 g for 4 min and washed several times with MilliQ water until no more anti-PD-L1 was observed in the filtrate by UV-vis at 280 nm using a Nanodrop One spectrophotometer. The IONP-aPDL1 was stored at 4°C and the protein concentration was quantified by a BCA assay.

*PD-L1 ELISA procedure:* The PD-L1 ELISA was performed following the manufacturer's procedure. Briefly, the capture Ab was added to the pre-coated plate and incubated for 1h at RT and 400 rpm on a Thermoshaker followed by removal of the supernatant and washing of the plate with a buffer solution 3x. PD-L1 standards at working concentration of 0 and 80 pg/mL and IONP-aPDL1/IONP-Mal at 57 nM IONP were added to the plate in duplicate. The plate was incubated for 1h at RT and the supernatants were removed. The plate washed 3x and the capture Ab was added followed by incubation for 1h at RT. The supernatants were then removed, and the plate washed 3x with buffer solution. The final step was the addition of the TMB substrate, incubation for 10 min at RT, and addition of the stop solution. The plate was then measured at 450 nm on a microplate reader.

### **16. BCA protein quantification assay**

The protein quantification was performed using the Thermo Scientific™ Pierce™ BCA Protein Assay Kits following manufacturer instructions. Briefly, 25 µL of sample and controls were added to a 96-well plate in duplicate and 200 µL of the working reagent (50:1 v/v, reagents A:B) was added. The plate was incubated for 2 h at 37°C in the absence of light after which the absorbance was measured at 550 nm. A BSA standard calibration curve was produced from 0-1000 µg/mL.

### **17. Synthesis of anti-PD-L1 functionalised diatoms (D-aPDL1)**

*D-amine synthesis method:* The method was modified from Cicco *et al.*<sup>291</sup> The commercial diatoms were purified from organic residues by acid and peroxide treatment performed by my PhD colleague, Joel Crane. The purified commercial diatoms (15 mg) were stirred in 450 µL of toluene for 10 min at RT under inert N<sub>2</sub> atmosphere and 5 µL of MilliQ water was added. 3-aminopropyl-trimethoxysilane (APTES) 97% (9 µL, 51.6 µmol) was added in 3 parts (3 µL every 10 min) and the solution refluxed at 70°C for 1 h. The modified diatoms were purified by centrifugation at 5000 g for 5 min followed by 3 washing cycles in toluene, ethanol and MilliQ water, sequentially, to remove residual unbound APTES. The pellet was dried overnight under reduced pressure and the resulting APTES-modified biosilica stored at 4°C. Characterisation was performed by XPS at emission current of 15 mA.

*D-maleimide synthesis method:* To D-amine (5mg) in 100 µL of MilliQ water was added sulfosuccinimidyl 4-(N-maleimidomethyl)cyclohexane-1-carboxylate (sulfo-SMCC) and the reaction was incubated at RT for 2 h. The product was purified by centrifugation at 5000 g for 5 min and the pellet washed with 500 µL MilliQ water 3x to remove any unreacted or

hydrolysed sulfo-SMCC. The pellet was dried overnight under reduced pressure and D-maleimide product was stored at 4°C. Characterisation was performed by XPS at emission current of 15 mA.

*D-aPDL1 synthesis method:* To Traut's reagent (2-iminothiolane) (0.738 µg, 5.38 nmol) in 68.7 µL of degassed 1x PBS pH 8 supplemented with 2 mM EDTA was added anti-PD-L1 (1.3 µL, 0.538 nmol) at Traut's reagent: anti-PD-L1 mol ratio of 10:1 and incubated for 1 h at RT at 800 rpm on a Thermoshaker. The thiol-modified antibody was purified from residual Traut's reagent by centrifugal filtration using 100 kDa MWCO spin filter devices at 4000 g for 3 min and washed 2x with PBS. The retentate was made up to 100 µL with 1x PBS pH 7 supplemented with 2 mM EDTA and D-maleimide (1 mg) was added followed by incubation overnight (19 h) at RT on a Thermoshaker at 1300 rpm. The product was purified by centrifugation and the pellet was washed with MilliQ water 5x at 5000 g for 5min to remove the unbound antibody. pellet was concentrated to 200 µL and stored at 4°C. Characterisation was performed by XPS at emission current of 15 mA. The protein concentration of the D-aPDL1 was determined through a BCA assay.

## **18. Diatom biosensor experiment**

To D-aPDL1 (0.017 mg, [anti-PD-L1] = 4.28 pmol) was added human recombinant (rh) PD-L1 (Sino Biological) (2.22 ng, 85.5 fmol) in 10 µL of MilliQ water in microcentrifuge tubes (0.5 mL capacity) at an anti-PD-L1: PD-L1 mol ratio of 50:1 and the reaction incubated for 15 min at RT at 1300 rpm on a Thermoshaker. The samples were centrifuged at 500 g for 5 min to remove unbound ligand and the supernatant discarded. To the pellet was added IONP-aPDL1 (4.96 µL, [Fe] = 1.09 mM, [anti-PD-L1] = 4.77 nmol) in 10 µL of MilliQ water at a PD-L1: anti-PD-L1 mol ratio of 1:56 and the reaction incubated at RT for 1 h at 1300 rpm. The mixture was centrifuged at 500 g for 5 min and an aliquot of the supernatant collected (4.60 µL). To the collected sample was added TMB (0.832 mM) and H<sub>2</sub>O<sub>2</sub> (30.0 mM) in 10 µL of sodium acetate buffer pH 4.5 (56.0 mM) at IONP-aPDL1 [Fe] = 0.50 mM. The peroxidase-like activity was analysed by measuring the absorbance at 652 nm at the start of the reaction and after 1 h of incubation at RT in the absence of light. The analysis was performed on a Nanodrop One instrument with baseline correction at 750 nm and photographs of the samples were taken at the start and end of the reactions for comparison. The control samples consisted of the combination of the D-aPDL1 sensor with the IONP-aPDL1 detecting agent in the absence of PD-L1. The reaction was performed in triplicate.

## 19. Synthesis of Diatom-IONP(-citrate)-GOx

The IONP(-citrate) were prepared by fellow PhD colleague, Marc Bilbao-Asensio, following an adaptation of a previously described method.<sup>292</sup> To commercial diatoms (1 mg) was added polyethylenimine (PEI) (1.8 kDa MW, 1.22  $\mu\text{mol}$ ) in 500  $\mu\text{L}$  of MilliQ water. The solution was allowed to interact at RT for 15 min under constant mixing at 1300 rpm on a Thermoshaker and the excess PEI purified by centrifugation at 5000 g for 5 min. The pellet was washed 3x with MilliQ water and the supernatant discarded. To the pellet was added 200  $\mu\text{L}$  of IONP(-citrate) ( $[\text{Fe}] = 11.6 \text{ mM}$ ) and the mixture was incubated at for 15 min under constant mixing at 1300 rpm. The product was purified by centrifugation at 5000 g for 5 min the pellet was washed with MilliQ water 4x and 0.1 M acetate buffer pH 4.5 1x. To the D-PEI-IONP pellet was added glucose oxidase from *Aspergillus niger* (GOx) (2  $\mu\text{L}$ , 11.6 pmol) in 100  $\mu\text{L}$  of MilliQ water and incubated for 15 min under constant shaking at 1300 rpm at RT followed by centrifugation at 5000 g for 5 min and washing cycles with MilliQ water 3x. The pellet was dried under reduced pressure and the pellet stored at 4°C.

## 20. Diatom peroxidase activity assays

The peroxidase-like activity of the diatom samples was characterised by UV-vis at 652 nm, the maximum absorbance of oxidised 3,3',5,5'-tetramethylbenzidine (TMB), on a microplate reader. Unmodified and functionalised commercial diatoms (1 mg or 0.25 mg) were suspended into wells of a 96-well plate in 0.1 M sodium acetate buffer pH 4.5 followed by the addition of  $\text{H}_2\text{O}_2$  (30 mM) and TMB (0.832 mM) made up to a total volume of 250  $\mu\text{L}$  per well. The plate was incubated at 37°C in the absence of light and the reaction kinetics were monitored for 10 min. The catalytic activity was measured with respect to the absorbance difference ( $\Delta \text{A.U.}$ ) at 652 nm between the initial ( $t = 0 \text{ min}$ ) and the final timepoint ( $t = 10 \text{ min}$ ).

## 21. Synthesis of *c,c,t*-[Pt(NH<sub>3</sub>)<sub>2</sub>Cl<sub>2</sub>(OH)<sub>2</sub>]

Cisplatin (0.18 g, 0.60 mmol) was dissolved in MilliQ water (1.5 mL) and  $\text{H}_2\text{O}_2$  (9 mL, 30% w/v) was added. The solution was stirred at 50°C for 3 h and then allowed to cool down overnight. The product was purified by vacuum filtration with ice-cold MilliQ water and ethanol followed by drying under vacuum for 24 h. Yield: 0.14 g (0.43 mmol), 71.7%.

<sup>1</sup>H-NMR (DMSO-*d*<sub>6</sub>):  $\delta 3.33$  (s, H<sub>2</sub>O),  $\delta 10.20$  (s, 2H, -OH).



## 22. Synthesis of c,c,t-[Pt(NH<sub>3</sub>)<sub>2</sub>Cl<sub>2</sub>(O<sub>2</sub>CCH<sub>2</sub>CH<sub>2</sub>CO<sub>2</sub>H)<sub>2</sub>]

c,c,t-[Pt(NH<sub>3</sub>)<sub>2</sub>Cl<sub>2</sub>(OH)<sub>2</sub>] (138 mg, 0.41 mmol) and succinic anhydride (165 mg, 1.65 mmol) were dissolved in DMSO (0.85 mL) and stirred at 70°C for 24 h. MilliQ water was added to the reaction mixture (4.2 mL) and the solution was lyophilized for 48 h. The resulting white solid was washed several times with ice cold acetone. Yield: 190 mg (0.36 mmol), 88.7%.

<sup>1</sup>H-NMR (D<sub>2</sub>O): δ2.61-2.64 (t, impurity), δ2.68 (s, impurity), δ2.71-2.73 (multiplet, 6H, -CH<sub>2</sub>COO-), δ2.73 (s, impurity).

## 23. Synthesis of DSPE-PEG(2000)-Pt(IV)

c,c,t-[Pt(NH<sub>3</sub>)<sub>2</sub>Cl<sub>2</sub>(O<sub>2</sub>CCH<sub>2</sub>CH<sub>2</sub>CO<sub>2</sub>H)<sub>2</sub>] ((9.6 mg, 18.0 μmol), dicyclohexylcarbodiimide (DCC) (3.7 mg, 18.0 μmol), and 4-(dimethylamino) pyridine (DMAP) (1.0 mg, 7.2 μmol) were dissolved in DMSO (130 μL). After 10 min, the activated platinum (IV) complex was added to a solution of DSPE-PEG(2000)-amine (10 mg, 3.6 μmol) in 170 μL DMSO. The resulting mixture was allowed to react at RT for 96 h at 1000 rpm on a Thermoshaker. The product was divided into 2 centrifuge tubes and MilliQ water was added to both batches (2 x 1 mL). The solutions were centrifuged, and the supernatant was passed through a 0.45 μm syringe filter to remove insoluble traces. The supernatant was dialyzed in a Slide-A-Lyzer Dialysis Cassete (Thermo Scientific) (2000k Da MWCO) against water (1 l) for 24 h. The dialysate, containing the pure product, was lyophilized and the residue dried under vacuum. Yield: 11.2 mg (3.4 μmol), 94.1%.

<sup>1</sup>H-NMR (D<sub>2</sub>O): δ2.56-2.71 (-CH<sub>2</sub>-CH<sub>2</sub> (succinimidyl)), δ3.71 (-CH<sub>2</sub>-CH<sub>2</sub> (PEG)).

## 24. Synthesis of Pt(IV)-loaded IONPs

DSPE-PEG(2000)-Pt(IV) (2.5 mg) and hydrophobic Fe<sub>3</sub>O<sub>4</sub> nanoparticles (1 mg) were dissolved in chloroform (500 μL). The solvent was allowed to evaporate overnight in a 5 mL vial at RT. Any remaining solvent was removed under vacuum for 1 h. The flask was placed in a water bath at 80°C for 30 s, after which 1 mL of MilliQ water was added. The solution was transferred to a centrifugation tube and centrifuged at 9700 g for 5 min. The pellet was discarded, and the supernatant was passed through a 0.45 μm syringe filter. This solution was ultracentrifuged (369 000 g, 45 min, 3 cycles) to remove empty micelles. Finally, the pellet was dissolved in MilliQ water. The IONP-filled micelles were stored at 4°C.

## 25. Pt quantification assay

The method was adapted from Basotra *et al.*<sup>293</sup> Briefly, for the calibration, cisplatin was serially diluted in DMF followed by the addition of 1x PBS (7.7% (v/v)) and o-phenylenediamine (OPD) (71.1 mM) in a total volume of 650  $\mu$ L. The Pt(IV)-loaded IONPs and the IONP-COOH samples were prepared under the same conditions as the cisplatin standards in 1x PBS (7.7% (v/v)) and OPD (71.1 mM) in 650  $\mu$ L DMF. The vials containing the solutions were sealed with Teflon and incubated at 80°C overnight at 1000 rpm in a Thermoshaker. The next morning a blank solution was elaborated under the same conditions in DMF (71.1 mM OPD, 7.7% 1x PBS (v/v)). UV-vis spectroscopy was performed in a 10 mm quartz cuvette and measurements were recorded in the absence of light at 706 nm with 2-point baseline correction at 600 nm and 800 nm.

## 26. Synthesis of IONP-DOTAP

DSPE-PEG(2000)-MeO (2 mg), 18:1 1,2-dioleoyl-3-trimethylammonium-propane (DOTAP) (1 mg) and hydrophobic Fe<sub>3</sub>O<sub>4</sub> nanoparticles (1 mg) were dissolved in chloroform (500  $\mu$ L). The solvent was allowed to evaporate overnight in a 5 mL vial at RT. Any remaining solvent was removed under vacuum for 1 h. The flask was placed in a water bath at 80°C for 30 s, after which 1 mL of MilliQ water was added. The solution was transferred to a centrifugation tube and centrifuged at 9700 g for 5 min. The pellet was discarded, and the supernatant was passed through a 0.45  $\mu$ m syringe filter. This solution was ultracentrifuged (369 000 g, 45 min, 3 cycles) to remove empty micelles. Finally, the pellet was dissolved in MilliQ water. The IONP-filled micelles were stored at 4°C.

## 27. Synthesis of IONP-DOTAP-pIC-R837

To IONP-DOTAP ([Fe] = 1.8 mM) was added pIC (78  $\mu$ g/mL) in 250  $\mu$ L of 10% PBS and the solution was incubated at RT overnight at 1000 rpm in a Thermoshaker. The following day the samples were made up to 1 mL with MilliQ water and large aggregates were removed by centrifugation (9.9k g, 1 min) followed by ultracentrifugation (369 000 g, 1 h) to remove any pIC that was not attached to the IONPs. The supernatant was analysed for the presence of pIC at  $\lambda$  = 260 nm. To the IONP-DOTAP-pIC solution was added R837 at a concentration ratio of [Fe] = 1.5 mM: [R837] = 9  $\mu$ g/mL and incubated at RT overnight at 800 rpm. The resulting immunomodulatory NPs were stored at 4°C.

## **28. IONP-DOTAP-pIC-R837 implant Transwell co-culture assay**

The IONP-DOTAP-pIC-R837 implant was prepared following the implant preparation procedure outlined in experiment 8 and containing 0.12 nmol IONP. The implant was allowed to gradually dissolve for 48 h in 700  $\mu$ L complete RPMI-1640 media supplemented with 18.2 nmol HAase and the released NPs were added to a co-culture of murine B16-F10 melanoma cells and RAW264.7 macrophages using a Transwell plate at working concentrations of [Fe] = 0.5 mM, [pIC] = 16  $\mu$ g/mL, [R837] = 3  $\mu$ g/mL and [HA] = 48 mg/mL. The Transwell setup contained cells in the top compartment in 100  $\mu$ L of culture media and the degraded implant solution deposited into the bottom compartment in 600  $\mu$ L of media and incubated for 24 h at 37°C and 5% CO<sub>2</sub>. As the negative control, a blank implant was prepared and degraded under the same conditions. The positive control was a fresh solution of IONP-DOTAP-pIC-R837, which was added to the cells at the same working concentrations. The cell viability of both cell lines was characterised by flow cytometry. The cell work was carried out by Marc Bilbao-Asensio.

# Chapter 3

**Development of a hyaluronic acid-based biomaterial functionalised with an IDO inhibitor for cancer immunomodulation**

## 3.1 Introduction

### 3.1.1 Hyaluronic acid (HA) for anti-cancer drug formulations

HA or hyaluronan is a naturally occurring biodegradable glycosaminoglycan polymer consisting of repeating units of D-glucuronic acid and N-acetyl-D-glucosamine. It is a highly versatile material with applications in tissue regeneration, cosmetics and known to have tumour targeting properties, due to its binding affinity to CD44, a transmembrane glycoprotein overexpressed in many malignant cells including in breast, ovarian, pancreatic and lung cancer.<sup>294</sup> Other cancer cell targeting receptors of HA include lymphatic vessel endocytotic receptor (LYVE-1) and receptor for HA-mediated motility (RHAMM) that enable tumour cell-specific internalisation and validates the use of HA as a compelling drug carrier.<sup>295</sup> The high hydrophilicity and non-immunogenicity of HA has the potential to improve the solubility and circulation time of HA modified immunomodulatory agents and anti-cancer drugs.<sup>296</sup> Furthermore, HA presents carboxyl, N-acetyl, and hydroxyl groups as sites for potential chemical modification with anti-cancer agents that can be designed to achieve targeted release at the tumour site through cleavable bonds.<sup>297,298</sup>

### 3.1.2 HA modification methods

HA modification with an anti-cancer agent is possible via covalent or non-covalent strategies. Covalent bonding through pH, redox or enzyme cleavable linkers offers the advantage of stimuli-responsive drug delivery and enhanced stability over non-covalent functionalisation.<sup>299</sup> Non-covalent binding can be achieved through electrostatic interactions and can avoid the use of potentially cytotoxic reagents as well as multiple synthesis steps and purifications.<sup>300</sup> In this chapter a covalent strategy was selected to functionalise HA with 1MT through an acid-labile and hydrolytically cleavable amide bond.

One approach for covalent HA modification is through the carbodiimide-mediated amide coupling of a primary amine to the carboxylic acid group of HA.<sup>301</sup> Typical carbodiimide coupling reagents are N-(3-dimethylaminopropyl)-N'-ethylcarbonate (EDC), N,N'-dicyclohexylcarbodiimide (DCC) and N,N'-diisopropylcarbodiimide (DIC), but the latter two being water-insoluble are unsuitable for HA coupling.<sup>302</sup> EDC forms an O-acylisourea intermediate with the HA, which is susceptible to nucleophilic attack by an amine-containing drug or biomolecule. However, the intermediate can be readily hydrolysed in the presence of water, thus, reforming the carboxylic acid or producing a stable N-acylurea through an intramolecular acyl transfer.<sup>303</sup> To minimise the formation of hydrolysis products, EDC is

often used in combination with other reagents such as sulfo-N-hydroxysulfosuccinimide (sulfo-NHS), 1-hydroxybenzotriazole (HOBT) or 1-hydroxy-7-azabenzotriazole (HOAt), which produce a more stable intermediate to enable improved coupling yields.<sup>304</sup> All the intermediates require the primary amine of the therapeutic drug or biomolecule to be in its unprotonated form. The sulfo-NHS intermediate is reactive at neutral to slightly alkaline pH, while the HOBT and HOAt intermediate products require lower pH for efficient amide coupling.<sup>298,305</sup> EDC-NHS amide coupling through the carboxylic acid group of HA is, therefore, a common pathway for HA functionalisation with amine containing drugs targeted towards applications in cancer therapy.<sup>306–308</sup> The coupling reagent carbonyldiimidazole (CDI) is frequently used for esterification and amide coupling reactions as it provides a one-pot reaction procedure and low cost.<sup>309,310</sup> For example, HA functionalisation using CDI has been adopted for the development of anti-cancer biomaterials and thermoresponsive polymers.<sup>311,312,254</sup> HA can also be coupled through the hydroxyl and N-acetyl groups, but the latter requires deacetylation to obtain a more reactive primary amine group and proceeds with relatively low yields and formation of undesired by-products.<sup>313–315</sup>

The different strategies discussed for HA modification are illustrated in **Figure 3.1**. The most suitable site for HA functionalisation depends on the intended conjugation chemistry and drug delivery approach, but the popularity of this versatile biodegradable polymer as drug delivery vehicle, scaffold and CD44 tumour targeting agent makes it an excellent candidate for the development of immunotherapeutic biomaterials, which were explored in this thesis.

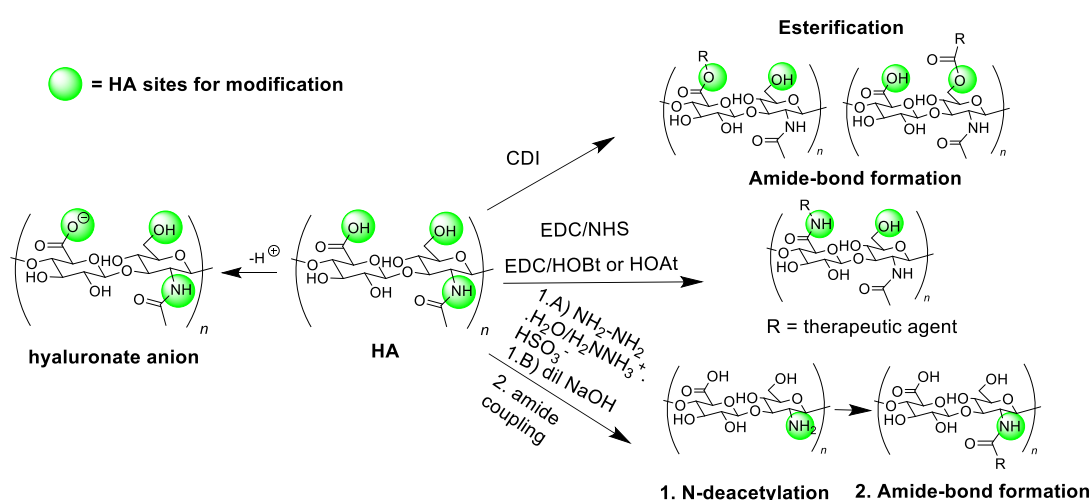


**Figure 3.1** Schematic representation of different HA covalent and non-covalent functionalisation strategies for cancer therapeutic applications. Typical HA covalent modification methods include esterification and amide bond formation through different sites on the HA monomer unit (green) using various coupling reagents.

### 3.1.3 HA functionalisation with anti-cancer agents

Due to its biocompatibility, hydrophilicity and tumour targeting properties, HA-based anti-cancer biomaterials have been mostly investigated as micelle systems or as a NP coating aiming to enhance drug circulation times, drug solubility, tumour targeting and release kinetics.<sup>316</sup> Han *et al.* developed a HA-polycaprolactone block copolymer that was cross-linked via reducible disulfide bonds.<sup>317</sup> The copolymer was first synthesised by reductive amination of the HA to obtain a terminal alkyne that was then conjugated via click-chemistry to the polycaprolactone molecule. The disulfide linker was functionalised onto the HA by amide coupling through the carboxyl group of HA. The amphiphilic nature of the polymer allowed for self-assembly into micelles with the incorporation of doxorubicin into the micelle core and demonstrated tumour targeted intracellular release in the presence of glutathione *in vitro* and favourable tumour size reduction *in vivo* in a murine squamous cell carcinoma model.

Electrostatic functionalisation of HA was exploited in a study by Thomas *et al.* in which an indocyanine derivative was synthesised for mitochondria-targeted photodynamic therapy.<sup>318</sup> The indocyanine-based dye was modified to produce a cationic derivative that spontaneously formed a micellar aggregate with HA, which showed preferential accumulation in the mitochondria of HeLa cells and with high therapeutic efficiency in a murine skin cancer model. HA has also been used as a coating layer of the positively charged polyethyleneimine (PEI) functionalised stearic acid nanoparticles whilst encapsulating the cotton seed-derived drug, gossypol, known for its inhibition properties of the tumour-overexpressed oncoprotein MDM2 and VEGF, through hydrogen bonding to the PEI-stearic acid nanovector. This double-layer HA coated nanoparticle system achieved higher tumour suppression *in vivo* compared to free drug and the empty nanoparticle control, proving its utility for tumour-targeted therapy.<sup>319</sup> Soleymany *et al.* used the anionic properties of a high molecular weight HA for the preparation of hydrophilic Fe<sub>3</sub>O<sub>4</sub> inorganic nanoparticles for magnetic hyperthermia therapy and enhanced tumour-targeting in CD44 expressing cancers.<sup>320</sup>

Combination therapies exploiting the HA platform have shown to be very promising for more effective treatment of a various cancer types, by both activating the immune system towards tumour cells and tumour targeting through improved delivery of anti-cancer agents. For example, in a recent study, pH-responsive HA nanoparticles loaded with DOX and the immunostimulatory adjuvant, resiquimod (R848), were developed for the treatment of breast cancer.<sup>321</sup> R848 was encapsulated in poly(L-histidine) to form multifunctional

nanoparticles that when exposed to the reduced pH of the tumour microenvironment (TME) release the adjuvant, while the DOX molecules were conjugated to HA through acid labile hydrazone bond linkages and then coated over the surface of the R848 nanocores. In that scenario, the HA acted as a targeting agent towards the CD44-overexpressing breast cancer cells and releasing the immunostimulant and chemotherapeutic vaccine in the TME and within the endosome/lysosome in a pH dependent manner. Several other combination cancer therapies using HA as a tumour targeting agent in pre-clinical and clinical studies have shown high biocompatibility, improved circulation times and improved tumour accumulation compared to the free drugs.<sup>322–325</sup>

### 3.1.4 HA hydrolysis and enzymatic degradation

HA undergoes hydrolysis in aqueous solutions at varying rates depending on the pH, temperature, and viscosity, but can also be degraded enzymatically by hyaluronidase (HAase). HAase is a naturally occurring enzyme consisting of an  $\alpha$ -domain with 361 N-terminal amino acid residues and a 347 C-terminal residue containing  $\beta$ -domain connected by a polypeptide linker with 11 residues.<sup>326</sup> HAase is overexpressed in some cancer cells and is responsible for the degradation of HA at the  $\beta$ -1,4-glycosidic bonds into small oligosaccharide fragments, which are then further degraded intracellularly by the enzymes  $\beta$ -D-glucuronidase and  $\beta$ -M-acetyl-hexosaminidase.<sup>327,328</sup> The X-ray crystal structure of the HAase-HA enzyme-substrate complex revealed that cleavage at the  $\beta$ -1,4 linkages may occur due to the 2-fold helical conformation of the HA polymer in solution leaving the  $\beta$ -1,4 linkage sites exposed, and the greater flexibility of these bonds compared to the  $\beta$ -1,3 linkages. The catalytic active site contains several positively charged and hydrophobic amino acid residues that bind the negatively charged HA through electrostatic and hydrophobic interactions at the active site (**Figure 3.2 A, B**).<sup>329</sup> In the human hyaluronidase, Hyal1, the catalysis involves the amino acid residues Glutamate 131 (Glu131) and aspartate 129 (Asp129) (**Figure 3.2 C**).<sup>327</sup>



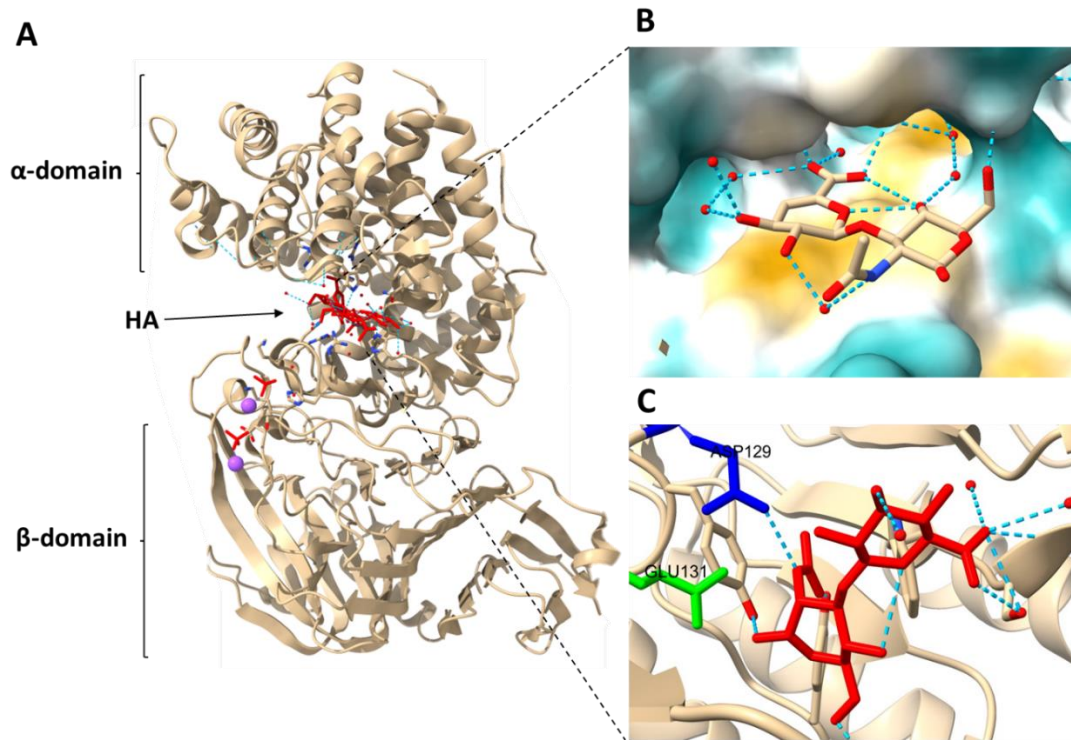


**Figure 3.2 Crystal structure of Hyal1 complexed to HA disaccharide unit at the substrate binding cleft.** (A) Full crystal structure of HAase complexed to HA (red). (B) Surface hydrophobicity representation of the enzyme-substrate binding site showing the hydrogen bonding to the amino acid residues of the enzyme (dotted blue lines). The hydrophobicity colour scheme ranges from blue (hydrophilic) to orange/red (hydrophobic). (C) Close up view of HA (red) interaction with Glu131 (green) and Asp129 (blue) amino acid residues involved in the degradation of HA.

A reaction mechanism was proposed by Zhang *et al.*, which is initiated by the intramolecular resonance form of the N-acetylglucosamine constituent of the HA forming a 5-membered ring stabilised by the negative charge of the Asp129 and the deprotonated Glu131.<sup>330</sup> The N-acetylglucosamine is restored by hydrolysis and protonation of Glu131 (**Figure 3.3**). The gradual enzymatic and hydrolytic degradation of HA can be exploited by functionalisation of anti-cancer agents with a HA biomaterial or incorporation into a NP system with localised release in the TME, which provides a suitable pH, enzyme concentration, and temperature conditions.<sup>331</sup>

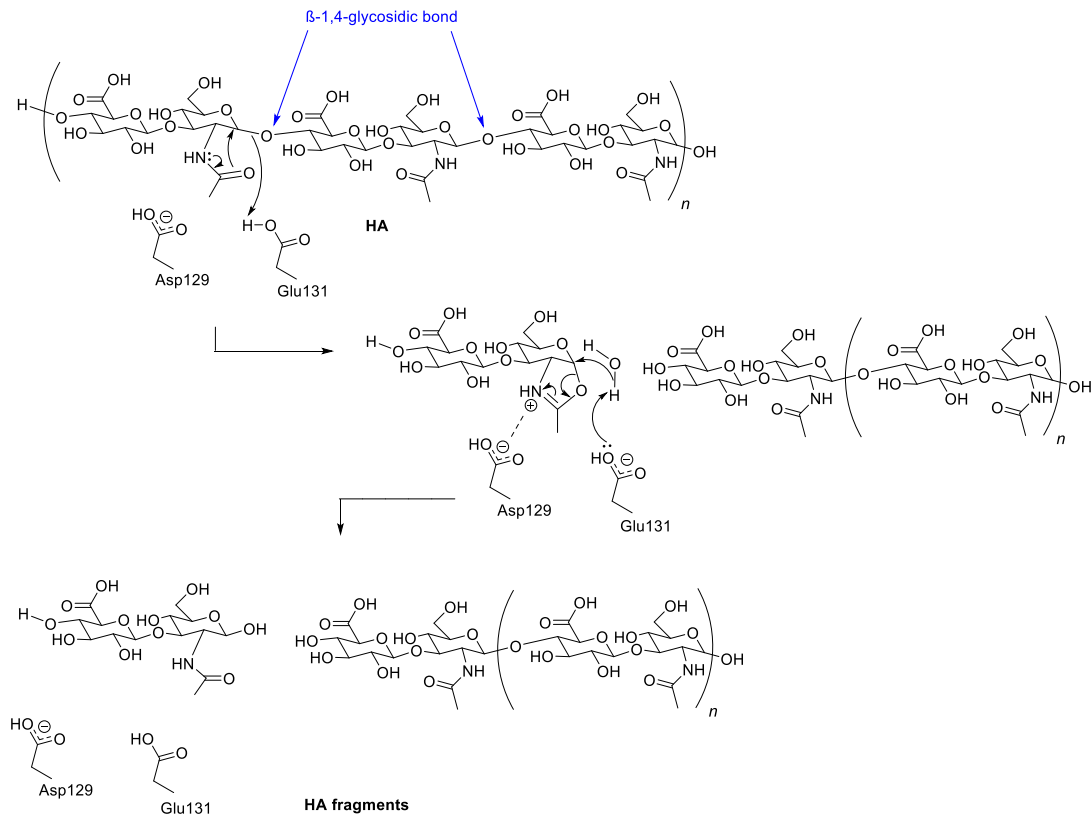


**Figure 3.3** The HA degradation mechanism as proposed by Zhang et al.<sup>330</sup> The HA degradation is catalysed the amino acid residues Asp129 and Glu131 of Hyal1, which initiate cleavage of the HA polymer at the  $\beta$ -1,4-glycosidic bonds resulting in smaller HA fragments.

HAase overexpressing tumours are also known to overexpress HA synthase, which aims to produce HA to then break it down into small tumorigenic fragments.<sup>332</sup> The small HA fragments generated (< 500 kDa) can interact with tumour cells receptors such as CD44, which initiates tumour angiogenic signalling, pro-inflammatory signalling, and metastasis. Specifically, they induce the release of proinflammatory cytokines and enzymes including TNF $\alpha$ , IL-1b, IL-1, IL-8 and MMPs.<sup>333</sup> On the other hand, high MW HA of (> 500 kDa) is known to have anti-inflammatory and anti-proliferative properties, whilst also being responsible for maintaining tissue homeostasis in in the extracellular matrix.<sup>334</sup> However, several inhibitors of HAase including vitamin C palmitate, polystyrene sulfonates and sulfonated HA have demonstrated promising preclinical results and could potentially be co-administered with HA-based therapies to prevent HA fragmentation, whilst maximising the benefits of using HA as a biodegradable anti-cancer delivery vehicle.<sup>335,336</sup>

### 3.1.5 Clinical investigation of small molecule inhibitors of the tryptophan catabolism pathway

Indoleamine-2,3-dioxygenase (IDO) is an enzyme overexpressed on cancer cells and dendritic cells that exerts immunoinhibitory functions known to contribute to tumour progression.<sup>337</sup> The enzyme is stimulated by the inflammatory cytokine, IFN- $\gamma$ , and regulates the degradation of tryptophan resulting in the production of N'-formylkynurenine, which is hydrolysed by the enzyme, N'-formylkynurenine formamidase, to form kynurenine (Kyn). This molecule is responsible for promoting the signalling of regulatory T cells and downregulation of effector T cells such as CD8<sup>+</sup> and CD4<sup>+</sup> T cells.<sup>338</sup> 1-Methyl-DL-tryptophan (1MT) is an IDO inhibitor that has provided promising preclinical results in combination with different chemotherapeutic agents. Muller *et al.* observed synergistic therapeutic effect of 1MT in combination with paclitaxel in a mice breast cancer model.<sup>339</sup> The inhibition constant ( $K_i$ ) of 1MT as competitive inhibitor of rabbit intestinal IDO was  $6.6 \pm 0.6 \mu\text{M}$ .<sup>340</sup>

The dextro-isomer of 1MT, also known as indoximod, is under ongoing investigation in clinical trials in combination with several chemotherapeutic agents, including docetaxel, temozolomide, gemcitabine and immunotherapeutic vaccines comprising sipuleucel-T and ipilimumab against various cancer types (**Figure 3.4**).<sup>341</sup> Navoximod, epacadostat and linrodostat are other examples of IDO1 inhibitors currently undergoing phase I-III clinical trials as single agents and combination therapies.<sup>342</sup> These inhibitors have shown to enter the hydrophobic pockets of the enzyme and interact through different mechanisms such as  $\pi$ - $\pi$  stacking, hydrophobic interactions, hydrogen bonding and coordination bonding to the Fe-bearing heme group.<sup>343-345</sup> Whilst IDO1 is a structurally and functionally well-established tryptophan catabolism enzyme and the most investigated as an inhibitor target, IDO2 and tryptophan-2,3-dioxygenase have also been found to play an important role in supporting the IDO1-mediated immunosuppression in cancers and have been explored as potential targets for small molecule inhibitors.<sup>346</sup> The promising clinical studies of IDO1 inhibitors in combination with other anti-cancer agents as well as further investigation into IDO2 and tryptophan-2,3-dioxygenase-specific inhibitors paves the way both for biomaterial-inhibitor constructs and the development of more effective small molecule inhibitor molecules to improve clinical benefits in combination therapies.

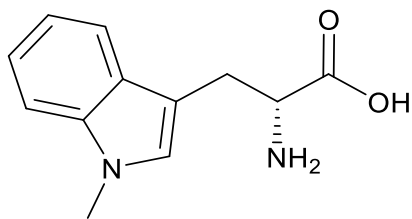


**Figure 3.4** Chemical structure of the IDO1 inhibitor indoximod (D-1MT) currently under clinical investigation for the treatment of different cancers.

### 3.1.6 Aims and objectives

- The covalent modification of the biodegradable polymer, HA, with the clinically investigated IDO inhibitor, 1MT, via an amide-bond coupling strategy in order to achieve a sustained drug release;
- Optimising the purification of the synthesised 1MT-HA biomaterial by exploring size-exclusion and ion-exchange-based purification methods and assessment by NMR;
- Investigating the release behaviour of 1MT from 1MT-HA at different pH conditions in the presence and absence of HAase to understand the release mechanism and the effect of HA fragmentation on the release.

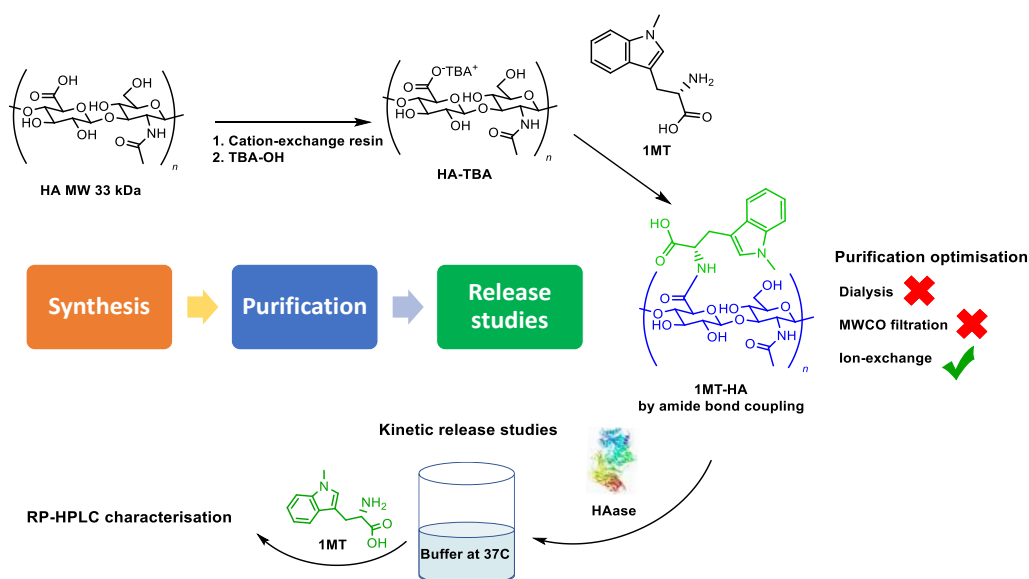


**Figure 3.5** Schematic overview of thesis Chapter 3. Illustrated is the 1MT-HA biomaterial synthesis via amide-bond coupling, subsequent purification method development and kinetic release studies in the presence and absence of HAase characterised by RP-HPLC.

## 3.2 Results

### 3.2.1 Synthesis and characterisation of the 1MT functionalised HA biomaterial

The 1MT-HA biomaterial was synthesised by amide bond coupling through the carboxylic acid group of HA and the amine group of 1MT using CDI as the coupling reagent and DMAP as the base. DMSO was chosen a suitable aprotic solvent in which all the reagents and reactants dissolved. To enhance the solubility of HA in DMSO, the HA sodium salt was first subjected to an ion-exchange procedure using a sulfonic acid-based resin to form the carboxylic acid of HA followed by treatment with tetrabutyl ammonium (TBA) hydroxide to obtain the HA-TBA salt (**Appendix 1**). The initial reaction step involved the activation of the carboxylate group of HA with CDI followed by the addition of 1MT under alkaline conditions (**Figure 3.6**). The crude product was purified by dialysis in a 1:1 mixture of MeOH and MilliQ followed by MilliQ water to remove DMAP, imidazole side product, and any unreacted 1MT. Due to the incomplete purification after dialysis, an additional cation-exchange purification step was required to ensure the complete removal of any remaining non-covalently bound impurities, which is discussed in more detail in the following section. The pure 1MT-HA material was lyophilized for 72 h, and the resulting white solid was characterised by NMR.

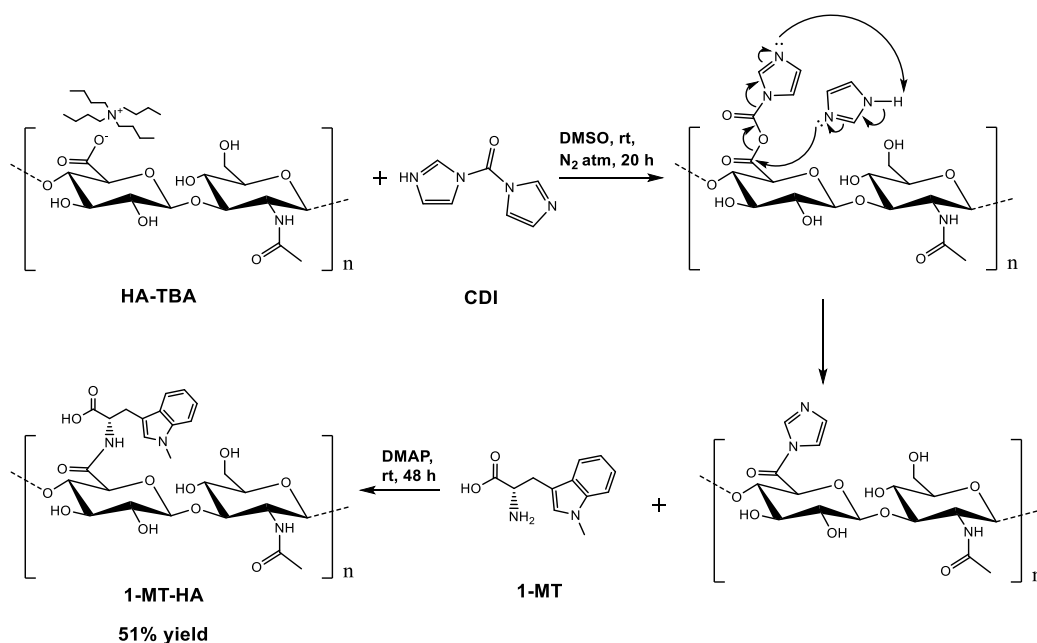


**Figure 3.6 Reaction scheme for the synthesis of the 1MT-HA biomaterial.** The carboxylate group of the HA-TBA polymer is first activated using CDI. 1MT and a base are added, and the solution mixed for 48 h until the amide bond coupling reaction was completed to obtain the 1MT-HA biomaterial.

The  $^1\text{H}$  NMR spectrum of 1MT-HA in  $\text{D}_2\text{O}$  shows the HA acetamido protons at 2.02 ppm and the disaccharide ring protons between 3.34-3.84 ppm (**Figure 3.7 A**). The aromatic 1MT protons do not interfere with the HA proton signals making them the suitable candidates for quantification. The degree of 1MT modification was evaluated based on the integration of the 1MT aromatic protons at 7.12-7.71 ppm in relation to the HA acetamido protons at 2.02 ppm, resulting in a 6% 1MT modification yield. There were no reaction impurities due to DMAP and TBA observed in the spectrum after the ion-exchange purification, demonstrating that this step was critical to obtain a pure product that is suitable for the subsequent functional activity assays.

The  $^{13}\text{C}$  NMR of 1MT-HA was performed in  $\text{D}_2\text{O}$  with 5%  $\text{DMSO-d}_6$  using its peak at 39.52 ppm as reference (**Figure 3.7 B**). One of the acetamide carbons ( $-\text{NCO}\underline{\text{C}}\text{H}_3$ ) is the most upfield peak at 24.12 ppm whilst the other carbon ( $-\text{N}\underline{\text{C}}\text{OCH}_3$ ) is downfield at 175.69 ppm as it is deshielded by both the adjacent oxygen and nitrogen atoms. The HA carboxylic acid carbon ( $-\text{COOH}$ ) is the most downfield peak at 176.49 ppm. The peak at 55.89 ppm corresponds to the carbon adjacent to the acetamide group and the HA ethoxy group carbon that links onto the 1MT is observed at 62.13 ppm. The peaks from 70.03 to 84.14 ppm are characteristic of the HA ring protons. The 1MT aromatic peaks observed from 110.92 to 138.25 ppm are further evidence of successful conjugation.

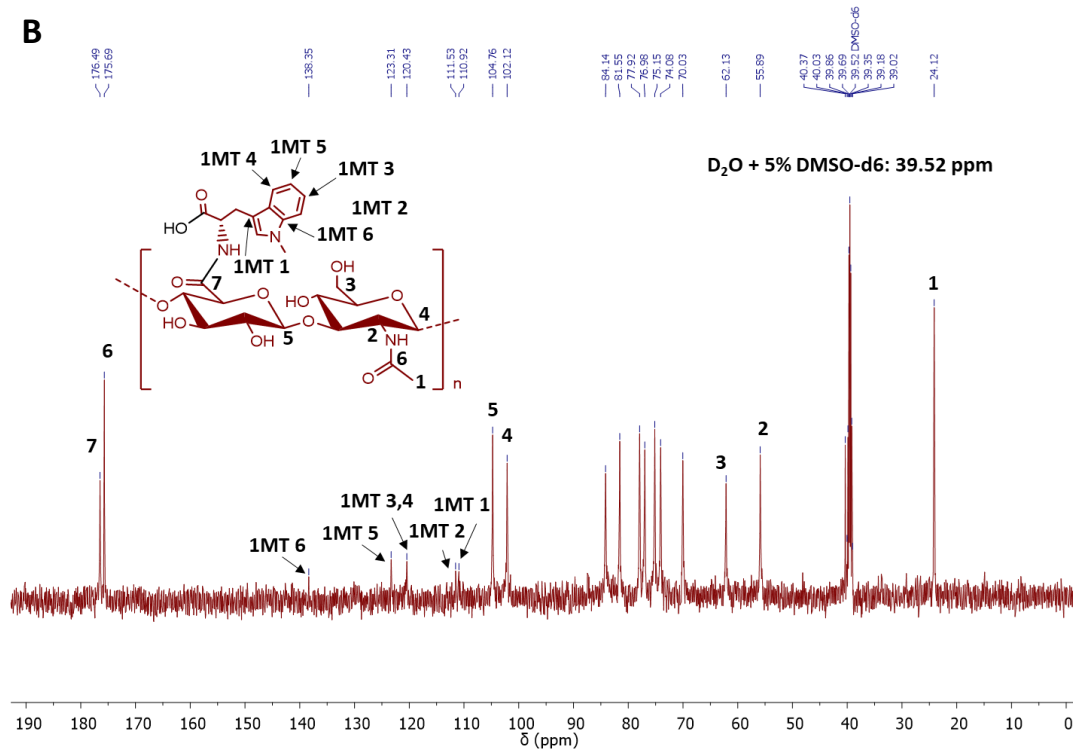
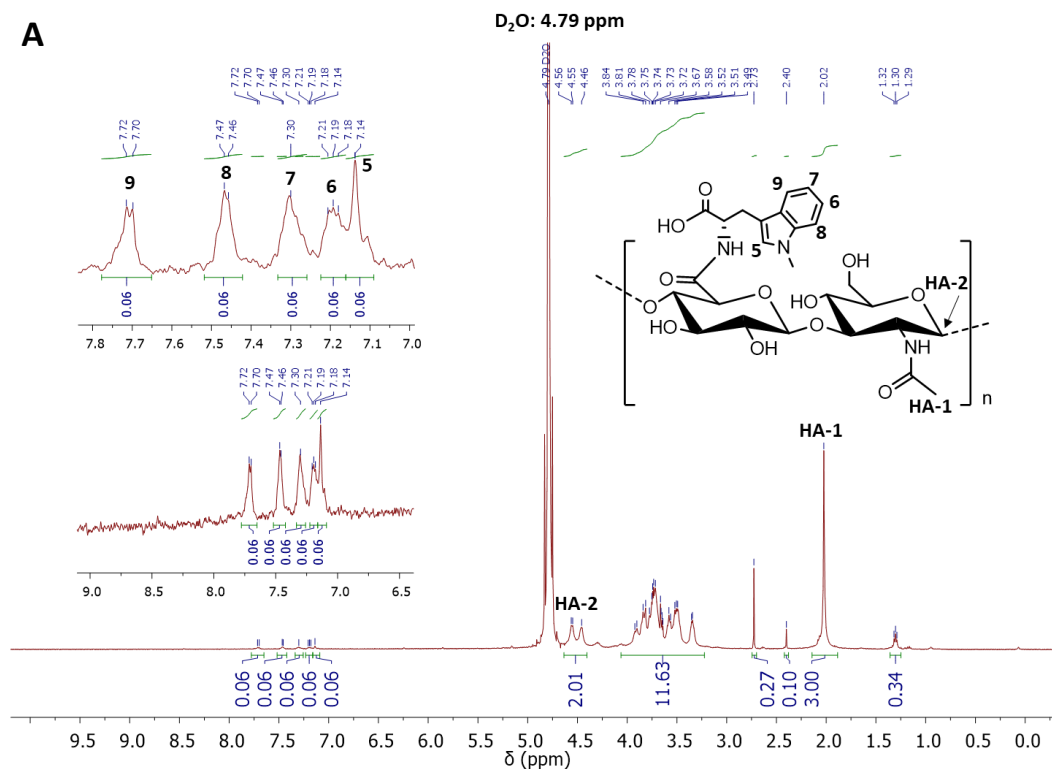


**Figure 3.7 NMR characterisation of 1MT-HA biomaterial.** (A)  $^1H$  NMR of 1MT-HA in  $D_2O$  and (B)  $^{13}C$  NMR of 1MT-HA in  $D_2O$  containing 5%  $DMSO-d_6$  with proton and carbon labelling, respectively.

The  $^1H$  NMR spectra of the 1MT, HA and 1MT-HA products shown in **Figure 3.8 A**, in a way that allows direct comparison of the aromatic peaks of the 1MT with those of the covalently

functionalised 1MT-HA product. The 1MT aromatic protons appear at 7.12-7.73 ppm and no significant shift in the aromatic peaks was observed for the functionalised 1MT-HA. The  $^{13}\text{C}$  NMR spectra of the 1MT and HA stacked above the 1MT-HA display peaks between 110.92 to 138.25 ppm that can be assigned to the aromatic 1MT peaks as they do not interfere with the carbon peaks of HA (**Figure 3.8 B**).

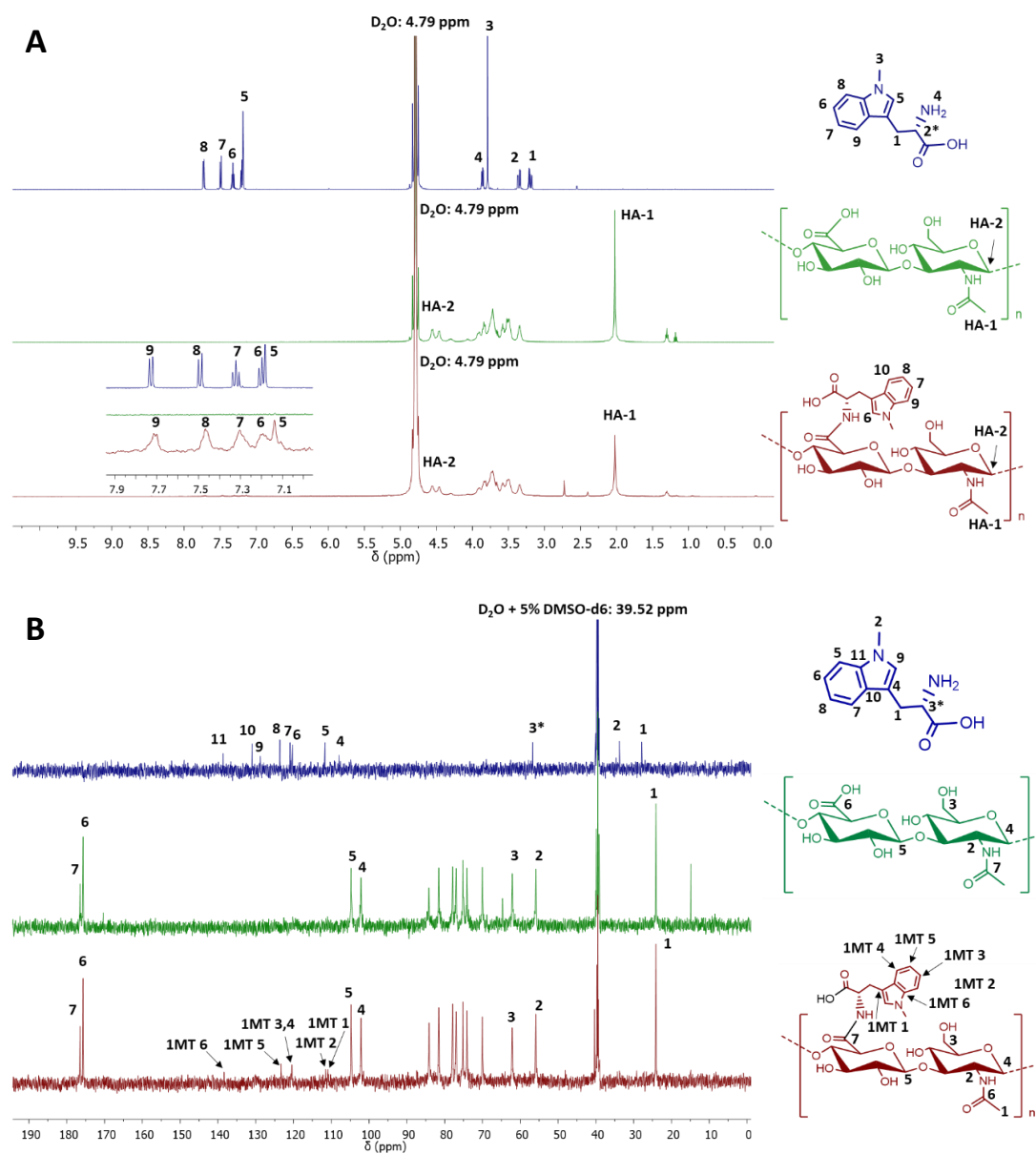


**Figure 3.8 Stacked (A)  $^1\text{H}$  NMR and (B)  $^{13}\text{C}$  NMR spectra of 1MT, HA and 1MT-HA (from top to bottom).**

### 3.2.2 Purification of the 1MT-HA biomaterial

Obtaining a pure 1MT-HA biomaterial required several purification steps due to the initially persistent impurities detected by NMR, potentially due to electrostatic interactions. The development of this efficient method of purification could be broadly applicable for other



biomaterial conjugations to an anticancer agent. The 1MT-HA biomaterial was first purified by dialysis over 72h and showed a 1MT modification yield of 8% by  $^1\text{H}$  NMR in  $\text{D}_2\text{O}$ , but significant impurities including imidazole (at 7.5 and 8.7 ppm) as the by-product of the CDI, DMAP (at 6.9 and 8.0 ppm) and TBA (at 1.0, 1.4, 1.7 and 3.2 ppm) were observed (**Figure 3.9**).

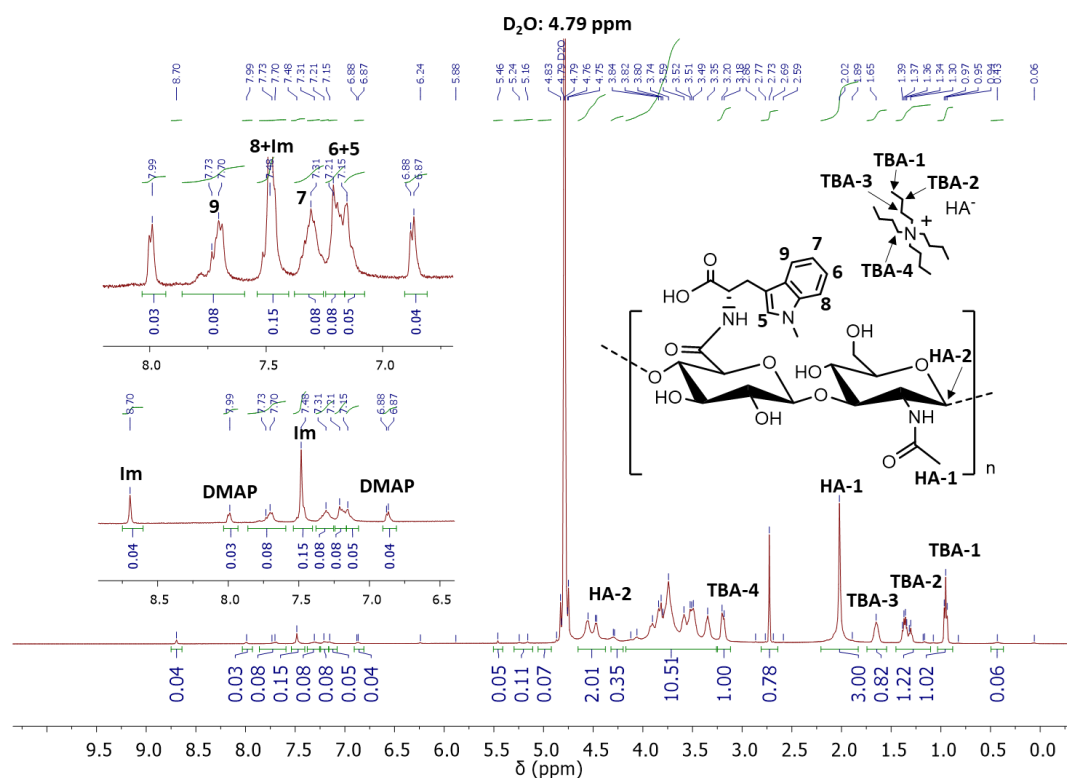


**Figure 3.9**  $^1\text{H}$  NMR of 1MT-HA after purification by dialysis in  $\text{D}_2\text{O}$  with proton labelling. Im-imidazole.

An additional purification step was carried out, which involved centrifugal filtration using size exclusion-based spin filters to not only remove reaction impurities, but also any non-covalently bound 1MT from the product. After centrifugation and washing cycles with MilliQ water, the modification yield remained unchanged by NMR suggesting that all the non-covalently bound 1MT had been removed in the first purification step, but the other impurities remained present (**Figure 3.10**).

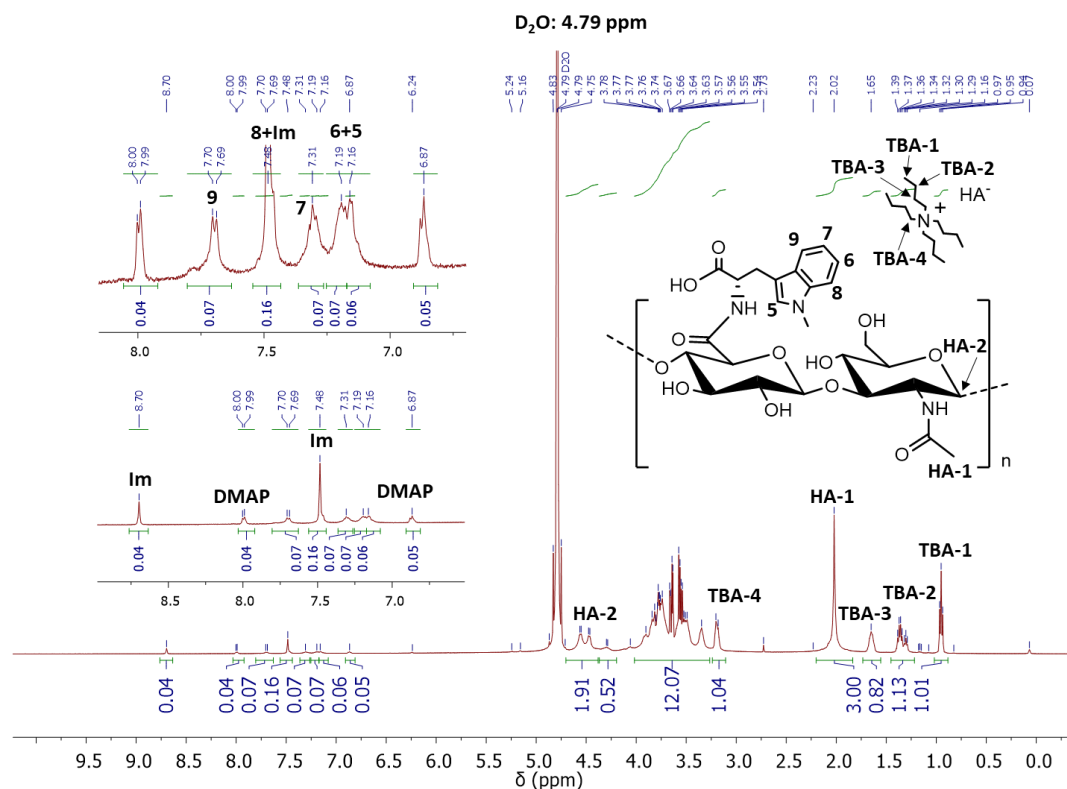


**Figure 3.10**  $^1\text{H}$  NMR of 1MT-HA after purification by centrifugal filtration in  $\text{D}_2\text{O}$  with proton labelling. Im-imidazole.

Since all these purification methods were not successful in removing all traces of impurities from the 1MT-HA, an alternative ion-exchange method using the sulfonic acid-based Dowex 50wx8 resin was investigated (**Figure 3.11**). The 1MT-HA samples were dissolved in MilliQ water and the resin was added under constant stirring until pH 3. The resin was allowed to interact with the polymer for 30 min followed by removal of the resin by vacuum filtration. The filtrates were pH neutralised by addition of dilute NaOH and then lyophilized for 72 h. Indeed, after using this purification procedure, the  $^1\text{H}$  NMR spectra of the 1MT-HA biomaterial following ion exchange purification showed no trace of DMAP, imidazole or TBA, establishing that this method of purification is the most effective (**Figure 3.7 A**). However, it is important to note that the persistent retention of other molecules through electrostatic interactions observed after the initial purification steps presents also an opportunity for the functionalisation of these biomaterials with other anti-cancer agents via non-covalent pathways for combination therapy applications.

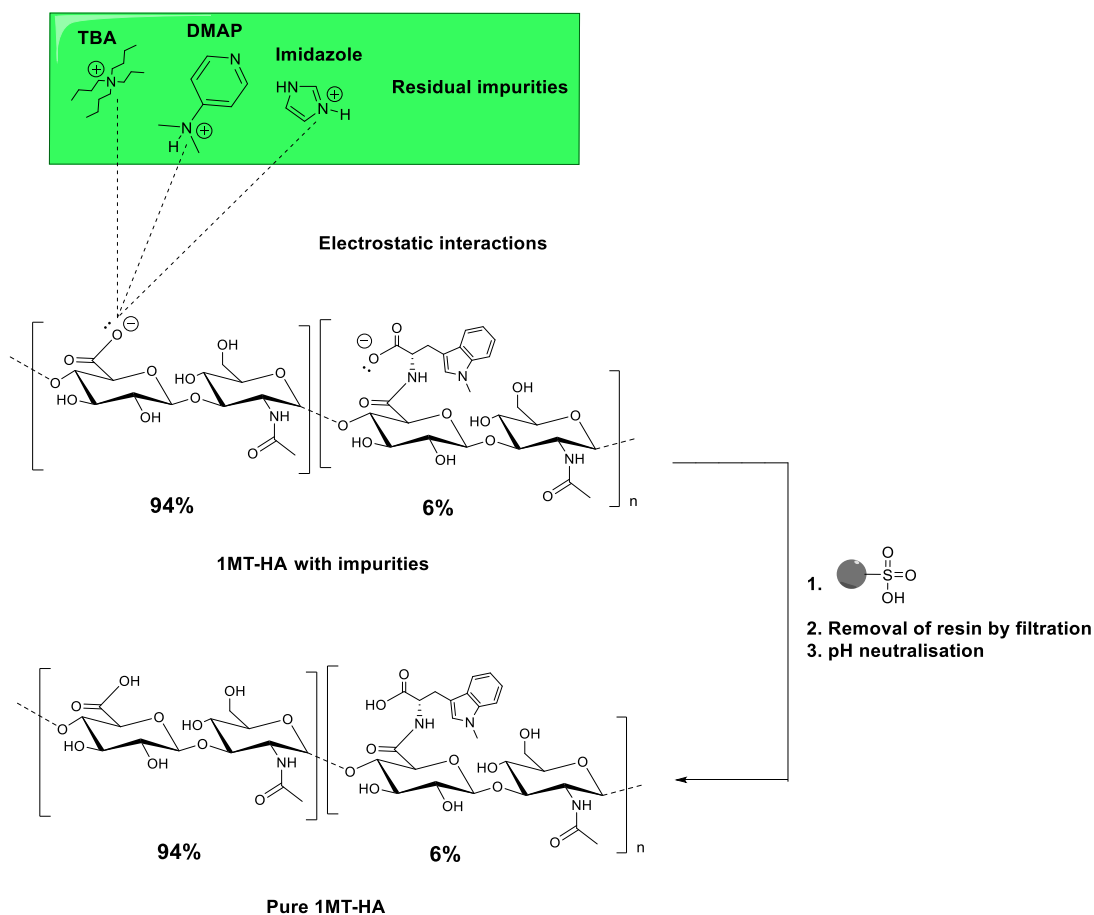


**Figure 3.11** Reaction scheme for ion-exchange purification of 1MT-HA using a sulfonic acid-based resin. Impurities in the 1MT-HA product including TBA, DMAP and imidazole were removed using a sulfonic acid-based ion-exchange resin. The resin was removed from the product by filtration and pH neutralised to obtain pure 1MT-HA.

### 3.2.3 Release of 1MT from 1MT-HA at different pH conditions

To evaluate the release kinetics of 1MT from 1MT-HA at the different physiological pH conditions the polymers were dissolved in PBS buffers at pH 5, pH 6.5 and pH 8 at 37°C. Additionally, hydrolysis at pH 6.5 was evaluated in the presence of 18.2 nmol of the HAase enzyme (pH 6.5 HAase). The hydrolysis at pH 5 gives an indication of the kinetic release of 1MT in the lysosomal compartment of cells, whilst pH 8 was chosen as an alkaline reference point at which hydrolysis is more favourable. The solutions were stirred gently using an orbital shaker and aliquots were collected at timepoints 0, 1, 6, 24 and 48 h. The samples were purified using 3 kDa MWCO spin filters and the filtrate containing the released 1MT was analysed by RP-HPLC using a C-18 column at 223 nm absorption wavelength with an isocratic elution method and a phosphate buffer-based mobile phase. For this, a calibration curve of 1MT ranging from 0-100  $\mu$ M 1MT was first obtained, using the same conditions and the concentration of 1MT was plotted in relation to the peak area (**Figure 3.12**).

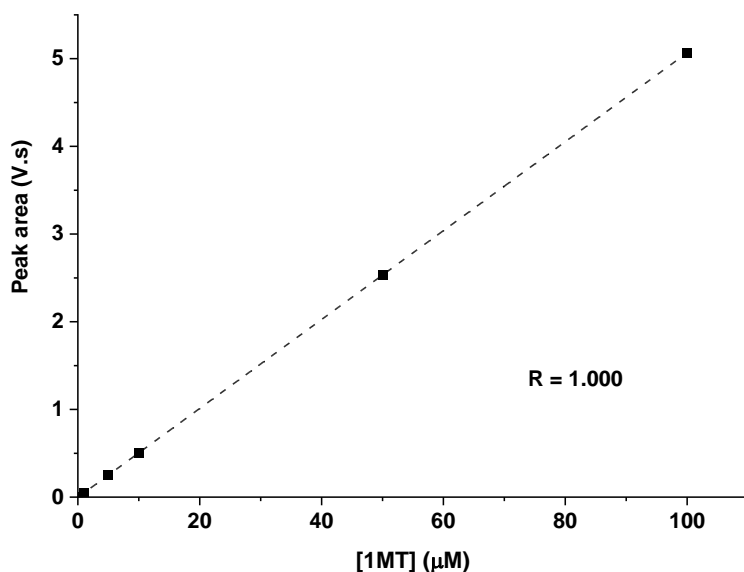


**Figure 3.12 1MT calibration curve by RP-HPLC and UV detection at 223 nm with a concentration range of 0-100 µM (N = 1).**

The release kinetics of 1MT from 1MT-HA at the different pH conditions is represented as concentration of 1MT released over time and the standard deviation is based on 3 experimental repeats (**Figure 3.13**). A gradual increase in the release of 1MT is observed for all conditions over 48 h that reach a plateau towards the end of the experiment. Both the rate and the overall 1MT release after 48 h is highest at pH 8, whilst no significant difference is observed for the other pH conditions. The presence of the HAase enzyme for the pH 6.5 condition did not show an increase in the 1MT release rate, which indicates that 1MT liberation is independent of the glycosidic bond cleavage mediated by the enzyme, but instead is the result of hydrolytic cleavage of the amide bond in 1MT-HA. However, as expected there was a visible reduction in viscosity for the HAase containing sample indicating an enhanced HA degradation. Thus, although HAase promotes the cleavage of the 1MT-HA biomaterial the fragments formed were most likely not small enough to be recovered after centrifugal filtration of the samples collected at different timepoints.

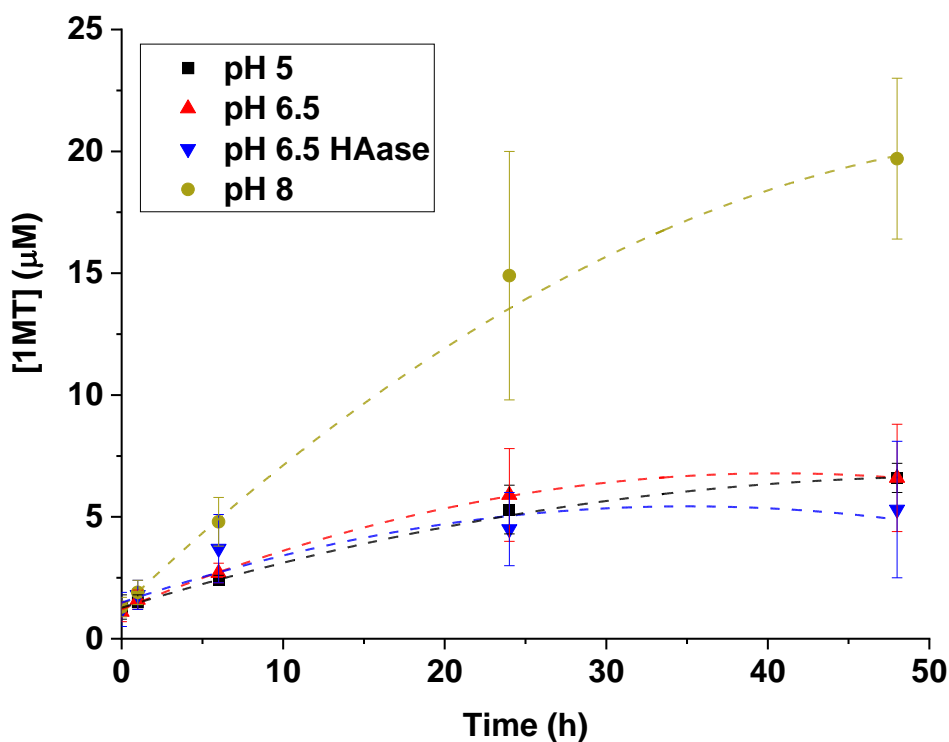


**Figure 3.13 Release of 1MT from 1MT-HA over 48 h at 37°C at pH 5, 6.5 and 8.** The pH 6.5 conditions was also evaluated in the presence of 18.2 nmol HAase (pH 6.5 HAase). 1MT was quantified by RP-HPLC at 223 nm using the calibration curve shown in Figure 3.12. The S.D. is based on 3 experimental repeats ( $N = 3$ ).

The full chromatograms of one of the 1MT-HA release experiments at the 48 h timepoint shows pure 1MT being released at retention time (RT) of 8.2 min, but also some HA fragments below 3 kDa observed at RT of 1-2 min can be observed (**Figure 3.14 A**). As shown in the previous figure the 1MT release after 48 h is highest for the pH 8 condition with almost no difference in the total 1MT release for the different conditions (**Figure 3.14 B**). However, analysis of the chromatogram region from RT 2-5.5 min revealed the increased presence of 1MT-HA fragments in the 1MT-HA biomaterials treated at pH 6.5 in the presence of HAase. This confirms that the enzyme is accelerating the breakdown of 1MT-HA into smaller fragments, which are larger and more hydrophilic than the pure 1MT released (**Figure 3.14 C**). Moreover, the peak at 6.0 min also points to the presence of other forms of 1MT being released.

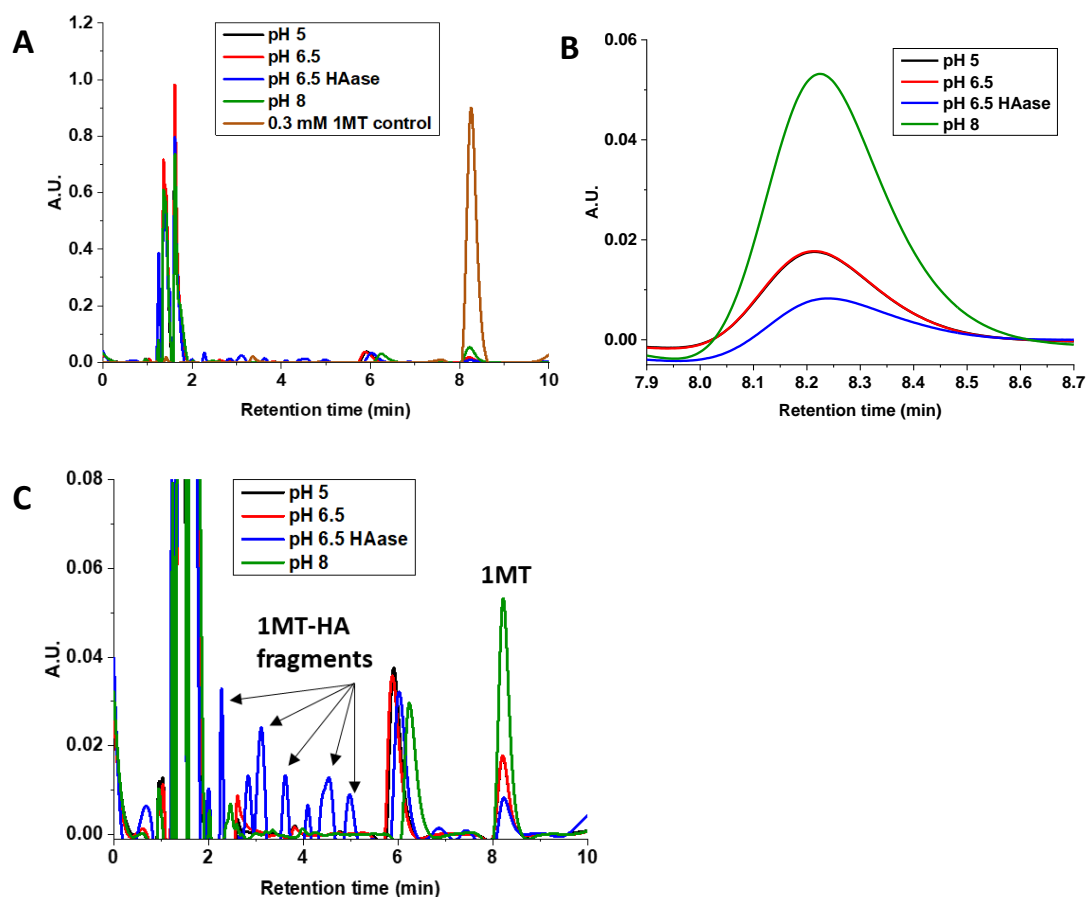


**Figure 3.14 RP-HPLC characterisation of 1MT-HA 48 h release study at different pH conditions.** (A) Full chromatograms from 0.0-1.2 A.U. of all pH conditions at timepoint  $t = 48$  h; (B) Chromatogram at RT 7.9-8.7 min and 0.00-0.06 A.U. showing pure 1MT release at the different conditions; (C) Full chromatogram from 0.00-0.08 A.U. illustrating 1MT-HA fragment release for the pH 6.5 HAase condition.

The total % 1MT released based on the 1MT modification yield determined by NMR is illustrated in the following table (**Table 3.1**). Overall these studies showed a slow and gradual release of 1MT and the effects of HAase in breaking down the 1MT-HA biomaterial, which is important for its biomedical application and also for understanding how the 1MT-HA maybe degraded and processed *in vitro* and *in vivo*.

**Table 3.1 Summary of the % 1MT released at the different pH conditions and timepoints based on the % 1MT modification yield by NMR. S.D. is based on 3 experimental repeats (N = 3).**

Sample	Time point/h	1MT released ( $\mu\text{M}$ )	% Released	S.D. (N = 3)
<b>pH 5</b>	0	1.3	0.10	0.07
	1	1.5	0.11	0.06
	6	2.4	0.16	0.06
	24	5.3	0.37	0.18
	48	6.6	0.46	0.19
<b>pH 6.5</b>	0	1.1	0.08	0.06
	1	1.6	0.12	0.07
	6	2.7	0.19	0.10
	24	5.9	0.44	0.30
	48	6.6	0.49	0.34
<b>pH 6.5 HAase</b>	0	1.2	0.09	0.09
	1	1.8	0.14	0.09
	6	3.7	0.28	0.20
	24	4.5	0.33	0.23
	48	5.3	0.41	0.36
<b>pH 8</b>	0	1.3	0.09	0.06
	1	1.9	0.14	0.09
	6	4.8	0.35	0.19
	24	14.9	1.10	0.77
	48	19.7	1.42	0.75

### 3.3 Discussion

In this chapter the biomaterial HA was covalently functionalised with the immunomodulatory agent 1MT via a hydrolysable amide bond linkage with the aim of promoting a gradual release of 1MT in the TME and afford a sustained inhibition of the immunosuppressive IDO enzyme overexpressed in various cancers.

The initial ion-exchange reaction to obtain the HA-TBA salt from sodium hyaluronate was performed to enhance the solubility of the biomaterial in DMSO required for the solubilisation of all the reagents involved in the amide coupling reaction using a procedure that has been previously reported in the literature.<sup>347,348</sup>

The coupling reaction via the carboxylic acid group of the HA using CDI as the coupling reagent was chosen due to being a one-pot, cost-efficient procedure that forms a hydrolytically cleavable bond between HA and 1MT (**Figure 3.6**).<sup>349</sup> The 1MT modification yield of 6% obtained from the <sup>1</sup>H-NMR of the 1MT-HA biomaterial was calculated using the ratio of integration of the 1MT aromatic protons in relation to the acetamide protons of HA and is comparable to literature values (**Figure 3.7**). For instance, Ye *et al.* observed a degree of 1MT modification to HA of 7% via an esterification route and using a comparable low molecular weight HA polymer.<sup>254</sup> In another study, a thermosensitive HA polymer was generated, in which HA was covalently bound to poly(N-isopropylacrylamide) and similarly obtained a modification yield of 7%.<sup>312</sup> Furthermore, other HA modifications proceeding through the hydroxyl group of HA have shown modification yields of less than 3%, which indicates that modification through the carboxylic acid group may be a more effective pathway.<sup>350,351</sup> The frequently low modification yield observed with HA may be due to steric hindrance effects of the large polymer with the approaching molecules resulting in a lower chance of interaction. It is known that HA has a double helical conformation in solution, which could make the carboxyl group less accessible to 1MT molecules.<sup>352</sup> Intra- and intermolecular H-bonding interactions between carboxylate and acetamido group within HA monomer units and adjacent HA molecules may also restrict access for modification at these sites.<sup>353</sup>

The HA carboxyl group has a pKa of approximately 3, which facilitates electrostatic interactions with cationic molecules at neutral pH.<sup>354</sup> Whilst this could pose an opportunity for electrostatic functionalisation of HA with therapeutic agents, it can also be a limitation by binding undesired molecules. In this chapter, the difficulties experienced in the purification



of the 1MT-HA biomaterial are likely due to electrostatic interactions between the HA carboxyl groups and cationic by-products and reagent impurities following the amide coupling reaction (**Figure 3.11**). Purification of modified HA by dialysis and centrifugal filtration are commonly reported in the literature,<sup>254,321,355</sup> but <sup>1</sup>H-NMR characterisation confirmed the presence of several impurities after both these techniques were performed in succession warranting the need for an alternative purification process. Luo *et al.* described the purification of a HA-DOX bioconjugate via gel permeation chromatography.<sup>356</sup> However, this purification method is based on size-exclusion equivalent to the previously stated methods that proved to be unsuitable. The developed ion-exchange purification using an anionic sulfonic acid resin was successful in the removal of all impurities. To my best knowledge, this technique has previously not been performed for the purification of covalently modified HA-drug conjugates and could provide a more effective and time-efficient alternative to other purification methods.

The release of 1MT from HA over time was analysed in buffer at pH 5, 6.5 and 8 and the pH 6.5 condition was performed both in the absence and presence of the HAase enzyme as this is the typical pH of the acidic TME in which HAase is overexpressed (**Figure 3.13**).<sup>357</sup> Hyaluronidases are also found in the lysosomal cell compartment and are known to have an optimal enzymatic activity at pH 6 and temperature conditions between 37 and 42 °C.<sup>358,359</sup> The results after 48 h incubation showed no increase in 1MT release in the presence of HAase at pH 6.5 most likely due to the enzyme cleaving the HA at the  $\beta$ -1,4-glycosidic bonds of the polymer as illustrated in the introduction, which generates smaller HA fragments, but leaves the amide bond linkages intact. HA polymer can also be hydrolysed in the absence of HAase with an increased rate at acidic and alkaline pH conditions compared to neutral pH, which is enhanced at higher temperatures.<sup>360</sup>

Interestingly, the highest rate of 1MT release from the 1MT-HA biomaterial was observed at pH 8, which confirms that the release is driven by hydrolytic degradation of the amide bond. The non-enzymatic amide bond scission of polymers by hydrolysis has been shown to be enhanced at alkaline pH conditions over neutral and acidic pH, which corroborates the results observed in this chapter.<sup>361</sup> Additionally, the covalent modification of hyaluronic acid is known to slow down the rate of enzymatic degradation by HAase likely due to steric hindrance, which favours the use of this biomaterial as the base material for the fabrication of biodegradable MNs and implants discussed in Chapter 5.<sup>362</sup>

Apart from the intended gradual 1MT release from HA, another motivation for the modification of HA through a labile bond is the amphiphilic nature of the resulting HA co-block polymer that enables the development of self-assembled NPs capable of releasing the drug load in response to enzymatic cleavage or pH changes at the target site, which is further elaborated in Chapter 4.

HA is a known ligand of the CD44 transmembrane receptor that is overexpressed in different cancer types including prostate cancer, lung cancer, breast cancer and ovarian cancer, and is involved in tumour angiogenic signalling, cell proliferation and metastasis.<sup>363,364</sup> CD44 expression is also found in tumour infiltrating DCs and activates CD4<sup>+</sup> T cell polarisation towards an immunosuppressive Th2 phenotype.<sup>365</sup> The tumour and dendritic cell uptake of HA via CD44 receptor mediated endocytosis provides a direct pathway for the internalisation and targeted release of 1MT into the IDO-residing cell cytosol.<sup>366</sup> However, in cancers where CD44 expression is not upregulated other tumour-targeting vehicles may be utilised for the intracellular delivery of 1MT such as the different nano and microparticle systems described in Chapter 4.

Overall, the high biocompatibility, biodegradability, intrinsic tumour targeting properties via CD44 and versatility for modification make HA an excellent biomaterial for drug delivery. The covalent modification of HA with a clinically relevant small molecule inhibitor of the tumour overexpressed IDO enzyme, 1MT, was achieved and an efficient purification method of the 1MT-HA biomaterial was developed. The gradual release of 1MT from the biomaterial observed at all the different pH conditions analysed was attributed to slow hydrolytic cleavage of the amide bond. Nevertheless, the amount of 1MT released, even at the small quantities observed, is still capable of inducing IDO inhibition as demonstrated in the functional assays outlined in Chapter 5, where this biomaterial was used for the fabrication of transdermal and implantable devices.

# Chapter 4

**Design and synthesis of immunomodulatory nanoparticle systems and biosilica-based theranostic constructs**

## 4.1 Introduction

### 4.1.1 Design of a HA-based NP system for cancer immunotherapy

The covalent HA modification with an immunotherapeutic agent (i.e., 1MT) ensures an enhanced stability over electrostatic functionalisation and accommodates the possibility of introducing a hydrophobic element to the HA polymer to form an amphiphilic compound that drives the HA NP self-assembly (**Figure 4.1**). The co-block polymer can self-assemble into polymersomes containing a bilayer membrane of the hydrophobic section with the hydrophilic block exposed to both the core and the outer aqueous environment. The size of the hydrophilic molecule and ratio of hydrophilic to hydrophobic block governs the size and shape of the NPs formed.<sup>367,368</sup> Polymersomes can benefit from higher membrane stability and reduced membrane permeability compared to liposomes due to the control over the hydrophobic block size that characterises the thickness of the bilayer.<sup>369</sup> The incorporation of an immunomodulatory drug (i.e. antibodies that target immune checkpoints) or a vaccine into the NP core provides an additional component that may act synergistically towards an enhanced therapeutic effect. Additionally, the hydrophobic bilayer can also be used to incorporate lipophilic drugs into the NPs. The negative charge of the carboxylate groups of the hyaluronate anion offers the possibility for further functionalisation of the HA biomaterial with anti-cancer agents through electrostatic interactions. For instance, Xu *et al.* developed an immunotherapeutic liposome-protamine HA NP system in which an anti-TGF- $\beta$  siRNA with negative surface charge was modified onto HA NPs coated with cationic protamine.<sup>370</sup> The core NPs were then surface coated with anionic liposomes loaded with a macrophage activating agent. This NP system showed favourable therapeutic response compared to individual administration of the immunomodulatory agents in a mouse melanoma model. The overexpression of hyaluronidases such as Hyal1 and Hyal2 in the TME of different cancers including melanoma, bladder cancer, breast cancer, colorectal cancer, ovarian cancer and pancreatic cancer has been associated with tumour progression through enhanced angiogenesis signalling, loss of CD44 receptor expression on tumour cells and the production of small HA fragments, which are known to contribute to tumour growth and metastasis in some cancers.<sup>327</sup> Duan *et al.* demonstrated that HA-NPs can act as a Hyal1 inhibitor by specifically binding to the enzyme and preventing HA degradation into smaller glycosaminoglycan units.<sup>371</sup> Additionally, the study reported that HA-NPs have a higher affinity than linear HA towards the CD44 ligand, which is overexpressed in some cancers, due to the high particle surface area that allows a high degree of localised HA presentation to the

CD44-expressing cells. This further favours the design and development of HA-NP systems that in parallel with the potential of multi-drug incorporation and gradual kinetic release, could also have intrinsic anti-tumour properties by inhibiting the activity of Hyal1 in the TME.

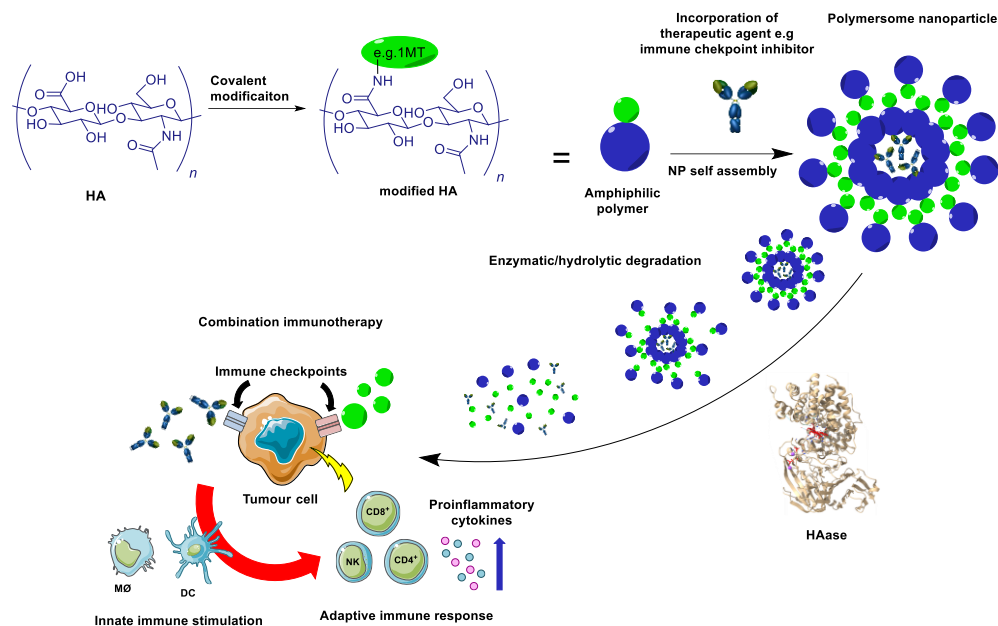


**Figure 4.1 Design of self-assembled HA-based NP system for combination immunotherapy.** HA NPs can be surface functionalised and incorporated with immunotherapeutic agents that are released in the presence of HAase or via hydrolytic degradation to overcome the immunosuppressive mechanisms of cancer cells.

#### 4.1.2 Functionalisation of SPIONs with platinum-based anti-cancer agents

SPIONs, typically composed of magnetite,  $\text{Fe}_3\text{O}_4$ , and  $\gamma$ -maghemite,  $\text{Fe}_2\text{O}_3$ , nanocrystals provide excellent drug delivery vehicles due to their biocompatibility, bioavailability, tuneable properties and surface that permits functionalisation with different molecules for active tumour targeting and specific release of vaccines at the tumour tissue.<sup>372,373</sup> Due to their paramagnetic properties, SPIONs can also be used to induce local hyperthermia in the TME and as MRI contrast agents for in vivo biodistribution analysis. Additionally, it has been found that SPIONs have intrinsic therapeutic properties by inducing ROS-mediated tumour cell death in the acidic TME in the presence of local  $\text{H}_2\text{O}_2$  through Fenton chemistry as described in more detail in Chapter 1.<sup>374,166</sup> They have also been found to elicit immunomodulatory properties by inducing M1 macrophage polarisation leading to the release of pro-inflammatory cytokines and ROS production in the tumour.<sup>375</sup>

Cisplatin (cis-diamminedichloroplatinum (II)) has had a major impact on the development of chemotherapeutics due to its particularly high efficiency for the treatment of testicular and

ovarian cancers.<sup>376</sup> However, the development of tumour drug resistance and the high off-target cytotoxicity remain its most critical limitations.<sup>377,378</sup> Pt(IV) prodrugs with an octahedral ligand geometry are inert and less cytotoxic as they are functionally inactive until they are reduced in the cell cytosol to the Pt(II) complex with the loss of its two axial ligands (**Figure 4.2**).<sup>379</sup> They can enter cells through passive diffusion or through copper transporter mediated internalisation.<sup>380</sup> Following the reduction of Pt(IV) to Pt(II) the Pt compound loses its chloride ligands by undergoing hydrolysis, which allows it to bind to DNA bases to form adducts that can lead to DNA damage and cell apoptosis.<sup>378</sup> The possibility of chemical coupling or combining complexes with immunotherapeutic agents is an appealing pathway for development of “dual action” cancer immuno-chemotherapy systems. This was recently evidenced by Awuah *et al.* with the conjugation of a Pt(IV) prodrug to an IDO inhibitor, which showed high therapeutic efficiency in a cisplatin-resistant ovarian cancer cell line.<sup>381</sup> It was also found that Pt-based therapies can intrinsically induce immunogenic cell death by promoting NK cell mediated cytotoxicity, inhibiting tumour cell immune evasion mechanisms and aid CTL recognition of cancer cells.<sup>382-385</sup> These immunomodulatory responses provide a compelling new strategy for the development of combination therapies that can elicit a higher therapeutic effect for more effective cancer treatment. The functionalisation of a Pt(IV) prodrug and other immunomodulatory agents exploiting IONPs was explored in this thesis as multifunctional therapeutic constructs that could be incorporated into biomaterial-based drug administration devices. A manuscript entitled "Redox-triggered Nanomedicine via Lymphatic Delivery: Inhibition of Melanoma Growth by Ferroptosis Enhancement and a Pt(IV)-Prodrug Chemoimmunotherapy Approach" is currently under review in *Advanced Therapeutics*.

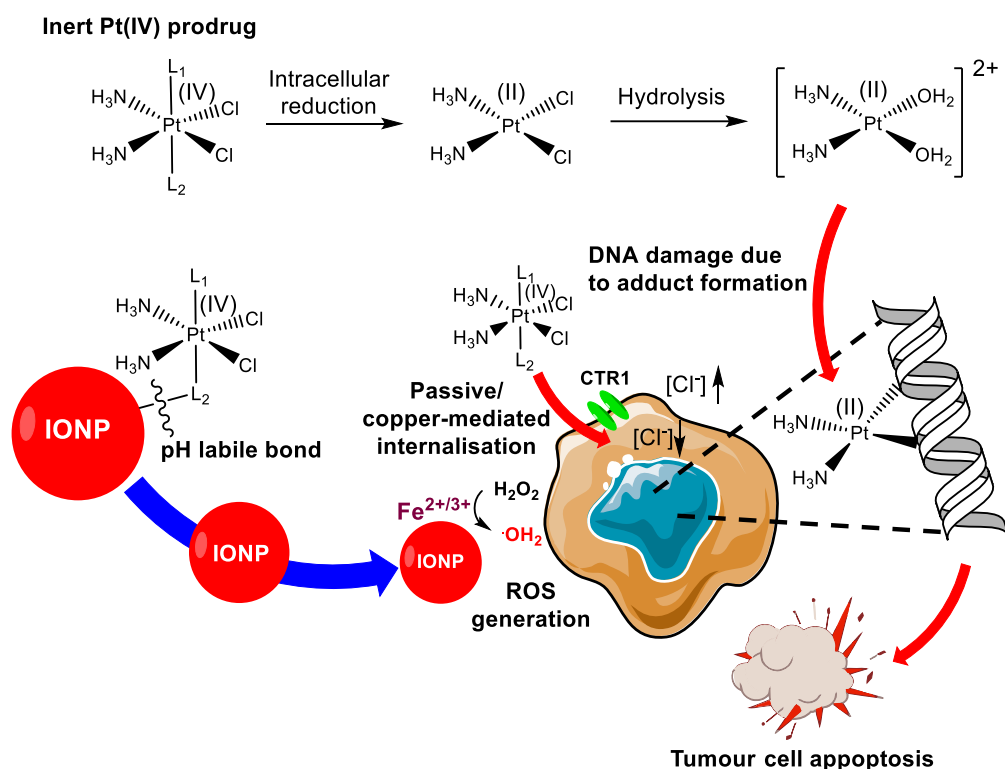


**Figure 4.2 Illustration of a Pt(IV) prodrug functionalised IONP system and its potential combination therapeutic anticancer mechanism.** The inert Pt(IV) prodrug released in the acidic TME and infiltrates the tumour cell through passive diffusion or copper transporter CTR1-mediated internalisation. The Pt(IV) is then reduced to Pt(II) by losing its axial ligands and undergoes hydrolysis. The hydrolysed Pt(II) complex coordinates to the DNA bases and prevents DNA repair and replication leading to tumour cell death. The therapeutic effect is enhanced through the intrinsic peroxidase-like activity of the IONPs in the TME leading to the generation of ROS that induce oxidative stress in tumour cells.

#### 4.1.3 Biosilica-based materials for cancer therapy

Biosilica is found abundantly in nature and can be cost efficiently extracted from unicellular microalgae, also known as diatoms.<sup>386</sup> Diatoms consist of a highly porous nanostructured siliceous cell wall, divided into two almost identical halves known as frustule and come in a plethora of shapes and sizes with over 100,000 species estimated (**Figure 4.3**).<sup>387</sup> They can be found globally in both ocean and fresh waters, with many of these diatom species measuring ~ 5-50  $\mu\text{m}$  in diameter or length.<sup>389,390</sup>

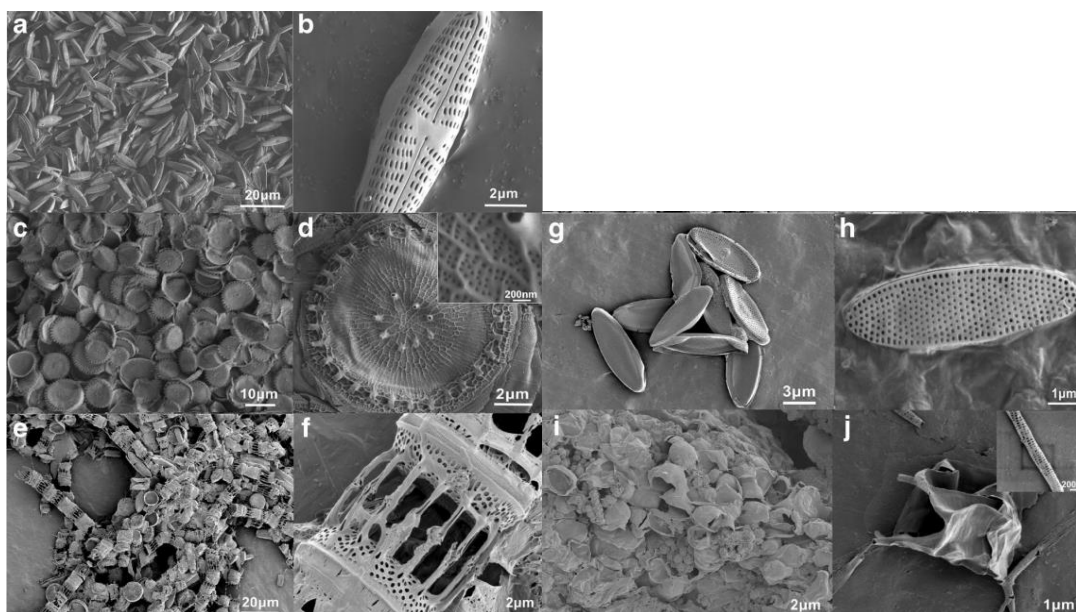


**Figure 4.3** Examples of different diatom species with varied frustule shapes. *a, b* *Navicula* sp.; *c, d* *Thalassiosira weissflogii*; *e, f* *Skeletonema* sp.; *g, h* *Closterium* sp.; *i, j* *Chaetoceros muelleri*. Reproduced from Jiang *et al.*.<sup>390</sup>

There are a range of commercially available diatoms in the food industry as a nutritional supplement and increasingly, they provide a promising natural alternative to synthetic porous silica for a broad range of biomedical, environmental, agricultural, and energy applications. In biomedical applications they are mainly explored as potential new biomaterials for use in drug delivery, tissue engineering and biosensing.<sup>391,392</sup> Diatoms have also generated interest for anticancer applications due to their well-established biocompatibility, porous structure, high surface area and aptness for surface modification.<sup>392-394</sup> The removal of organic matter and inorganic impurities from the desired silica-based diatom skeleton is achieved by a multistep purification process that generally relies on acid and high temperature treatments.<sup>395</sup> The diatoms can be characterised by electron microscopy (SEM or TEM) to determine size and morphological features, while energy dispersive X-ray spectroscopy (EDS) and FTIR are common methods used to assess their chemical composition.<sup>390,396</sup>

While, to date, there is very limited literature of diatom-based systems demonstrating success or even evaluated in pre-clinical *in vivo* studies for cancer therapy, several proof-of-concept studies validate their potential as new natural biomaterial carrier of anticancer agents for clinical applications. Delasoie *et al.* exploited the porous diatom structure as a transport vehicle of 3 hydrophobic, chemotherapeutic drugs and a covalently modified the diatom surface with vitamin B12, known to target colorectal and breast cancer cells.<sup>397</sup> The



release kinetics showed the ability of the diatom silica shell to provide slow and prolonged release (over a period of 5 days) of a ruthenium-based drug. This system showed also the possibility of attaching to the diatom surface several entities for cell targeting via covalent conjugation and non-covalent immobilisation, providing a platform for advanced chemotherapy. Delalat *et al.* followed an alternative diatom bioengineering approach by producing genetically modified *Thalassiosira pseudonana* diatoms with the IgG binding domain of protein G to attach cell targeting antibodies.<sup>398</sup> Two different chemotherapeutic agents were loaded into micelles and liposomes, which were electrostatically attached to the diatoms. The modified diatoms were functionalised with neuroblastoma specific antibodies and the therapeutic efficiency of this system was assessed *in vivo* showing significant tumour volume reduction after 2 weeks. We reasoned that these biosilica-based systems could provide also an excellent new biomaterial platform for vaccine immobilisation/delivery, whereby the slow-release mechanism would ensure prolonged vaccine retention in the TME and targeted delivery through conjugation of cancer-cell specific biomolecules. The relevance of these systems for medical applications is gaining interest in cancer research, but the development of biosilica in the context of immunotherapy remains unexplored. This thesis explores strategies for development of biosilica-based theranostic systems and as biosensor nanotechnology for cancer immunotherapy.

#### **4.1.4 Design of a biosilica-based theranostic system for combination cancer therapy and as biosensor device**

The aim of this research is to elucidate the intrinsic peroxidase-like activity and the versatility of commercial diatoms for use as new biomaterial scaffold for the delivery and slow and prolonged release of immunomodulatory and other anti-cancer agents, including nanomedicines. The peroxidase activity combined with the proven biocompatibility, low cost and availability make them ideal candidates to create systems for intrinsically therapeutic carrier-mediated combination therapies. The high porosity of the frustules and the silanol (Si-OH) surface groups allows for different pathways for functionalisation either through covalent conjugation or electrostatic interactions. In our design we functionalised the diatoms with the polycation PEI, which has been demonstrated to be useful in gene delivery and IONPs.<sup>399</sup>

IONPs are known to have intrinsic anti-cancer properties by producing ROS in the oxidative and acidic TME and can be functionalised with anionic surface groups to promote electrostatic attraction towards a cationic diatom system.<sup>166</sup> The PEI-modified diatoms are

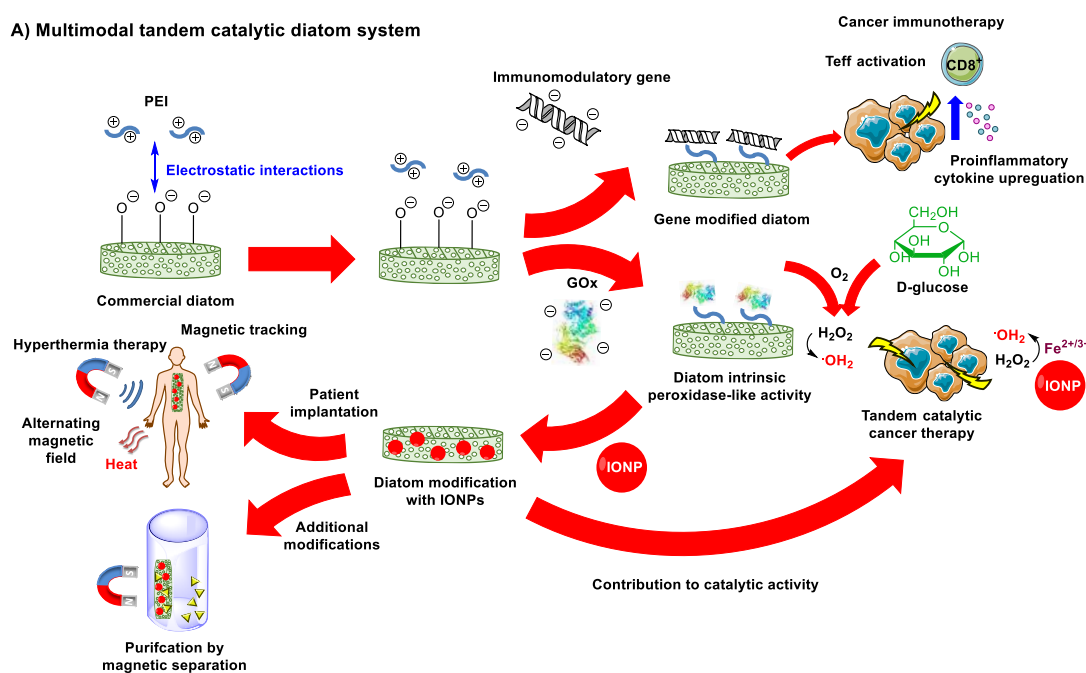
also co-functionalised with GOx, which is an enzyme that catalyses the oxidation of D-glucose into H<sub>2</sub>O<sub>2</sub> and D-glucono-1,5-lactone in the presence of O<sub>2</sub>. The negative surface charge of GOx can be exploited to promote electrostatic interaction with the cationic diatom system to produce tandem catalytic scaffolds that provide multimodal synergistic therapy. Thus, it could potentially have a dual anti-tumour effect by enhancing the therapeutic effect due to the increased H<sub>2</sub>O<sub>2</sub> levels whilst at the same time depleting the glucose supply to tumour cells in the TME required for tumour growth and progression.<sup>400</sup> Furthermore the magnetic properties of the IONP-loaded diatom system has potential applications in hyperthermia therapy, *in vivo* tracking and purification (**Figure 4.4 A**).

Additionally, the diatoms were explored as multimodal agents with biosensor applications for the detection of biomolecules that could lead to development of cost-efficient alternative to or in combination with commercially available ELISA kits. Monoclonal antibodies (MAbs) are commonly used in these kits as targeting agents for tumour associated antigens such as cluster differentiation proteins and growth factors expressed on the tumour cells surface.<sup>401</sup> MAbs can also be used to stimulate host tumour-antigen-specific immune responses in cancer immunotherapy (e.g. the recent discovery of immune checkpoint inhibitors such as anti-PD-1/anti-PD-L1 and anti-CTLA).<sup>402</sup> In our design we target the PD-1/PDL-1 interaction as it has been shown to result in safer and more effective immunotherapy. PD-1 is a protein expressed on the surface of activated T-cells, which are deactivated when they bind to its ligand PD-L1, which is known to be overexpressed in some cancers and APCs. This ligand-receptor interaction results in immune tolerance and inhibits the activation of CTLs towards cancer cells. The immune checkpoint inhibitor anti-PD-L1 binds to the PD-L1 ligand on the tumour cell or APC surface and prevents the immunosuppressive effect by reinvigorating the antitumor function of the immune cells.<sup>99</sup> Typical methods of covalent antibody conjugation are through the reduction of the antibody's disulfide bridges using reducing agents including tris(2-carboxyethyl)phosphine (TCEP), 2-mercaptoethylamine (2-MEA) or dithiothreitol (DTT) to obtain surface sulfhydryl groups or modification through the amine-terminal lysine groups.<sup>403,404</sup> A less destructive thiolation technique involves the use of 2-iminothiolane (Traut's reagent), which converts the lysine residues into sulfhydryl groups that are reactive towards maleimides.<sup>404</sup>

This chapter provides proof-of-concept demonstration of biosilica-based PD-L1/PD-1 targeted biosensor system through covalent modification of the diatoms with a suitable terminal group such as a maleimide or carboxylic acid that could propagate conjugation to an immunomodulatory antibody (**Figure 4.4 B**). 3,3',5,5'-Tetramethylbenzidine (TMB) is

molecule commonly used in ELISAs that produces a blue coloured compound upon oxidation by peroxidases such as horseradish peroxidase (HRP) that can be quantified by spectrophotometry.<sup>405</sup> The intrinsic peroxidase-like activity of the diatom and/or IONPs can be harnessed to detect and potentially quantify the amount of ligand captured by the diatom-based theranostic system. This theranostic system has the potential to both reduce the development cost based on the inexhaustible source of diatoms in nature and exceed the sensitivity of conventional biomolecular detection kits due to the high surface area of the diatoms enabling a high antibody to diatom ratio.

#### A) Multimodal tandem catalytic diatom system



#### B) Therapeutic or diagnostic diatom system

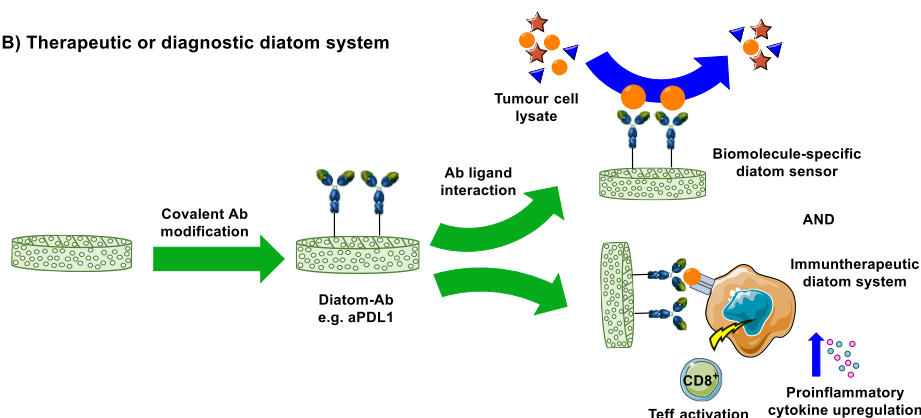


**Figure 4.4 Proposed design of biosilica-based systems.** (A) a multimodal diatom tandem catalytic system incorporating IONPs and GOx via electrostatic interactions and (B) a therapeutic or diagnostic diatom system with applications as a biosensor device and cancer immunotherapy developed by covalent modification with an immunomodulatory antibody.

#### 4.1.5 Aims and objectives

- The development and characterisation of self-assembled 1MT-HA NPs as well as carrying out NP loading and release studies with the immune checkpoint inhibitor, anti-PD-L1;
- Preparation and characterisation of IONP micelles and investigating the functionalisation with immunomodulatory agents via electrostatic interactions;
- Multistep synthesis of a Pt(IV) prodrug and covalent functionalisation onto IONPs as a multimodal therapeutic platform;
- Exploring the intrinsic peroxidase-like activity of diatoms and the fabrication of a tandem catalytic system aimed towards the glucose-rich TME through electrostatic modification with IONPs and glucose oxidase;
- Development of a proof-of-concept multimodal biosilica-based biosensor of the tumour overexpressed PD-L1 immune checkpoint via the covalent modification of diatoms with anti-PD-L1.

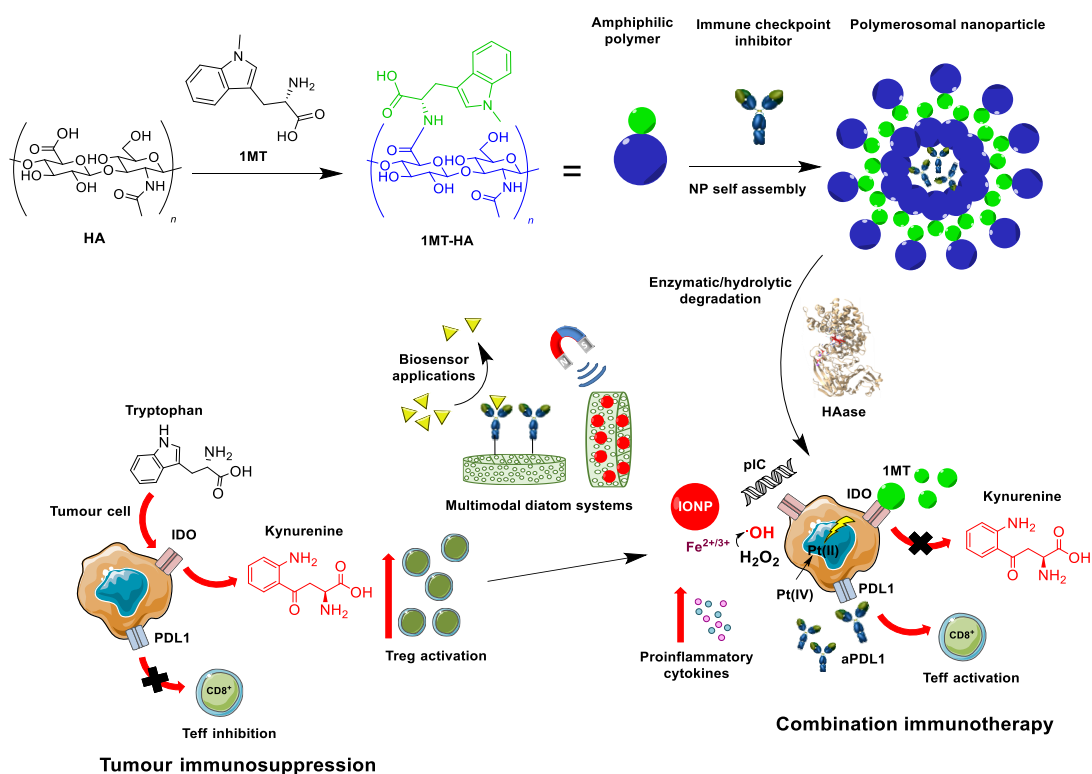


**Figure 4.5 Overview schematic of chapter 4.** Illustrated are the anti-PD-L1 incorporated biodegradable 1MT-HA NPs, different immunomodulatory IONP systems including IONP-DOTAP-pIC and the Pt(IV) prodrug bound IONP; and multimodal diatom systems with utility for combination cancer therapies and as a biosensor.

## 4.2 Results

### 4.2.1 Synthesis and characterisation of anti-PD-L1 loaded 1MT-HA

#### NPs (1MT-HA@anti-PD-L1 NPs)

The covalently functionalised 1MT-HA biomaterial obtained in Chapter 2 was used here to produce self-assembled NPs enabled by the amphiphilic nature of the 1MT-modified polymer. The anti-PD-L1 incorporated NPs (1MT-HA@-anti-PD-L1 NPs) were created using a 1MT-HA biomaterial synthesised via ester bond formation using 280 kDa MW HA. The preparation involved the addition of 1MT-HA and anti-PD-L1 at 10:1 w/w ratio to a mixture of MilliQ water: methanol (2:1 v/v) and the emulsion was stirred at 4°C for 2 h. The organic solvent was removed by dialysis against MilliQ water (10 kDa MWCO) for 72 h. The NPs were purified from free anti-PD-L1 by centrifugal filtration (300 kDa MWCO) and the retentate washed several times with MilliQ water. The final 1MT-HA@-anti-PD-L1 NP suspension was characterised by DLS, NTA, SEM and FPLC. The DLS size distribution by intensity and NTA average particle size is comparable and in the 300-350 nm range (**Figure 4.6 A, C**). Consistent with the carboxylate groups of the HA biopolymer, the 1MT-HA NPs exhibited a negative zeta potential (**Figure 4.6 B, D**). The SEM further confirmed successful NP formation and the good agreement in the size estimated using different characterisation techniques (**Figure 4.6 E**) (**Appendix 2**).

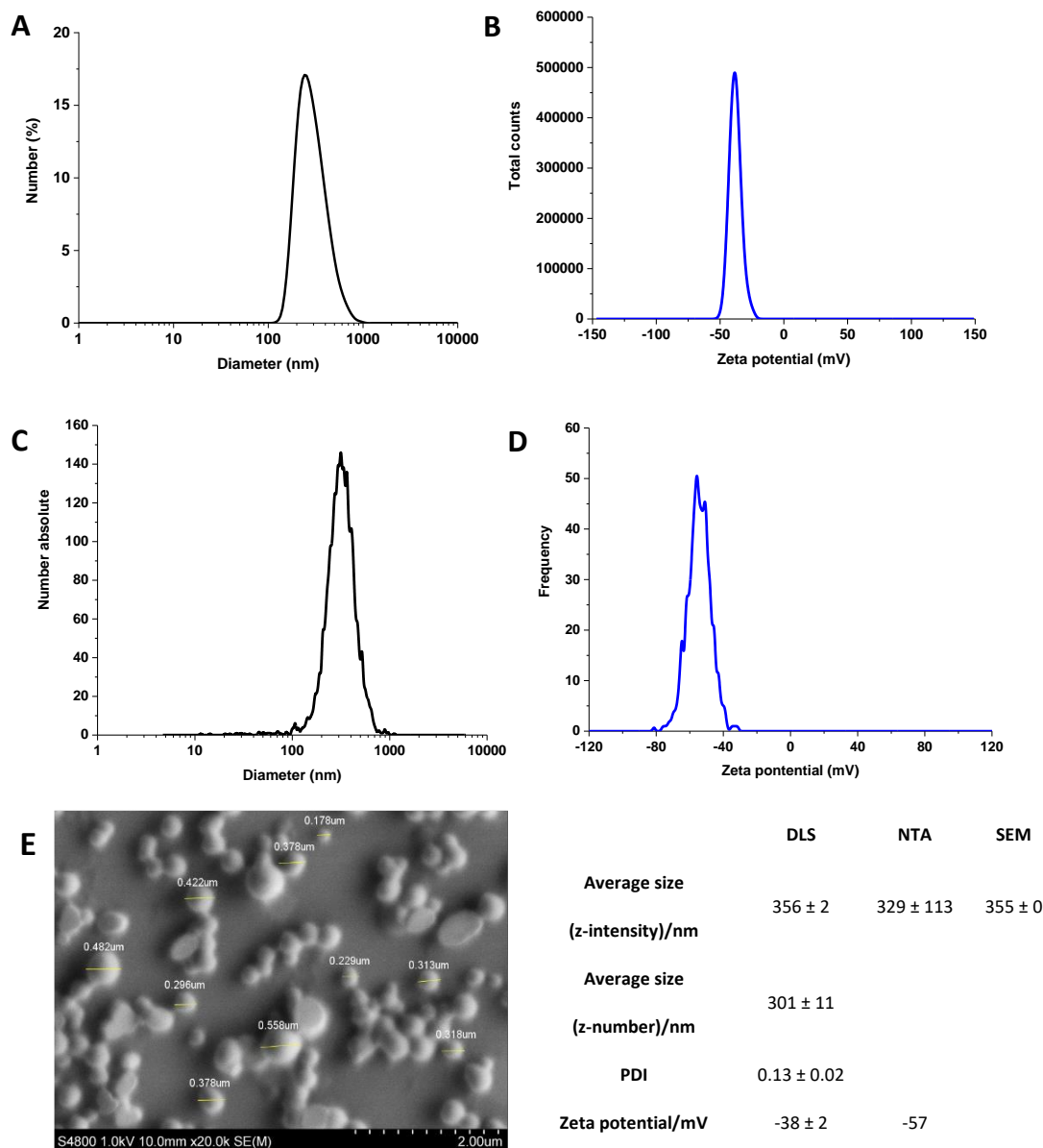


**Figure 4.6 1MT-HA@anti-PD-L1 NP characterisation.** (A) DLS by intensity and number distribution and (B) zeta potential of NPs in MilliQ water (mean of 3 measurements). (C) NTA particle diameter and (D) zeta potential analysis. (E) SEM imaging of NPs and average size calculation based on randomly selected particles ( $N = 10$ ).

To determine the % encapsulation efficiency (% EE) of the antibody in the NP, a bicinchoninic acid (BCA) assay was performed. The filtrate recovered from the 1MT-HA@anti-PD-L1 NPs purification was concentrated to the original volume of the NP stock (1mg/mL) using 3 kDa MWCO spin filters and then added to a 96-well plate in duplicates. As controls, anti-PD-L1 (+ control) and empty 1MT-HA NPs (- control) in MilliQ water were analysed at concentrations of 100  $\mu\text{g/mL}$  and 1 mg/mL, respectively. A BSA calibration curve was performed simultaneously at concentrations from 0-1000  $\mu\text{g/mL}$  and the absorbance was measured at 550 nm after 2 h incubation at 37°C. The absence of anti-PD-L1 in the filtrate indicated that

all of the anti-PD-L1 added had been incorporated into the 1MT-HA@anti-PD-L1 NPs (**Figure 4.7**)

	Average A.U.	[Protein] µg/ml	[anti-PD-L1] µg/ml	% EE
1MT-HA@anti-PD-L1 NP filtrate	0.020	0.00	0.00	100
Anti-PD-L1 (+ control)	0.338	131	100	
Empty 1MT-HA NPs (- control)	0.032	3.30	2.50	

**Figure 4.7** BCA protein assay for the quantification of anti-PD-L1 incorporated 1MT-HA NPs. Tabular summary of BCA results of the 1MT-HA@anti-PD-L1 NP filtrate. A sample of anti-PD-L1 at 0.1 mg/mL was used as the positive control and empty 1MT-HA NPs at 1 mg/mL were the negative control (N = 1).

The incorporation of anti-PD-L1 into the 1MT-HA to form 1MT-HA@antiPD-L1 NPs was further confirmed by FPLC. Representative FPLC chromatogram profiles of 1MT-HA, anti-PD-L1, 1MT-HA@antiPD-L1 NPs were analysed separately at of 225 nm and 280 nm (**Figure 4.8**). The anti-PD-L1 showed an intense peak at 15-16 mL retention volume at 225 nm UV detection wavelength. The peak at ~ 20 mL is due to smaller 1MT-HA fragments. The anti-PD-L1 control does not show a UV absorbance peak at 280 nm, while the 1MT-HA control appears at a retention volume of 8.8 mL (**Figure 4.8 A**).

The FPLC chromatogram of the 1MT-HA@anti-PD-L1 NPs shows distinct peaks at 225 nm and 280 nm at 8.4 mL retention volume (**Figure 4.8 B**). The absence of the anti-PDL1 peak at ~ 15 mL suggests successful anti-PD-L1 incorporation. The peak shift from 8.8 mL to 8.4 mL at 225 nm of the NPs system compared to the 1MT-HA polymer control could be an additional confirmation of NP formation since the larger 1MT-HA@anti-PD-L1 NPs can be expected to elute earlier from the size exclusion column.

As an additional control, the HA without 1MT modification was mixed with anti-PD-L1 following the same NP synthesis and purification procedure and characterised by FPLC (**Figure 4.8 C**). The chromatogram shows the characteristic anti-PD-L1 peak at 15 mL retention volume, confirming that 1MT is required for NP formation and anti-PD-L1 incorporation. These results confirms that the 1MT does not only provide an immunotherapeutic element to this NP system, but also enables NP self-assembly due the formation of the required amphiphilic polymer.

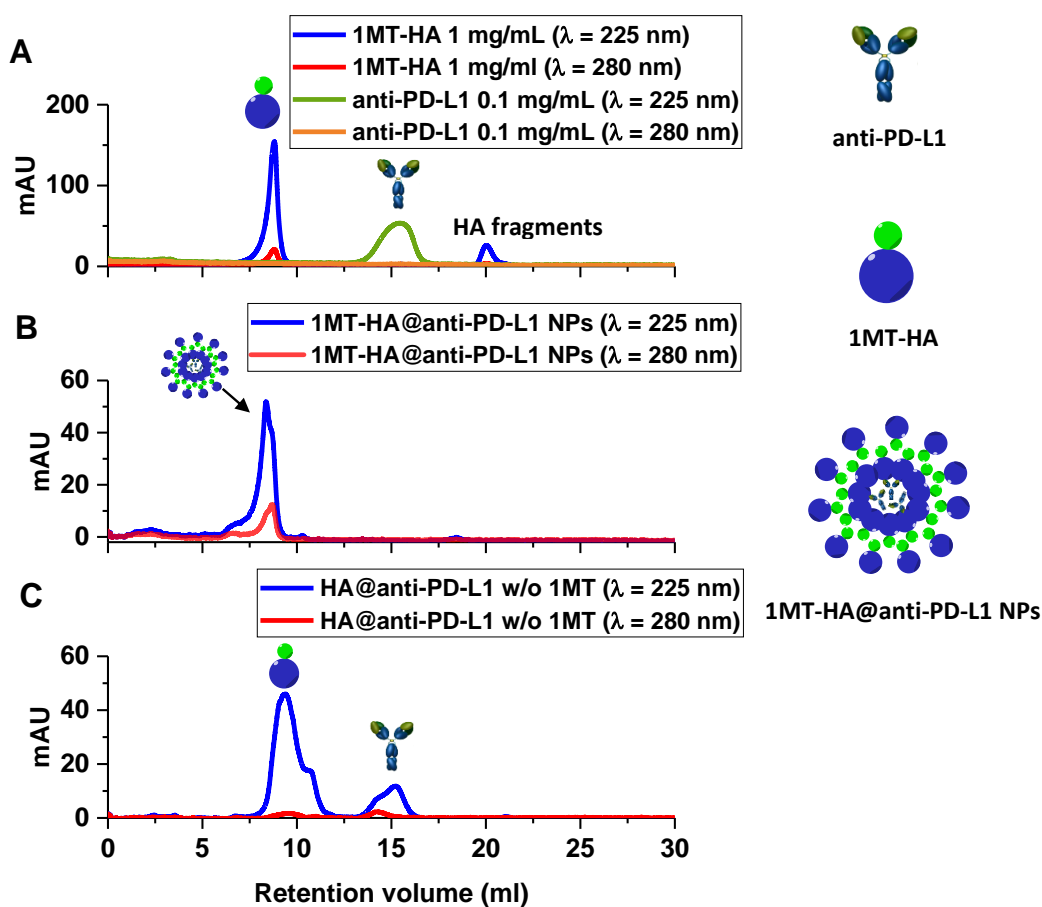
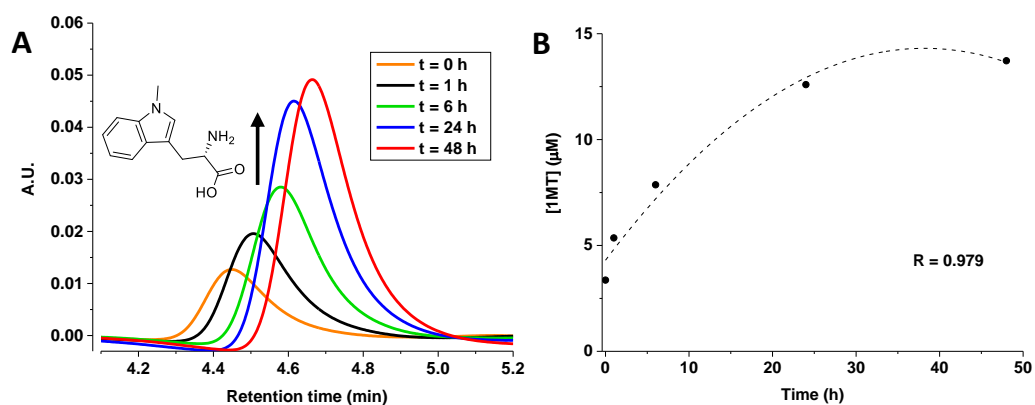


**Figure 4.8 FPLC characterisation of 1MT-HA@anti-PD-L1 NPs.** (A) Chromatogram of 1MT-HA at 1 mg/mL and anti-PD-L1 at 0.1 mg/mL in MilliQ water at 225 and 280 nm as controls. (B) Chromatograms of 1MT-HA@anti-PD-L1 NPs and (C) HA@ anti-PD-L1 in the absence of 1MT at 225 and 280 nm, which demonstrates that the 1MT drives NP formation and is essential for anti-PD-L1 incorporation. The experiment was performed on a size-exclusion column at 0.5 mL/min using MilliQ water as the mobile phase ( $N = 1$ ).

#### 4.2.2 Release studies of immunomodulatory agents from HA NPs

To determine the 1MT release kinetics from 1MT-HA NPs, the NPs were dissolved in PBS containing 18 nmol HAase at pH 6.5 and incubated at 37°C for 48 h. Aliquots were collected at 0, 1, 6, 24 and 48 h, purified by centrifugal filtration and the filtrate analysed by RP-HPLC. The studies showed the fastest 1MT release takes place during the first hour and reaches a “plateau” after 48 h, when an accumulated release of 1 % of the 1MT was observed based on the  $^1\text{H-NMR}$ -derived 1MT modification yield of the 1MT-HA biomaterial (**Figure 4.9 A-C**).





C	Time point/h	[1MT]/ $\mu\text{M}$	% 1MT release
	0	3.4	0.32
	1	5.4	0.52
	6	7.9	0.76
	24	12.6	1.22
	48	13.7	1.33

**Figure 4.9 1MT-HA@anti-PD-L1 NP degradation experiment.** (A) Overlay of RP-HPLC chromatograms of 1MT released from NPs from  $t = 0-48$  h; (B) Kinetic analysis of 1MT released from NPs over time; (C) Tabular representation of kinetic release data and % 1MT release ( $N = 1$ ).

The released kinetics of anti-PL-D1 from the 1MT-HA@anti-PD-L1 NPs was evaluated by FPLC. The 1MT-HA@anti-PD-L1 NPs were degraded as previously described and aliquots were collected at timepoint 0, 1, 3, 24 and 48 h. The samples were directly injected into the FPLC for analysis in MilliQ water (**Figure 4.10**). The peak at 8-10 mL retention volume is characteristic of the NPs, whilst the peak at 20 mL retention volume could indicate the presence small HA fragments as the result of the biomaterial breakdown by hydrolysis or HAase enzyme activity. Antibody release was not observed until the 24 h timepoint with a characteristic peak at 15 mL retention volume and a small increase in anti-PD-L1 release was recorded for the 48-h sample, indicating a gradual release of the immune checkpoint inhibitor from the NPs upon degradation. The reduction of the NP peak at 8-10 mL retention volume and increase of the peak at  $\sim 20$  mL over time is a further indication of gradual biomaterial degradation.

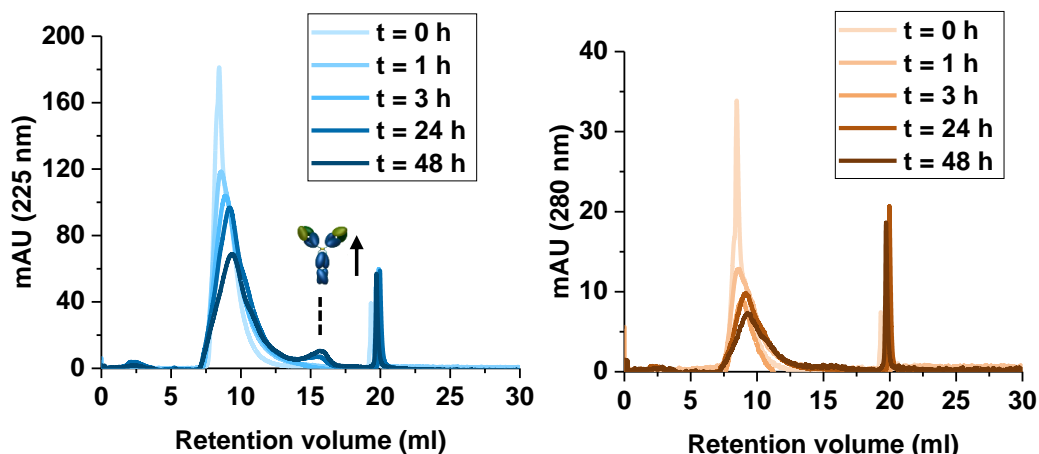


**Figure 4.10** Overlaid FPLC chromatograms of anti-PD-L1 released from 1MT-HA@anti-PD-L1 NPs in the presence of HAase. Samples were collected at timepoints 0, 1, 3, 24 and 48 h and injected into the FPLC without purification. UV absorbance was analysed at 225 nm and 280 nm ( $N = 1$ ).

The self-assembly method for the preparation of this biomaterial-based NP system and its ability to incorporate and gradually release complementary/synergistic immunomodulatory drugs highlights its potential as a biodegradable vehicle, making them attractive candidates to create devices for local drug delivery of the immunotherapy.

### 4.2.3 Development of immunomodulatory IONP systems

The hydrophobic IONPs of 6-7 nm were obtained by thermal decomposition of iron acetyl acetonate ( $\text{Fe}(\text{acac})_3$ ) in benzyl ether, in the presence of oleic acid and oleyl amine, and hydrophilic IONP-loaded micelles were synthesised using a thin film-hydration method. The micelle formation involved the suspension of the hydrophobic NPs with amphiphilic lipids (in our case PEGylated phospholipids) in chloroform followed by the evaporation of the solvent overnight to form a thin film. Upon hydration of this film, the IONPs formed the micelles by a self-assembly process, with the fatty acid chains interacting with the NP surface and the phosphate/PEG groups in contact with the aqueous phase. Purification of the IONPs was performed by an initial centrifugation cycle to remove large IONP aggregates followed by ultracentrifugation to remove unbound phospholipid molecules and empty (IONP-free) micelles. The type of terminal groups on the IONP micelle surface are dependent on the choice of phospholipid used for the micelle synthesis and offered opportunities for the covalent and non-covalent functionalisation with the immunomodulatory and anti-cancer agents (Pt(IV) prodrugs and poly(IC)).

#### 4.2.3.1 Synthesis and characterisation of IONP-Pt(IV)

A Pt(IV)-prodrug was prepared and covalently conjugated to IONPs in a multi-step synthesis. The first step was the reaction of the cisplatin, Pt(II) complex, with hydrogen peroxide to produce  $c,c,t$ -[Pt(NH<sub>3</sub>)<sub>2</sub>Cl<sub>2</sub>(OH)<sub>2</sub>]. The trans Pt(IV) dihydroxo product was reacted with succinic anhydride to form the trans Pt(IV) dicarboxylate,  $c,c,t$ -[Pt(NH<sub>3</sub>)<sub>2</sub>Cl<sub>2</sub>(O<sub>2</sub>CCH<sub>2</sub>CH<sub>2</sub>CO<sub>2</sub>H)<sub>2</sub>]. This functionalisation step does not only provide increased hydrophilicity, but also unlocks additional possibilities for modification through the terminal carboxylic acid groups. To anchor the Pt(IV) prodrug to the SPIONs, the prodrug was covalently functionalised with an amine terminal PEGylated phospholipid through amide bond coupling followed by IONP coating with the resulting DSPE-PEG-Pt(IV) species to form the hydrophilic micelles (**Figure 4.11**).

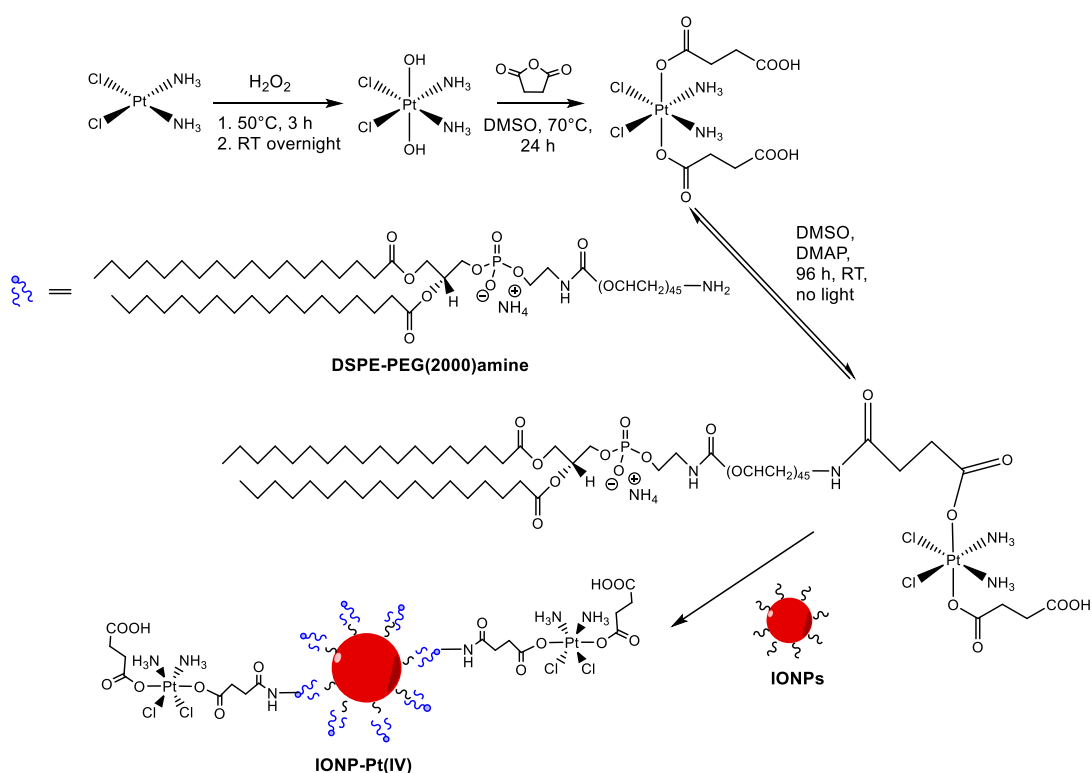


**Figure 4.11 Reaction scheme for IONP-Pt(IV) synthesis.** Cisplatin Pt(II) was oxidised by the addition of hydrogen peroxide to form  $c,c,t$ -[Pt(NH<sub>3</sub>)<sub>2</sub>Cl<sub>2</sub>(OH)<sub>2</sub>], which was further reacted with succinic anhydride to form  $c,c,t$ -[Pt(NH<sub>3</sub>)<sub>2</sub>Cl<sub>2</sub>(O<sub>2</sub>CCH<sub>2</sub>CH<sub>2</sub>CO<sub>2</sub>H)<sub>2</sub>]. The Pt(IV) prodrug was covalently modified to the phospholipid through a reversible amide-bond formation. The IONP-Pt(IV) was synthesised via the thin-film hydration method with the Pt(IV) modified phospholipid coating.

The Pt(IV) prodrug modification steps were characterised by <sup>1</sup>H-NMR and the IONP-Pt(IV) was characterised by DLS and zeta potential measurement. The <sup>1</sup>H-NMR of  $c,c,t$ -[Pt(NH<sub>3</sub>)<sub>2</sub>Cl<sub>2</sub>(OH)<sub>2</sub>] shows a singlet peak at 10.2 ppm corresponding to the axial hydroxyl

ligand protons (**Figure 4.12 A**). A clear difference was observed in the  $^1\text{H-NMR}$  spectrum of the  $c,c,t\text{-[Pt(NH}_3)_2\text{Cl}_2(\text{O}_2\text{CCH}_2\text{CH}_2\text{CO}_2\text{H})_2]$  complex with the hydroxyl proton peaks no longer present and the  $-\text{CH}_2\text{CH}_2-$  group protons of the axial ligands appearing as a multiplet at 2.71-2.73 ppm (**Figure 4.12 B**).

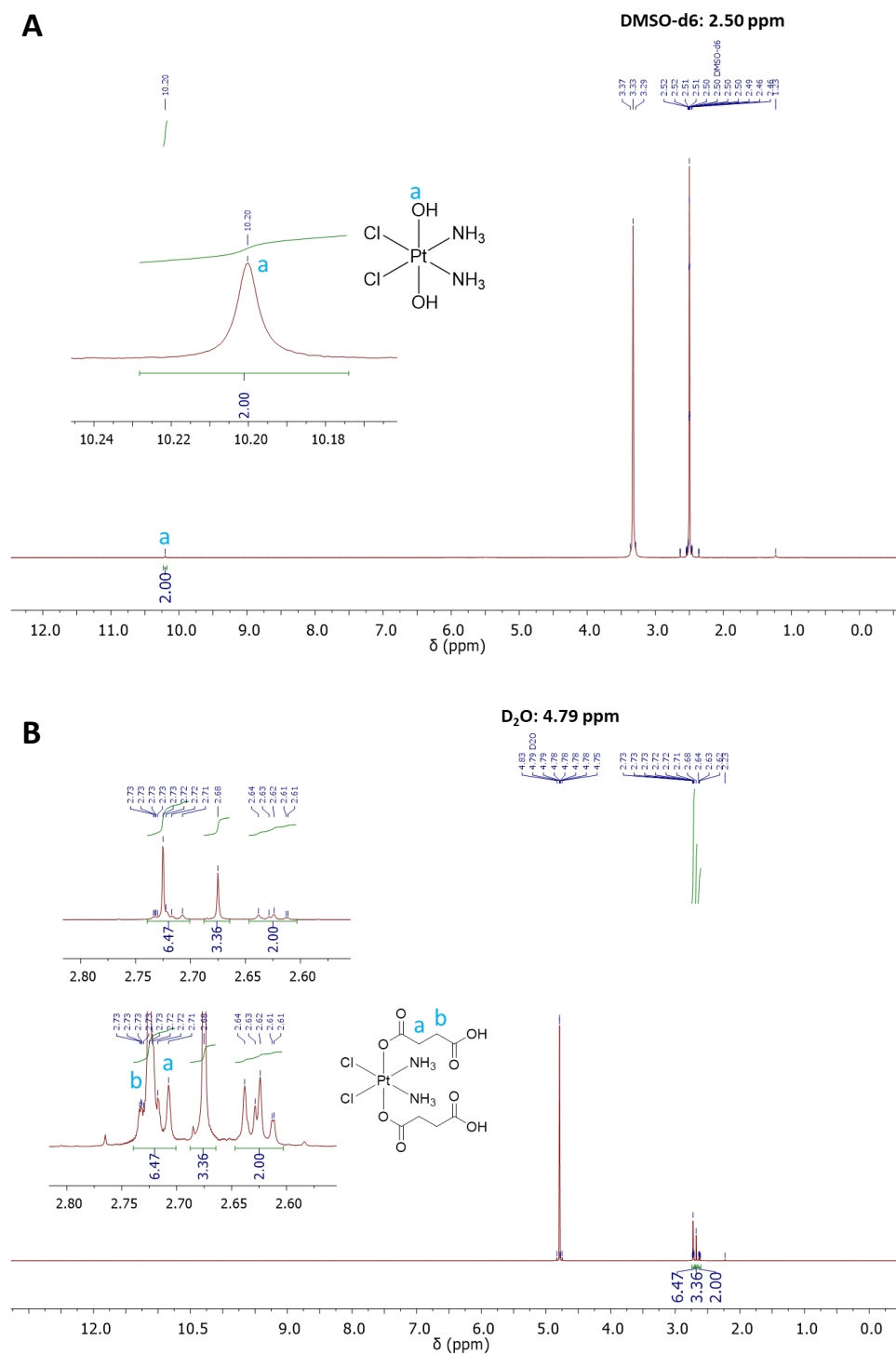


**Figure 4.12**  $^1\text{H-NMR}$  spectra of (A)  $c,c,t\text{-[Pt(NH}_3)_2\text{Cl}_2(\text{OH})_2]$  in DMSO-d<sub>6</sub> and (B)  $c,c,t\text{-[Pt(NH}_3)_2\text{Cl}_2(\text{O}_2\text{CCH}_2\text{CH}_2\text{CO}_2\text{H})_2]$  in D<sub>2</sub>O.

The resulting Pt(IV) prodrug was covalently attached to the DSPE-PEG(2000)-amine phospholipid by amide bond formation for 96 h to ensure reaction completion followed by purification by dialysis in MilliQ water for 24 h. The  $^1\text{H-NMR}$  characterisation illustrates the succinimidyl protons of the Pt(IV) prodrug at 2.50-2.75 ppm and alkyl ether protons for PEG units at 3.71 ppm confirming the formation of the DSPE-PEG(2000)-Pt(IV) product (**Figure 4.13**). Individual NMR spectra are included in the Appendix section (**Appendix 3 and 4**).

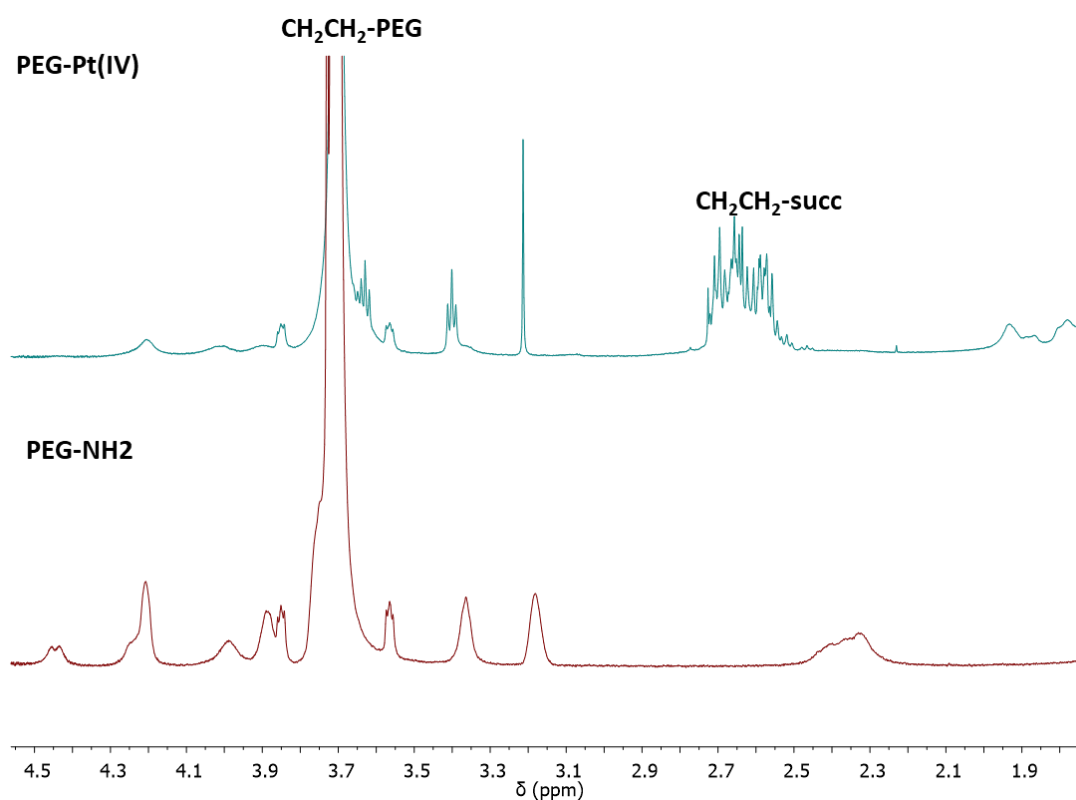


**Figure 4.13**  $^1\text{H-NMR}$  stacked spectra of PEG-Pt(IV) (top) and the unmodified PEG-NH<sub>2</sub> phospholipid (bottom) in D<sub>2</sub>O.

The TEM images of the hydrophobic IONPs prior to micelle preparation showed a mean particle size of 7.5 nm (**Figure 4.14 A**). The hydrophobic IONPs were coated with the PEG-Pt(IV) phospholipid by thin film hydration and purified by centrifugation. The IONP concentration in the IONP-Pt(IV) micelles was derived from a UV-vis calibration curve from an IONP micelle sample of known Fe concentration determined by inductively coupled plasma optical emission spectrometry (ICP-OES) followed by a conversion of Fe to IONP as described in the experimental section (**Figure 4.14 B**). The DLS characterisation of the IONP-Pt(IV) showed an average hydrodynamic diameter of 43 nm, good monodispersity with a PDI of below 0.3 and a negative zeta potential due to the carboxylate groups of the Pt(IV) prodrug (**Figure 4.14 C, D**).

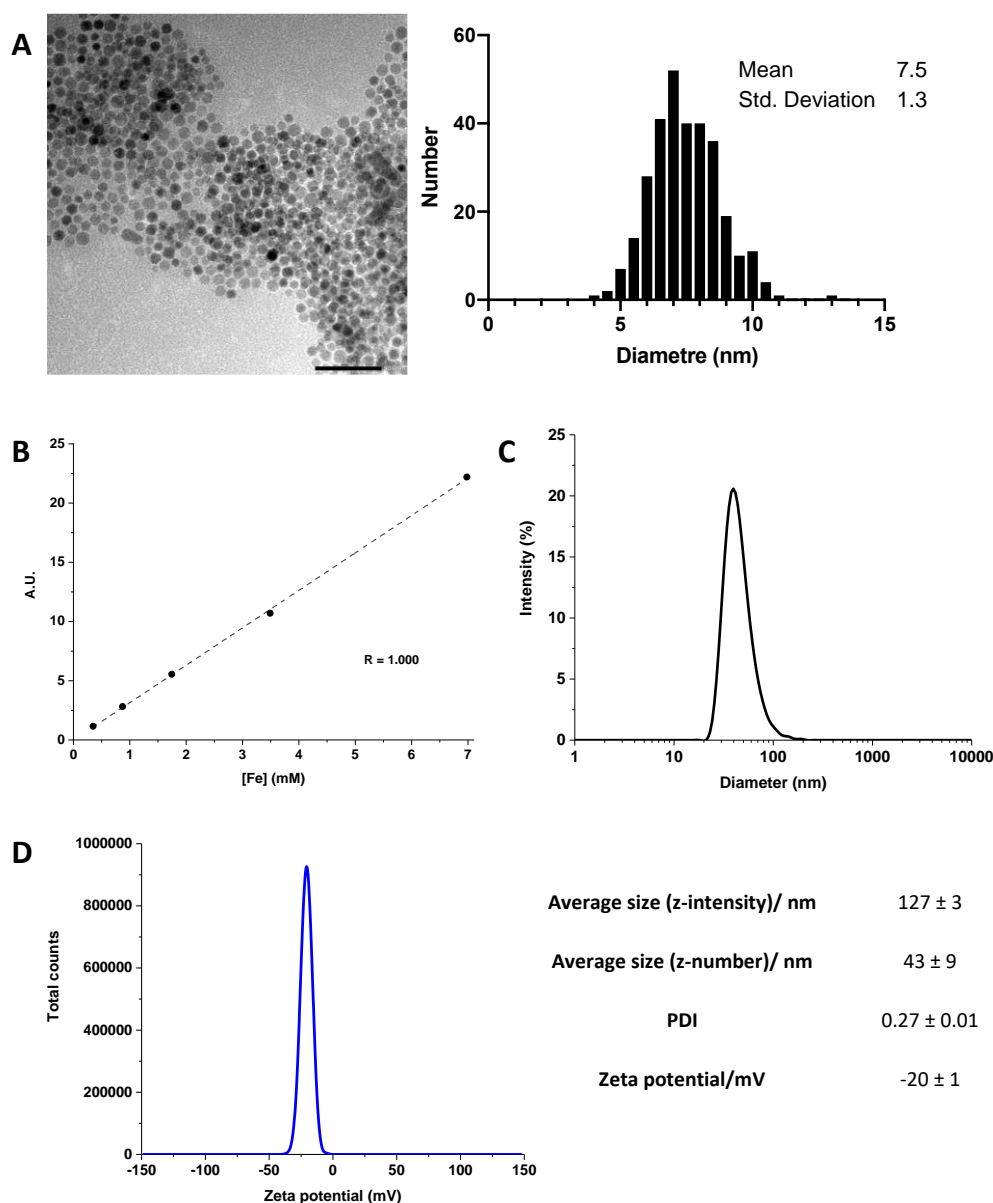


**Figure 4.14 Characterisation of IONP and IONP-Pt(IV).** (A) TEM image and size distribution of hydrophobic IONPs (scale bar: 50 nm). (B) UV-vis calibration of Fe concentration in IONP micelles ( $N = 1$ ). (C) DLS by number distribution and (D) zeta potential of IONP-Pt(IV) micelles (average of 3 measurements).

The Pt concentration on the NPs was assessed by a o-phenylenediamine (OPD) assay resulting in colorimetric detection of the OPD-Pt complex at 706 nm by UV-vis spectroscopy. OPD acts as a reducing agent by reducing the Pt(IV) prodrug to Pt(II) cisplatin, whilst the OPD itself is oxidised in the presence of oxygen. The resulting Pt(II) species forms a complex with excess OPD, which can be detected at an absorbance of 706 nm and results in the release of HCl (**Figure 4.15 A**). Cisplatin was used as the standard for the assay and a calibration curve was performed at Pt concentrations ranging from 0.0  $\mu\text{M}$  to 12.2  $\mu\text{M}$  (**Figure 4.15 B**). The Pt concentration obtained in the IONP-Pt(IV) sample corresponded to a Pt(IV):IONP mol ratio of

130:1 (**Figure 4.15 C**). The developed micellar IONP-Pt(IV) system was incorporated into an implantable HA-based device (Chapter 5) as a new strategy to achieve a gradual localised release and integrate chemo-immunotherapy properties.

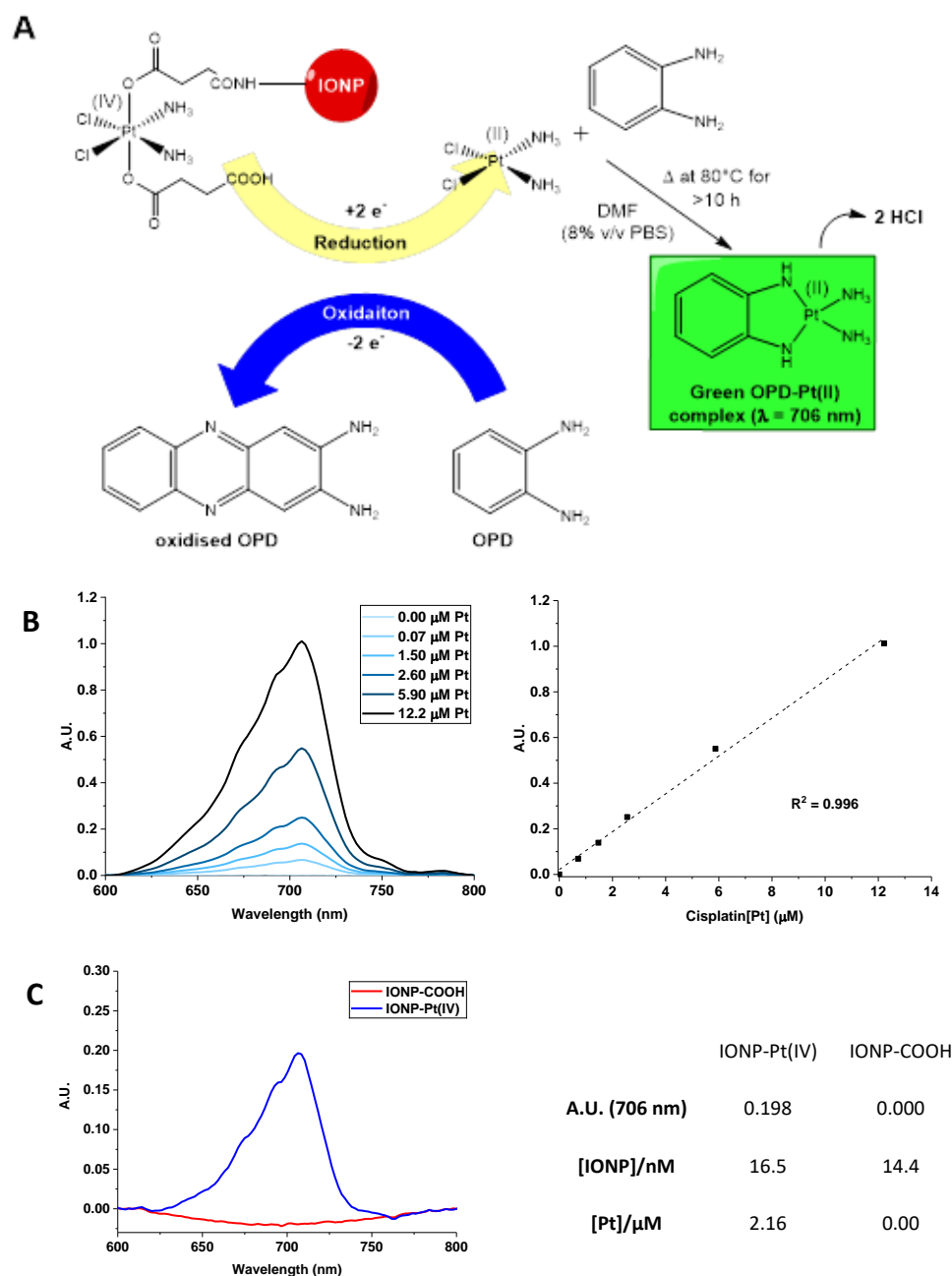


**Figure 4.15 Characterisation of IONP-Pt(IV) using an OPD assay.** (A) Schematic representation of OPD assay redox reaction involving the reduction of the Pt(IV) prodrug by OPD in the presence of oxygen, which itself is oxidised to form an OPD dimer. The Pt(II) forms a complex with the excess OPD that absorbs visible light at 706 nm and leads to the release of HCl. (B) Pt calibration of IONP(IV) using a OPD assay and cisplatin standards. The cisplatin calibration standards were analysed at concentrations of 0-12.2 μM [Pt] at 706 nm. UV-vis spectra of calibration points illustrated on the left with the calibration graph on the right. (C) UV-vis spectra of the IONP-Pt(IV) at [IONP] = 16.5 nM, IONP-COOH control at [IONP] = 14.4 nM and the 12.5 μM cisplatin calibration point for direct comparison (N =1).

### 4.2.3.2 Synthesis and characterisation of IONP-DOTAP-pIC

An immunostimulatory IONP system was developed in which the IONP-loaded micelles were functionalised with polyinosinic: polycytidylic acid (pIC). The hydrophilic IONP micelles were prepared by the thin film hydration method as previously described using a 2:1 (w/w) ratio of methoxy-terminal phospholipid and 1,2-dioleoyl-3-trimethylammonium-propane (DOTAP) followed by characterisation by DLS and zeta potential measurement. Additionally, the cationic IONP-DOTAP surface allows functionalisation with negatively charged therapeutic agents by electrostatic interaction. Due to its overall surface negative charge, pIC was attached to the DOTAP modified IONPs via electrostatic interactions. The pIC and IONP-DOTAP mixture were allowed to interact overnight followed by purification by ultracentrifugation to remove any unbound pIC (**Figure 4.16**).

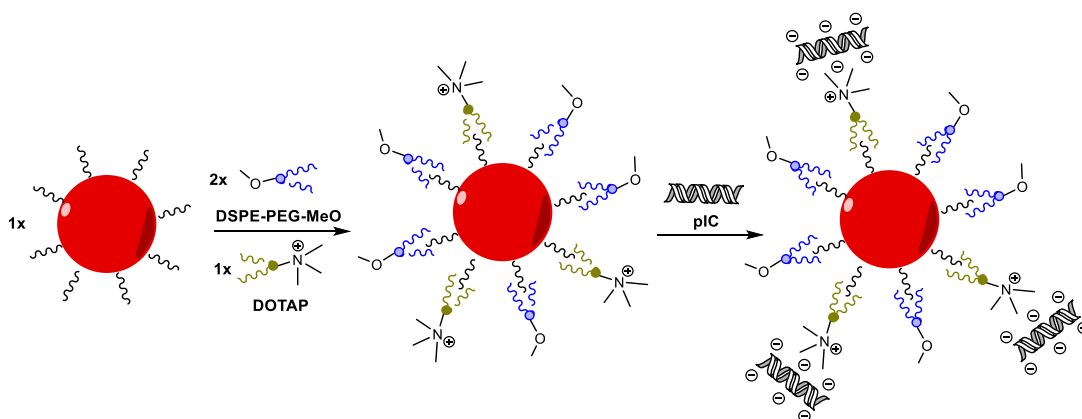
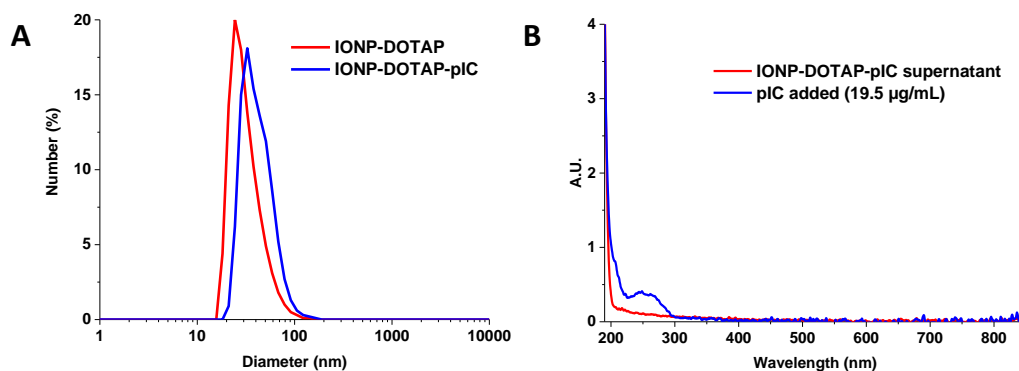


**Figure 4.16 Reaction scheme for IONP-pIC synthesis.** Hydrophilic IONPs prepared by the thin-film hydration method using IONP: DSPE-PEG-OMe: DOTAP weight ratios of 1:2:1. pIC was functionalised onto the IONPs by electrostatic interactions to produce the immunomodulatory IONP-DOTAP-pIC.

The average hydrodynamic size by DLS of the IONP-DOTAP micelles was  $\sim 33$  nm (**Figure 4.17 A**). The PDI of 0.23 corroborates a good monodispersity of the NPs, whilst the positive zeta of 9 mV potential confirms successful DOTAP surface coverage (**Appendix 5**). The DLS of IONP-DOTAP-pIC shows an increase in hydrodynamic diameter to 43 nm, which indicates the electrostatic attachment of pIC to the NPs (**Figure 4.17 A**). The UV-vis characterisation of IONP-DOTAP-pIC after purification by ultracentrifugation showed peaks at 245 and 260 nm. By calculating the absorbance ratio at 260 nm of pIC added to the NPs compared to the pIC remaining in the supernatant, the resulting functionalisation yield of pIC was 72.9 %. (**Figure 4.17 B**).





	IONP-DOTAP	IONP-DOTAP-pIC
Average size (z-intensity)/nm	116 ± 2	165 ± 5
Average size (z-number)/nm	33 ± 5	43 ± 13
PDI	0.23 ± 0.01	0.40 ± 0.03
Zeta potential/mV	9 ± 1	

**Figure 4.17 Characterisation of IONP-DOTAP and IONP-DOTAP-pIC by DLS.** (A) DLS by number distribution of IONP-DOTAP and IONP-DOTAP-pIC. (B) UV-vis characterisation of the supernatant of IONP-DOTAP-pIC after purification by ultracentrifugation to determine the % yield of pIC modification ( $N = 1$ ).

The immunostimulatory and direct cancer cell killing properties of pIC in combination with the adjuvant properties of DOTAP and IONPs offers the potential to induce synergistic therapeutic anticancer effects and provides an additional nano-construct for incorporation into the biomaterial-based transdermal or implantable devices discussed in Chapter 5, which are aimed at localised delivery of combination therapies as well as promoting sustained and localised vaccine release.

## 4.2.4 Development of an immunomodulatory biosilica-based scaffold

### 4.2.4.1 Intrinsic peroxidase-like activity of commercial diatoms

The diatoms used in this thesis were isolated from commercially available diatomaceous earth. The diatoms were purified to remove the organic matter from the silica-based frustules and the surface activation through the induction of silanol groups treatment with  $H_2SO_4$  and  $H_2O_2$ . The diatoms were characterised by SEM displaying predominantly elliptical shaped structures, with a mixture of structurally intact and smaller fractured frustule pieces throughout the sample ranging up to 11  $\mu m$  length and 4  $\mu m$  width (**Figure 4.18**). The pore diameters are in the nanoscale region ranging from 50 to 200 nm and the high porosity

suggests that this diatom species has a large surface area per volume ratio, which is ideal for surface modification.

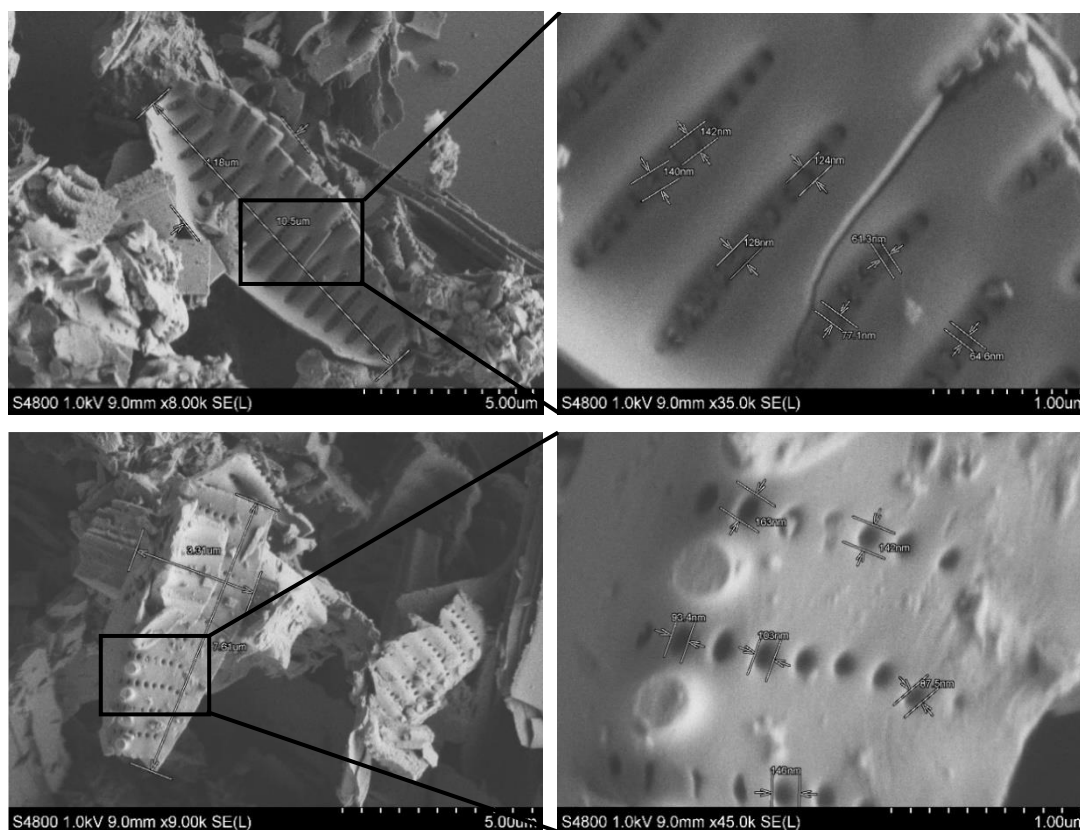


**Figure 4.18 SEM of purified commercial diatoms showing micron-sized elliptical structures and fragments with nano-sized pores.**

To determine whether these diatoms have an intrinsic peroxidase-like activity an assay was performed using TMB as the substrate, which oxidises in the presence of  $H_2O_2$  and the catalyst. Initially, the catalytic activity of the diatoms was assessed at different  $H_2O_2$  concentrations over time. Diatom samples were combined with different concentrations of  $H_2O_2$  ranging from 0.0 to 0.8 mM in sodium acetate buffer at pH 4.5, followed by addition of 0.83 mM TMB. The absorbance of the oxidised TMB species was analysed at 652 nm on a microplate reader over 30 min (**Figure 4.19 A, B**). An increase in catalytic activity was observed as the  $H_2O_2$  concentration was increased, confirming that the diatoms exhibit an intrinsic peroxidase-like activity. First a polynomial fitted calibration curve from 0.0 to 0.8 mM  $H_2O_2$  and then a linear calibration curve was derived, but the linearity was only preserved within the range of 0.0 to 0.2 mM (**Figure 4.19 C, D**). This may be due to increased adsorption of oxidised TMB onto the diatom surface through non-covalent interactions, which led a decrease in the absorbance values as the  $H_2O_2$  concentration was increased beyond 0.2 mM.

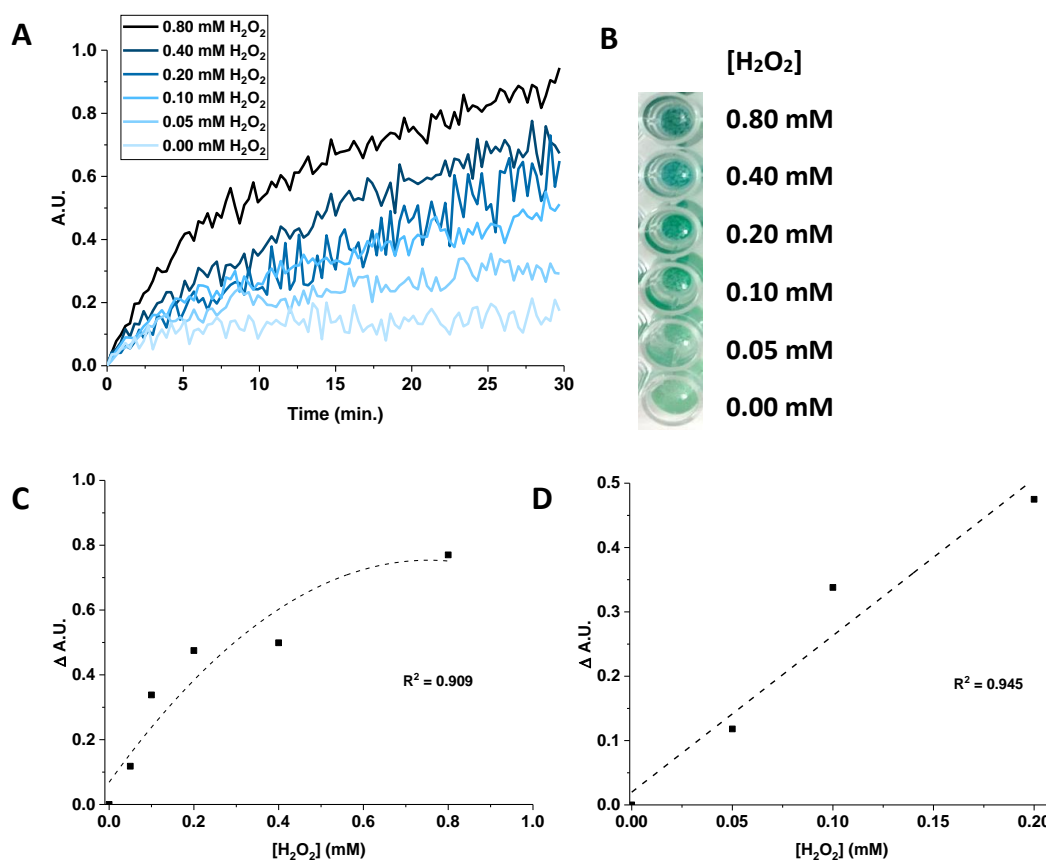


**Figure 4.19 Peroxidase-like activity assay of commercial diatoms at different H<sub>2</sub>O<sub>2</sub> concentrations.** (A) UV-vis spectrum of peroxidase-like activity assay using H<sub>2</sub>O<sub>2</sub> concentrations ranging from 0.0-0.8 mM and absorbance analysed at 652 nm over 30 min with measurements recorded at 18 s intervals. (B) Images of samples in a 96-well plate after the experiment was completed. (C) Calibration curve based on polynomial fit of diatom peroxidase-like activity at H<sub>2</sub>O<sub>2</sub> concentrations of 0-0.8 mM. (D) Linear calibration by exclusion of 0.8 mM and 0.4 mM H<sub>2</sub>O<sub>2</sub> data points ( $N = 1$ ).

#### 4.2.4.2 Diatom functionalisation with glucose oxidase

The hydrogen peroxide generation from the glucose oxidation catalysed by GOx in the presence of O<sub>2</sub> was analysed in the presence of the diatoms in tandem catalysis experiments. In these experiments an initial GOx-mediated catalytic reaction to produce H<sub>2</sub>O<sub>2</sub> from glucose oxidation is followed by the H<sub>2</sub>O<sub>2</sub>-mediated oxidation of TMB with the diatoms acting as the catalyst. The diatoms were suspended in acetate buffer pH 4.5 followed by addition of D-glucose (Glu) and GOx (D+Glu+GOx) at working concentrations of 0.2 mM and 46.5 nM, respectively. TMB was added to this mixture and the absorbance measured over 30 min. Several control samples were prepared including a diatom sample without Glu and GOx addition (D Glu alone (D+Glu), GOx alone (D-GOx), and diatoms, Glu and an excess of GOx (2.3 μM instead of 46.5 nM) (D+Glu+GOx (excess GOx)). To explore the substrate specificity in another control glucose was replaced with sucrose (D+Suc+GOx). The results

demonstrated the tandem catalytic activity of the D@GOx construct showing the ability to use glucose to oxidise TMB. Indeed, the D+Glu+GOx samples showed much ability to oxidise TMB compared to the controls (**Figure 4.20 A-D**).

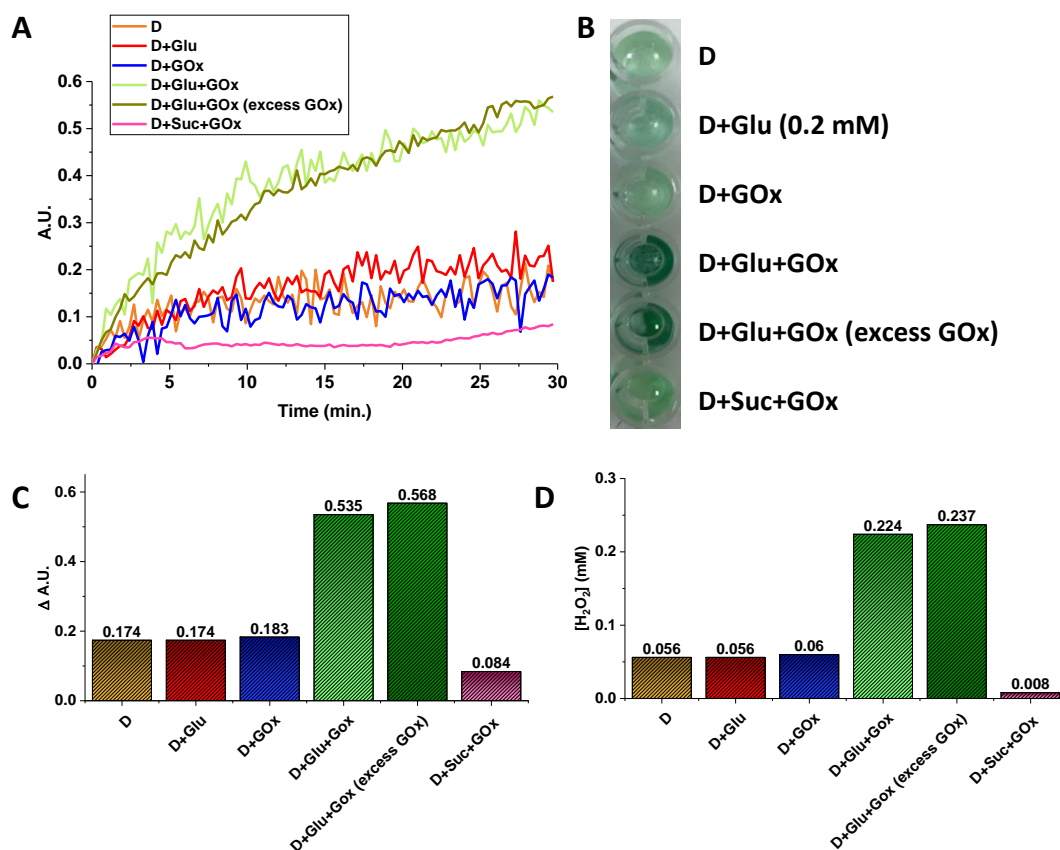
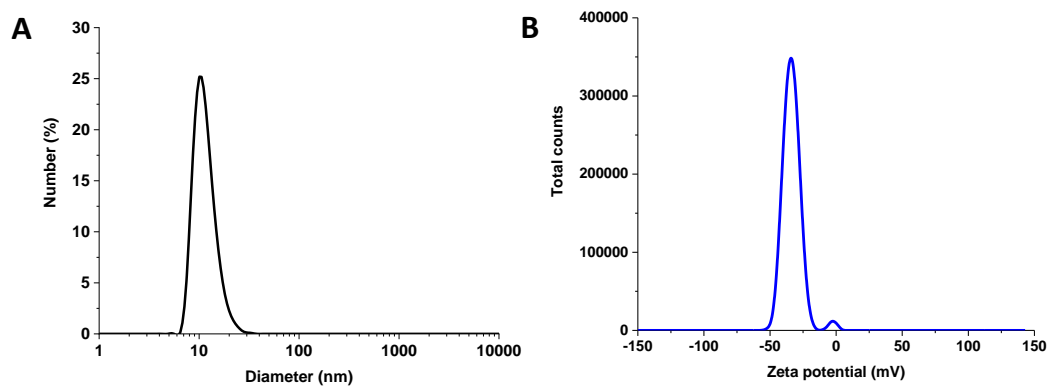


**Figure 4.20 Tandem catalysis-based peroxidase-like activity assay of diatoms in the presence of Glu and GOx and controls.** (A) UV-vis spectrum of peroxidase-like activity assay. All measurements were performed at an absorbance of 652 nm over 30 min. The excess GOx signifies a working concentration of 2.3  $\mu$ M instead of 46.5 nM. (B) Images of the samples after experiment completion in a 96-well plate. Summary of the catalytic activity of the sample and controls based on (C)  $\Delta$  A.U. (D) H<sub>2</sub>O<sub>2</sub> calibration. D-Diatoms, Glu-glucose, GOx-glucose oxidase, Suc-sucrose ( $N = 1$ ).

#### 4.2.4.3 Diatom functionalisation with IONPs

Next, we explored if the catalytic activity of the diatoms could be further enhanced by co-functionalisation with IONPs. The high surface area of the porous diatom structure ensures a high loading capacity and localised catalytic activity. Citrate modified IONP micelles were prepared using a microemulsion method and then characterised by DLS. The micelles had a homogeneous average particle size of  $\sim 12$  nm and zeta potential of -34 mV due to the presence of citrate anions on the IONP surface (**Figure 4.21**).



Average size (z-intensity)/nm	32 ± 2
Average size (z-number)/nm	12 ± 0
PDI	0.47 ± 0.02
Zeta potential/mV	-34 ± 0

**Figure 4.21** Characterisation of IONP-citrate micelles by DLS and zeta potential. (A) DLS and (B) zeta potential of IONP-citrate micelles in MilliQ water (average of 3 measurements).

To promote electrostatic interaction of the anionic IONPs with the diatoms, the diatoms were first modified with the cationic polymer, PEI, through chemisorption, facilitated by the deprotonated silanol groups at the surface of the diatoms at neutral pH. The cationic surface charge of the resulting diatom construct then enabled the surface modification with the citrate coated-IONPs through electrostatic interactions. The magnetic properties of the resulting D-IONP system were visually observed when placed near a magnet resulting in displacement of the pellet (**Figure 4.22 A**). The D-IONP was characterised by SEM and energy dispersive X-ray spectroscopy (EDX) to analyse its morphological features and the presence of Fe, respectively. IONPs of sizes larger than 30 nm can be visualised on the diatom surface by SEM (**Figure 4.22 B**). Images at high magnification became distorted at the required accelerating voltage due to surface charging, therefore, lower magnification images were required for EDX characterisation. The EDX spectrum of the D-IONP show the peaks associated with diatom elements, namely, Si and O (**Figure 4.22 C**) and contained the peaks arising from Fe L $\alpha$  and K $\alpha$  electron transitions with energies of 0.705 keV and 6.398 keV, respectively. As a control, an unmodified diatom sample was characterised under the same conditions (**Figure 4.22 D**). The visual charging in the EDX image of the D-IONP sample, seen as the white light reflection in certain areas, is an additional indication of successful IONP modification to the diatoms.

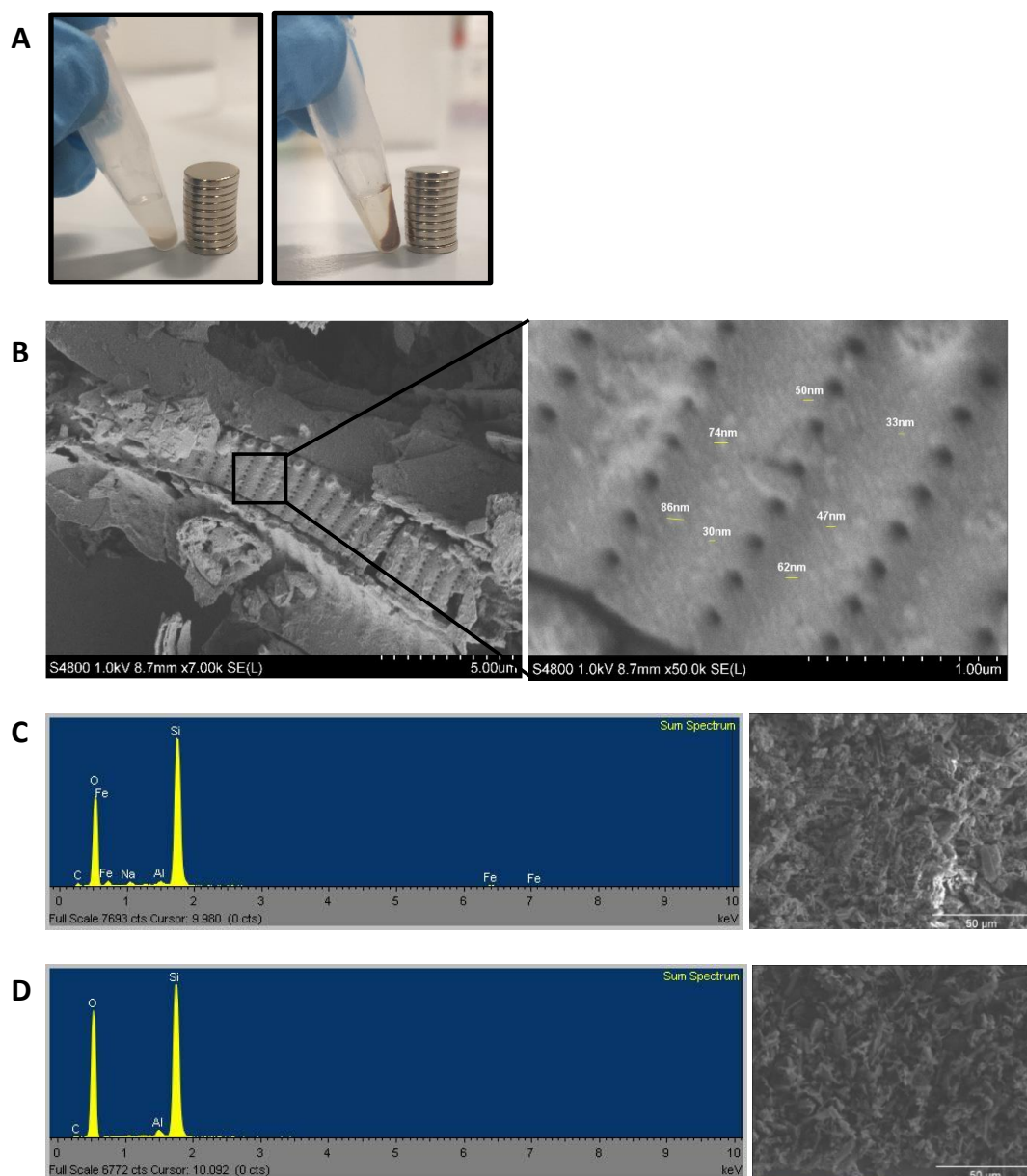


**Figure 4.22 Characterisation of IONP functionalised diatoms by SEM-EDX.** (A) Images showing magnetic properties of D-IONP (right) compared to an unmodified diatom sample (left). (B) SEM images of D-IONP at low and high magnification. EDX spectra and corresponding SEM images of the (C) D-IONP and (D) unmodified diatom sample as a control.

GOx has an isoelectric point of 4.2, implying that it carries a net negative charge at neutral pH. The cationic PEI modified diatoms enabled the capture of both IONPs and GOx via electrostatic interactions to form a multifunctional D-IONP-GOx complex. The peroxidase-like activity assay was performed to evaluate the catalytic activity of the IONP-GOx-loaded diatoms in the presence of 0.2 mM Glu (**Figure 4.23 A-D**). As controls the diatoms were analysed in the absence of IONP and GOx (D), diatoms functionalised only with IONP (D-IONP), D-IONP-GOx with an excess of GOx (2.3  $\mu$ M instead of 46.5 nM) (D-IONP-GOx (excess

GOx)) and a D-IONP sample with 0.2 mM H<sub>2</sub>O<sub>2</sub> (D-IONP + H<sub>2</sub>O<sub>2</sub>). The peroxidase-like activity was higher for the D-IONP + H<sub>2</sub>O<sub>2</sub> compared to the D without IONP even at higher H<sub>2</sub>O<sub>2</sub> concentrations (**Figure 4.19**), which demonstrates the enhanced peroxidase activity achieved with the IONP surface modification. The D-IONP-GOx sample again shows the ability to oxidase TMB in the presence of glucose (**Figure 4.23 D**). However, the activity of the D-IONP-GOx is lower than D-IONP+H<sub>2</sub>O<sub>2</sub> and lower than D-GOx (**Figure 4.20**). Most likely this is because both IONP and GOx are anionic and therefore are in competition with each other for the PEI-modified diatom surface. Since the IONP greatly enhances the peroxidase activity of the system, adding excess GOx (to enhance the conversion of glucose to H<sub>2</sub>O<sub>2</sub> and gluconic acid) can displace some of the IONP making the D-IONP-GOx system less effective at the tandem catalytic reaction as it loses some of the peroxidase activity provided by the IONP. Nevertheless, the D-IONP-GOx sample undergoing the desired tandem catalysis shows a favourable catalytic performance compared to all the other controls.

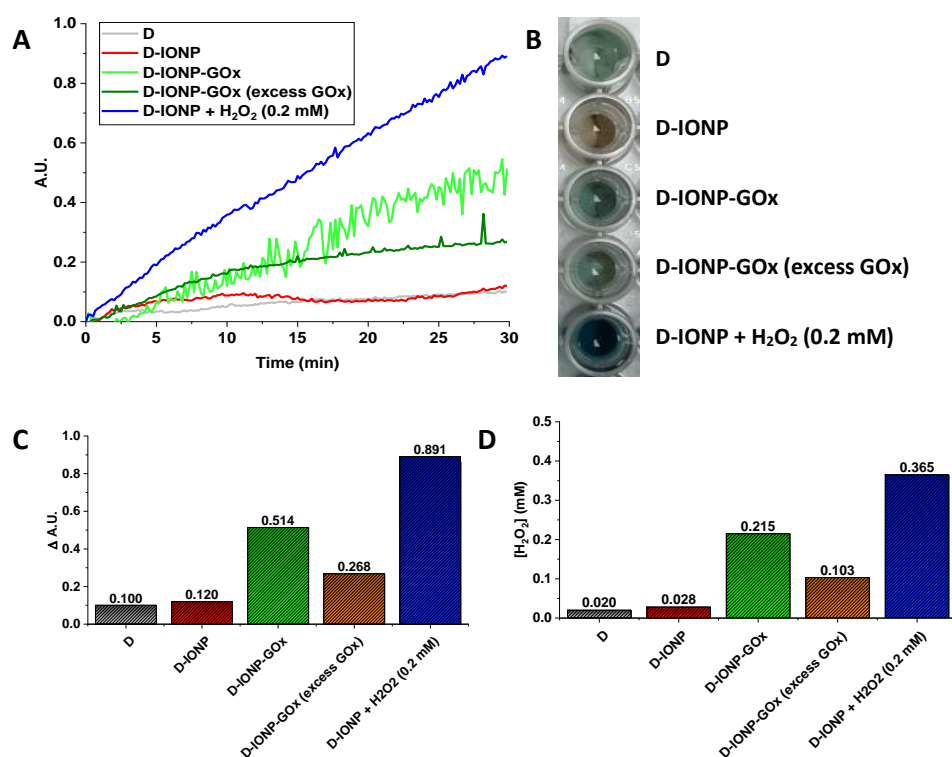


**Figure 4.23** Peroxidase-like activity assay of diatoms modified with IONPs and GOx (D-IONP-GOx) and control samples. (A) Spectrophotometric analysis of catalytic activity over 30 min at 652 nm. (B) Image of diatom sample and controls after experiment completion. (C) Summary of the catalytic activity represented as absorbance difference and (D) in terms of mM H<sub>2</sub>O<sub>2</sub> generated (N = 1).

## 4.2.5 Development of a diatom-based biosensor

### 4.2.5.1 Synthesis and characterisation of anti-PD-L1 functionalised diatoms

As a proof of concept, the commercial biosilica diatoms were modified with the ligand of the immune checkpoint inhibitor, anti-PD-L1, to develop a PD-L1-specific biosensing and immunotherapeutic diatom-based construct. The first stage of development involved the covalent functionalisation of the diatoms with the anti-PD-L1 antibody in a multistep surface modification process (**Figure 4.24**) in which each reaction product was characterised by X-ray photoelectron spectroscopy (XPS).

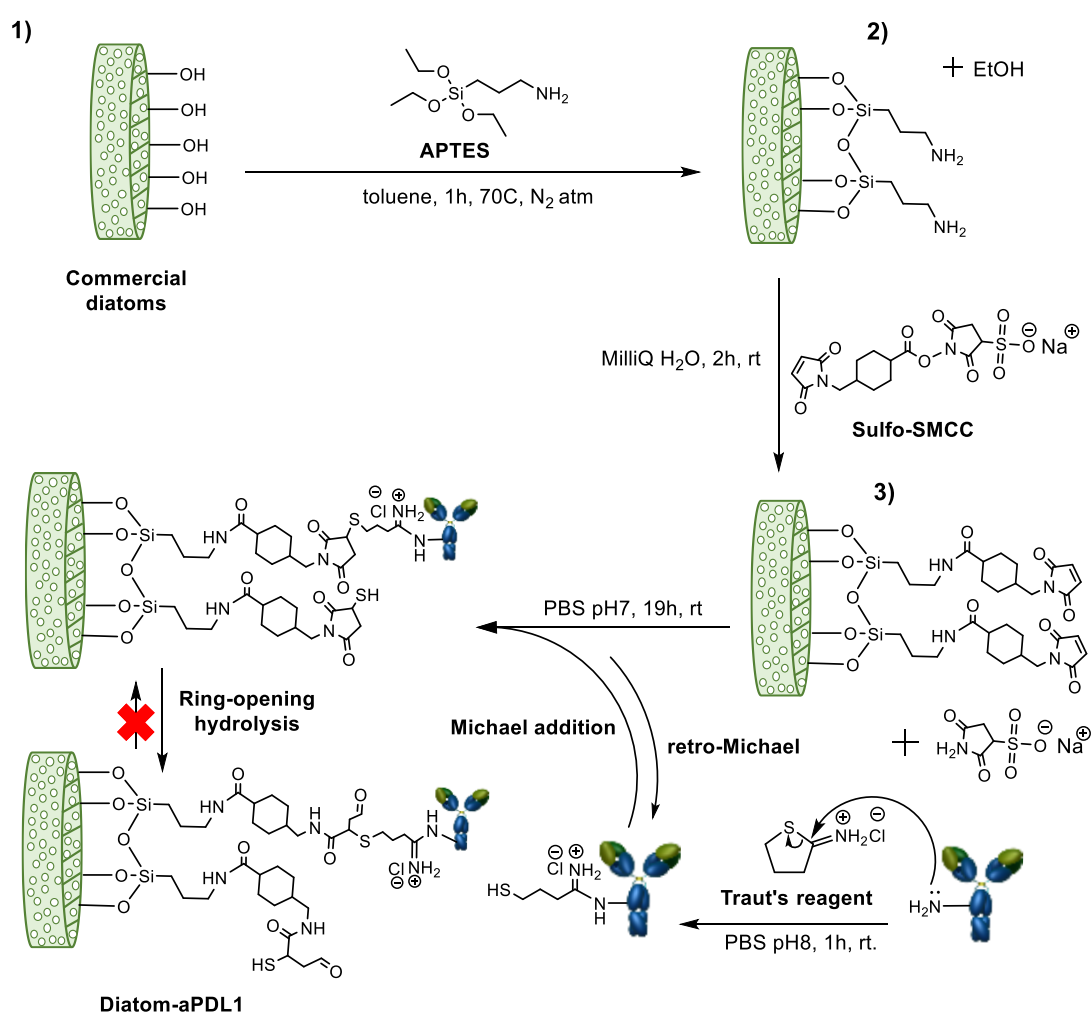


**Figure 4.24** Reaction scheme for the multistep synthesis of Diatom-anti-PD-L1 (D-aPDL1) as a sensing device for PD-L1. 1) Diatom functionalised with APTES to obtain amine terminal groups; 2) D-amine was then functionalised with Sulfo-SMCC to produce D-maleimide; 3) D-maleimide was modified with activated Ab molecules through thioether bond formation to afford D-aPDL1.



Initially the diatoms were functionalised with APTES by a condensation reaction in toluene under an inert atmosphere at 70°C resulting in a terminal amine functionality (**Figure 4.24 step 1**). The characteristic XPS peaks for the N 1s electron binding energy of the amine can be observed with the deprotonated amine appearing at 399 eV and the protonated counterpart at slightly higher binding energy of 401 eV (**Figure 4.25**). These peaks are absent in the unmodified diatom (D-unmodified) sample.

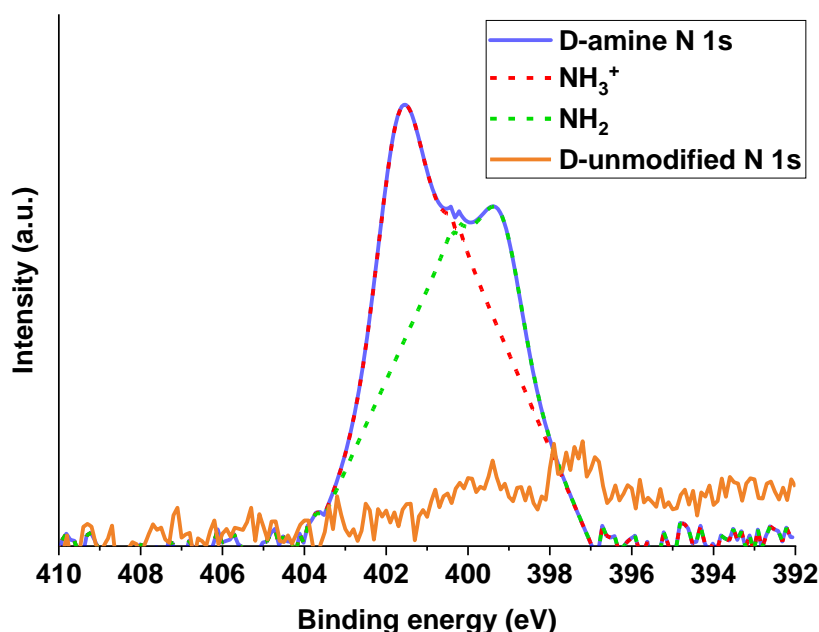


**Figure 4.25** Overlay of XPS spectra of at D-amine and D-unmodified comparing the N 1s binding energy.

The amine functionalised diatoms were further modified via amide bond coupling to the sulfo-SMCC crosslinking agent to generate a terminal maleimide group on the diatom surface (**Figure 4.24 step 2**). The diatom-maleimide product was purified by centrifugation cycles in MilliQ water in order to remove any unreacted or hydrolysed sulfo-SMCC. The C 1s XPS spectrum for the D-maleimide shows additional peak components due to alteration in the electron binding properties of the carbon atoms on account of the introduced maleimide group at 289 eV (**Figure 4.26**). The C 1s peak at 286 eV could be attributed to the amide bond carbon but is not clearly distinguishable from the signal corresponding to the C-O bond. Comparatively, the D-amine C 1s spectrum shows peaks for C-C and C-O bonding present in the APTES unit.

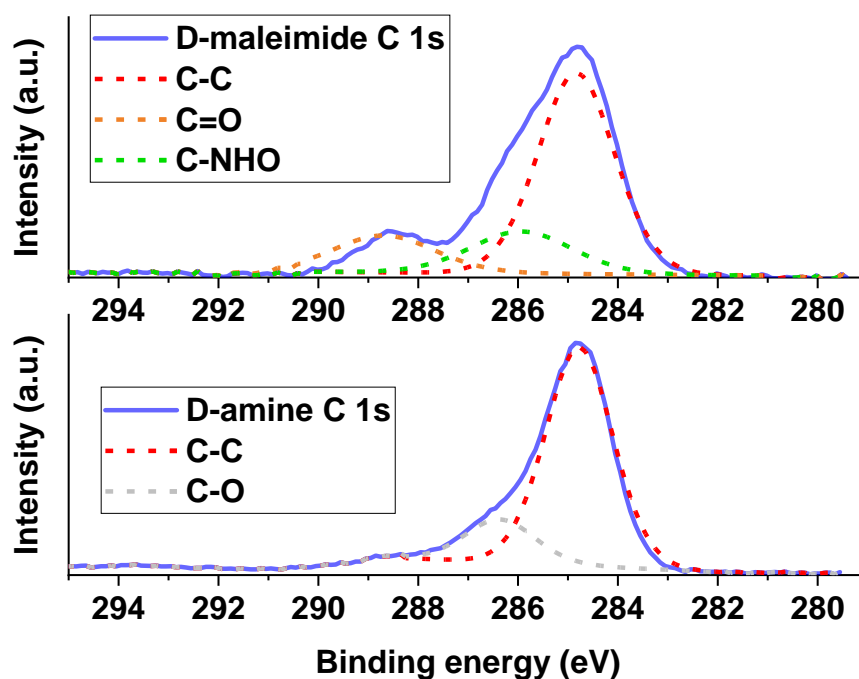


**Figure 4.26** XPS spectra of D-maleimide (top) and D-amine (bottom) comparing the C 1s binding energy.

The reactivity of the maleimide group towards sulfhydryl groups was utilised to conjugate the anti-PD-L1 antibody. To activate the antibody, Traut's reagent (2-iminothiolane) was used to convert lysine groups containing terminal amines into thiol groups without the need for harsh modification methods that could compromise the structural integrity of the antibody. This was achieved using a 10-fold mol excess of Traut's reagent to anti-PD-L1 and allowed to react for 1 h at rt in PBS. The nucleophilic thiol groups on the anti-PD-L1 were covalently attached to the maleimide functionalised diatoms via Michael addition to form thiosuccinimide groups. The hydrolysis of the ring forms a stable succinamic acid thioethers preventing retro-Michael reaction (**Figure 4.24 step 3**). Characterisation of the resulting D-anti-PD-L1 by XPS showed that the C 1s spectrum differs from the one observed for D-maleimide with a higher intensity C=O peak at 288 eV, potentially due to the amide bonding in the amino acid constituents of the antibody (**Figure 4.27**). The additional peaks at 285-286 eV are likely attributed to the carbon atoms adjacent to the thiol and amine groups from cysteine and lysine residues, respectively. A BCA protein quantification assay was used to determine the concentration of antibody that was covalently bound to the diatoms. This protein quantification test involves the reduction of  $\text{Cu}^{2+}$  to  $\text{Cu}^+$  promoted by peptide bonds from amino acid residues and other moieties found in proteins. The  $\text{Cu}^+$  species forms a blue organometallic complex with 2 molecules of BCA that has an absorbance at 550 nm and can be quantified by UV-vis spectroscopy. The BCA assay determined an anti-PD-L1

functionalisation yield of 47.6%, corresponding to a diatom:anti-PD-L1 ratio of  $1:5 \times 10^{-5}$  (wt/wt) (**Appendix 6**). Overlaid and wide XPS spectra of intermediate diatom modification products and D-anti-PD-L1 are included in the appendix (**Appendix 7 and 8**)

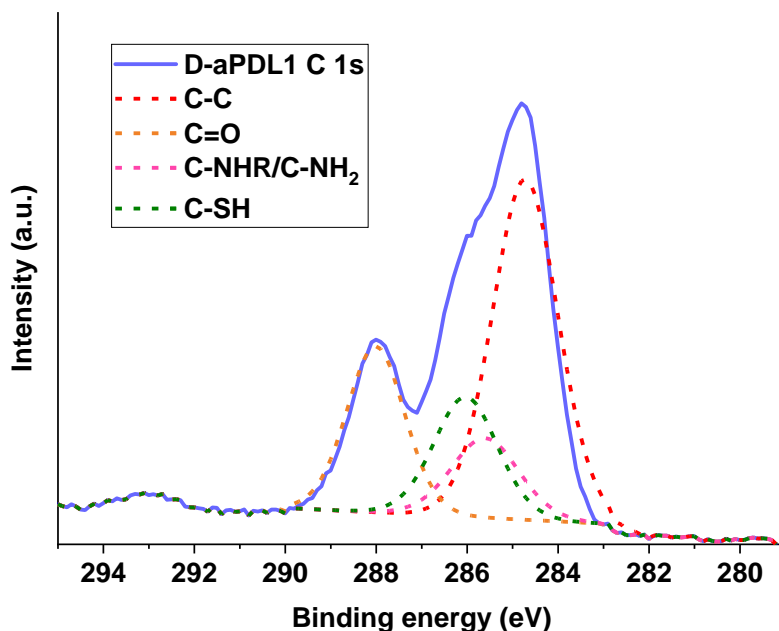


**Figure 4.27** XPS spectrum of D-aPD-L1 analysing the C 1s binding energy.

#### **4.2.5.2 Synthesis and functional activity of anti-PD-L1 modified IONPs**

Anti-PD-L1 functionalised SPIONs were chosen as the detecting element of the biosensor due to their intrinsic catalytic activity. The hydrophilic IONP micelles were prepared with a maleimide-terminal phospholipid coating as previously described, followed by conjugation to the activated anti-PD-L1 using Traut's reagent (**Figure 4.28**).

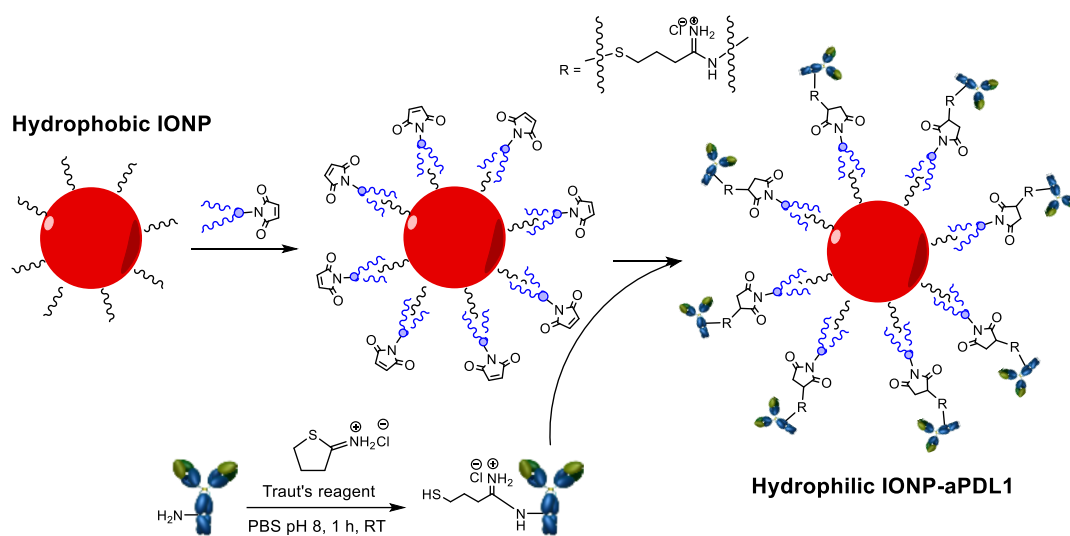
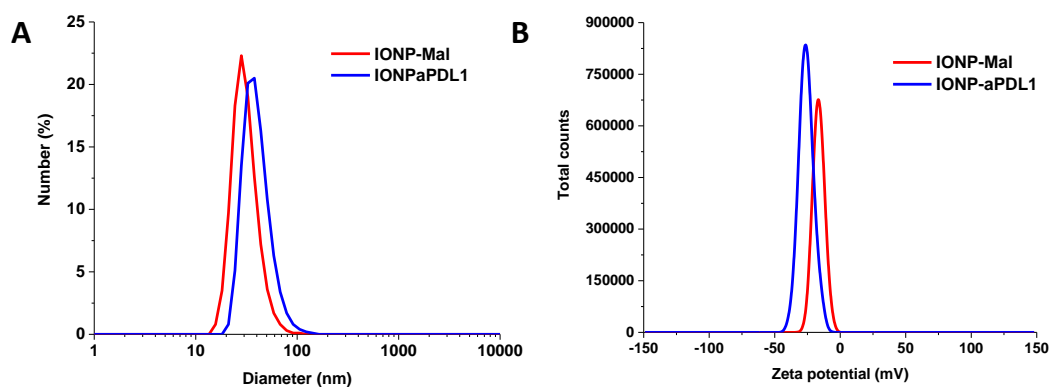


**Figure 4.28** Reaction scheme for the covalent functionalisation of IONP with anti-PD-L1. The antibody was first modified using Traut's reagent to obtain thiol-terminal groups. Hydrophobic IONPs were coated with the maleimide-terminal phospholipid to afford water soluble micelles followed by functionalisation to the anti-PD-L1 (IONP-aPDL1).

The IONP-maleimide (IONP-Mal) and IONP-aPDL1 were synthesised and characterised by DLS, zeta potential, UV-vis, and BCA protein assay. The DLS of the IONP-Mal showed a homogenous size distribution with an average particle diameter of 32 nm by number distribution, while the zeta potential average was -14.6 mV, due to the slightly negative charge of the maleimide terminal phospholipid (**Figure 4.29 A, B**). After functionalisation of the IONPs with the activated anti-PD-L1 the average diameter increased to 41 nm and the zeta potential decreased to -25 mV, potentially due to the predominantly negatively charged amino acid residues on the immunoglobulin surface. A BCA assay was performed to quantify the covalent functionalisation of anti-PD-L1 to the IONPs and determined a modification yield of 29.1%, which corresponds to an anti-PD-L1 to IONP mol ratio of 3.9 (**Appendix 6**).



	IONP-Mal	IONP-aPDL1
Average size (z-intensity)/nm	92 ± 1	94 ± 1
Average size (z-number)/nm	32 ± 4	41 ± 5
PDI	0.38 ± 0.00	0.23 ± 0.01
Zeta potential/mV	-15 ± 0	-25 ± 0

**Figure 4.29 Characterisation of IONP-Mal and IONP-aPDL1.** (A) DLS by number distribution and (B) zeta potential in MilliQ water (average of 3 measurements).

The functional activity of the IONP-aPDL1 was characterised using a PD-L1 ELISA, in which the IONP-Mal was used as the control system. The assay protocol was followed according to the manufacturer using 2 standard concentrations of 80 pg/mL and 0 pg/mL PD-L1. The IONP-aPDL1 micelles were added at the same time as the PD-L1 ligand, which competed with the capture antibody for interaction with the ligand. The removal of the supernatant containing IONP-aPDL1 bound PD-L1 resulted in a reduced absorbance at 450 nm due to the lower concentration of PD-L1 in those wells, which demonstrated that the IONP-aPDL1 immunomodulatory system is functionally active. As a control, IONP-Mal was analysed under the same experimental conditions showing no reduction in the PD-L1 concentration, as expected (**Figure 4.30 A-C**).

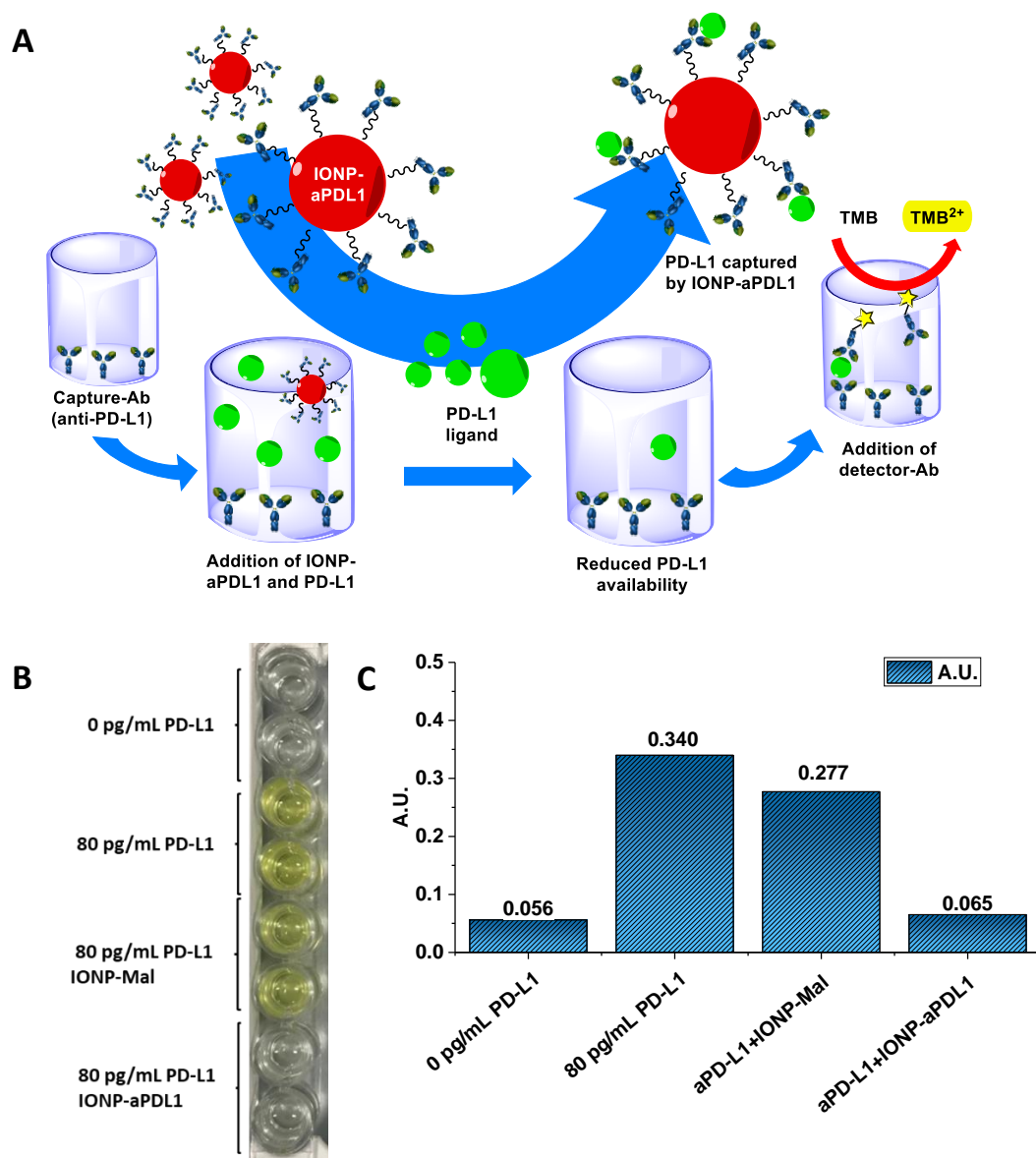


**Figure 4.30 Functional PD-L1 ELISA of IONP-aPDL1.** (A) IONP-aPDL1 and PD-L1 ligand are added to the wells containing the capture antibody. The ligand bound to the IONP-aPDL1 remains in the supernatant and is removed during the washing step resulting in reduced absorbance. (B) Image of ELISA plate after assay completion showing lack of colour in the wells in which IONP-aPDL1 was added, whereas the IONP-Mal control sample is comparable to the 80 pg/mL PD-L1 standard. (C) Characterisation by visible light absorbance at 450 nm on a microplate reader confirmed the reduced absorbance of the IONP-aPDL1 containing wells, which indicates the retention of the functional activity of the anti-PD-L1 after covalent attachment to IONPs (N = 1).

#### 4.2.5.3 Methodology and functional evaluation of D-antiPD-L1 biosensor

The D-anti-PD-L1 sensor capability of capturing PD-L1 through antibody-ligand binding was evaluated by measuring peroxidase-like activity of the anti-PD-L1 functionalised SPIONs

following incubation with D-PD-L1. The diatom-bound anti-PD-L1 was combined with its ligand, human recombinant PD-L1, in MilliQ water at a 50:1 mol ratio and the resulting D-PD-L1 was purified from unbound PD-L1 protein by centrifugation. The IONP-aPDL1 were added to the D-PD-L1 at a mol ratio of 1:56 and incubated for 1 h, after which the suspension was centrifuged, and the supernatant collected to perform a peroxidase-like activity assay (**Figure 4.31**).

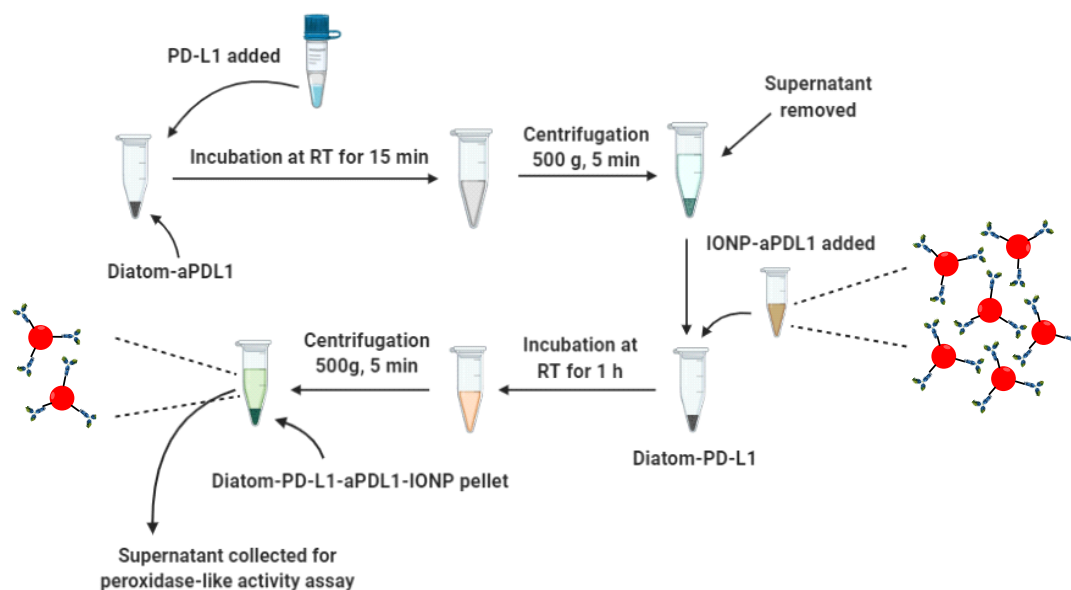


**Figure 4.31** Developed method for biosilica-based PD-L1 sensor. D-aPDL1 was incubated with the PD-L1 ligand at RT followed by addition of IONP-aPDL1 and further incubation at RT for 1 h to ensure complete interaction between the Ab functionalised IONPs and the D-PDL1 sensor. After pelleting by centrifugation, the supernatant containing the remaining IONP-aPDL1 was removed and an indirect peroxidase-like activity assay was performed.

The working concentrations in the peroxidase assay were 0.5 mM Fe (IONP-aPDL1), 30 mM H<sub>2</sub>O<sub>2</sub>, 0.832 mM TMB in 0.1 M sodium acetate buffer pH 4.5 in a total volume of 10  $\mu$ L. The absorbance was measured at 652 nm by UV-vis immediately after addition of TMB and after the incubation period of 1 h whilst protected from light (**Figure 4.32**). The absorbance difference is proportional to the degree of catalytic activity of the IONPs as a result of TMB oxidation, which is also reflected in the blue colour change of the solution. As a control, the aPDL1-IONPs were incubated with D-aPDL1 in the absence of the ligand and the supernatant analysed under the same reaction conditions.

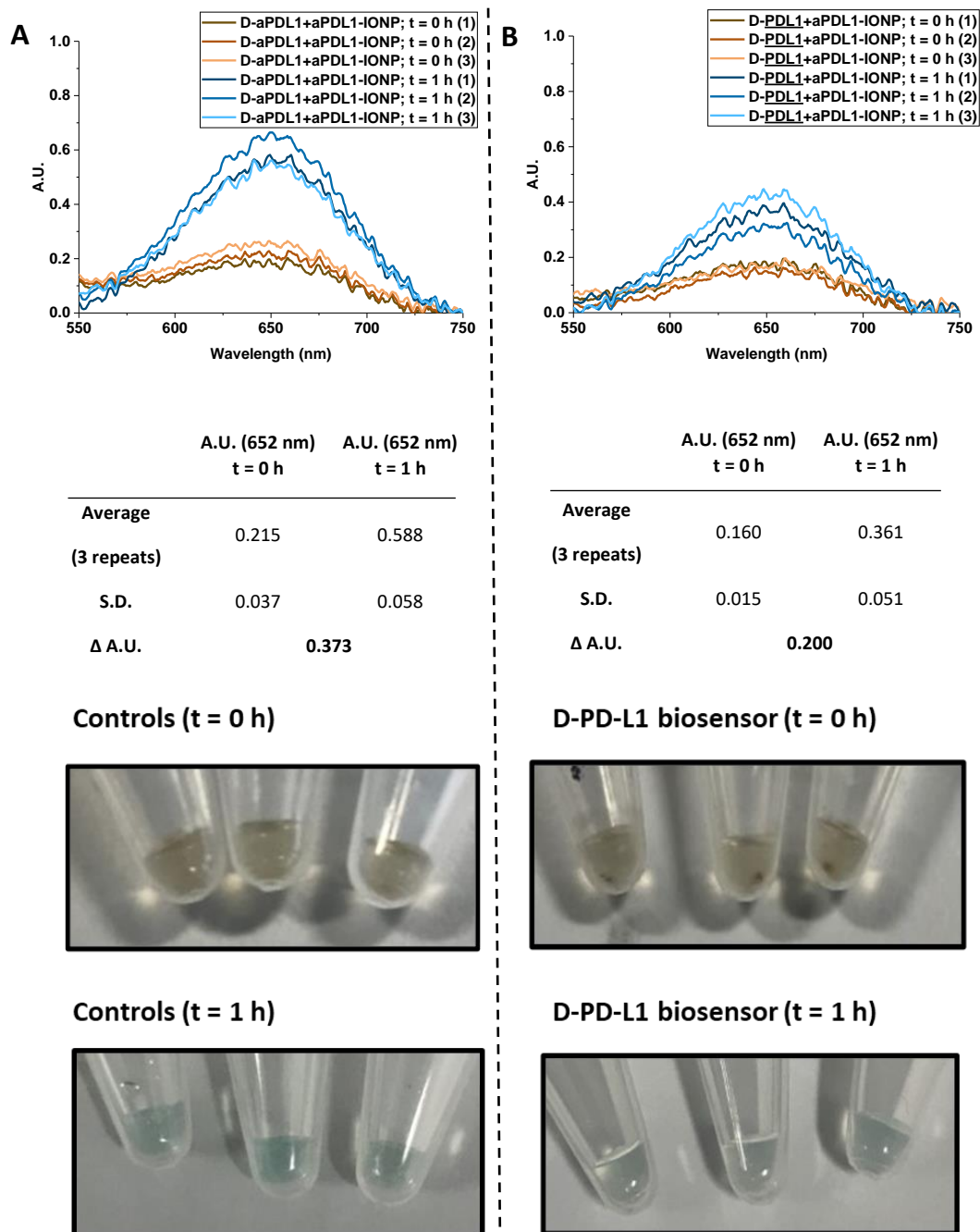


**Figure 4.32 Peroxidase-like activity assay of the biosilica-based PD-L1 sensor.** (A) Peroxidase-like activity assay of the control sample in the absence of PD-L1 and (B) D-PD-L1 biosensor. IONP-aPDL1 supernatants were incubated with TMB for 1 h in acetate buffer pH 4.5 and the peroxidase-like activity measured by UV-vis spectroscopy based on the absorbance difference between  $t = 0$  and 1 h at 652 nm. D-PD-L1 biosensor at  $t = 0$  h shows red pellet formation, indicating that IONPs have bound to the diatoms. The reduced absorbance difference ( $\Delta$ A.U.) for the biosensor compared to the control is the result of IONP binding to the diatom pellet through specific Ab-ligand interaction ( $N = 1$ ).

The reduction in the peroxidase-like activity for the aPDL1-IONPs after incubation with the D-PD-L1 compared to the control demonstrated that the diatom sensor has captured some of the NPs leading to a reduced SPIONs concentration in the peroxidase-like activity reaction



**(Figure 4.32 A, B).** The lower catalytic activity is only faintly visible in the image, where the blue colour intensity was slightly less strongly manifested in the D-PD-L1 biosensor sample compared to the control. The presence of a visible red pellet formation in the sample prior to the peroxidase-like activity assay is a further indication that IONPs have bound to the diatoms. These studies demonstrated the synthesis and characterisation of a commercial diatom biosensor using the immune checkpoint PD-L1 as a model biomolecule. While this work only provided a qualitative demonstration of the biosensor, it has the potential for further development for quantitative analysis of the biomolecule requiring only small sample volumes and avoids the need for a costly kit.

## 4.3 Discussion

The amphiphilic 1MT-HA biomaterial prepared in the Chapter 3 introduced the possibility for the self-assembly into NPs with immunomodulatory properties. The polymersome-like NP self-assembly was achieved by 1MT-HA suspension in a mixture of an aqueous and organic solution with the HA interacting with the aqueous core and external medium, while the 1MT component aligns in between the inner and outer phase to form a bilayer that constitutes the vesicle membrane.<sup>368</sup>

The 1MT-HA NPs had an average hydrodynamic size of 356 nm and zeta potential of -38 mV (**Figure 4.6**), which compares to literature values with degree of HA substitution in the range of 6-8%.<sup>406,407</sup> Notably, lower HA NPs sizes have been reported in which a higher degree of HA substitution was achieved using either non-therapeutic hydrophobic molecules or therapeutic agents constituting the hydrophobic block such as DOX or the photosensitiser chlorin e6.<sup>408-410</sup> However, even at larger sizes the HA NPs have demonstrated successful receptor-mediated endocytosis in CD44 overexpressing cancer types *in vitro* and *in vivo* tumour targeting in a murine model.<sup>406</sup>

The aqueous NP core permitted the incorporation of the clinically used immune checkpoint inhibitor, anti-PD-L1. A weight ratio of 10:1 1MT-HA: anti-PD-L1 was chosen based on a method reported by Ye *et al.* in which HA NPs were incorporated with a different immune checkpoint inhibitor, anti-PD-1.<sup>254</sup> The complete encapsulation of anti-PD-L1 observed in this thesis (**Figure 4.7**) could be due to the larger size of these particles leading to a higher core capacity and indicates that encapsulation of higher doses of the immune checkpoint inhibitor could be explored in the future research. The incorporation of anti-PD-L1 into the 1MT-HA NPs was additionally characterised by FPLC (**Figure 4.8**). The anti-PD-L1 peak observed at 16 mL retention volume at 225 nm UV detection wavelength correlates with the typical absorption wavelength of proteins and is due to  $\pi$  to  $\pi^*$  transitions in the peptide linkages of the antibody, while additional absorption peaks between 230-300 nm may be observed due to aromatic side chains and disulfide bonds.<sup>411</sup> The 1MT-HA absorbance at 225 nm is also in accordance with literature values for low MW HA, while the peak observed at 280 nm is predominantly due to the absorbance of 1MT.<sup>412,413</sup> The peak shift of the anti-PDL-1 peak in the 1MT-HA@anti-PD-L1 NPs indicates that the antibody has been successfully incorporated. This study also demonstrated that the presence of 1MT in the polymer is crucial for achieving NP self-assembly and encapsulation of anti-PD-L1.

The release of the immunomodulatory agents 1MT and anti-PD-L1 from the NPs was performed at pH 6.5, which is typical of the TME, in the presence of HAase over 48 h. The slow 1MT release is consistent with the release observed from the 1MT-HA biomaterial in Chapter 3 due to the slow hydrolytic cleavage of the amide bond at these conditions (**Figure 4.9**). The anti-PD-L1 release from the NPs was assessed qualitatively by FPLC and showed a gradual release over 48 h (**Figure 4.10**). This NP system can overcome some of the main challenges cancer drug development by ensuring a localised and sustained immunostimulatory response and has potential as a drug delivery vehicle for immunotherapy or combination therapies.

A chemotherapeutic Pt(IV) prodrug with immunostimulatory properties was synthesised and then attached IONP micelles using a thin-film hydration method. The TEM images of the hydrophobic IONPs prior to micelle preparation showed a mean particle size of 7.5 nm, which increases to 44 nm upon micelle formation by coating with the Pt(IV) prodrug bound phospholipid is consistent with literature values (**Figure 4.14**).<sup>166,414</sup> Ma *et al.* developed a siRNA and Pt(IV) prodrug loaded NP system consisting of a self-assembled protamine/HA nanocarrier coated with polyglutamic acid onto which the Pt(IV) prodrug was bound covalently forming acid labile ester bonds.<sup>415</sup> The Pt(IV) loaded NPs demonstrated intracellular release of siRNA and reduction of Pt(IV) to the active Pt(II) species leading to an enhanced therapeutic effect compared to individual administration of these agents in a Pt-resistant lung cancer model. The loading of a Pt(IV) prodrug into polymer-based NPs has also been previously demonstrated by Dhar *et al.*<sup>416</sup> This nanocarrier consisted of a biodegradable PLGA-PEG micelle system incorporated with the Pt(IV) prodrug through a nanoprecipitation method. The NPs were surface functionalised with an prostate-specific membrane antigen aptamer to enable prostate cancer cell-specific delivery of the Pt(IV) prodrug. The innovative Pt(IV) prodrug functionalised IONP system developed in this thesis has potential to improve the therapeutic outcome in Pt-resistance cancers though the synergistic action of the Pt-based chemotherapy and peroxidase-like activity of the IONPs. The potential for functionalisation of a Pt(IV) prodrug to an IDO inhibitor, such as 1MT, provides a possibility for the future development of an immuno-chemotherapeutic platform.<sup>417</sup>

Additionally, IONP-DOTAP micelles were functionalised with the immunostimulatory TLR3 agonist, pIC, by electrostatic interactions resulting in a multimodal nanosystem (**Figure 4.16**). DOTAP is a lipid with a terminal cationic quaternary ammonium ion group, which is used for gene transfection. It can cross the phospholipid bilayer of cell membranes and studies have

shown that it can also act as a potent adjuvant to immunotherapy by stimulating DCs and inducing ROS production.<sup>418,419</sup> PIC aims to mediate innate and adaptive antitumour immune responses through proinflammatory cytokine production and directly promoting tumour cell apoptosis and has shown beneficial therapeutic response in combination therapies of different types of cancer.<sup>420,421</sup> The average hydrodynamic size of the IONP-DOTAP-pIC micelles of 43 nm is comparable to previously prepared IONP micelle systems and the Zeta potential of 9 mV of the IONP-DOTAP micelles is indicative of the cationic surface charge of the micelles that drives the electrostatic interactions with the net negatively surface charged pIC (**Figure 4.17**). Colapicchioni *et al.* loaded pIC into cationic core-shell liposome-silica hybrid NPs via electrostatic interactions followed by coating with PEG to afford enhanced pharmacokinetics.<sup>422</sup> This system demonstrated improved internalisation and significant reduction in cell viability in prostate and breast cancer cells compared to pIC alone. The incorporation of pIC into a NP system is favourable to increase its stability, enable tumour cell targeting as well as providing a platform for the delivery of combination therapies.<sup>423-425</sup> The incorporation of the IONP-DOTAP-pIC system into a biomaterial-based implant to enable a gradual and localised release of the NPs was demonstrated in Chapter 5.

A multifunctional biosilica-based therapeutic device was developed in which the commercially available diatoms were functionalised with GOx and IONPs through electrostatic interactions. The unmodified diatoms showed intrinsic peroxidase-like activity, which to my best knowledge has not been previously reported in the literature (**Figure 4.19**). GOx has an isoelectric point of 4.2, therefore, it carries a net negative charge at neutral pH.<sup>426</sup> To promote electrostatic interaction of the anionic GOx and IONPs with the diatoms, the diatoms were first modified with the cationic polymer, PEI, through chemisorption, facilitated by the deprotonated silanol groups at the surface of the diatoms at neutral pH.<sup>427,428</sup> The GOx modified diatoms containing 45.6 nM GOx demonstrated an increased peroxidase-like activity in the presence of D-glucose, which is oxidised in the presence of GOx and O<sub>2</sub> to gluconic acid and H<sub>2</sub>O<sub>2</sub> (**Figure 4.20**).

To boost the peroxidase-like activity and provide magnetic properties, the GOx modified cationic diatoms were loaded with anionic IONP micelles (**Figure 4.22**). This system achieved peroxidase-like activity through tandem catalysis, in which H<sub>2</sub>O<sub>2</sub> is locally generated in the presence of O<sub>2</sub> and glucose, and subsequently broken down into ROS due to the catalytic activity of the IONPs and the diatoms (**Figure 4.23**). The increased catalytic activity observed in the H<sub>2</sub>O<sub>2</sub> supplemented sample is potentially due to some displacement of GOx from the diatom surface when the IONPs are added during the D-GOx-IONP preparation. This tandem

catalytic system has not been previously explored in the context of diatoms but GOx loaded IONPs have demonstrated enhanced ROS-mediated tumour cell cytotoxicity compared to IONP alone both *in vitro* and *in vivo*.<sup>429-431</sup> The combined catalytic activity of the developed tandem catalytic system could lead to an enhanced therapeutic effect in the peroxide rich and acidic TME, whilst its magnetic properties present potential application for *in vivo* tracking, hypothermia therapy and magnetic purification.

Furthermore, the diatoms were also explored as a cancer diagnostic device. A proof-of-concept PD-L1 biosensor was developed by a multistep covalent functionalisation of the diatoms with anti-PD-L1 (**Figure 4.24**). PD-L1 was chosen due to its overexpression in different types of cancers and is a clinically relevant target for immunotherapy.<sup>432,433</sup> The silanol diatom surface was first modified with APTES to afford terminal amine groups followed by addition of sulfo-SMCC to obtain terminal maleimide groups that are reactive towards thiol groups. The anti-PD-L1 was activated via modification of lysine residues with terminal thiol groups using a 10-fold molar excess of Traut's reagent (2-iminothiolane), which is an optimised ratio used in the literature that ensures high thiolation yields without compromising the functional and structural properties of the antibody.<sup>434,435</sup> The hydrolysis of the succinimidyl ester ring forms a stable succinamic acid thioethers preventing premature release of anti-PD-L1 through retro-Michael reaction.<sup>436</sup> Each step of the synthesis was characterised by XPS that confirmed the presence of the surface functional groups present based on the electron binding energies of abundant surface atoms including N, C and O (**Figures 4.25 – 4.27**).

An anti-PD-L1 functionalised IONP system was also synthesised by first generating maleimide terminal IONP micelles using the thin-film hydration method followed by reaction of the maleimide groups with the thiol group activated anti-PD-L1 (**Figure 4.28**). The resulting IONP-anti-PD-L1 micelles had a hydrodynamic diameter of 42 nm and a PDI of 0.23, which indicates good monodispersity (**Figure 4.29**). The reduction of the zeta potential to -25 mV compared to the IONP-maleimide micelles, could be due to the net negative surface charge of the antibody.<sup>437</sup> The functional activity of IONP-anti-PD-L1 is essential for the biosensor assay to work. Therefore, a PD-L1 ELISA was performed and demonstrated specific binding of the PD-L1 ligand to anti-PD-L1 bound to the NPs (**Figure 4.30**). The BCA protein quantification assay of both the diatom and IONP modified anti-PDL-1 determined a modification yield of 48% and 29%, respectively. The NPs were an integral part of the developed biosilica-based PD-L1 sensor assay (**Figure 4.31**).

There is a high appeal for using diatom as a biosensor platform due to the high surface area of their nanoporous structure and high versatility for chemical modification. Several examples of diatom-based biosensors have been reported for different applications including as a cancer diagnostic tool but due to their early stage of development none have been approved for clinical use to this date.<sup>438-440</sup> Rea *et al.* developed an optoelectronic diatom sensor using cylindrical shaped *aulacoseira sp.* diatom species that was covalently modified with protein A followed by conjugation to mouse antibody anti-His-tag.<sup>440</sup> This diatom system showed binding affinity His-tagged p53, a tumour suppressor biomarker, characterised through photoluminescence imaging. The biosilica PD-L1 biosensor assay involves the incubation of PD-L1 with D-anti-PD-L1, which bind to the diatoms through antibody-ligand interaction. After the removal of the supernatant, IONP-anti-PD-L1 is added and allowed to interact with the PD-L1 bound diatoms. The supernatant of this mixture was analysed in a peroxidase-like activity assay alongside a control sample in which the PD-L1 was not added to the diatoms in the first step (**Figure 4.32**). A reduced peroxidase-like activity was observed for the D-PD-L1 sensor sample compared to the control which indicates that the biosensor assay was successful. However, this is an early-stage proof-of-concept design and further experimentation is necessary for the complete development of this biosensor. Nevertheless, this diatom-based PD-L1 biosensor has the potential to be used in combination or as an alternative to ELISA kits, whilst also offering the possibility to be used as an immunotherapy against PD-L1 overexpressed cancers.

# Chapter 5

**Synthesis, functionalisation and characterisation of biodegradable hyaluronic acid-based MNs and implantable devices for cancer immunotherapy**

## 5.1 Introduction

### 5.1.1 Biodegradable microneedles (MNs) for cancer immunotherapy

Transdermal drug delivery vehicles have sparked an increased interest for the administration of cancer immunotherapies due to the potential they have to improve access to the large numbers of professional APCs and other specialised immune cells in the dermal skin layer.<sup>441</sup> Direct administration of immunomodulatory agents into the skin compared to conventional drug administration methods such as by subcutaneous or intramuscular injections can enhance the desired immune response and ensure a high local drug bioavailability.<sup>442,443</sup> Furthermore, the local and gradual delivery of immunomodulatory agents via a biodegradable MN administration system can also prevent or mitigate the immune-mediated adverse effects associated with high-dose bolus injections of immune checkpoint inhibitors leading to systemic immune hyperactivation.<sup>444</sup> Microneedle drug administration is non-invasive and painless as the needles do not penetrate far enough into the skin to damage the blood vessels and nerves found in the dermis, thereby, reducing the risk of bruising, discomfort hypersensitivity and improving patient compliance.<sup>445,446</sup> Another advantage of biomaterial-based MNs over hypodermic needles is the reduction in generation of hazardous waste and cost of waste management since the MNs are designed to dissolve in the skin and the base of the MN patch is often made out of the same biodegradable material.<sup>447</sup> The potential for self-administration of MNs patches without the need for specialist training is another benefit and further aids patient compliance in contrast to the use of hypodermic needles.<sup>447</sup>

Dissolvable and biodegradable MNs can be fabricated from a variety of natural as well as synthetic polymers as discussed in the introduction,<sup>448</sup> but this chapter focusses on the fabrication, characterisation, and functionalisation of HA-based MNs. HA MN degradation occurs via hydrolysis or in the presence of HAase in order to release the incorporated drug load. Whilst the HA MN matrix biodegradation upon skin insertion already provides a gradual release of the drug, the release kinetics can be further controlled by incorporation of the drug into a stimuli-responsive NP system. Hao *et al.* developed near-infrared responsive HA MN system for the treatment of epidermoid cancer.<sup>449</sup> Pegylated-gold nanorods and a chemotherapeutic agent were incorporated into a HA-based MN patch. The release of drug load could be controlled though on-demand near-infrared irradiation at the site of MN application, whilst simultaneously inducing thermal ablation of tumour cells due to the photothermal properties of the gold nanorods. A pH-sensitive HA-based MN system was



reported by Wang *et al.* in which the MNs were incorporated with a biodegradable dextran NPs containing GOx and anti-PD-1.<sup>225</sup> Upon MN skin insertion, glucose in the TME can interact with the GOx-loaded NPs resulting in the production of gluconic acid that promoted degradation of the NPs and sustained release of anti-PD-1. It showed a superior therapeutic response *in vivo* compared to intratumoural administration of anti-PD-1 alone in a murine melanoma model.

There are a variety of fabrication methods for polymeric MNs, but the HA MNs in this thesis were prepared using the micromolding process. Micromolding by the casting method is beneficial due to the ease of fabrication, upscaling, high reproducibility, and low processing temperature, convenient for the incorporation of thermally unstable drugs.<sup>450</sup> The casting method typically comprises the use of inverted MN molds fabricated by laser ablation, a process in which a focussed laser beam is irradiated onto the chemically inert polydimethylsiloxane (PDMS) surface creating cavities with controllable depth, shape and tip angle (**Figure 5.1**).<sup>451</sup> Other micromolding techniques including hot embossing method, injection molding and investment molding involve higher processing temperatures that may adversely affect the drug activity.<sup>450,255</sup>

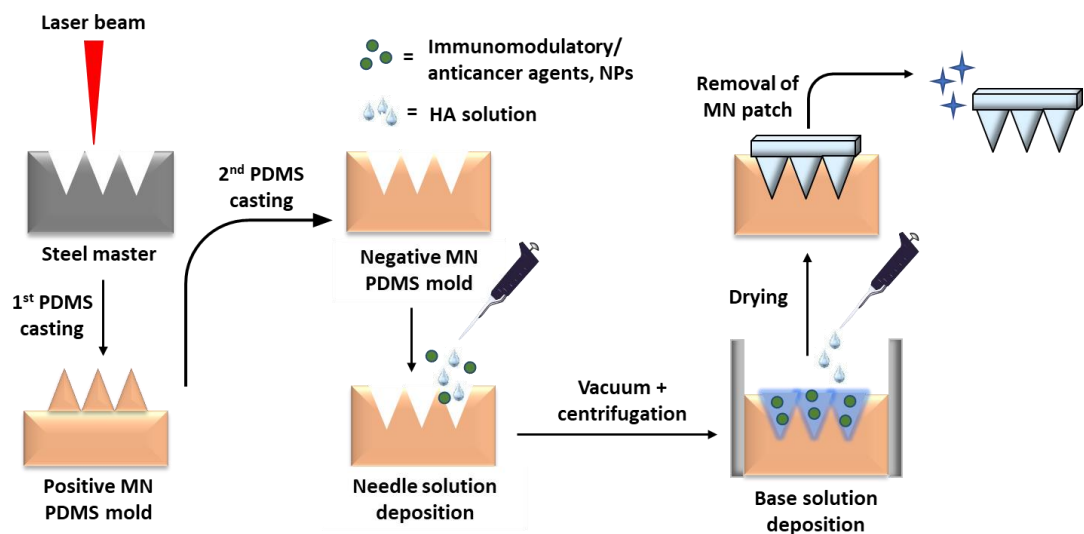


**Figure 5.1 Micromolding by casting for polymeric MN fabrication.** The PDMS mold is fabricated by laser ablation of a steel master structure followed by a 2-step PDMS casting process to create inverted MN shaped cavities. The needle solution is added to the mold followed by vacuum and centrifugation cycles. To the mold is then added the MN base solution within a micromold reservoir and the MNs are allowed to dry. Once dried, the MN patch can be removed from the mold and is ready for use.

The targeted inhibition of immune checkpoints overexpressed on the surface of tumour cells is of major interest in cancer immunotherapy as it can help expose tumour cells to the

adaptive immune system by promoting the reactivation and recruitment of tumour specific cytotoxic T lymphocytes (CTL). Yang *et al.* developed a polymeric core-shell MN system for the combined delivery of two immune checkpoint inhibitors, namely the IDO inhibitor, 1MT, and PD-L1 inhibitor, anti-PD-L1.<sup>452</sup> The MN loading was maximised through electrostatic interactions between the anti-PD-L1 and chitosan polymer matrix in the shell and hydrogen bonding between the 1MT and PVA/PVP polymer mixture that made up the core of the MNs. The functional studies showed an improved therapeutic efficiency in a murine melanoma model compared to intra-tumoral injection of 1MT and anti-PD-L1 at the same dose. MNs also provide an excellent platform for combination therapies due to the possibility of incorporating different therapeutic agents into the matrix of a polymer-based MN patch. Chen *et al.* designed a HA MN system combining a photodynamic therapy and an immunotherapy constituent.<sup>453</sup> The photosensitiser and the immune checkpoint inhibitor anti-CTLA-4 were encapsulated into pH sensitive dextran NPs prior to loading into the MNs. The *in vivo* studies demonstrated that the initial photodynamic therapy activated the immune system via increased cytokine production and an enhanced immunomodulatory effect from the anti-CTLA-4 treatment, which led to tumour size reduction in a murine breast tumour model.

### **5.1.2 Dissolvable biomaterial-based implantable devices for cancer immunotherapy**

Implantable biomaterial-based devices as administration systems of immunomodulatory and anticancer agents have the potential to improve therapeutic outcomes due to their direct placement into the tumour and, thereby, reducing the undesirable toxic side effects on surrounding healthy tissue associated with off-target cytotoxicity.<sup>454-456</sup> They can also ensure a local and gradual release of the active agent into the target site to attain a prolonged therapeutic effect, which cannot be achieved by bolus subcutaneous injection.<sup>17</sup> Polymer implants have sparked a particular interest for the treatment of brain cancers due to the difficulty of delivering drugs and vaccines that can overcome the blood brain barrier via routes other than surgery.<sup>457</sup> In contrast to MN delivery, implantable devices have the additional benefit of achieving a significantly higher loading capacity, but require an invasive administration pathway that involves surgical treatment.

In this thesis the HA biomaterial-based implants have been developed using the casting method, which is a cost and time efficient method that avoids the need for specialised equipment or harsh temperature conditions that could affect the stability of the incorporated

immunomodulatory payloads. Implants can be applied either as neoadjuvants by intratumoural administration prior to the main treatment or as adjuvants by deposition into the site of the tumour resection to prevent cancer recurrence.<sup>267</sup> Solid implantable biomaterial devices for applications in cancer immunomodulation offer an exciting new delivery platform with the potential for enhanced therapeutic benefits. However, there is only limited literature available addressing this specific approach of drug delivery. A HA and collagen biomaterial implantable immune niche was synthesised for the post-operative treatment of advanced-stage breast cancer.<sup>458</sup> The implant incorporated a chemotherapeutic agent with immunomodulatory properties, capable of depleting immunosuppressive MDSCs, and a nanogel functionalised with pIC and tumour cell lysates to activate DCs and promote proinflammatory cytokine secretion in the TME. *In vivo* studies in a breast tumour murine model in which the implant was administered post-surgery prevented both tumour recurrence and metastasis. In another study by Park *et al.*, a biodegradable cross-linked hyaluronic acid implant loaded with different immunomodulatory agents including the TLR7/8 agonist, R837, and an agonist of stimulator of interferon genes (STING) showed a local release at the tumour resection site in a murine breast cancer model.<sup>459</sup> The results revealed enhanced T cell proliferation and proinflammatory cytokine activation leading to a higher mice survival rate compared to systemic and local solution-based administration of the immunomodulatory agents. The localised and controlled release of immunomodulatory agents using an implantable device could have applications beyond cancer immunotherapy, for instance, for tissue regeneration and in organ transplantation by inducing local immune tolerance.<sup>460</sup>

### **5.1.3 Design of the immunotherapeutic MN and implantable devices**

This chapter describes the design, development, and characterisation of biomaterial-based transdermal and implantable drug administration devices for the localised and gradual release of immunomodulatory and other anticancer agents as a platform for cancer immunotherapies and combination therapies. The MNs are designed for the delivery of the incorporated anticancer agent into the skin, which makes them especially suitable for the treatment of melanomas and other skin diseases, although it can provide a viable treatment option also for other cancer types (e.g., breast cancer). On the other hand, implants benefit from being implanted directly into the tumour site during tumour resection and gradually release the therapeutic agents locally, which can then activate the immune system to detect and eliminate any residual tumour cells as well as helping to prevent tumour recurrence. The fabrication of these MNs and implants using the casting method allows for any water-soluble

therapeutic agent, such as small molecules, antibodies, and other anticancer agents, to be homogeneously mixed into the HA matrix and casted into the desired shape using molds. Furthermore, the incorporated therapeutic agents can be encapsulated, or included into an NP theranostic system, such as those presented in Chapter 3, prior to loading into an implant or MNs to promote a local and sustained release and provides a new platform for combination therapies and multimodal imaging (**Figure 5.2**).

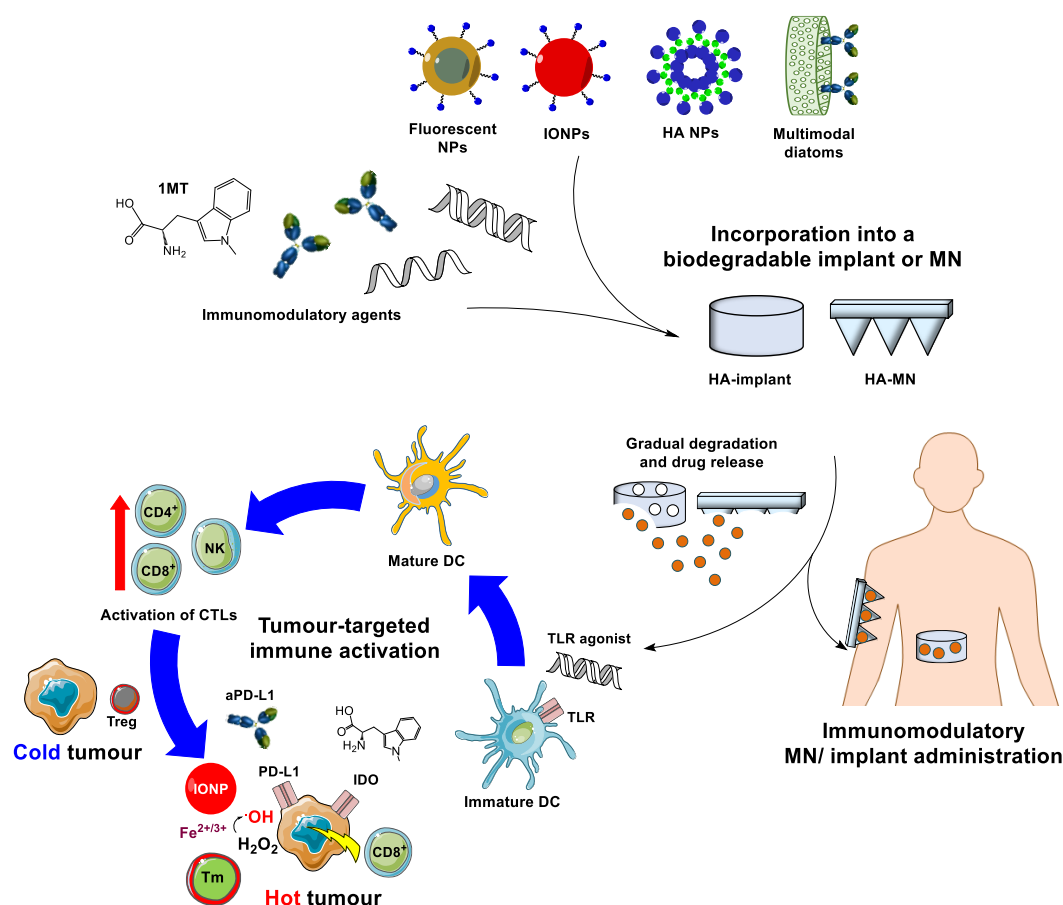


**Figure 5.2 Design of HA-based biodegradable MNs and implantable devices for cancer immunotherapy.** The implants and MNs can be loaded with different NPs and immunomodulatory agents, which are gradually released as the implant or the MNs dissolves and degrades. The released payload from the implant or MN can be selected to activate dendritic cells (DC) to prime antitumor T cell responses, to target macrophages to improve the treatment efficacy of cancer therapies, to program or reprogram T cells to attack cancer cells and to overcome tumour immune evasion mechanisms converting a cold tumour into a hot tumour. The combined effect of different immunomodulatory and anticancer agents leads to specific tumour cell death and the development of memory T cells (T<sub>m</sub>) provides long-term protection from tumour recurrence.

### 5.1.4 Aims and objectives

- The fabrication and optimisation of a homogeneous HA MN patch using the micromolding method and structural characterisation by SEM;
- Skin penetration efficiency assays using a porcine skin model and investigating the effect of HAase on MN degradation in the skin;
- The incorporation of different NPs systems and immunomodulatory agents developed in Chapter 4 into the MN patch and analysing the release over time as well as the retention of functional activity of the released agents;
- Fabrication of HA implantable devices and incorporation with immunomodulatory IONPs and a biomaterial (i.e. 1MT-HA);
- Functional activity studies of the developed immunomodulatory HA implants using different human and murine tumour cell types.

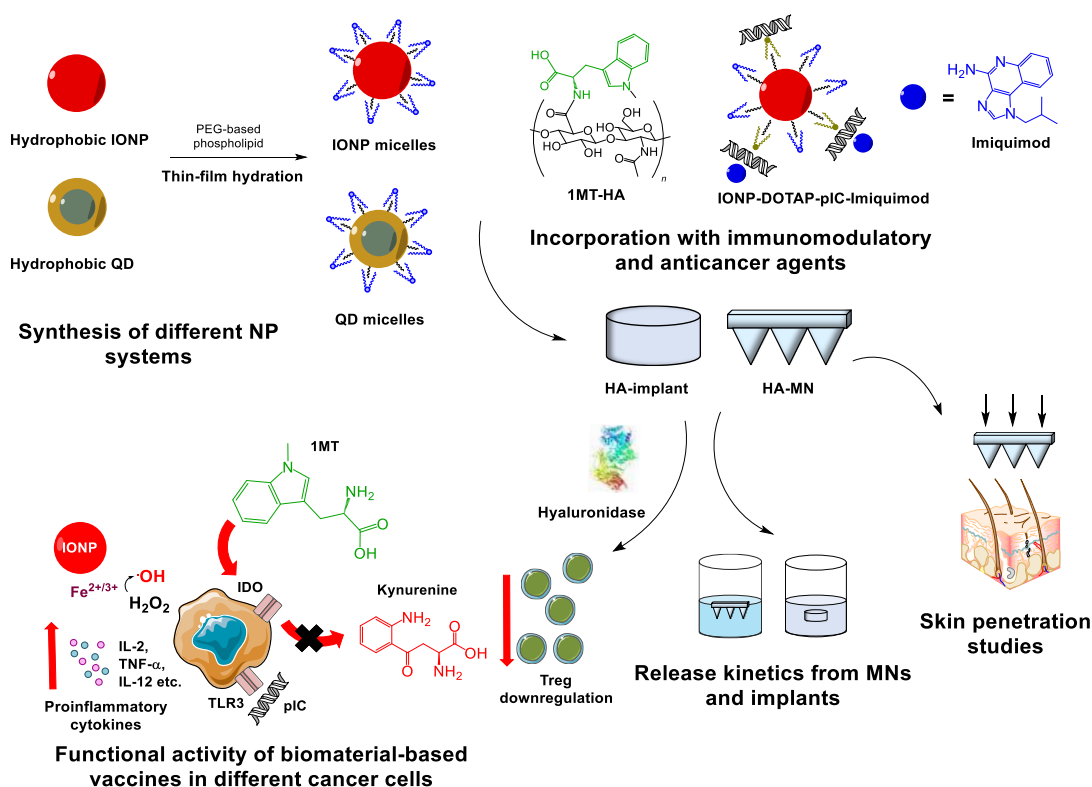


**Figure 5.3 Overview of NP systems and immunomodulatory agent incorporated into HA MNs and HA implants.** Overview of NP systems and immunomodulatory agent incorporated into HA MNs and HA implants. All incorporated drug delivery systems were characterised, and the release kinetics evaluated. MNs were further characterised in skin penetration efficiency studies. The functional activity of 1MT and immunomodulatory IONP systems released from the biodegradable drug delivery systems was evaluated in vitro using different cancer cell lines.

## 5.2 Results

### 5.2.1 HA MN fabrication, optimisation, and characterisation

The HA MNs were fabricated following the micromolding technique using reusable inverted MN PDMS molds consisting of a 15 x 15 array of needles on a square base. Considering the specific requirements of future *in vivo* studies and applications, the MNs were designed to be 800  $\mu\text{m}$  in length and have a base diameter of 300  $\mu\text{m}$  and centre-to-centre spacing of 600  $\mu\text{m}$ . The fabrication method was optimised by designing a 3D-printed box and a silicone wall aimed at preventing leaking of the solution during the centrifugation and drying process. The fabrication starts with the deposition of a viscous HA solution in MilliQ water onto the inverse-MN shaped silicone mold and placed under vacuum for 10 min to allow the HA solution to enter the mold cavities. The mold was then placed into a plastic box, which was placed into a centrifugation tube and then centrifuged at 3000 g for 1 h to compress the HA solution into the cavities, whilst the box prevented the solution from leaking. The remaining solution was collected and could be stored for further use. An adhesive tape was placed around the sides of the mold, and a HA solution was deposited into the micromold reservoir to form the base of the MN patch. The MNs were allowed to dry for 5 days at room temperature and atmospheric pressure. The mild drying conditions ensured high MN homogeneity and prevented unwanted air bubble formation. Once the MN patch had dried, it was carefully removed from the mold and cut to the desired shape. MNs fabrication was also attempted under vacuum and elevated temperature conditions to reduce the fabrication time, but these approaches led to a reduction in MN quality due to a higher risk of leaking from the reservoir and air bubble formation. Ultimately, the fabrication conditions mentioned above were found to produce the most consistent and homogeneous MN patches. The MN morphology was characterised by SEM with additional characterisation by energy dispersive X-ray analysis (EDX) and confocal laser scanning microscopy (CLSM), depending on the loading agent.

The SEM imaging of the blank HA MN showed almost complete homogeneity throughout the patch with a conical shape and needle tip thickness of approximately 20  $\mu\text{m}$ , which would suggest good skin penetration properties (**Figure 5.4**). The actual needle length of the MNs was around 700  $\mu\text{m}$ , which is long enough to penetrate the human dermal layer. Minor features of roughness were observed in the high magnification images, but the sharp tip and the smooth cone shape of the needles would suggest no issues with skin penetration.

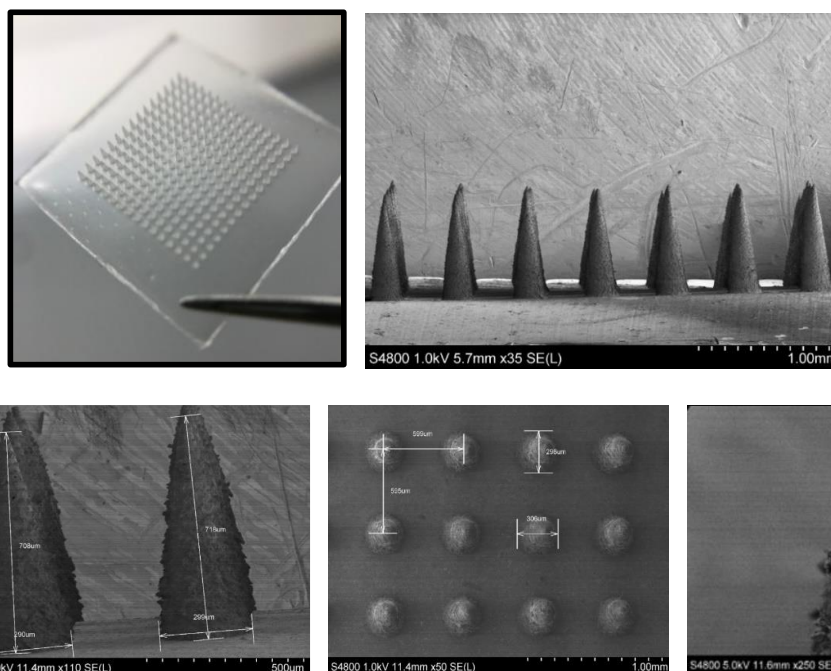


**Figure 5.4 Photograph and SEM imaging of blank HA MNs.** The Photograph shows full 15x15 array of needles in a blank HA MN patch. SEM illustrates surface features of MNs from a top and horizontal view. MNs had a height of  $\sim 700\ \mu\text{m}$  length, base diameter of  $\sim 300\ \mu\text{m}$  and tip diameter of  $\sim 25\ \mu\text{m}$ .

## 5.2.2 MN skin penetration efficiency experiments

Polymeric MNs require sufficient mechanical strength and needle tip sharpness to penetrate skin without fracturing or deformation and to deliver the drug load into the immune cell-rich dermal skin layer. The MN penetration efficiency was characterised using porcine skin as a suitable model for human skin. The porcine skin was thawed on the day of the experiment and the surface dried from excess moisture. The MNs were applied onto the skin for 1 min and then held in place with medical tape. The MN patch was carefully removed from the skin and the MN application area was stained with a solution of methylene blue (MB) (2% wt/wt). The surface residual dye was removed after 15 min using dry medical wipes and the skin rinsed with MilliQ water followed by ethanol to expose the points of penetration stained by the dye (**Figure 5.5**). The MNs were characterised before and after skin penetration by SEM to analyse the morphology and degradation behaviour.

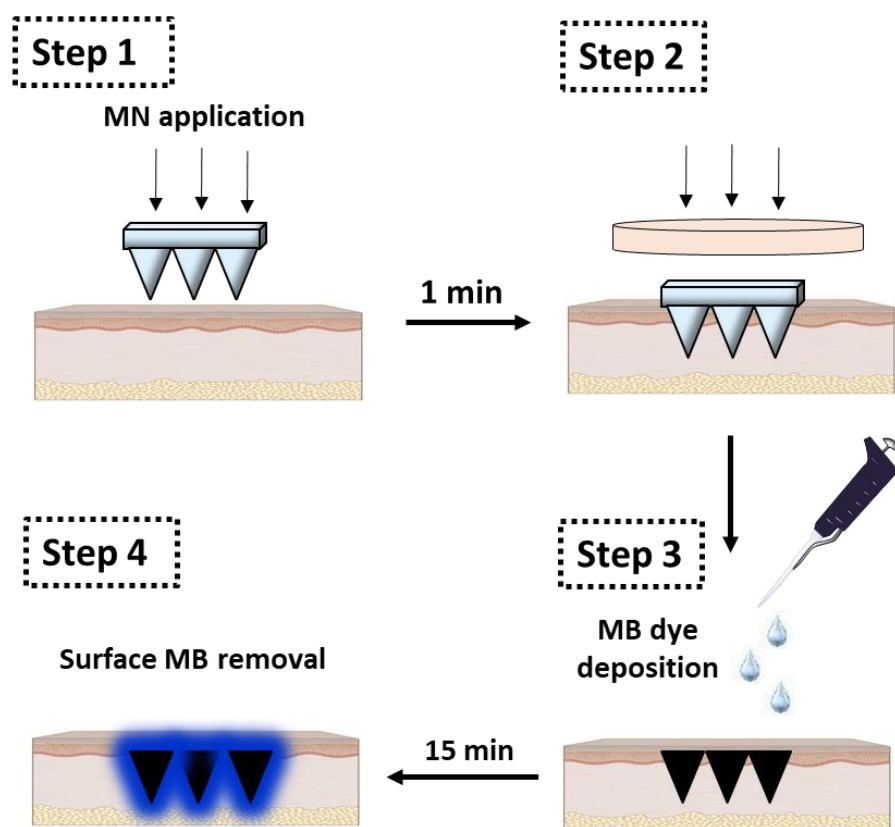
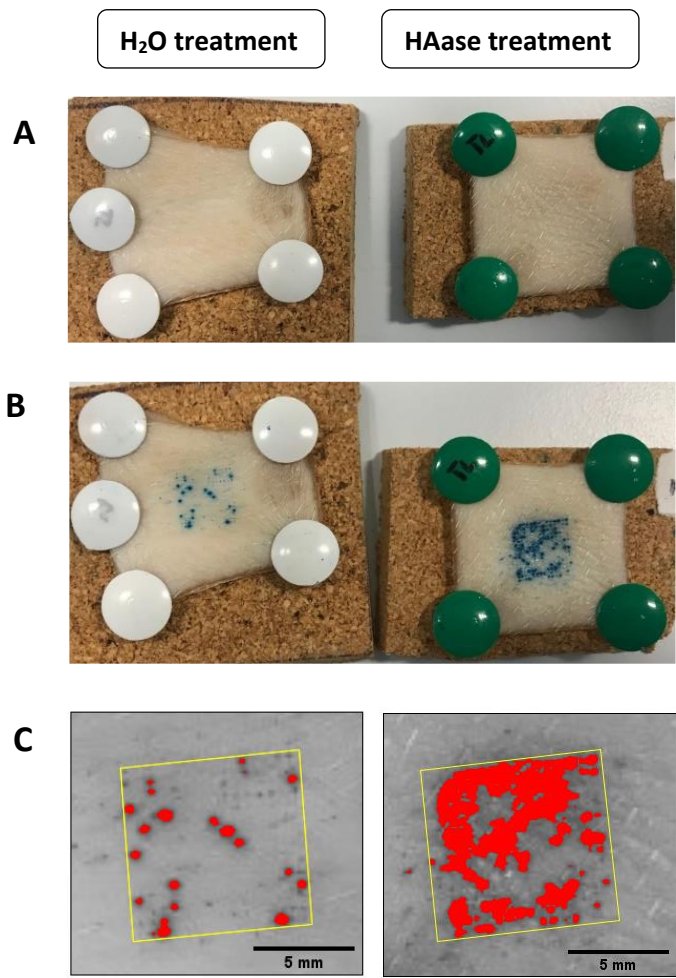


**Figure 5.5 Schematic of MN skin penetration experiment method.** Step 1: MNs were applied onto a shaved section of porcine skin using thumb pressure for 1 min; Step 2: MN immobilisation by medical tape application for a set amount of time to allow the needles to dissolve; Step 3: MN removal and skin staining with MB solution and incubated for 15 min; Step 4: Surface dye removal with  $H_2O$ , then EtOH followed by skin penetration analysis.

To compare the effect of HAase pre-treated skin sample with an untreated sample on the MN penetration efficiency, a 1 mg/mL HAase solution in MilliQ water was applied onto a porcine skin sample and allowed to evaporate for 2 h. As the control, a second skin sample was treated with MilliQ water. Once the skin surfaces had dried, a blank HA MN was applied onto each skin sample for 1 h before it was carefully removal. Following the dye application and surface dye removal, images were taken, and the % penetration area coverage analysed. The images show a clear increase in penetration efficiency with the HAase pre-treated skin compared to the control, resulting in a % penetration area of 40.3 % and 4.1 %, respectively (**Figure 5.6**). However, the MN treated skin images illustrate that the obtained % penetration area might be underestimated since the Image J software was not able to detect the more faintly coloured penetration points. The 10-fold higher penetration efficiency for the HAase treated skin shows that the HAase is catalytically active and facilitates the penetration and degradation of the MNs in the skin.





Skin sample	Analysis area/mm <sup>2</sup>	% Penetration area
H <sub>2</sub> O pre-treatment	76	4.1
HAase pre-treatment	76	40.3

**Figure 5.6 MN porcine skin penetration experiment for 1h.** (A) Images of skin samples pre-treated with water (left) and HAase (right). (B) Images of skin samples after MN penetration with water (left) and HAase (right). (C) % penetration area analysis with the area border marked in yellow.

The MNs were characterised before and after the skin penetration experiment by SEM to determine the degree of degradation and morphological changes. The SEM images show that the average length of both MN has reduced by approximately half, indicating that longer application times may be required for complete MN degradation and an enhanced % penetration yield (**Figure 5.7**).

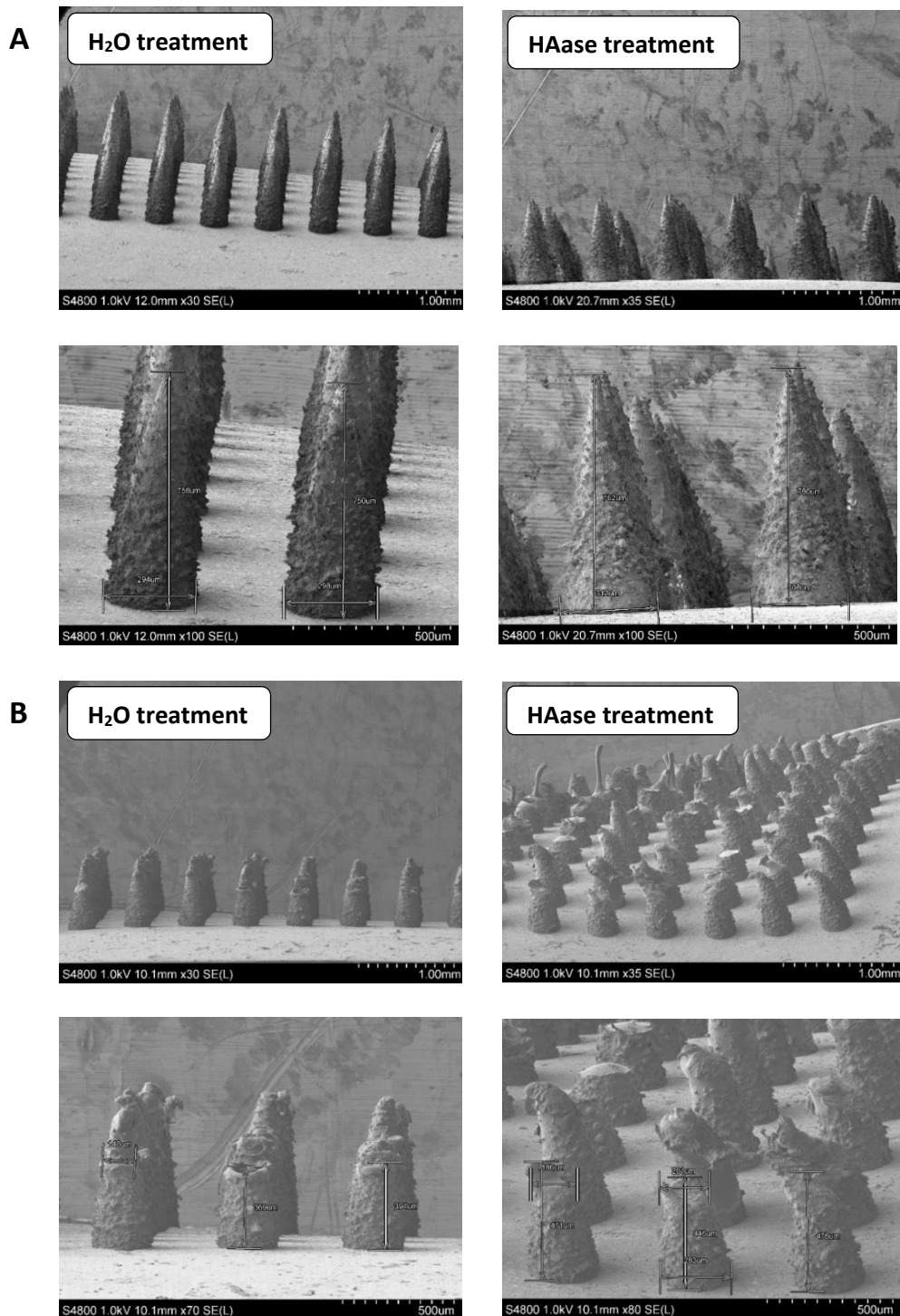
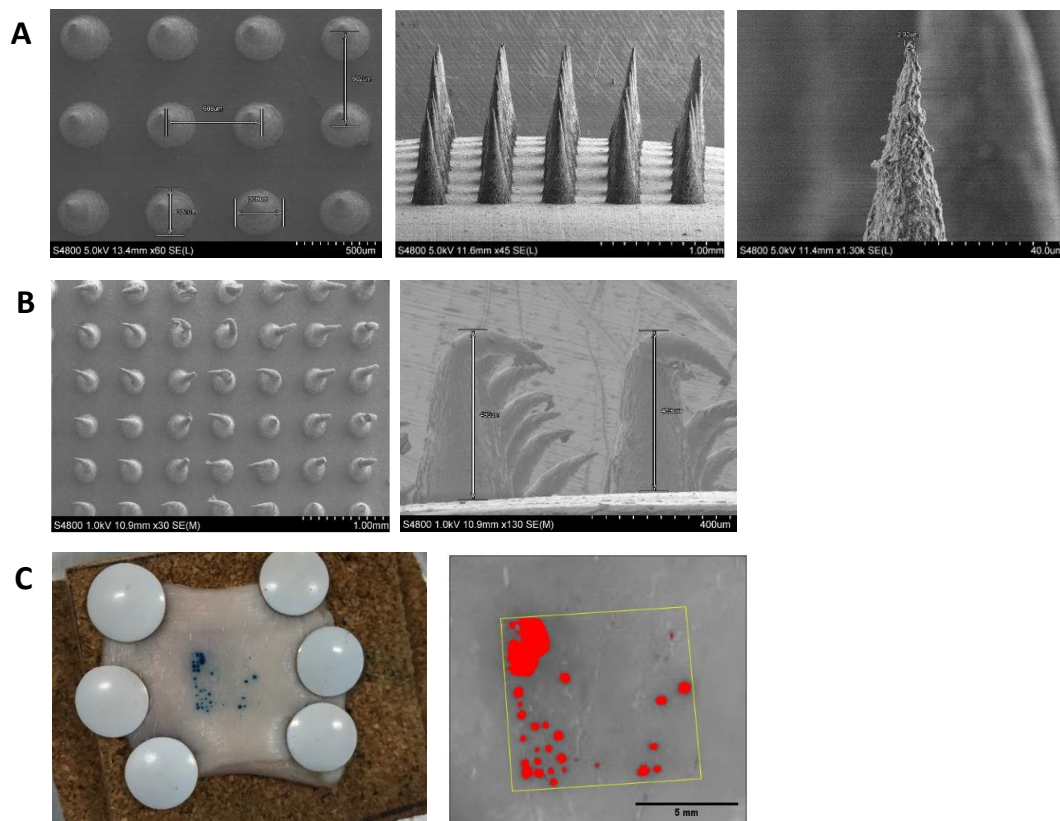


**Figure 5.7 SEM of MN porcine skin penetration experiment for 1 h. (A) SEM characterisation of MNs before skin penetration. Both MN patches are homogenous with a needle height of ~700 nm. (B) SEM imaging of MNs after skin penetration. The needle height reduced to ~400 nm suggesting incomplete MN biodegradation at 1 h application time. MNs on the left were applied onto H<sub>2</sub>O pre-treated porcine skin and the MNs on the right onto HAase pre-treated skin).**

As an additional assessment for the effect of HAase activity in MN skin penetration assays, a MN patch loaded with the HAase enzyme was fabricated and characterised by SEM. The

resulting needles were untypically sharp with a tip diameter of approximately 3  $\mu\text{m}$  (**Figure 5.8 A**), which can be expected to improve skin penetration. Indeed, the % penetration area of 9.6% and the SEM images after skin penetration suggest that this MN provides around two-fold enhancement in skin penetration due to the enhanced needle sharpness (**Figure 5.8 C**). However, the curvature of the MN tips from the SEM analysis post-penetration showed that that majority of the needles succumbed to inelastic deformation upon contact with the skin, presumably due to less mechanical strength (**Figure 5.8 B**). Therefore, the incorporation of HAase enzyme into the MNs with aim of sharpening and accelerating the degradation rate and potentially improving drug release is a viable option, but skin pre-treatment with HAase appears to be an even more suitable approach.

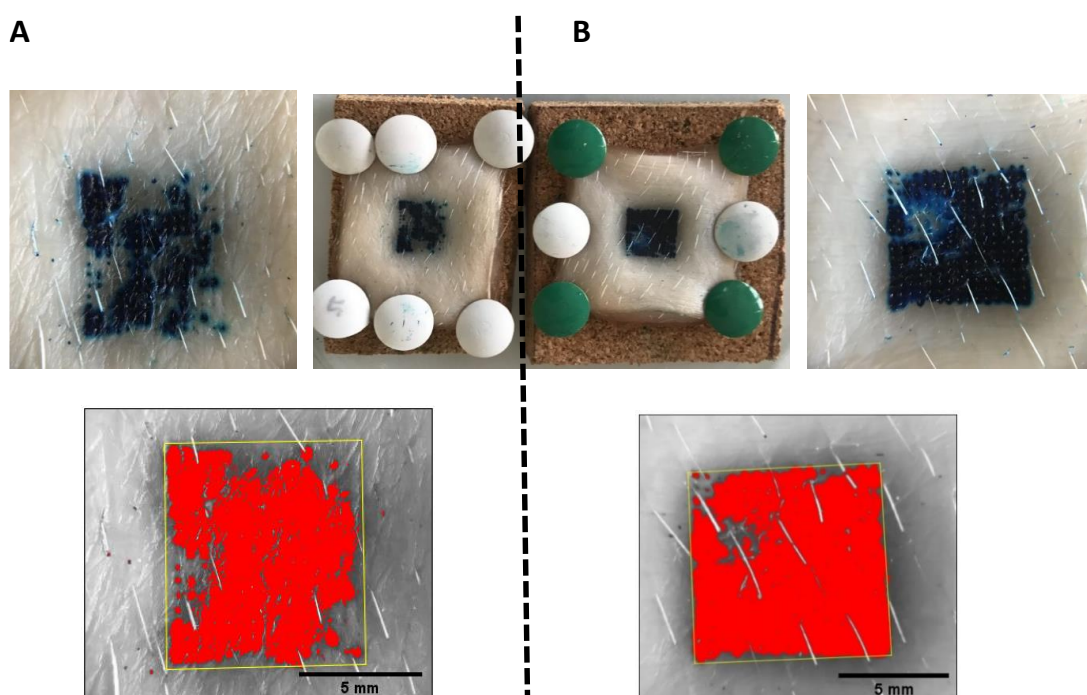


Sample	Analysis area/ $\text{mm}^2$	% Penetration area
HAase loaded MN	76	9.6

**Figure 5.8 HAase incorporated MN porcine skin penetration for 1 h.** (A) SEM imaging of HAase MN before skin penetration. (B) SEM imaging of HAase MN after skin penetration. (C) Image of porcine skin after MN penetration and % penetration area analysis.

Next, the penetration efficiency was investigated over a longer MN application time of 24 h. Following the same procedure, one skin sample was treated with HAase prior to MN application, while a control sample was treated with MilliQ water and allowed to evaporate

until the skin surface was dry. The penetration efficiency showed a significant increase compared to the 1 h experiments, with the water treated skin achieving 64% skin penetration coverage (**Figure 5.9 A**) and the HAase treated skin achieving an increased skin penetration area of 84% (**Figure 5.9 B**).



Sample	Analysis area/mm <sup>2</sup>	% Penetration area
H <sub>2</sub> O pre-treatment	76	64.3
HAase pre-treatment	76	84.0

**Figure 5.9 HA MN porcine skin penetration experiment for 24 h.** (A) Images and penetration area analysis of H<sub>2</sub>O treated skin after MN penetration; (B) Images and penetration area analysis of HAase treated skin after MN penetration.

The photographs and SEM images of the MNs before skin penetration show high homogeneity as expected (**Figure 5.10 A, B**). There was no remaining MNs after 24 h of skin application due to complete degradation and the base had turned from a solid into a gel state in both cases (**Figure 5.10 C, D**). This experiment demonstrates that a longer skin application not only enhance skin penetration area coverage but is also beneficial to allow the MNs enough time to dissolve entirely and release any incorporated drug load into the skin.

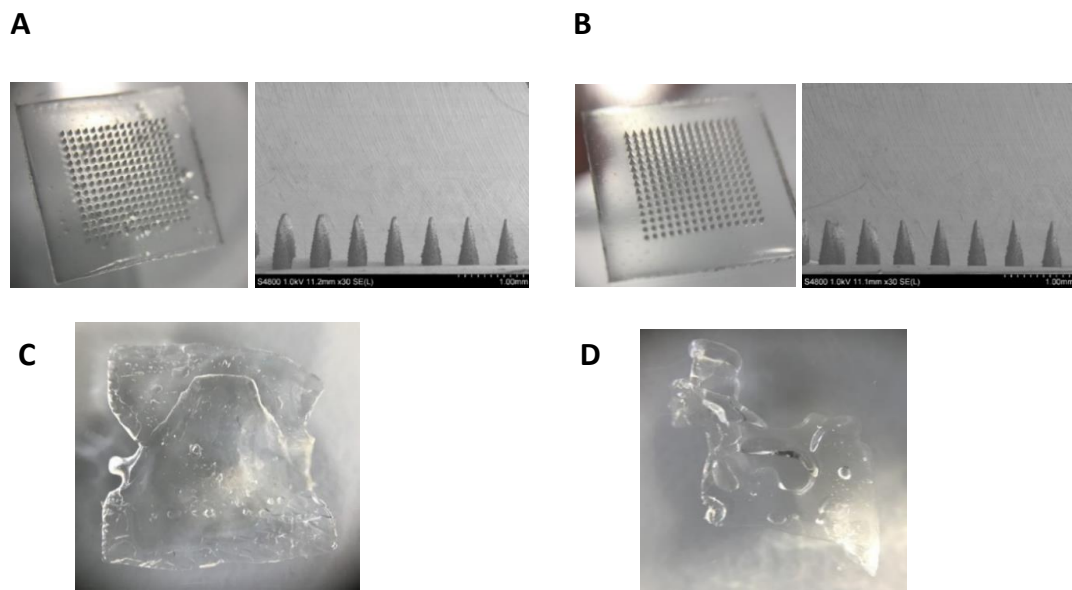


**Figure 5.10** Images of HA MN porcine skin penetration experiment for 24 h. (A) and (B) photograph and SEM image of blank MNs before penetration. Photograph of MNs after 24 h skin penetration on (C) H<sub>2</sub>O treated skin and (D) HAase treated skin.

To analyse the skin penetration depth of the HA MNs, the skin sample from 24 h penetration experiments were frozen and then cut into three pieces along the stained points of MN penetration. The skin pieces were the placed flat onto a glass slide and imaged using an optical microscope. The MB staining of the skin visualised on the microscope shows that the penetration reached an average depth of  $559.5 \pm 71.6 \mu\text{m}$  (**Figure 5.11**). The images show that some MNs within the same patch penetrate deeper into the skin than others potentially due to differences in penetration pressure during the application. The experiment showed that the penetration depth is on average 80% of the total length of the MNs, demonstrating that these MNs not only achieve a high penetration area as shown in the previous experiments, but can also reach the required penetration depth to deliver the incorporated drug load into the dermal skin layer.

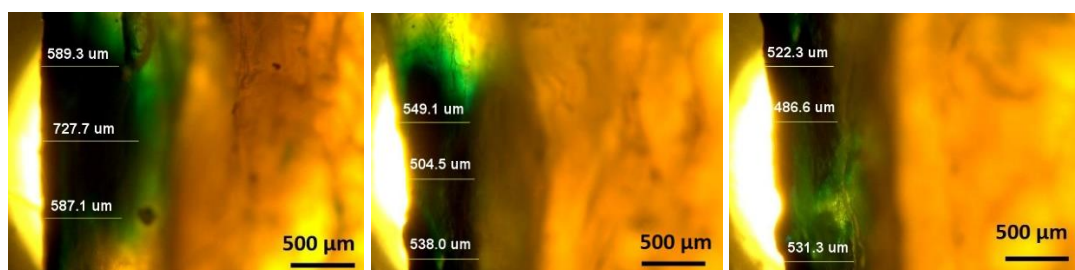


**Figure 5.11** Analysis of MN porcine skin penetration depth. The depths of 3 stained areas were analysed from the MN skin penetration experiment for 24 h using an optical microscope.

### 5.2.3 MN biocompatibility studies

We anticipated the HA MNs would be “fit-for-purpose” for application *in vivo* due to its established biocompatibility and biodegradability. Nevertheless, a cytotoxicity assay was carried out in immune cells and cancer cells to confirm the biocompatibility of the synthesised HA MNs and eliminate the possibility of potential contaminants introduced during the fabrication process and storage. A blank HA MN patch was prepared, and the needles were separated from the base using a sterile scalpel. Both the needles and the MN base were analysed for cytotoxicity in a co-culture assay with B16F10(OVA) melanoma cells and RAW264.7 macrophages. The MN base was added to the cells at a 10-fold dilution to reduce the high viscosity, while the needles were added without dilution and incubated for 24 h at 37°C prior to cell viability analysis of both cell types by flow cytometry. The cell viability was evaluated by standardising to a sample of untreated cells in media as the negative control. For both the needles and the MN base the cell viability was above 93% compared to the negative control with the MN base displaying values slightly exceeding 100% (Figure 5.12). The blank HA MNs show no signs of cytotoxicity in both the melanoma and macrophage cell lines, demonstrating the high biocompatibility of these MNs in different cell types and suitability for potential clinical use.

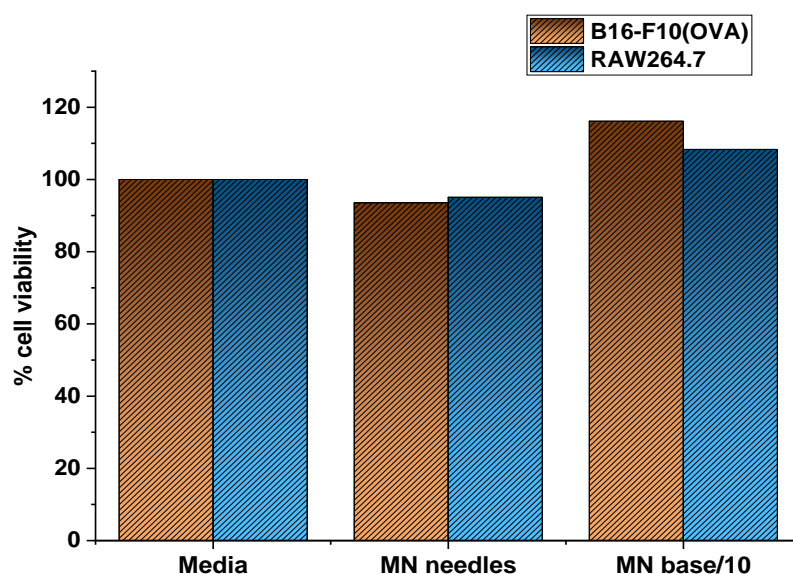


**Figure 5.12 Co-culture cell viability assay of HA MNs.** The co-culture was performed using B16-F10(OVA) melanoma cells and RAW264.7 macrophages for 24 h and the cell viability characterised by flow cytometry (N = 1).

#### 5.2.4 Fluorescent QD incorporated HA MNs

To demonstrate the loading versatility of the HA MNs and the possibility of characterisation by fluorescence, the MNs were loaded with CdSe/ZnS core/shell QD-filled micelles. QDs are known to have exceptional fluorescence quantum yields and high stability against photobleaching making them excellent candidates to demonstrate the incorporation into the HA MNs. The hydrophobic QDs were coated with a carboxylic acid-terminal DSPE-PEG phospholipid to form water-soluble micelles using a thin-film hydration method. The micelles were purified by centrifugation followed by ultracentrifugation cycles to remove large aggregates and unbound phospholipid molecules, respectively.

The QD MN patch was prepared by addition of HA to a solution of QD-filled micelles in MilliQ water followed by the micromolding method described in the previous section. The resulting MN patch was characterised by SEM and CLSM. The latter was performed using an excitation wavelength of 405 nm and emission wavelength window of 562-712 nm (**Figure 5.13 A-F**). The z-stack of both the QD loaded MN and a blank MN consisted of 45 slices starting at the needle tip and terminating at 800  $\mu\text{m}$  distance towards the MN base, which were represented as 3D rendered images (**Figure 5.13 C, D**). QD incorporation into the MNs was evidenced by the red colour in the z-stack image across the needle length (**Figure 5.13 C**). An increased abundance of QDs was observed towards the needle tip, potentially due to the centrifugal force pressing the QD solution into the mold cavities during the MN preparation process. Considering that the needle penetration depth can vary as observed in the porcine skin penetration assays, this could be beneficial by ensuring that entire payload is delivered into the skin. No fluorescence was observed in the blank MNs, which further validates QD loading (**Figure 5.13 D**). Additionally, the top view image of an intermediate z-stack slice, a brightfield image and a fluorescence-brightfield overlay for both the QD MNs and blank MNs demonstrate that the z-stack was focused on a single needle (**Figure 5.13 E, F**).

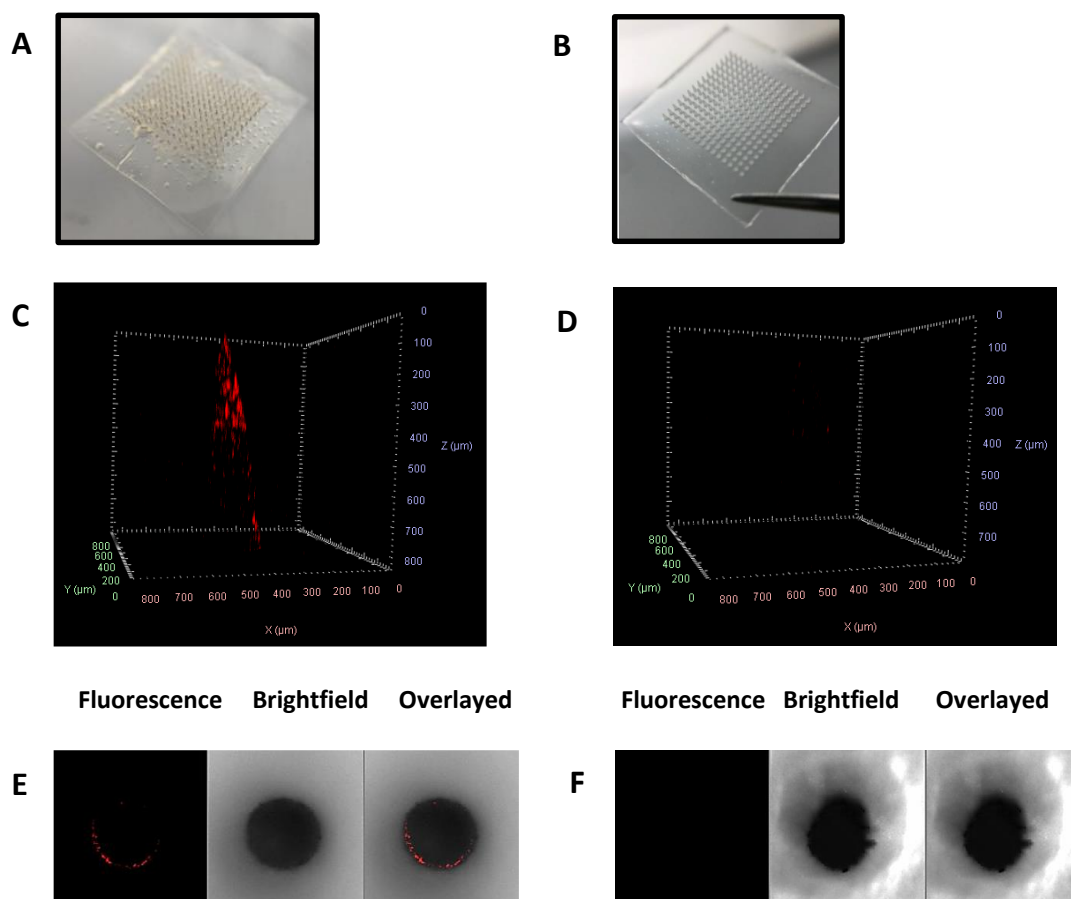


Figure 5.13 QD MN loading characterisation by fluorescence microscopy. CLSM imaging of (A) QD incorporated MN compared with (B) a blank MN including (C, D) z-stack 3D render images of 45 slices. Images were taken at 800  $\mu\text{m}$  along the length of a needle and brightfield images of a single slice below. Fluorescence, brightfield and overlaid images for the (E) QD MNs and (F) blank MNs.

## 5.2.5 Theranostic IONP loaded HA MNs

### 5.2.5.1 Fabrication and characterisation of IONP MNs

The IONP micelles were first synthesised by the thin-film hydration method as described previously and in Chapter 3. The IONP stock solution was gently mixed with HA in MilliQ water until homogenous and this solution was used for the MN fabrication as previously described. The preparation was optimised compared to previous experiments by using a silicone wall that allowed a reduced MN fabrication volume in order to increase the % incorporation yield. The resulting MN patch contained visible red coloured needle tips suggesting successful incorporation of the IONPs. The morphology and homogeneity of the needles were characterised by SEM, while the presence of iron was analysed by EDX (**Figure 5.14 A**). This is both a qualitative and quantitative technique since the kinetic energy is characteristic to each element and the X-ray signal intensity is proportional to abundance of that element



under analysis. The EDX spectrum showed peaks at 0.705 keV and 6.403 keV corresponding to the Fe L $\alpha$ 1 and K $\alpha$ 1 x-ray emission energies. This was also reflected in the iron density map and overlay image with the iron signal observed throughout the length of the needle, but more abundantly towards the tip. As a control, a blank MN was analysed by EDX to confirm that the iron peak was only due to the IONPs (**Figure 5.14 B**). The highest elemental abundance was observed for oxygen, carbon, and sodium as the main components of the HA matrix from which the MNs were fabricated.

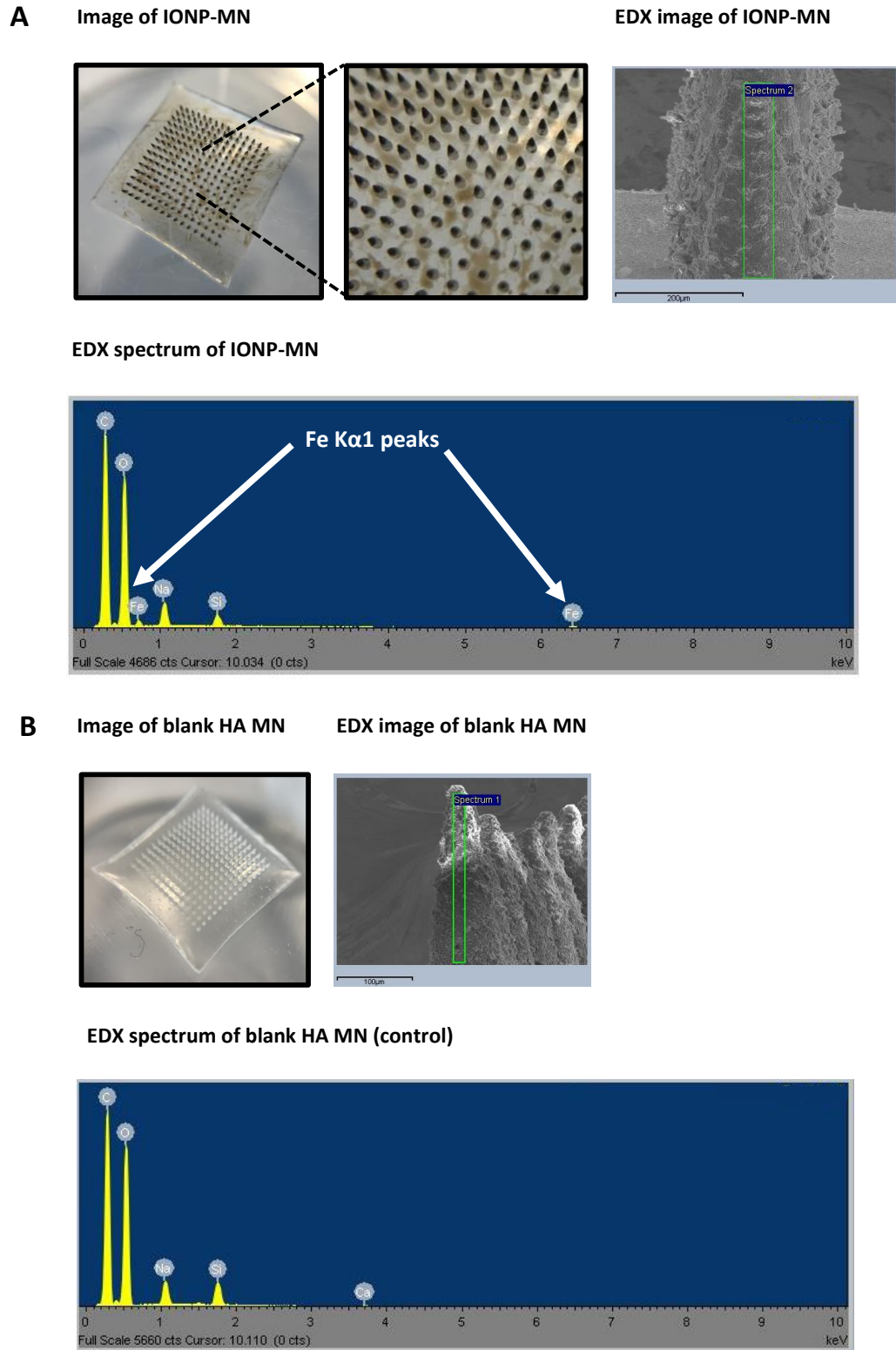


**Figure 5.14** Characterisation of IONP MNs. Images and characterisation of (A) IONP loaded MNs and (B) blank MN (control) by SEM and EDX.

### 5.2.5.2 IONP MN release and functional activity assays

The IONP release kinetics and MN loading efficiency was determined by the degradation of the IONP loaded MN in a phosphate buffer solution containing the HA degrading enzyme, HAase, at pH 6.5 and 37°C (**Figure 5.15 A**). Samples were collected at timepoints 0, 1, 6 and 24 h followed by purification from HA and HAase by centrifugal filtration using 300 kDa MWCO filters and characterised by UV-vis spectroscopy and DLS (**Figure 5.15 B, C and Figure 5.16**). The Fe concentration was calculated based on the previously performed calibration curve (**Chapter 4: Figure 4.14 B**) and converted to IONP concentration using a formula outlined in the materials and methods section. A total IONP release of 87 nM was recorded after 24 h degradation.

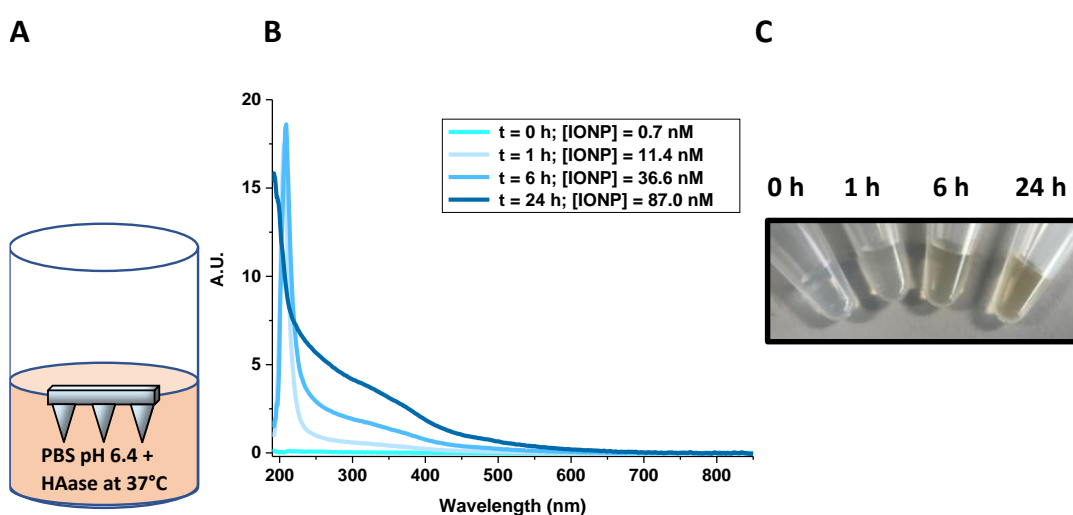


**Figure 5.15 IONP release study from IONP MNs over 24 h characterised by UV-vis spectroscopy.** (A) Scheme of MN degradation experiment. (B) UV-vis analysis of IONP micelle release from gradually degrading MN. (C) Images of IONP samples at different MN degradation timepoints ( $N = 1$ ).

The DLS analysis of the collected samples from the IONP loaded MNs although showed slightly increased average particle sizes compared to the IONP micelles prior to MN incorporation they still carry a negative zeta potential consistent with encapsulation in the carboxy-terminated phospholipids (-28 mV for the IONPs released after 24 h, see **Appendix 9**) (**Figure 5.16**). The size increase can be attributed to some degree of NP aggregation and the potential presence of HA impurities that could not be entirely removed.

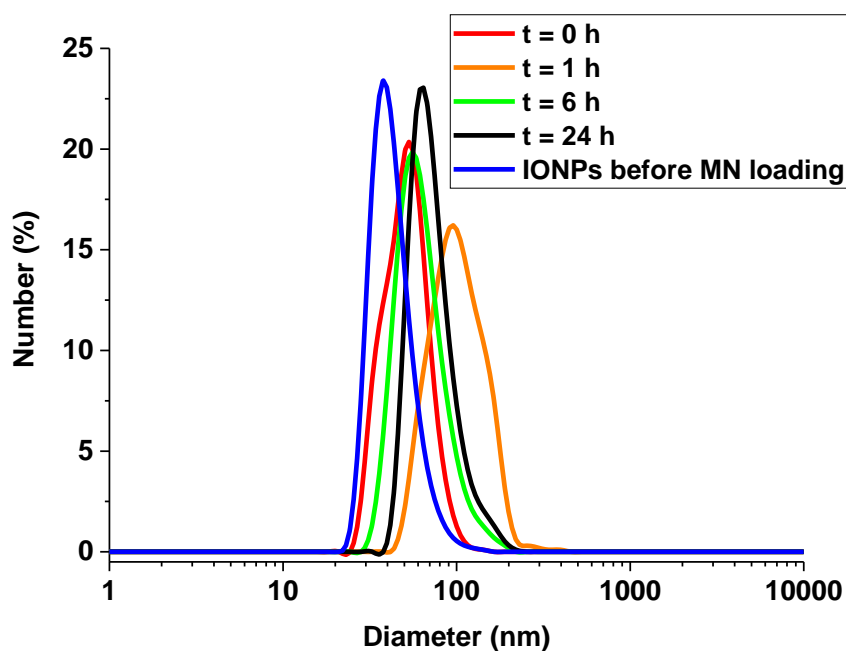


**Figure 5.16 DLS characterisation of IONPs released from IONP MN.** Hydrodynamic size analysis of IONP micelles released from MNs at timepoints 0, 1, 6 and 24 h. The average size distribution of the IONP micelles before loading into the MN is shown in blue (each curve represents the average of 3 repeat measurements) ( $N = 1$ ).

To evaluate the preservation of the functional properties of IONPs after release from the HA MNs, the 24 h IONP sample was used to perform a peroxidase-like activity assay using TMB as the colorimetric indicator, which as discussed in previous chapters oxidises in the presence of  $H_2O_2$  to form a blue coloured product with a maximum absorbance at 652 nm. The sample was diluted in sodium acetate buffer to a working concentration of 0.5 mM Fe and to this solution was added  $H_2O_2$  and TMB at 30 mM and 0.83 mM, respectively. As controls, a fresh sample of IONPs was prepared at the same concentration and the released solution from a blank MN. The UV-vis absorbance at 652 nm was recorded at timepoints 0 and 30 min (**Figure 5.17 A, B**). The absorbance difference was used as a measure of the peroxidase-like activity and the % TMB oxidation determined in relation to the IONP control (**Figure 5.17 C**). Although the IONP released from the MNs showed peroxidase-like activity, the amount of oxidised TMB was ~40% compared to with the IONP control sample. This is most likely be due to the increase in size, which reduces the surface area of the catalyst. It is clear from these studies that IONP micelles released from the MNs retain the key functional features, and therefore, that the HA-based MNs can be used as a theranostic IONP transdermal delivery system.

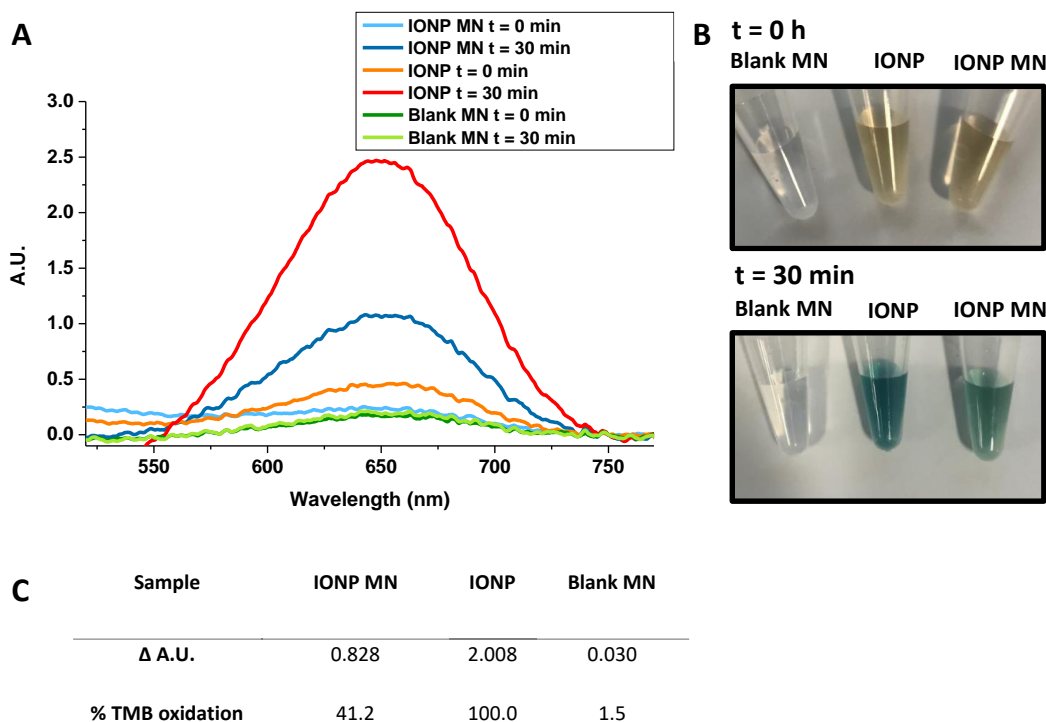
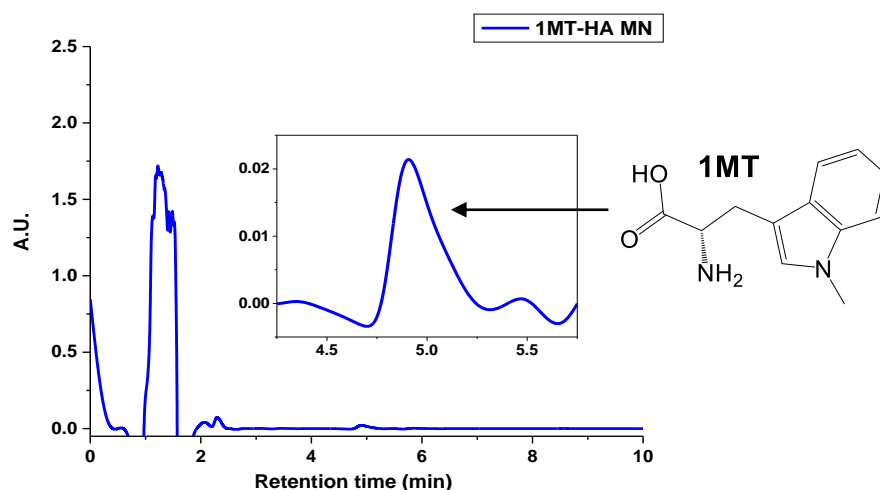


**Figure 5.17 Peroxidase-like activity assay of IONPs after release from HA MN.** (A) UV-vis characterisation of IONP MN sample and controls after 24 h release at 652 nm. (B) Images of sample and controls at the start and end of the reaction. (C) Table summary of  $\Delta$  absorbance measurements and % TMB oxidation ( $N = 1$ ).

### 5.2.6 Immunomodulatory 1MT-HA MN fabrication and release study

A covalent modification of HA with 1MT via amide bond coupling was developed in Chapter 2. This 1MT-HA biomaterial was used as the matrix for the MN fabrication and the amount of 1MT released after MN degradation was analysed. The MN degradation was performed as previously described. After 48 h the released 1MT was purified by centrifugal filtration using 3 kDa MWCO spin filters and the filtrate collected for quantification analysis by RP-HPLC as previously described (**Figure 5.18**). This study demonstrates that the immunomodulatory 1MT-HA biomaterial can be used as the matrix for the MN fabrication and 1MT remains structurally intact after incorporation and release from the MNs under physiological conditions.



Sample	1MT-HA used/ $\mu\text{mol}$	% 1MT modification ( $^1\text{H-NMR}$ )	1MT released/nmol
1MT-HA MN	34.51	6.0	3.61

**Figure 5.18 RP-HPLC characterisation of 1MT released from 1MT-HA MNs.** Shown are the full chromatogram of 1MT-HA MN with UV detection at 223 nm and the section of interest from 4.25-5.75 min RT in which 1MT is observed. 1MT was quantified based on % 1MT modification yield characterised by  $^1\text{H-NMR}$  and a previously performed 1MT calibration curve by HPLC.

### 5.2.7 Fabrication, functionalisation, and characterisation of HA-based implants

For the fabrication of the dissolvable HA-based implantable drug delivery device, a 3 mM solution of low molecular weight (33 kDa) HA in MilliQ water was deposited into a well of a 48-well plate and the water evaporated for 3 days under reduced pressure. The resulting disc with a diameter of 11 mm was carefully removed and stored at 4°C until further use (**Figure 5.19**). The following sections describe the incorporation of immunomodulatory agents into HA implants, their release behaviour, and functional evaluation for use in anti-cancer applications.

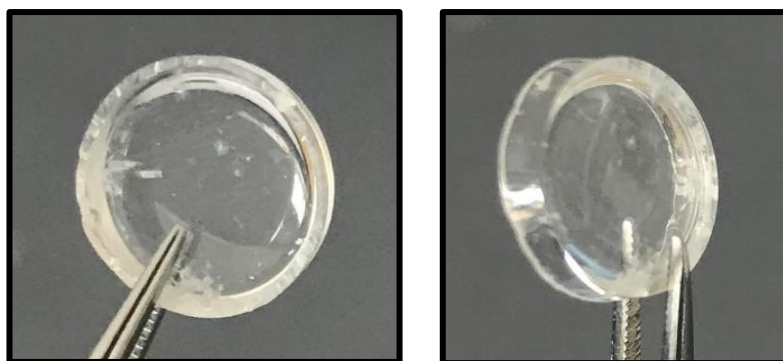


**Figure 5.19** Images of a blank HA implantable disc as a biodegradable drug administration device.

### 5.2.8 IONP micelle loaded HA implant

The loading of IONP micelles into the HA matrix to create IONP releasing HA implants was investigated. For this, a solution of 83.5 nM IONPs in MilliQ water was added HA to form the implant matrix, which was homogenised prior to deposition into the mold followed by the drying process as previously described. To determine the release profile of the IONP from the implant, the disc was degraded in phosphate buffer supplemented with 18.2 nmol HAase at 37°C for 48 h and aliquots were collected at timepoint 0, 24 and 48 h. The samples were purified by centrifugal filtration and washed several times with MilliQ water. The retentate solutions were analysed by UV-vis and DLS to establish the release kinetics, incorporation efficiency and particle integrity compared to the IONPs prior to implant incorporation. The UV-vis analysis was carried out at 380 nm from which the concentration of Fe in the nanoparticle solution was determined based on a previously performed calibration curve. A total of 88.5% of IONP was released from the implant after 48 h, but interestingly only a small increase was observed with respect to the previous 24 h timepoint, proving that most of the implant has been degraded within the 24 h timepoint (**Figure 5.20**). The entire IONP solution was incorporated into the implant and the preparation consists of a single step, which explains the considerably higher incorporation efficiency compared to the MN devices. The sharp peak at 210 nm indicates that some HA aggregates do not pass through the centrifugal filter and could, therefore, not be entirely removed from the sample. However, this peak does not interfere with the IONP absorbance at 380 nm. The remaining 11.5% of IONP were potentially lost in the centrifugal filter devices during the purification process.

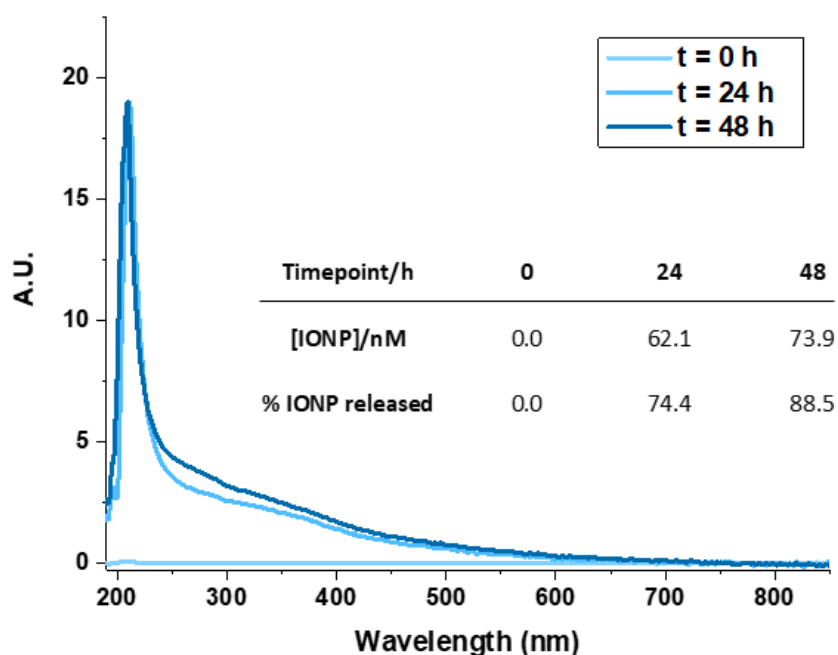


**Figure 5.20 IONP implant degradation experiment UV-vis characterisation.** IONP samples collected at 0, 24 and 48 h were collected and analysed by UV-vis at 380 nm. As a control, the IONP stock solution used for the implant preparation was analysed. The IONP concentration was calculated based on a previously performed calibration curve and conversion calculation based on the particle surface area.

The average hydrodynamic size of the IONP micelles by DLS showed an increase from 38 nm before incorporation to 110 nm after 48 h implant degradation, indicating the presence of small aggregates (**Figure 5.21**). The derived count rate can be a useful parameter to estimate the NP concentration in the sample. The low average derived count rate at the 0 h timepoint was consistent with the UV-vis results showing almost complete absence of NPs in the solution, while for the 24 h and 48 h samples the count rate was between 2500-2600 suggesting no significant increase in particle concentration between the latter 2 timepoints. The different characterisation methods showed consistency in the rate of IONP micelle release from the implant and demonstrate that the particles were gradually released and remained structurally intact with minor aggregation.



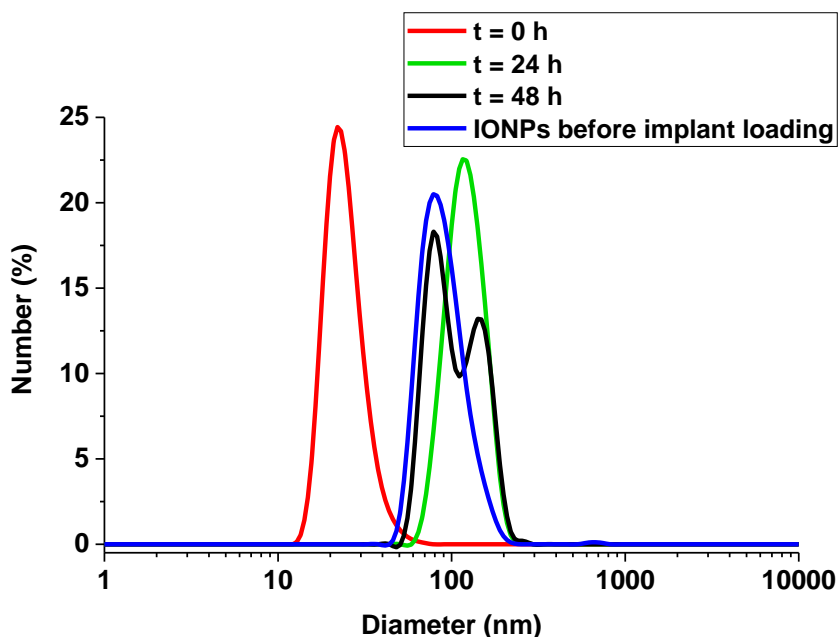
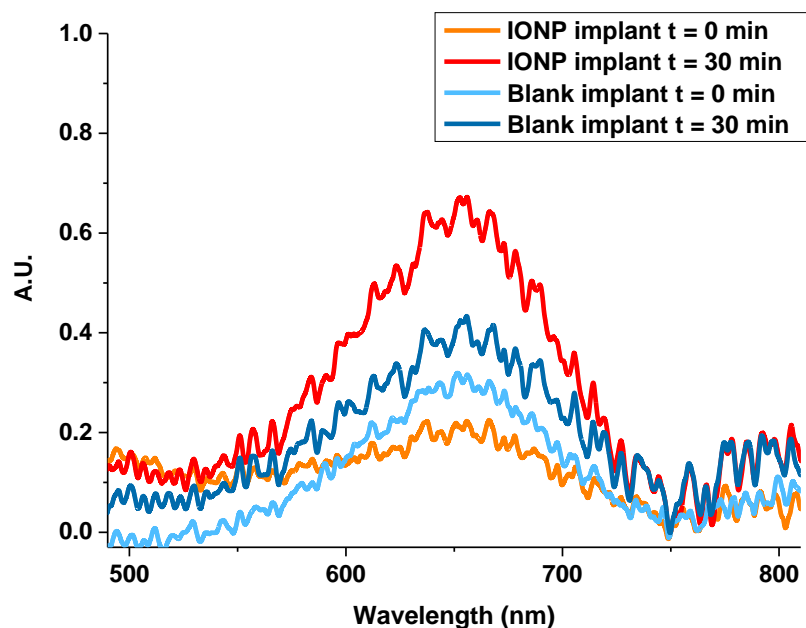


**Figure 5.21 DLS characterisation of IONP micelle released from IONP implant.** Illustrated is the IONP micelle average size by number distribution of IONP release from implant at timepoints  $t = 0, 24$  and  $48$  h. The average size distribution of the IONP micelles before loading into the implant is shown in blue (each curve represents the average of 3 repeat measurements) ( $N = 1$ ).

To determine whether the IONP released from an implantable device retain their functional activity, a peroxidase-like activity assay was performed as previously described. The IONP released from the HA implant after 48 h was diluted to a working Fe concentration of 0.2 mM and UV absorbance measured at timepoints 0 and 30 min after TMB addition. The IONP samples show almost a 5-fold higher  $\Delta$  A.U. compared to a blank implant control sample without IONPs, suggesting that the IONPs retain their catalytic activity after incorporation and release from the HA-based implantable device (**Figure 5.22**).



	IONP implant	Blank implant (Control)
$\Delta$ A.U.	0.458	0.094

**Figure 5.22 Peroxidase-like activity assay of IONP released from HA implant.** The Peroxidase-like activity of the IONP micelles released from the implant after 48 h degradation was analysed based on the absorbance difference at 652 nm at timepoints  $t = 0$  and 30 min after TMB addition ( $N = 1$ ).

### 5.2.9 IONP-DOTAP-pIC-R837 loaded HA implant

The IONP-DOTAP-pIC immunomodulatory construct that was synthesised and characterised in Chapter 3 (**Figure 3.16**) was incubated with the TLR7 agonist, imiquimod (R837), overnight at RT to allow for electrostatic adsorption to the IONPs followed by incorporation of this mixture into a HA implant using the casting process, as previously described. Once dried, the IONP-DOTAP-pIC-R837 loaded HA implant was degraded in the presence of HAase in culture medium under sterile conditions for 48 h at 37°C. Simultaneously, a blank HA implant was degraded under the same conditions as the negative control. The solution from the degraded implants were collected and the functional activity analysed in a Transwell co-culture assay using B16-F10(OVA) melanoma cells and RAW264.7 macrophages. This setup allowed the released payload from the implant to gradually pass through the membrane that and interact with the cells (**Figure 5.23 A**). As the positive control, a fresh solution of IONP-DOTAP-pIC-R837 was prepared and maintained at a working concentration of Fe = 0.5 mM. The cells were seeded into the top compartment of the Transwell and incubated overnight followed by the addition of the treatment and control samples into the bottom compartment and

incubated for 24 h. The cells were then removed, and the cell viability characterised by flow cytometry (**Figure 5.23 A-D**).

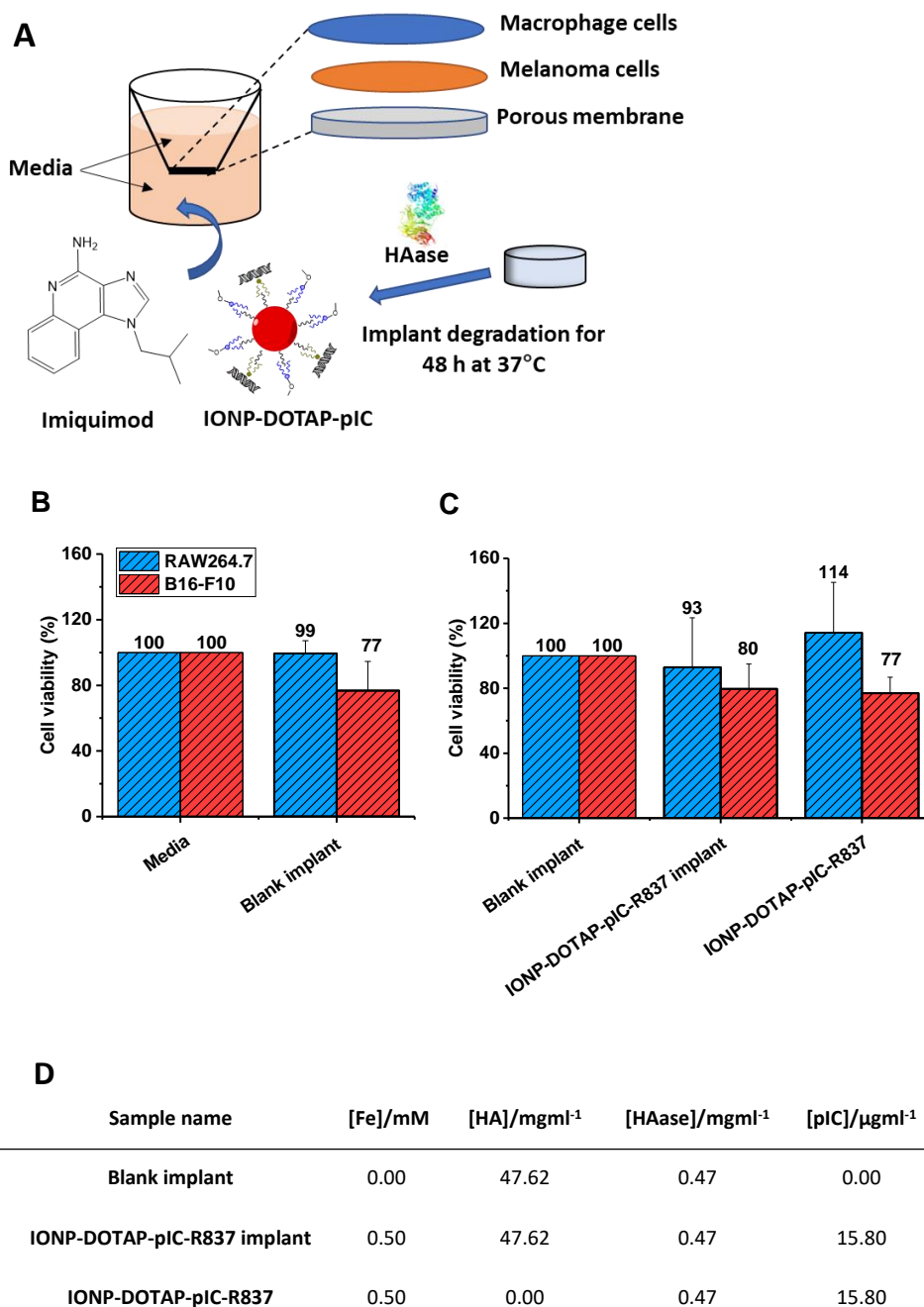
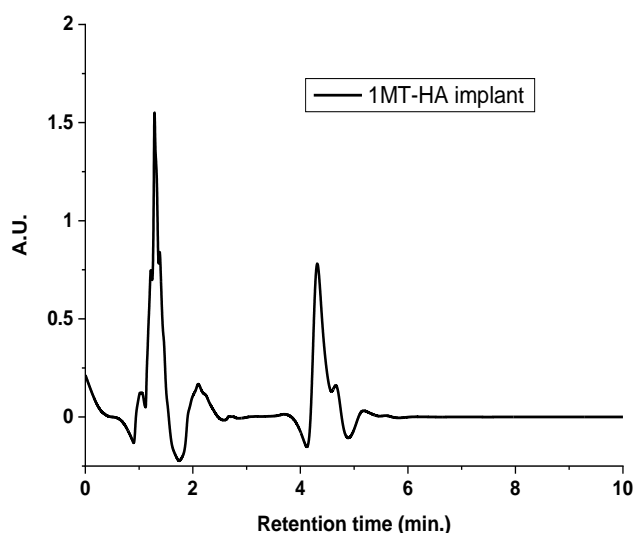


**Figure 5.23 Transwell co-culture assay of IONP-DOTAP-pIC implant.** (A) Illustration of Transwell set-up with melanoma cells (B16-F10(OVA)) and macrophages (RAW263.7) in the top compartment and the immunomodulatory drug load released from the implant added to the bottom compartment, which were separated by a porous membrane. (B) % Cell viability of both cell lines normalised to the media control after 24 h incubation with the blank HA implant based on flow cytometry ( $N = 3$ ). (C) % Cell viability of the cells after 24 h incubation with the IONP-DOTAP-pIC-R837 implant and controls normalised to the blank implant ( $N = 3$ ). (D) Summary table of working concentrations of the therapeutic agents in the implants and controls.

The blank implant itself already showed a reduction in the cell viability of the melanoma cells after 24 h incubation (**Figure 5.23 B**). When the cell viability results were normalised to the blank implant in order to analyse the therapeutic contribution of the loading agent, a 20% reduction in cell viability of the melanoma cells was observed for the immunomodulatory IONP-loaded implant compared to the blank implant control (**Figure 5.23 C**). This suggests that the released nanovaccine maintained its functional activity, acting synergistically through both the intrinsic peroxidase-like activity of the IONP and the immunostimulatory effects of the TLR3 and TLR7 agonists. The reduction in tumour cell viability for the IONP-DOTAP-pIC-R837 implant was consistent with the positive control sample. Therefore, it can be reasoned that tumour cell targeted cytotoxicity observed from the immunomodulatory implant in this experiment is significant and presents a promising vaccine delivery platform that can incorporate and locally release therapeutic agents without compromising their functional activity.

### 5.2.10 1MT-HA loaded implant

An implantable disc incorporating the 1MT-HA biomaterial that was synthesised and characterised in Chapter 2 was prepared using the previously described casting method and then degraded to determine the release efficiency. The degradation of the implant was carried out for 48 h, and the 1MT released was analysed by RP-HPLC as previously described (**Figure 5.24**). The 1MT peak recorded at a retention time of 4.3 min showed a release of 600 nmol. This experiment demonstrated that 1MT-HA can be incorporated into a HA-based implantable device and the 1MT released over a period of 48 h can be quantified by HPLC, which suggests that the 1MT retains its structural integrity throughout covalent modification to HA, incorporation into a solid implant and release from the implant. The next stage of this chapter will assess the immunomodulatory activity of the released 1MT in representative *in vitro* IDO inhibition assays.



Sample	1MT-HA incorporated/ $\mu$ mol	1MT incorporated/ $\mu$ mol	1MT released/ $\mu$ mol
1MT-HA implant	155.3	9.3	0.6

**Figure 5.24 Characterisation of 1MT-HA implant degradation experiment by RP-HPLC.** Presented is the chromatogram of 1MT released from the 1MT-HA implant after degradation for 48 h characterised by RP-HPLC at 223 nm UV ( $N = 1$ ).

## 5.2.11 Functional assays with an immunomodulatory 1MT-HA implant

### 5.2.11.1 Non-cell based IDO inhibition assay with 1MT-HA implant

The degree of IDO inhibition by 1MT can be analysed by determining the amount of L-kynurenine generated by IDO in the presence of the inhibitor by RP-HPLC. The IDO inhibition assay involved the addition of a solution of the 1MT released from the 1MT-HA implant at working concentration of 0.5 mM 1MT to the assay medium containing IDO enzyme and L-tryptophan (Trp) substrate and the mixture was incubated at 37°C for 1 h to allow complete metabolism of tryptophan into N-formylkynurenine (+Trp/+1MT-HA (0.5 mM 1MT)). Following the incubation period, trichloroacetic acid (TCA) was added followed by incubation of the reaction for a further 15 min at 60°C to hydrolyse the intermediate product into L-kynurenine. The positive control sample was performed in the absence of 1MT (+Trp/-1MT). As a negative control, a fresh sample of 1MT was added at the same concentration (+Trp/+0.5 mM 1MT) and another control was an IDO in the absence of L-tryptophan (-Trp/-1MT). The samples were purified by centrifugation and the amount of L-kynurenine generated was quantified by RP-HPLC at UV absorbance of 360 nm based on a calibration curve of L-

kynurenine produced using the same assay conditions (**Figure 5.25**) (**Appendix 10**). To demonstrate that the kynurenine peak had no interference from other component in the reaction, samples of individual components including 1MT and L-tryptophan were analysed under the same conditions (**Appendix 11**).

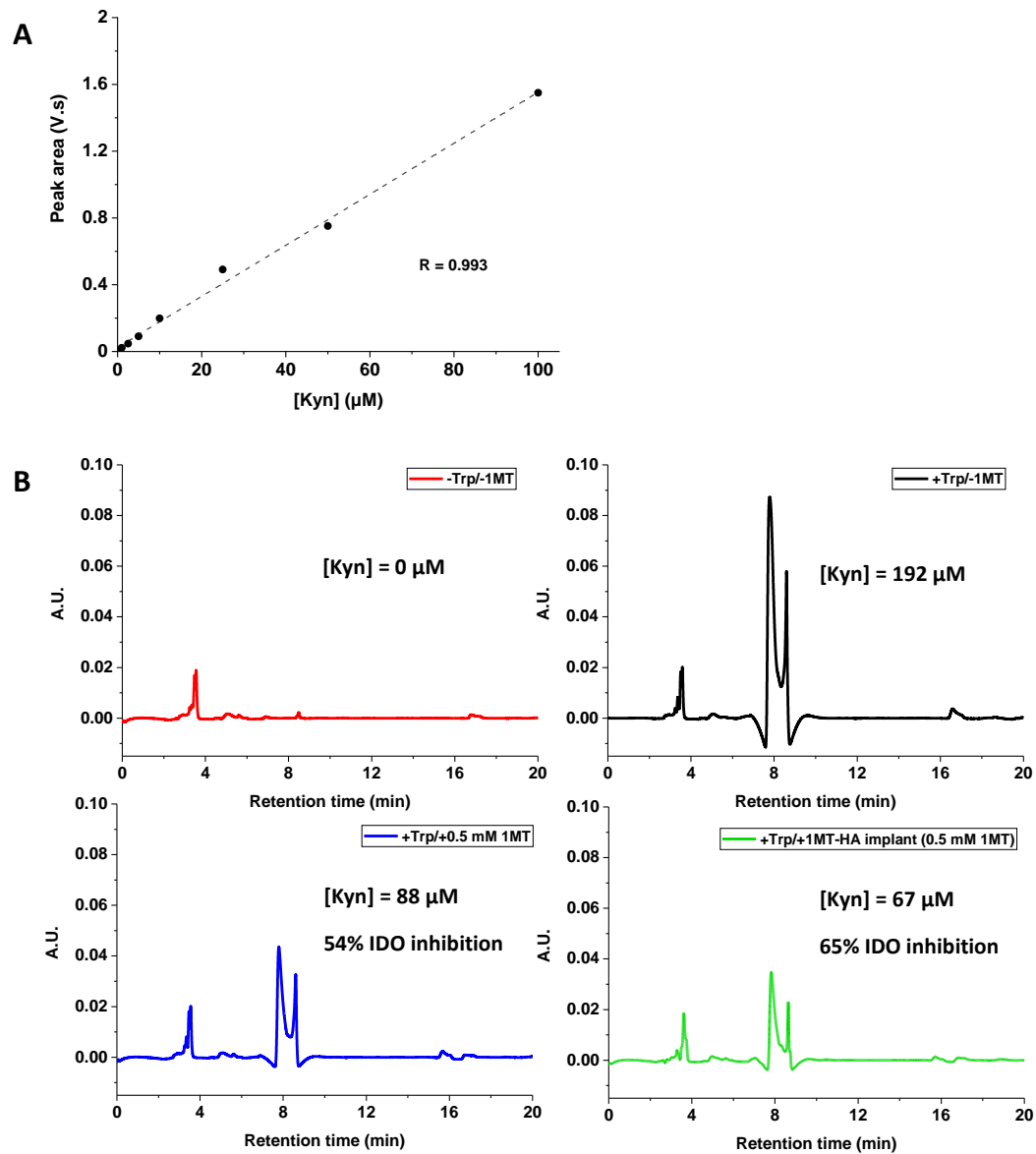


**Figure 5.25 Representative non-cell based IDO inhibition assay with the 1MT-HA implant.** (A) Kynurenine calibration curve from 0-100  $\mu\text{M}$  based on peak area at 360 nm ( $N = 1$ ). (B) HPLC chromatograms of positive controls without the inhibitor (+Trp/-1MT) and with the inhibitor (+Trp/+1MT), negative control (-Trp/-1MT) and 1MT-HA implant sample (+Trp/+1MT-HA implant (0.5 mM 1MT)) ( $N = 1$ ).

The amount of L-kynurenine produced in the +Trp/-1MT control was 192  $\mu\text{M}$ , whereas the sample containing the 1MT released from the 1MT-HA implant yielded 67  $\mu\text{M}$  L-kynurenine corresponding to 65% IDO inhibition. This experiment confirms that 1MT released from a 1MT-HA biomaterial implant retains its functional properties by suppressing IDO activity.

### 5.2.11.2 IDO inhibition assay with 1MT-HA implant using HeLa cells

The IDO inhibition properties of 1MT were characterised using a human cervical cancer cell model (HeLa cells). Since the experimental conditions have changed with respect to the non-cell-based assay, a new L-kynurenine calibration curve was produced from 0.0-0.2 mM. The calibration curve shows a linear concentration-absorbance relationship with an  $R^2$  of 0.999 (Figure 5.26) (Appendix 12).

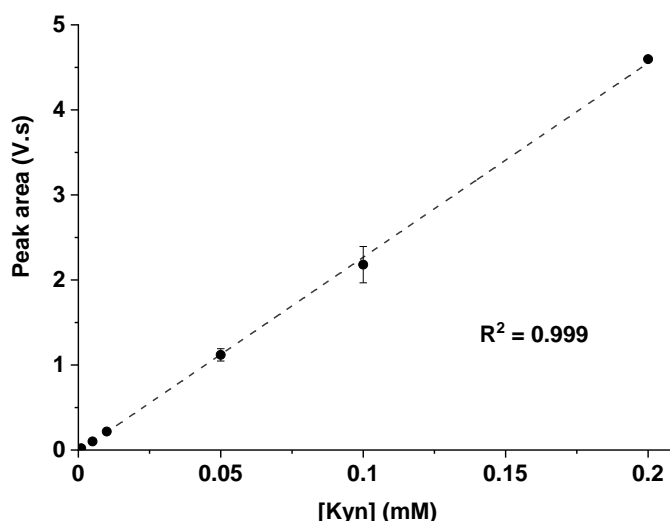


**Figure 5.26** L-kynurenine calibration by RP-HPLC at UV absorbance detection of 360 nm ( $N = 3$ ).

To demonstrate the increase in inhibitory activity of 1MT, the IDO inhibition assay was first carried out at different concentrations of 1MT from 0-500  $\mu$ M. HeLa cells were seeded at  $2 \times 10^5$  cells per well in a 96-well plate in culture medium. After 20 h, IFN- $\gamma$  at 0.4  $\mu$ g/ml and the 1MT samples were added to the cells in triplicate. The negative control was prepared in the absence of IFN- $\gamma$  and 1MT to evaluate the presence of any impurities that could interfere with the kynurenine peak in the chromatograms. The cells were incubated overnight, after which the supernatants were collected and treated with TCA to precipitate large biomolecules and residual cells as well as to ensure complete hydrolysis of N-formylkynurenine into L-kynurenine. The cell supernatants were purified by centrifugation and then characterised by RP-HPLC with UV detection of kynurenine at 360 nm.

The overlaid chromatograms show a steady decrease in kynurenine concentration as the inhibitor concentration increased at a retention time of 7.5-8.5 min confirming that the HeLa cells respond functionally towards cytokine stimulation and the inhibitor in a concentration dependent manner. No peak was observed in this region for the negative control, demonstrating that there were no interfering compounds after purification of the cell

supernatants (**Figure 5.27 A**). A maximum kynurenine production of 38.6  $\mu\text{M}$  was observed in the absence of the inhibitor under these experimental conditions, whilst the highest inhibition of 53.9% was recorded using 500  $\mu\text{M}$  1MT (**Figure 5.27 B**). The cell viability for all samples was > 98% demonstrating that the 1MT was not toxic to the cells at concentrations up to 0.5 mM (**Figure 5.27 C**).

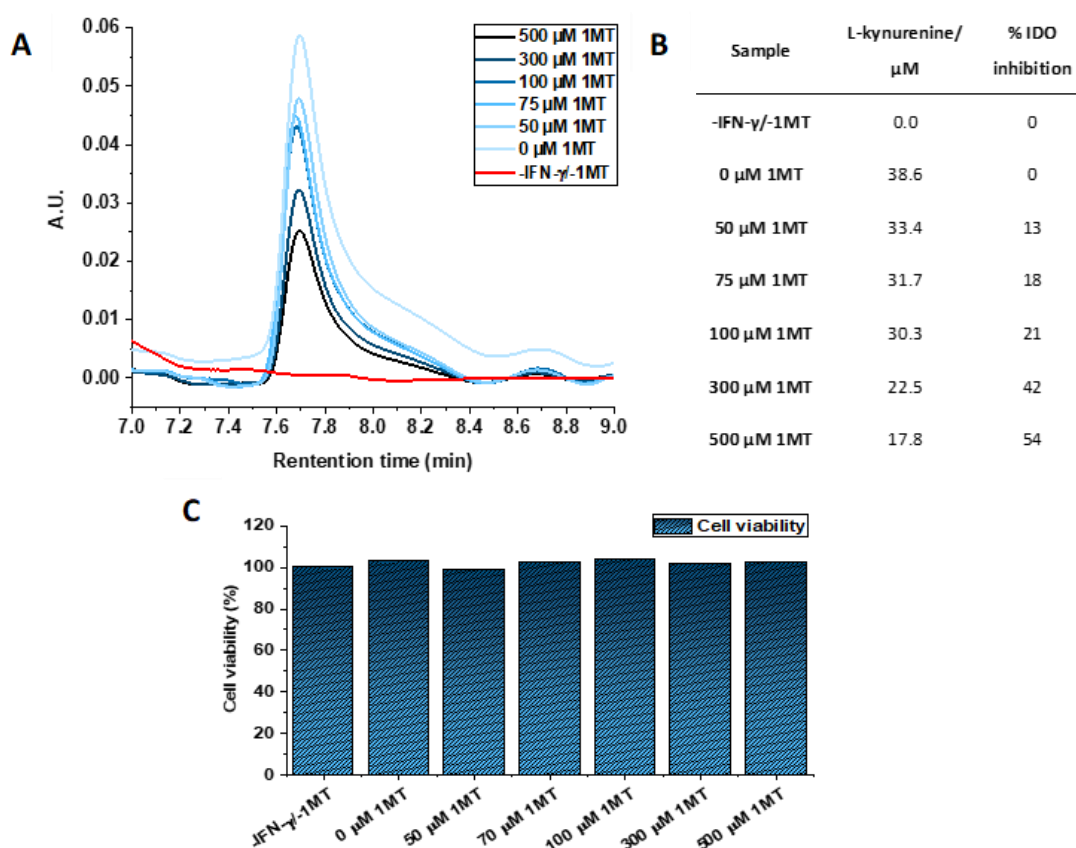


**Figure 5.27 HeLa cell IDO inhibition screening at different concentrations of 1MT.** (A) RP-HPLC characterisation of L-kynurenine produced by HeLa cells treated with 1MT at concentrations from 0 to 500  $\mu\text{M}$ . (B) Graph representation of 1MT concentration to % IDO inhibition relationship. (C) MTT cell viability assay following HeLa cell incubation with 1MT samples for 20 h. % Cell viability presented in relation to -IFN- $\gamma$ /-1MT control ( $N = 1$ ).

To determine the IDO inhibition with the immunomodulatory 1MT-HA implant, the 1MT released from the implant following degradation in the HAase over 48 h was added to HeLa cells under the same experimental conditions as previously described at a fixed 1MT concentration of 100  $\mu\text{M}$  (**Figure 5.28 A**). As a control, an equimolar amount of 1MT was prepared ((+IFN- $\gamma$ /+1MT) and an additional control in the absence of both 1MT and IFN- $\gamma$  was analysed (-IFN- $\gamma$ /-1MT). The positive control was prepared in the absence of the inhibitor to evaluate the maximum amount of L-kynurenine produced (+IFN- $\gamma$ /-1MT). An additional control was a blank HA implant without 1MT incorporation to assess the effect of the HA and



account for possible impurities or contaminants in the preparation and degradation process of the implant. A cell viability assay was performed after the supernatant collection to demonstrate that the samples were free from potentially cytotoxic impurities (**Figure 5.28 C**). Shown in the table below are the IDO inhibition results derived from the RP-HPLC quantification of L-kynurenine and the HeLa cell viability assay for the 1MT-HA implant and the control samples (**Figure 5.28 D**). The L-kynurenine concentration reduced for the 1MT-HA implant compared to the +IFN- $\gamma$ -1MT control, corresponding to 18% IDO inhibition (**Figure 5.28 B, D**). This is confirmation that 1MT retained its therapeutic activity after covalent HA modification, incorporation into a biomaterial-based implant and release from the implant under physiological conditions. The blank HA implant did not induce any IDO inhibition indicating that there were no interfering compounds in the sample. As expected, the -IFN/-1MT did not produce any L-kynurenine, confirming that cytokine stimulation is essential to induce IDO expression in the HeLa cells. This assay confirms that the synthesised 1MT-HA implant is functionally active and has the potential for future clinical development as an implantable drug delivery device for cancer immunotherapy.

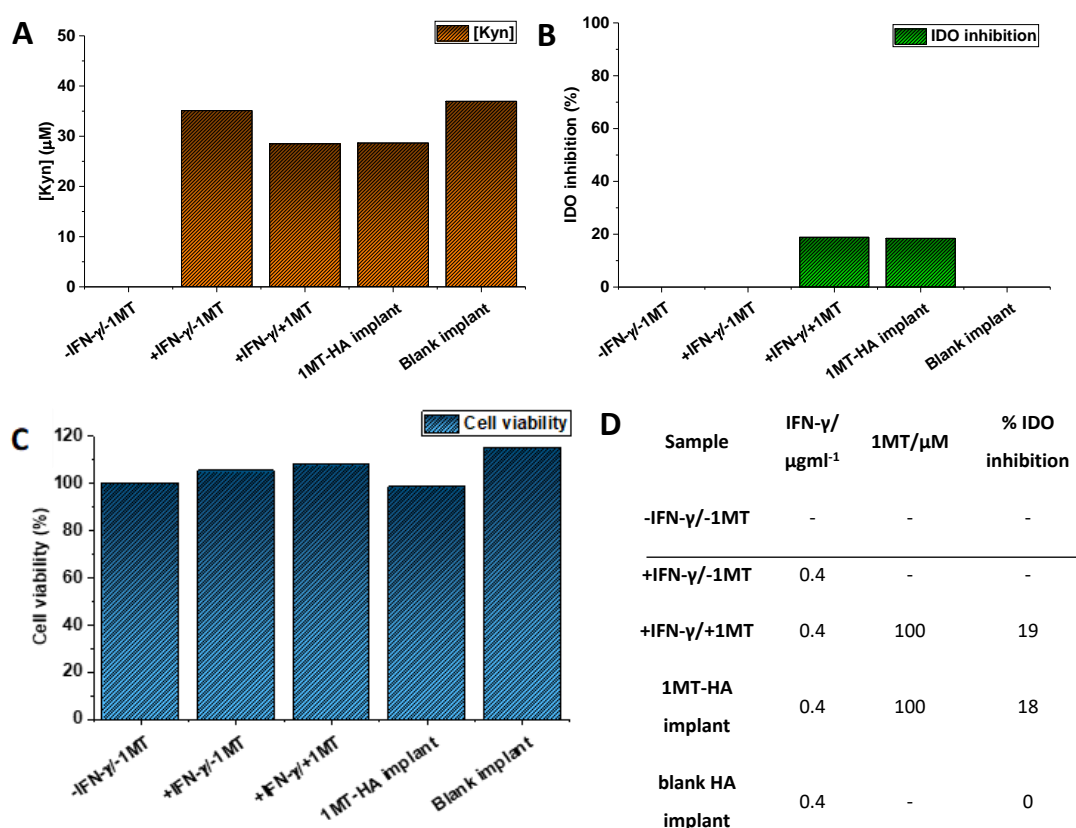


**Figure 5.28 Representative IDO inhibition assay with 1MT-HA implant using HeLa cells.** (A) RP-HPLC quantification of L-kynurenine generated and (B) % IDO inhibition analysis. -IFN-  $\gamma$ /-1MT corresponds to the cells without stimulation of IFN- $\gamma$ , while the +IFN- $\gamma$ /-1MT corresponds to the cells incubated in the presence of IFN- $\gamma$ , but without the inhibitor. +IFN- $\gamma$ +1MT means

the cells were incubated in the presence of IFN- $\gamma$  and a fresh sample of 1MT at 100  $\mu$ M. The blank implant was an additional control in which the cells were incubated in the presence of IFN- $\gamma$  under the same conditions as the functional 1MT-HA implant. (C) MTT viability assay with HeLa cells after treatment with implant sample and controls. (D) Tabular summary of conditions used for the assay and % IDO inhibition. (D) Summary of conditions used % IDO inhibition (N = 1).

### 5.2.11.3 Screening of IDO inhibition of 1MT-HA implant on different cancer cell lines

To explore the potential IDO inhibition properties of the 1MT-HA implant on other cancer cell models, a screening of different murine and human cancer cell lines was performed including a murine colon cancer model (MC-38), murine melanoma (B16-F10), murine breast cancer cells (4T1), human lung adenocarcinoma (LC2/ad) and human ovarian cancer cells (OVCAR8 and Skov3). Initially the cell lines were analysed for IDO expression and 1MT inhibition with an unmodified 1MT sample at different experimental conditions as outlined in **Table 5.1**.

**Table 5.1 Experimental conditions used for the analysis of IDO expression in different cancer cell lines.**

	Seeding density (cells/well)	[L-tryptophan]/ $\mu$ mol	[IFN- $\gamma$ ]/ $\mu$ gml <sup>-1</sup>
<b>Conditions A</b>	10,000	80	0.1
<b>Conditions B</b>	20,000	80	0.4

The cells were stimulated with either human or murine derived IFN- $\gamma$  in combination with the 1MT inhibitor and incubated at 37 °C overnight. The supernatants were collected the following day and the amount of L-kynurenine released was quantified by RP-HPLC. With regards to the human cell lines, the OVCAR8 cells showed IDO stimulation and inhibition in the presence of 1MT with a maximum L-kynurenine generation of 11.6  $\mu$ M and 27% IDO inhibition using conditions B. The Skov3 cells demonstrated IDO stimulation in the presence of IFN- $\gamma$ , but no inhibition was observed in the presence of 1MT at both experimental conditions. In contrast, the LC2/ad cells showed negligible IDO stimulation as illustrated in **Figure 5.29**.

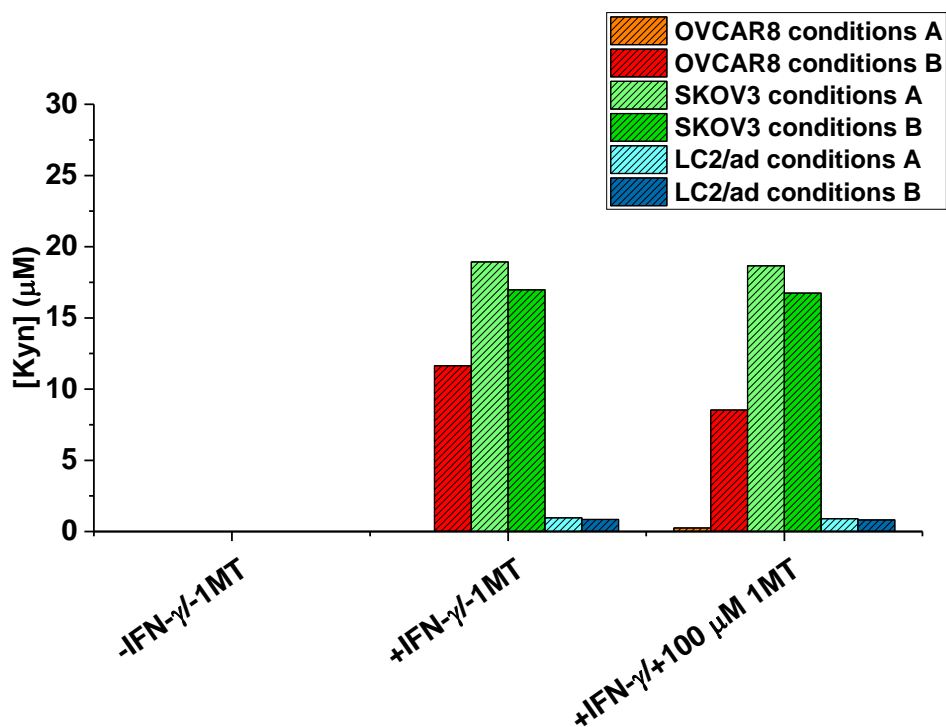


**Figure 5.29 Representative IDO inhibition assay of different human cancer cell lines.** Supernatants recovered from IDO inhibition assay using ovarian OVCAR8 and Skov3 cells as well as the lung adenocarcinoma LC2/ad cells were characterised by RP-HPLC. Kynurenine was detected at 360 nm with characteristic peak at RT 7.5 - 8.0 min. The -IFN-γ/-1MT control corresponds to the cells without stimulation of IFN-γ and without the inhibitor, whilst the +IFN-γ/-1MT control corresponds to the cells incubated in the presence of IFN-γ, but without the 1MT inhibitor (N = 1).

On the other hand, the murine MC38 cells exhibit both IDO stimulation and some inhibition in the presence of 1MT using conditions B indicating that these cells do not respond as efficiently to the inhibitor compared to the OVCAR8 cells. Stimulation of both the B16-F10 and 4T1 cells did not induce significant IDO expression under these conditions as shown in **Figure 5.30**.

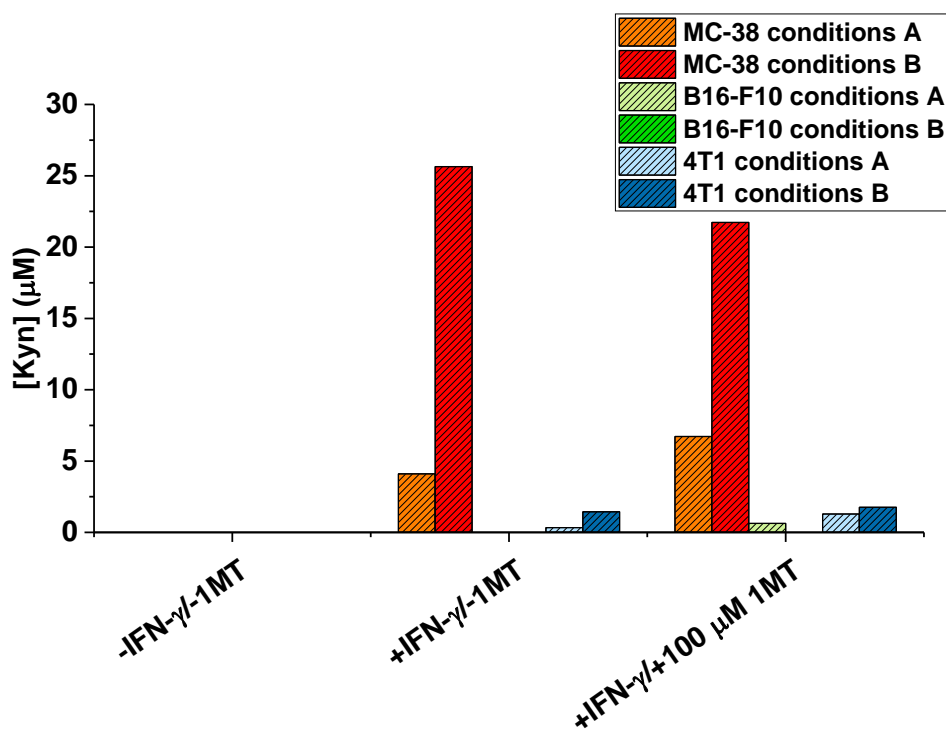


**Figure 5.30** IDO inhibition assay of different murine cancer cell lines. Cell supernatants recovered from IDO inhibition assay using colon adenocarcinoma MC-38 cells, melanoma B16-F10 cells and breast cancer 4T1 cells were characterised by RP-HPLC. Kynurenic acid was detected at 360 nm with characteristic peak at RT 7.5-8.0 min. The -IFN-γ/-1MT control corresponds to the cells without stimulation of IFN-γ, while the +IFN-γ/-1MT control corresponds to the cells incubated in the presence of IFN-γ, but without the 1MT inhibitor (N = 1).

#### 5.2.11.4 IDO inhibition assay with 1MT-HA implant using OVCAR8 and MC38 cells

The cell lines that favourably showed both IDO stimulation and inhibition with 1MT, were selected for further analysis for the functional activity assays with the immunomodulatory 1MT-HA implant. The 1MT released from the implant after degradation for 48 h was added to the OVCAR8 and MC-38 cells and the IDO inhibition was monitored using 'conditions B' as outlined in **Table 5.1**. In the assay with the OVCAR8 cells, the quantification of L-kynurenic acid in the cell supernatants by RP-HPLC showed an IDO inhibition of 14% with the 1MT-HA implant, whilst the blank HA implant produced a comparable amount of L-kynurenic acid to the +IFN-γ/-1MT control (**Figure 5.31 A-D**). The +IFN-γ/+1MT corresponding to 0.1 mM 1MT also exhibited 14% IDO inhibition. No reduction in cell viability was observed with the controls and implants based on the MTT assay (**Figure 5.31 C**), which proved that the inhibitor released from the implant was functionally active and non-cytotoxic.

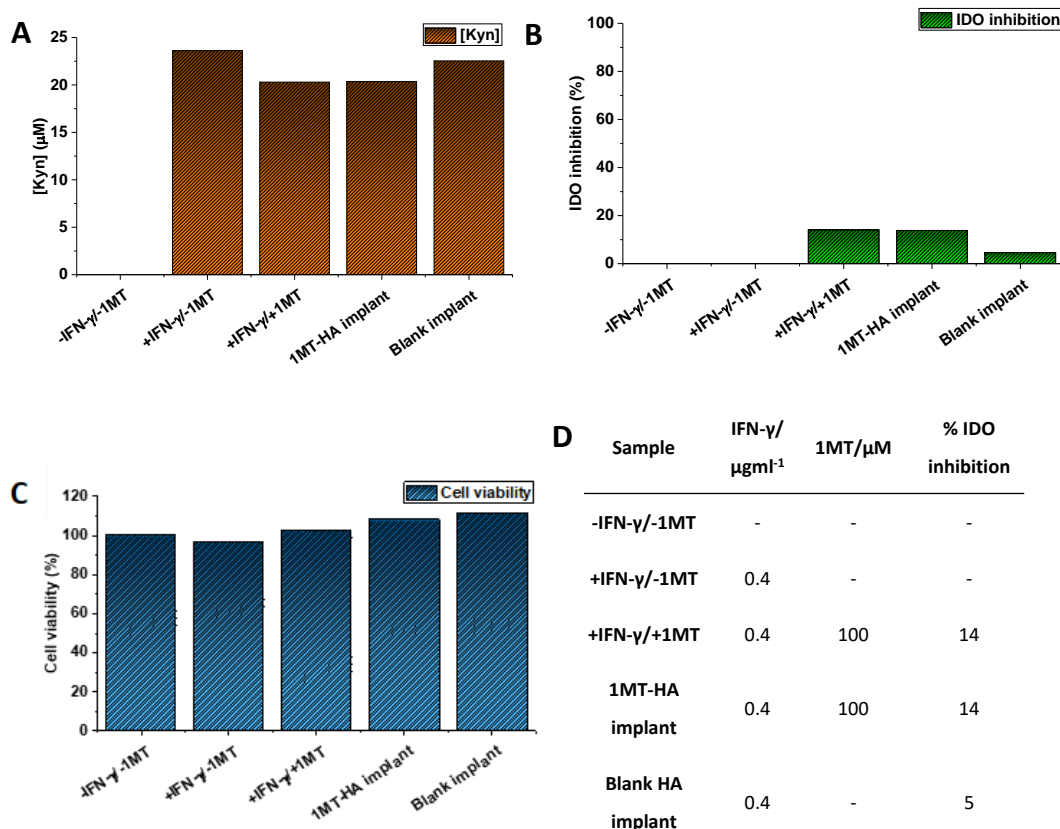


**Figure 5.31 Representative IDO inhibition assay with 1MT-HA implant and controls using OVCAR8 cells.** (A) RP-HPLC quantification of L-kynurenine generated and (B) % IDO inhibition analysis. (C) MTT assay of the tumour cells after completion of IDO inhibition experiment. The -IFN-γ/-1MT control corresponds to the cells without stimulation of IFN-γ, while the +IFN-γ/-1MT control corresponds to the cells incubated in the presence of IFN-γ, but without the inhibitor. -IFN-γ/+1MT control means the cells were incubated in the presence of IFN-γ and a fresh sample of 1MT at 0.1 mM. The blank implant was an additional control in which the cells were incubated in the presence of IFN-γ under the same conditions as the 1MT-HA implant (D) Tabular summary of conditions used for the assay and % IDO inhibition (N = 1).

In the case of the MC38 cells, the assay showed a clear reduction in L-kynurenine generation when the cells were treated with the blank HA implant without a decrease in cell viability, which could be due to non-specific IDO inhibition by HA fragments in these cells (**Figure 5.32 A**). To my best knowledge, this interference of HA of IDO activity in MC38 cells has not been reported and was not observed in the other cell lines investigated in this work. Furthermore, an IDO inhibition of 81.2% was observed with the 1MT-HA implant demonstrating that the 1MT released retained its functional activity (**Figure 5.32 B, D**). The IDO inhibition with the immunomodulatory implant was higher compared to the -IFN-γ/+1MT control at the same 1MT concentration due to the additional contribution from the implant itself as observed with the blank HA implant. There was no reduction in cell viability recorded for all the controls and the implants proving that the high reduction in L-kynurenine production was not due to cell cytotoxicity (Figure 5.32 C).

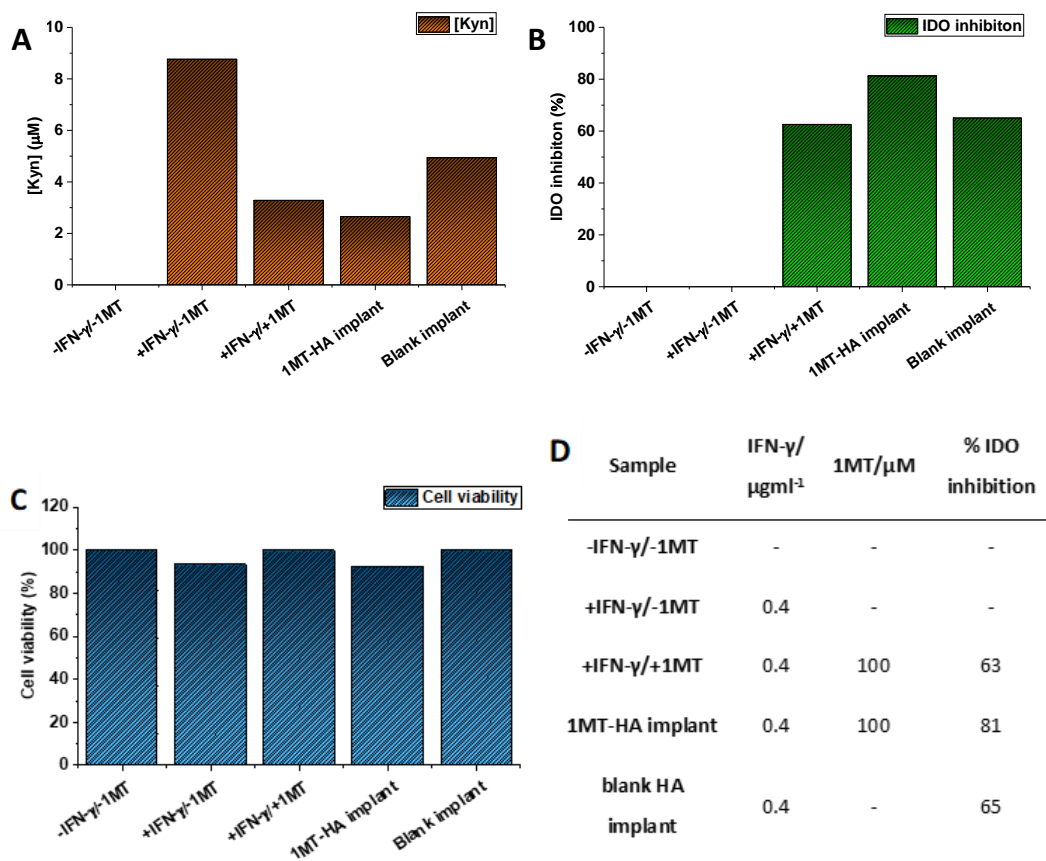


**Figure 5.32 Representative IDO inhibition assay with 1MT-HA implant and controls using MC38 cells.** (A) RP-HPLC quantification of L-kynurenine generated and (B) % IDO inhibition analysis. (C) MTT assay of the tumour cells after completion of IDO inhibition experiment. The -IFN-γ/-1MT control corresponds to the cells without stimulation of IFN-γ, while the +IFN-γ/-1MT control corresponds to the cells incubated in the presence of IFN-γ, but without the inhibitor. The +IFN-γ/+1MT control means the cells were incubated in the presence of IFN-γ and a fresh sample of 1MT at 0.1 mM. The blank implant was an additional control in which the cells were incubated in the presence of IFN-γ under the same conditions as the functional 1MT-HA implant. (D) Tabular summary of conditions used for the assay and % IDO inhibition (N = 1).

## 5.3 Discussion

This chapter describes the fabrication of biodegradable biomaterial-based HA MNs, and implantable devices incorporated with different NPs systems, immunomodulatory agents and anti-cancer agents including QD micelles, IONP micelles, 1MT and the 1MT-HA biomaterial. The optimised HA MNs with a needle length of approximately 700  $\mu\text{m}$  and tip diameter of 20  $\mu\text{m}$  had high homogeneity throughout the MN patch and reproducibility between different patches (**Figure 5.4**). This would be suitable for human skin administration since the dermal layer thickness is around 2 mm at a depth of approximately 120  $\mu\text{m}$  from the skin surface, although these parameters can vary depending on factors such as body part, gender, and age.<sup>461</sup>

The successful skin penetration depends on parameters such as needle tip sharpness as well as MN mechanical strength. For example, a study by Chen *et al.* reported that chitosan MNs with a tip diameter of 5  $\mu\text{m}$  penetrated much better than MNs with a tip diameter of 10  $\mu\text{m}$ .<sup>462</sup> The MN penetration efficiency was characterised using porcine skin, which is a suitable model for human skin due to its similar physical properties such as hair sparseness and thickness.<sup>463</sup> Skin pre-treatment with HAase enhanced MN degradation rate with optimal MN application time observed after 24 h (**Figure 5.9**). We observed a maximum penetration efficiency of 84% (**Figure 5.11**), which is comparable to the penetration efficiency reported by Todd *et al.* using polymeric PMMA microneedle patches with similar dimensions.<sup>464</sup> Similar results were observed in a human skin model by van der Maaden *et al.* achieving 80% penetration efficiency using a silicon MN patch.<sup>465</sup> The inherent porcine and human skin elasticity, topography, and hairs are known causes for typical MN penetration efficiencies below 100%.<sup>466</sup> The skin penetration depth evaluated on the cross section of a stained skin sample after MN application showed an average depth of 560  $\mu\text{m}$ , which corresponds to 80% of the needle length. This is comparable to literature values of MN skin penetration assays with other polymer-based dissolving MNs although also lower values have been reported.<sup>467-</sup>

469

The blank MNs showed high cell viability in a melanoma-macrophage co-culture assay (**Figure 5.12**). The cell viability observed for the MN base exceeding 100% is possibly due to the known proliferative effect of HA on cells via CD44 signalling.<sup>364</sup> The preparation and characterisation of QD micelle loaded fluorescent MNs patch established the potential to incorporate any hydrophilic anti-cancer and immunomodulatory agent in these HA MNs (**Figure 5.13**). The incorporation of IONP micelles into MNs was confirmed visually due to

the red colour of the tips and by EDX, which showed Fe L $\alpha$ 1 and K $\alpha$ 1 emission energies corresponding to literature values (**Figure 5.14**).<sup>470</sup> A gradual release of IONP from the MNs was observed over 24 h in the presence of HAase, although some aggregation was detected (**Figure 5.15, Figure 5.16**). However, the IONPs were still in the desirable size range reported, for instance, for immunoliposome in clinical oncology applications and for effective biomaterial and drug delivery via the lymphatic system to improve immunological responses.<sup>471-473</sup> The subsequent peroxidase-like activity assay with the IONPs released from the MNs demonstrated significant retention of their functional activity, which highlights the potential of this MN system for the delivery of IONP-based anticancer therapies.

Furthermore, the incorporation and release of the immunomodulatory agent 1MT from HA MNs without compromising its structural integrity was demonstrated (**Figure 5.18**). The biodegradable nature of the HA MNs developed in this thesis allows for the loading of any biomolecule without affecting their functional activity and potentially increasing their stability within the solid matrix of the needles facilitating storage and transport compared to liquid formulations.<sup>474</sup>

The HA-based implantable devices developed in this chapter are designed for patient administration at the tumour resection site during surgical intervention to induce a local immune response and prevent tumour recurrence. An immunomodulatory system based on IONPs surface functionalised with TLR agonists, pIC and R837, through electrostatic interactions was incorporated into a biomaterial-based HA implantable device. A co-culture assay using both immune and cancer cells demonstrated the retention of functional activity of the loading agents after release from the implant. The blank implant already showed a reduction in the cell viability of the melanoma cells after 24 h incubation (**Figure 5.23 A**), which could potentially be due to macrophage activation by the low MW HA towards a proinflammatory state as previously observed by Sokolowska *et al.*<sup>475</sup> The decreased cell viability observed only in tumour cells for the immunomodulatory implant was consistent with the IONP-DOTAP-pIC-R837 control, which is established to have therapeutic properties *in vivo* (**Figure 5.23 B**).<sup>166</sup>

The 1MT-HA biomaterial synthesised in Chapter 3 was used to prepare an implant. The 1MT-HA implant was degraded over 48 h and determined a 1MT release of 600 nmol (400  $\mu$ M), which is a clinically relevant amount, considering that Kumar *et al.* reported an EC<sub>50</sub> of 30  $\mu$ M (**Figure 5.24**).<sup>476</sup> The functional activity of the 1MT released from this implant was initially characterised in a non-cell-based IDO inhibition assay (**Figure 5.25**). This experiment



confirmed the retention of functional activity of 1MT by suppressing IDO activation which is shown in the significant reduction of kynurenine content released compared to the control and is in close agreement with a similar study carried out by Matin *et al.*<sup>477</sup> Following the successful demonstration of functional activity in a non-cell-based assay, the IDO inhibition properties of 1MT released from the implant were characterised using a human cervical cancer cell model (HeLa cells) as it characteristically has a high expression of IDO.<sup>478</sup> An IDO inhibition of 18% was achieved in HeLa cells without cytotoxicity at a concentration of 0.1 mM 1MT, which demonstrated that the 1MT remained structurally intact and functionally active (**Figure 5.28**).

The IDO inhibition of the 1MT-HA implant was also analysed on a range of different human and murine cancer cell lines available, out of which an inhibition effect was observed in colon cancer MC38 cells and ovarian cancer OVCAR8 cells (**Figure 5.29**, **Figure 5.30**). The OVCAR8 cells showed a comparable inhibition to the HeLa cells at the same 1MT concentration (**Figure 5.30**). The MC38 cells exhibited less IDO stimulation in the compared to the OVCAR8 and HeLa cells in the presence of IFN- $\gamma$  potentially due to the expression of IDO through IFN- $\gamma$ -independent mechanisms (**Figure 5.32**).<sup>479</sup> A significant IDO inhibition in the MC38 cells was observed when treated with the blank implant which could be due to small HA fragments interfering in the IDO activation pathway in this cell type although, to my best knowledge, this has not been previously reported. However, further experimentation would be required to confirm these findings. Ultimately, the synthesised biomaterial-based 1MT-HA implant has shown an immunotherapeutic response in different cancer cell types and could potentially be incorporated with multiple anticancer agents for the local and sustained delivery of combination therapies, whilst also having potential application in tissue regeneration.

# Final discussion and outlook

This thesis demonstrates the fabrication of biomaterial-based microneedles and implantable devices for the local administration and gradual release of immunomodulatory and other anticancer agents offering the potential for enhanced immuno- and combination therapies. The first results chapter (Chapter 3) explored the covalent functionalisation of 1MT, an inhibitor of the tumour overexpressed and immunosuppressive IDO enzyme, to a HA biomaterial through an amide bond coupling strategy. The synthesised 1MT-HA biomaterial initially had persistent impurities but could ultimately be eliminated with the development of an ion-exchange resin-based purification method. The 1MT kinetics release study at different pHs over 48 h in the presence and absence of HAase showed a gradual release over time for all conditions, but interestingly the highest release was observed at mild alkaline conditions, which suggest that the release is driven by hydrolysis of the amide bond. Whilst the presence of HAase did not affect the 1MT release rate, its effect on HA degradation was observed due to a reduction in viscosity and an increased presence of small HA fragments. This study suggests that longer time periods are required for complete HA degradation and release of 1MT. However, the slow release of 1MT from the immunomodulatory biopolymer could be beneficial feature in an *in vivo* setting as the 1MT could be retained in the TME for longer time periods without the requirement for repeated dose administrations. The versatility of the biopolymer also allows for this biomaterial to be molded into different shapes such as microneedles and implantable devices that can incorporate other anticancer agents and immunomodulatory agents, as explored in later chapters.

In Chapter 4 several immunomodulatory NP and microparticle systems were synthesised and characterised including biodegradable HA-based NPs, IONPs and biosilica-based diagnostic and therapeutic systems. The amphiphilic characteristic of the 1MT-HA biomaterial allowed for the synthesis of self-assembled NPs, into which the immune checkpoint inhibitor, anti-PD-L1, was incorporated. The 1MT-HA@anti-PD-L1 NPs showed a gradual release of 1MT

over 48 h, which is consistent with the slow release observed with the 1MT-HA biomaterial due to the hydrolytic amide bond cleavage. The anti-PD-L1 release from the NPs was qualitatively assessed showing a gradual release over 48 h. Clinically, this biomaterial-based NP system has the potential to improve tumour targeting and internalisation in CD44-expressing tumour cells as well as the prolonged delivery of combination immunotherapies to overcome the limitations of free drug administration.

Two multimodal IONP systems were developed for the potential incorporation into the biomaterial based MNs and implants produced in Chapter 5. A Pt(IV) prodrug was synthesised from cisplatin by addition of two axial ligands that were used for the covalent attachment to the amine-terminal PEG-based phospholipid coated IONP surface via amide bond coupling. This IONP construct combines both the intrinsic ferroptosis-mediated anticancer properties and magnetic characteristics of the IONPs with the chemotherapeutic and immunomodulatory effect of the Pt(IV) prodrug that could act in synergy to achieve an enhanced therapeutic effect.<sup>164,385,480</sup> The second IONP system involved the functionalisation with the immunomodulatory agents, pIC and R837 through electrostatic interactions. The IONPs were first modified with DOTAP, a cationic lipid, to promote electrostatic interactions with the surface negatively charged pIC. The anionic surface of the IONP-DOTAP-pIC system enabled then the attachment of R837 due to its cationic charge, which resulted in a multifunctional immunomodulatory nanosystem. The synergistic effect of these endosome-targeting immunomodulatory agents and their antitumour response *in vivo* have been previously reported.<sup>481</sup> The incorporation of these NP systems into a MN or implantable device developed in this thesis has the potential improve the therapeutic response in different cancers through localised and gradual delivery.

Furthermore, biosilica-based diatoms were explored as multimodal scaffold for combination therapy and as a biosensor. Commercial diatoms were functionalised with PEI and GOx through electrostatic interactions. This afforded a tandem catalytic system with therapeutic properties due to its potential to locally starve the tumour of its glucose supply whilst generating H<sub>2</sub>O<sub>2</sub> that is broken down into cytotoxic ROS due to the intrinsic peroxidase-like activity of the diatoms.<sup>482</sup> This system was also functionalised with IONPs that added magnetic properties to the diatoms and enhanced its range of potential applications for *in vivo* tracking, magnetic hyperthermia therapy and purification. The peroxidase-like activity assays demonstrated that the IONPs could enhance the catalytic activity of the diatoms, whilst the tandem catalytic system (Diatom+GOx) was more effective in the absence of the IONPs potentially due to the IONPs displacing the GOx from the diatoms during the synthesis.

The commercial diatoms were also covalently functionalised with anti-PD-L1 in a multistep synthesis approach to produce an immunomodulatory diatom system, whilst also having application as a PD-L1 sensor. The PD-L1 biosensor experiment using the anti-PD-L1 functionalised diatoms gave qualitative evidence of PD-L1 detection based on the reduced peroxidase-like activity observed compared to the unmodified diatom control sample. However, further development is required to evaluate its viability as a biosensor device. This diatom-based biosensor has the potential to be used as a cost-efficient alternative or in combination with ELISA kits. Whilst diatoms are yet to be approved for clinical applications in biomedicine, the diatom systems developed in this thesis have shown to have multiple potential applications in cancer therapy and diagnostics and provide an excellent platform for combination therapies due to their intrinsic catalytic activity, bioavailability, biocompatibility, and porosity facilitating modification.

Chapter 5 demonstrates the fabrication of biodegradable HA-based MNs and implantable devices as drug administration devices enabling a sustained delivery of combination anticancer and immunotherapies that could overcome the limitations of bolus administrations often associated with rapid drug clearance and off-target adverse effects. Whilst the MNs provide a non-invasive, transdermal delivery pathway into the immune-cell rich dermal skin layer,<sup>483</sup> which is particularly suited towards melanoma and breast cancer treatment, the implants are designed for administration into the tumour resection site after surgical intervention to eliminate residual cancer cells and prevent tumour recurrence. These implantable devices capable of releasing the incorporated drug load overtime at the tumour site offer an alternative route for the treatment of brain tumours due to the current challenges of overcoming the blood brain barrier using solution-based therapies.<sup>484</sup>

The HA MNs were fabricated using a micromolding method that produced homogenous patches and sharp MN tips that showed efficient skin penetration in porcine skin, which is a suitable model for human skin.<sup>463</sup> Additional imaging of the skin samples after MN application by optical coherence tomography (OCT) to analyse the penetration depth and skin layers more reliably would be of interest in future work.<sup>485</sup> The development of the fluorescent QD micelle loaded MNs demonstrated that these MNs are capable of loading different agents including NPs. Subsequently, the MNs were loaded with some of the NP and immunomodulatory systems developed in previous chapters. Intrinsically therapeutic IONPs were loaded into a HA MN patch, which was confirmed by EDX analysis showing characteristic Fe emission energies for the IONP-MNs but not in the blank MNs. The gradual IONP release observed from the MNs in a buffer solution in the presence of HAase and the

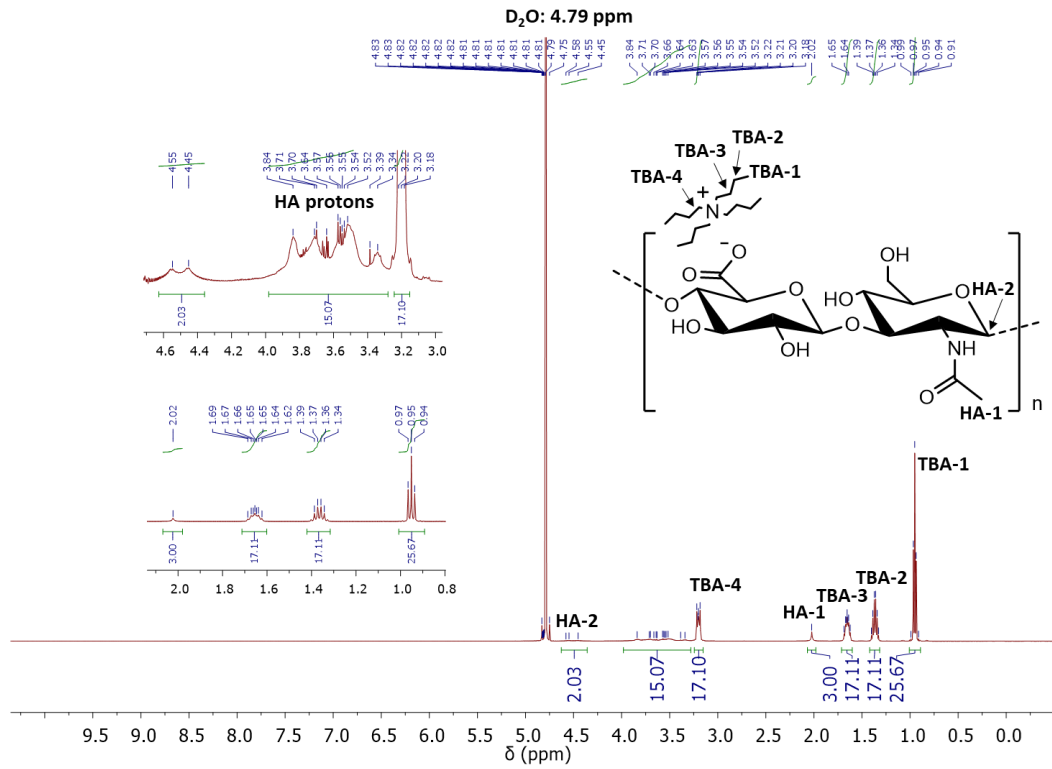
retention of functional activity assessed in a peroxidase-like activity assay suggests that these MNs are suitable for the delivery of IONPs into the TME to afford a prolonged antitumour effect. To replicate the physiological conditions more accurately, the MN release studies could be performed in human serum in future development.

The IONP-DOTAP-pIC-R837 system generated in Chapter 4 was incorporated into an implantable device and its functional properties were proven in a co-culture assay in which the immunomodulatory implant induced cell death in melanoma cells but not in macrophages, consistent with the NPs control in the absence of the implant. An immunomodulatory 1MT-HA implant was fabricated using the 1MT-HA biomaterial developed in Chapter 3 targeted towards the treatment of IDO overexpressed tumours whilst exploiting the gradual release kinetics of 1MT from the HA-based implant as it degrades over time. The 1MT released from the implant demonstrated favourable IDO inhibition in a non-cell-based assay and was then probed in various human and murine tumour cell lines.

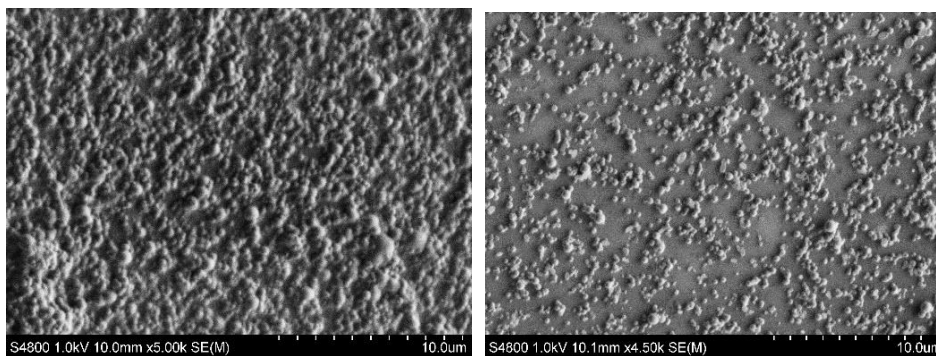
In a cervical cancer model (HeLa cells) an IDO inhibition of 18% was achieved when treated with the 1MT-HA implant at a concentration of a 100  $\mu$ M 1MT. The IDO expression is known to be high in HeLa cells and IDO inhibition was reported previously. References Human ovarian cancer cells, OVCAR8, and murine colon cancer cells, MC38, also showed IDO stimulation and inhibition was demonstrated in these cell lines when they were treated with the 1MT released from the 1MT-HA implant. This work shows promising preliminary evidence of the functional activity of the 1MT-HA implant in different tumour cell models, but further *in vitro* evaluation is required to confirm these findings and proceed to the next development stages.

A future interest is to explore the IDO inhibition effect in a brain cancer model as a favourable target for these implants. For instance, Wainwright *et al.* demonstrated that the downregulation of IDO in IDO overexpressed glioblastoma multiforme can suppress tumour growth and improve patient prognosis.<sup>486</sup> Additionally, the activation of immune cells mediated by IDO inhibition could be further analysed in a co-culture assay using a tumour and immune cell model.<sup>487</sup> The work accomplished in this thesis offers the possibility to load unexplored combinations of the developed immunomodulatory NP and microparticle platforms into a biodegradable MN or implantable device and through a sustained and local release of combination therapies potentially achieve an enhanced therapeutic response.

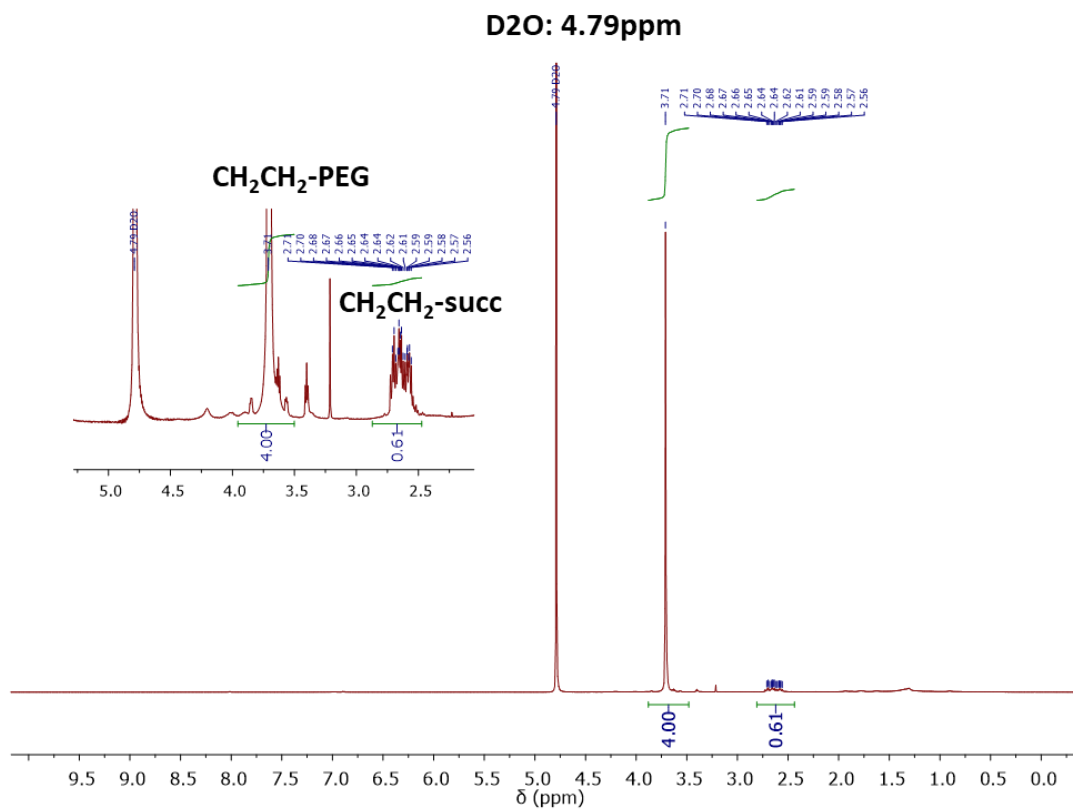
# Appendix



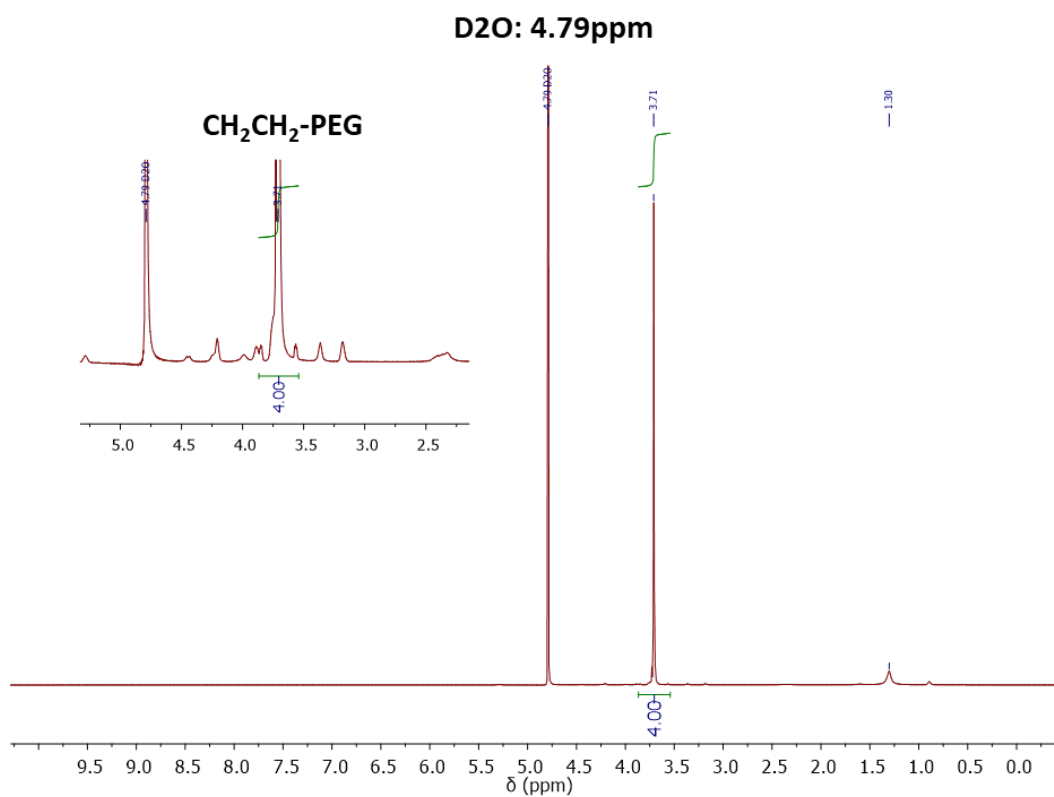
**Appendix 1 <sup>1</sup>H-NMR of HA-TBA in D<sub>2</sub>O with proton labelling.**



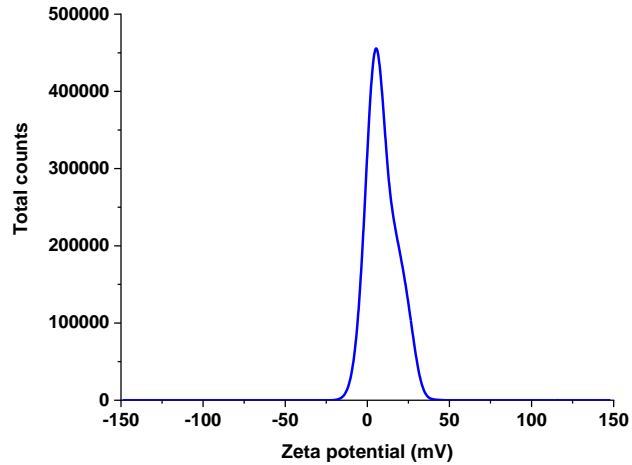
**Appendix 2 SEM images of 1MT-HA@anti-PD-L1 NPs at lower magnification.**



**Appendix 3**  $^1\text{H-NMR}$  spectrum of DSPE-PEG-Pt(IV) prodrug in  $\text{D}_2\text{O}$ .



**Appendix 4**  $^1\text{H-NMR}$  spectrum of DSPE-PEG-amine phospholipid in  $\text{D}_2\text{O}$ .

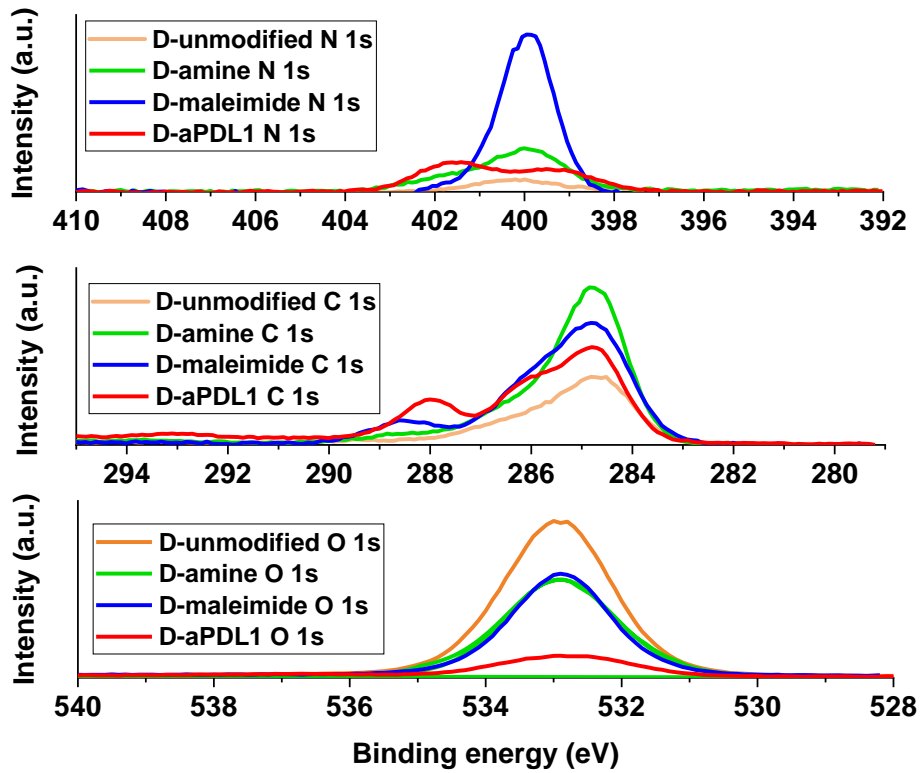


**Appendix 5 Zeta potential characterisation of IONP-DOTAP micelles.** The micelles were suspended in MilliQ water containing 0.02 % NaCl (average of 3 measurements).

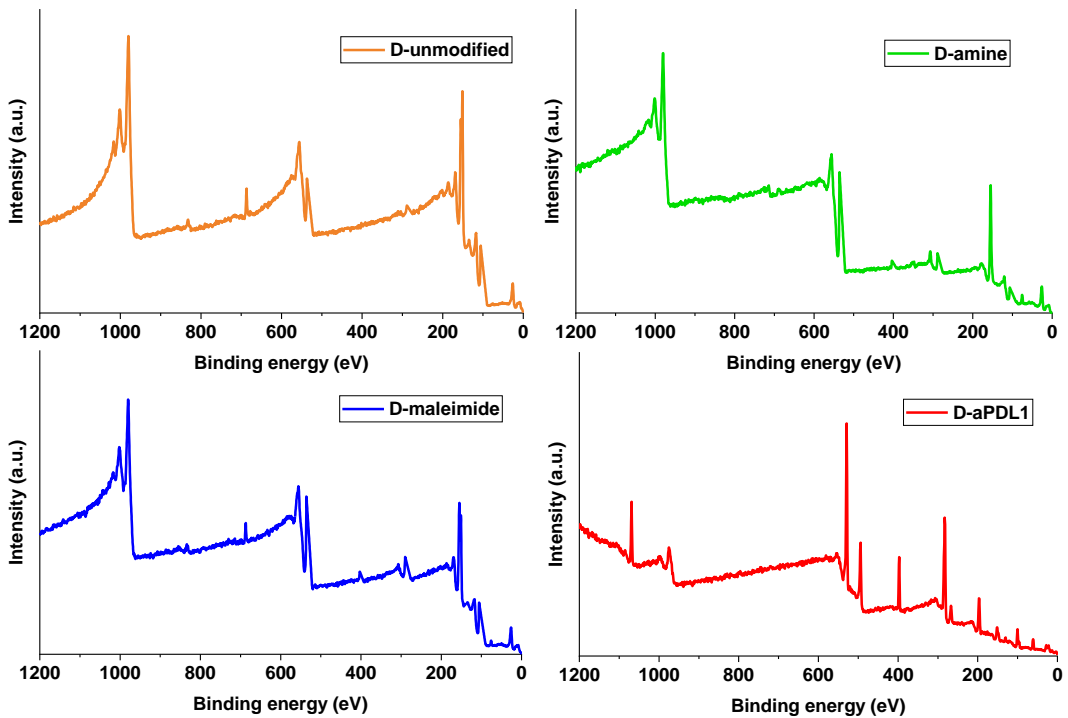
**Appendix 6 Table summary of BCA assay and anti-PD-L1 modification yield calculation (N = 1).**

	[anti-PD-L1] ( $\mu\text{g/mL}$ )	% Yield
IONP-Mal (-control)	10.7	
IONP-anti-PD-L1	29.8	29.1
PD-L1 (+control)	65.5	
D-Mal (-control)	65.9	
D-anti-PD-L1	251.4	47.6
Anti-PD-L1 (+control)	390.0	

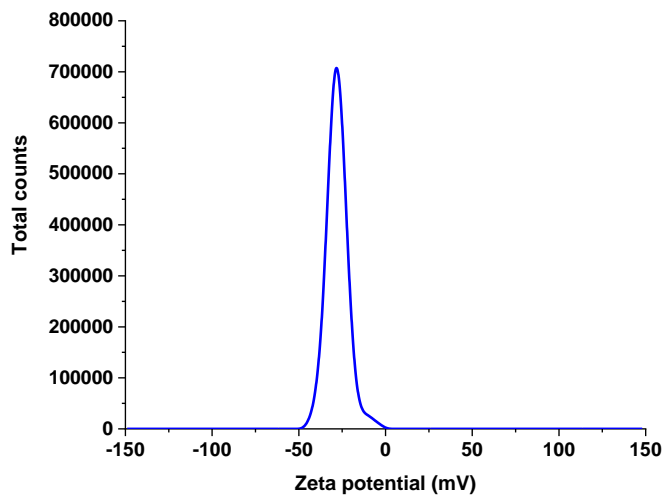




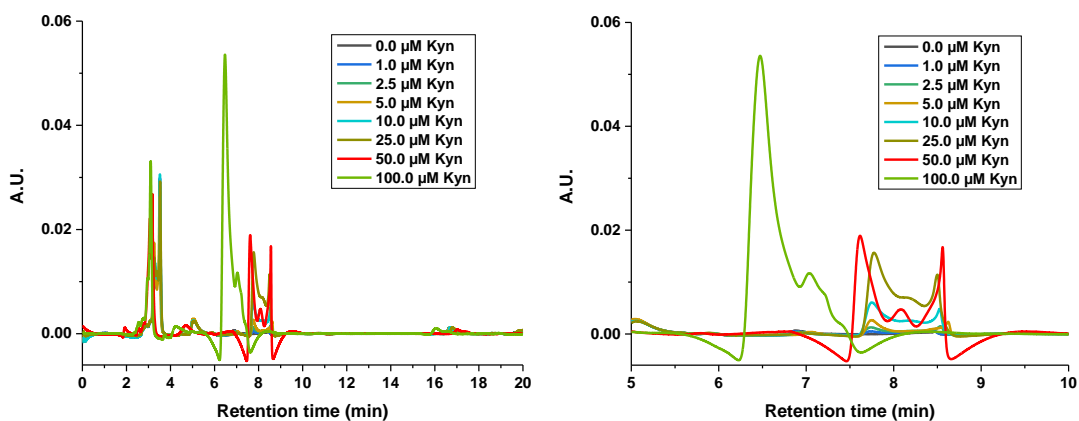
**Appendix 7** Overlay XPS spectra of D-unmodified, D-amine, D-maleimide and D-anti-PD-L1. Binding energies corresponding to N 1s, C 1s and O 1s were analysed.



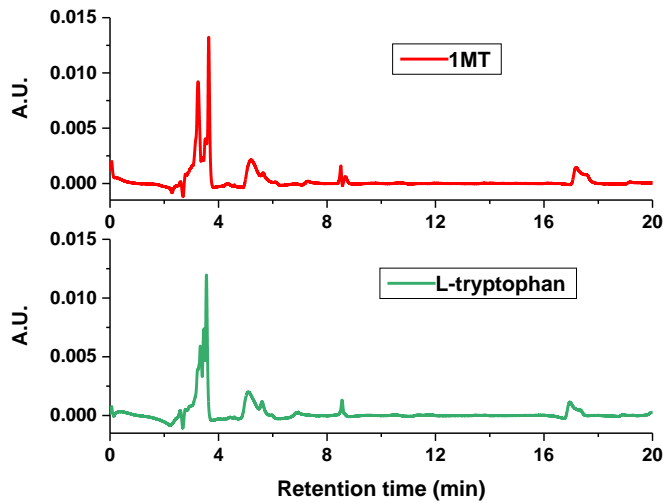
**Appendix 8** Wide XPS spectra of D-unmodified, D-amine, D-maleimide and D-anti-PD-L1.



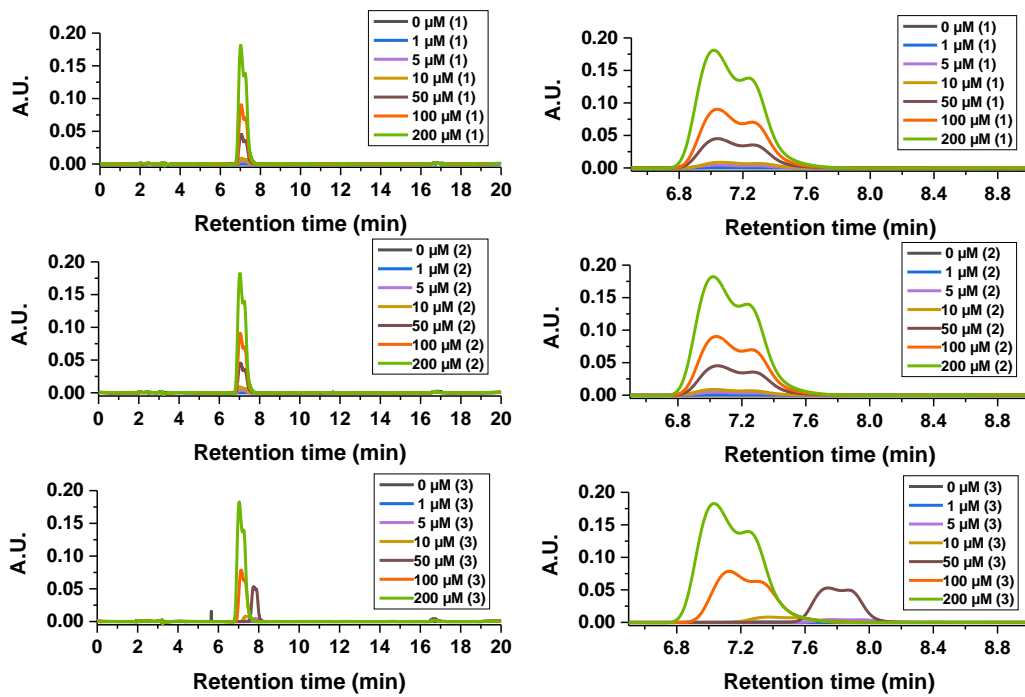
**Appendix 9 Zeta potential of IONP micelles after 24 h release from IONP-MN.** The micelles were suspended in MilliQ water containing 0.02 % NaCl (curve represents average of 3 measurements).



**Appendix 10 RP-HPLC calibration of L-kynurenine for non-cell based IDO inhibition assay.** (A) Full range and (B) chromatogram from RT 6-10 min of L-kynurenine from 0-100 μM and absorbance measured at 360 nm.



**Appendix 11 RP-HPLC chromatograms of 1MT and L-tryptophan additional control samples for non-cell-based IDO inhibition assay. Absorbance was measured at 360 nm.**



**Appendix 12 PR-HPLC chromatograms of L-kynurenine calibration for in vitro IDO inhibition assay. Absorbance was measured at 360 nm (N = 3). (Left: 0-20 min RT; Right: 6.5-9 min RT).**

# Bibliography

- (1) Aristizábal, B.; González, Á. Innate Immune System. In *Autoimmunity: From Bench to Bedside*; Anaya, J. M., Shoenfeld, Y., Rojas-Villarraga, A., Levy, R. A., Cervera, R., Eds.; El Rosario University Press, Bogota D.C, 2013.
- (2) Zhao, E. *et al.* Bone Marrow and the Control of Immunity. *Cell. Mol. Immunol.* **2012**, *9* (1), 11–19. <https://doi.org/10.1038/cmi.2011.47>.
- (3) Medzhitov, R.; Janeway, C. A. Innate Immunity: The Virtues of a Nonclonal System of Recognition. *Cell* **1997**, *91* (3), 295–298. [https://doi.org/10.1016/S0092-8674\(00\)80412-2](https://doi.org/10.1016/S0092-8674(00)80412-2).
- (4) Mahla, R. S.; Reddy, M. C.; Vijaya Raghava Prasad, D.; Kumar, H. Sweeten PAMPs: Role of Sugar Complexed PAMPs in Innate Immunity and Vaccine Biology. *Front. Immunol.* **2013**, *4* (SEP), 248. <https://doi.org/10.3389/fimmu.2013.00248>.
- (5) Amarante-Mendes, G. P. *et al.* R. Pattern Recognition Receptors and the Host Cell Death Molecular Machinery. *Front. Immunol.* **2018**, *9* (OCT), 2379. <https://doi.org/10.3389/fimmu.2018.02379>.
- (6) Mogensen, T. H. Pathogen Recognition and Inflammatory Signaling in Innate Immune Defenses. *Clin. Microbiol. Rev.* **2009**, *22* (2), 240–273. <https://doi.org/10.1128/CMR.00046-08>.
- (7) Uematsu, S.; Akira, S. Toll-Like Receptors (TLRs) and Their Ligands. In *Handbook of Experimental Pharmacology*; Springer, Berlin, Heidelberg, 2008; Vol. 183, pp 1–20. [https://doi.org/10.1007/978-3-540-72167-3\\_1](https://doi.org/10.1007/978-3-540-72167-3_1).
- (8) Jin, M. S.; Lee, J. O. Structures of the Toll-like Receptor Family and Its Ligand Complexes. *Immunity* **2008**, *29* (2), 182–191. <https://doi.org/10.1016/j.immuni.2008.07.007>.
- (9) Li, D.; Wu, M. Pattern Recognition Receptors in Health and Diseases. *Signal Transduct. Target. Ther.* **2021**, *6* (1), 291. <https://doi.org/10.1038/s41392-021-00687-0>.
- (10) Kawasaki, T.; Kawai, T. Toll-Like Receptor Signaling Pathways. *Front. Immunol.* **2014**, *5* (SEP), 461. <https://doi.org/10.3389/fimmu.2014.00461>.
- (11) Hayden, M. S.; West, A. P.; Ghosh, S. NF-KB and the Immune Response. *Oncogene* **2006**, *25* (51), 6758–6780. <https://doi.org/10.1038/sj.onc.1209943>.
- (12) Belardelli, F.; Ferrantini, M. Cytokines as a Link between Innate and Adaptive Antitumor Immunity. *Trends Immunol.* **2002**, *23* (4), 201–208. [https://doi.org/10.1016/S1471-4906\(02\)02195-6](https://doi.org/10.1016/S1471-4906(02)02195-6).
- (13) Lacy, P.; Stow, J. L. Cytokine Release from Innate Immune Cells: Association with Diverse Membrane Trafficking Pathways. *Blood* **2011**, *118* (1), 9–18. <https://doi.org/10.1182/blood-2010-08-265892>.

- (14) Liu, Z.; Roche, P. A. Macropinocytosis in Phagocytes: Regulation of MHC Class-II-Restricted Antigen Presentation in Dendritic Cells. *Front. Physiol.* **2015**, *6* (JAN), 1. <https://doi.org/10.3389/fphys.2015.00001>.
- (15) Shpacovitch, V.; Feld, M.; Hollenberg, M. D.; Luger, T. A.; Steinhoff, M. Role of Protease-Activated Receptors in Inflammatory Responses, Innate and Adaptive Immunity. *J. Leukoc. Biol.* **2008**, *83* (6), 1309–1322. <https://doi.org/10.1189/jlb.0108001>.
- (16) Unterholzner, L.; Almine, J. F. Camouflage and Interception: How Pathogens Evade Detection by Intracellular Nucleic Acid Sensors. *Immunology* **2019**, *156* (3), 217–227. <https://doi.org/10.1111/imm.13030>.
- (17) Chaplin, D. D. Overview of the Immune Response. *J. Allergy Clin. Immunol.* **2010**, *125* (2), 3–23. <https://doi.org/10.1016/j.jaci.2009.12.980>.
- (18) Burnet, F. M. A Modification of Jerne's Theory of Antibody Production Using the Concept of Clonal Selection. *CA: Cancer J. Clin.* **1976**, *26* (2), 119–121. <https://doi.org/10.3322/canjclin.26.2.119>.
- (19) Hewitt, E. W. The MHC Class I Antigen Presentation Pathway: Strategies for Viral Immune Evasion. *Immunology* **2003**, *110* (2), 163–169. <https://doi.org/10.1046/j.1365-2567.2003.01738.x>.
- (20) Roche, P. A.; Furuta, K. The Ins and Outs of MHC Class II-Mediated Antigen Processing and Presentation. *Nat. Rev. Immunol.* **2015**, *15* (4), 203–216. <https://doi.org/10.1038/nri3818>.
- (21) Ruddle, N. H.; Akirav, E. M. Secondary Lymphoid Organs: Responding to Genetic and Environmental Cues in Ontogeny and the Immune Response. *J. Immunol.* **2009**, *183* (4), 2205–2212. <https://doi.org/10.4049/jimmunol.0804324>.
- (22) Zhao, Y.; Niu, C.; Cui, J. Gamma-Delta ( $\Gamma\delta$ ) T Cells: Friend or Foe in Cancer Development. *J. Transl. Med.* **2018**, *16* (1), 1–13. <https://doi.org/10.1186/s12967-017-1378-2>.
- (23) Zeissig, S.; Blumberg, R. S. Analyzing Antigen Recognition by Natural Killer T Cells. In *Antigen Processing: Methods and Protocols*; van Endert, P., Ed.; Springer New York: New York, NY, 2019; pp 439–453. [https://doi.org/10.1007/978-1-4939-9450-2\\_30](https://doi.org/10.1007/978-1-4939-9450-2_30).
- (24) Luckheeram, R. V.; Zhou, R.; Verma, A. D.; Xia, B. CD4 +T Cells: Differentiation and Functions. *Clin. Dev. Immunol.* **2012**, *12* (1), 1–12. <https://doi.org/10.1155/2012/925135>.
- (25) Kaiko, G. E.; Horvat, J. C.; Beagley, K. W.; Hansbro, P. M. Immunological Decision-Making: How Does the Immune System Decide to Mount a Helper T-Cell Response? *Immunology* **2008**, *123* (3), 326–338. <https://doi.org/10.1111/j.1365-2567.2007.02719.x>.
- (26) Okeke, E. B.; Uzonna, J. E. The Pivotal Role of Regulatory T Cells in the Regulation of Innate Immune Cells. *Front. Immunol.* **2019**, *10* (APR), 680. <https://doi.org/10.3389/fimmu.2019.00680>.
- (27) Attias, M.; Al-Aubodah, T.; Piccirillo, C. A. Mechanisms of Human FoxP3+ Treg Cell Development and Function in Health and Disease. *Clin. Exp. Immunol.* **2019**, *197* (1), 36–51. <https://doi.org/10.1111/cei.13290>.

- (28) Li, Y.; Yin, Y.; Mariuzza, R. A. Structural and Biophysical Insights into the Role of CD4 and CD8 in T Cell Activation. *Front. Immunol.* **2013**, *4* (JUL), 206. <https://doi.org/10.3389/fimmu.2013.00206>.
- (29) Sela-Culang, I.; Kunik, V.; Ofran, Y. The Structural Basis of Antibody-Antigen Recognition. *Front. Immunol.* **2013**, *4* (OCT), 302. <https://doi.org/10.3389/fimmu.2013.00302>.
- (30) Elgueta, R. *et al.* Molecular Mechanism and Function of CD40/CD40L Engagement in the Immune System. *Immunol. Rev.* **2009**, *229* (1), 152–172. <https://doi.org/10.1111/j.1600-065X.2009.00782.x>.
- (31) Obukhanych, T. V.; Nussenzweig, M. C. T-Independent Type II Immune Responses Generate Memory B Cells. *J. Exp. Med.* **2006**, *203* (2), 305–310. <https://doi.org/10.1084/jem.20052036>.
- (32) Zhao, E. *et al.* W. Bone Marrow and the Control of Immunity. *Cell. Mol. Immunol.* **2012**, *9* (1), 11–19. <https://doi.org/10.1038/cmi.2011.47>.
- (33) Cullen, S. P.; Martin, S. J. Mechanisms of Granule-Dependent Killing. *Cell Death Differ.* **2008**, *15* (2), 251–262. <https://doi.org/10.1038/sj.cdd.4402244>.
- (34) Wang, L.; Du, F.; Wang, X. TNF- $\alpha$  Induces Two Distinct Caspase-8 Activation Pathways. *Cell* **2008**, *133* (4), 693–703. <https://doi.org/10.1016/j.cell.2008.03.036>.
- (35) Knight, M. J.; Riffkin, C. D.; Muscat, A. M.; Ashley, D. M.; Hawkins, C. J. Analysis of FasL and TRAIL Induced Apoptosis Pathways in Glioma Cells. *Oncogene* **2001**, *20* (41), 5789–5798. <https://doi.org/10.1038/sj.onc.1204810>.
- (36) Ratajczak, W.; Niedźwiedzka-Rystwej, P.; Tokarz-Deptuła, B.; Deptuła, W. Immunological Memory Cells. *Cent. Eur. J. Immunol.* **2018**, *43* (2), 194–203. <https://doi.org/10.5114/ceji.2018.77390>.
- (37) Hansson, G. K.; Libby, P.; Schönbeck, U.; Yan, Z. Q. Innate and Adaptive Immunity in the Pathogenesis of Atherosclerosis. *Circ. Res.* **2002**, *91* (4), 281–291. <https://doi.org/10.1161/01.RES.0000029784.15893.10>.
- (38) Wu, S.; Zhu, W.; Thompson, P.; Hannun, Y. A. Evaluating Intrinsic and Non-Intrinsic Cancer Risk Factors. *Nat. Commun.* **2018**, *9* (1), 1–12. <https://doi.org/10.1038/s41467-018-05467-z>.
- (39) Golemis, E. A. *et al.* Molecular Mechanisms of the Preventable Causes of Cancer in the United States. *Genes Dev.* **2018**, *32* (13–14), 868–902. <https://doi.org/10.1101/gad.314849.118>.
- (40) Hecht, S. S. Tobacco Smoke Carcinogens and Lung Cancer. *J. Natl. Cancer Inst.* **1999**, *91* (14), 1194–1210. <https://doi.org/10.1093/jnci/91.14.1194>.
- (41) Sarich, P. *et al.* Alcohol Consumption, Drinking Patterns and Cancer Incidence in an Australian Cohort of 226,162 Participants Aged 45 Years and Over. *Br. J. Cancer* **2021**, *124* (2), 513–523. <https://doi.org/10.1038/s41416-020-01101-2>.
- (42) Chan, D. S. M. *et al.* Red and Processed Meat and Colorectal Cancer Incidence: Meta-Analysis of Prospective Studies. *PLoS One* **2011**, *6* (6), e20456.

- (43) Cadet, J.; Douki, T. Formation of UV-Induced DNA Damage Contributing to Skin Cancer Development. *Photochem. Photobiol. Sci.* **2018**, *17* (12), 1816–1841. <https://doi.org/10.1039/C7PP00395A>.
- (44) Takahashi-Kanemitsu, A.; Knight, C. T.; Hatakeyama, M. Molecular Anatomy and Pathogenic Actions of Helicobacter Pylori CagA That Underpin Gastric Carcinogenesis. *Cell. Mol. Immunol.* **2020**, *17* (1), 50–63. <https://doi.org/10.1038/s41423-019-0339-5>.
- (45) K, W. M.; S, P. J.; Kamel, K. Viruses and Human Cancers: A Long Road of Discovery of Molecular Paradigms. *Clin. Microbiol. Rev.* **2014**, *27* (3), 463–481. <https://doi.org/10.1128/CMR.00124-13>.
- (46) Chatterjee, N.; Walker, G. C. Mechanisms of DNA Damage, Repair, and Mutagenesis. *Environ. Mol. Mutagen.* **2017**, *58* (5), 235–263. <https://doi.org/10.1002/em.22087>.
- (47) Aunan, J. R.; Cho, W. C.; Søreide, K. The Biology of Aging and Cancer: A Brief Overview of Shared and Divergent Molecular Hallmarks. *Aging Dis.* **2017**, *8* (5), 628–642. <https://doi.org/10.14336/AD.2017.0103>.
- (48) Song, S.; Johnson, F. B. Epigenetic Mechanisms Impacting Aging: A Focus on Histone Levels and Telomeres. *Genes* **2018**, *9* (4), 201. <https://doi.org/10.3390/genes9040201>.
- (49) Nair, S. S.; Kumar, R. Chromatin Remodeling in Cancer: A Gateway to Regulate Gene Transcription. *Mol. Oncol.* **2012**, *6* (6), 611–619. <https://doi.org/10.1016/j.molonc.2012.09.005>.
- (50) Kawakami, Y. *et al.* Identification of Human Tumor Antigens and Its Implications for Diagnosis and Treatment of Cancer. *Cancer Sci.* **2004**, *95* (10), 784–791. <https://doi.org/10.1111/j.1349-7006.2004.tb02182.x>.
- (51) Kontomaolis, E. N. *et al.* Z. Role of Oncogenes and Tumor-Suppressor Genes in Carcinogenesis: A Review. *Anticancer Res.* **2020**, *40* (11), 6009. <https://doi.org/10.21873/anticanres.14622>.
- (52) Wang, L. H.; Wu, C. F.; Rajasekaran, N.; Shin, Y. K. Loss of Tumor Suppressor Gene Function in Human Cancer: An Overview. *Cell. Physiol. Biochem.* **2019**, *51* (6), 2647–2693. <https://doi.org/10.1159/000495956>.
- (53) Weinstein, I. B.; Joe, A. Oncogene Addiction. *Cancer Res.* **2008**, *68* (9), 3077–3080. <https://doi.org/10.1158/0008-5472.CAN-07-3293>.
- (54) Vicente-Dueñas, C.; Romero-Camarero, I.; Cobaleda, C.; Sánchez-García, I. Function of Oncogenes in Cancer Development: A Changing Paradigm. *EMBO J.* **2013**, *32* (11), 1502–1513. <https://doi.org/10.1038/emboj.2013.97>.
- (55) Collado, M.; Serrano, M. Senescence in Tumours: Evidence from Mice and Humans. *Nat. Rev. Cancer* **2010**, *10* (1), 51–57. <https://doi.org/10.1038/nrc2772>.
- (56) Shortt, J.; Johnstone, R. W. Oncogenes in Cell Survival and Cell Death. *Cold Spring Harb. Perspect. Biol.* **2012**, *4* (12), 9829. <https://doi.org/10.1101/cshperspect.a009829>.
- (57) Aubrey, B. J.; Kelly, G. L.; Janic, A.; Herold, M. J.; Strasser, A. How Does P53 Induce Apoptosis and How Does This Relate to P53-Mediated Tumour Suppression? *Cell Death Differ.* **2018**, *25* (1), 104–113. <https://doi.org/10.1038/cdd.2017.169>.

- (58) Shibue, T. *et al.* Differential Contribution of Puma and Noxa in Dual Regulation of P53-Mediated Apoptotic Pathways. *EMBO J.* **2006**, *25* (20), 4952–4962. <https://doi.org/10.1038/sj.emboj.7601359>.
- (59) Dyson, N. J. RB1: A Prototype Tumor Suppressor and an Enigma. *Genes Dev.* **2016**, *30* (13), 1492–1502. <https://doi.org/10.1101/gad.282145.116>.
- (60) Seo, A. *et al.* Mechanism for Survival of Homozygous Nonsense Mutations in the Tumor Suppressor Gene BRCA1. *Proc. Natl. Acad. Sci. U. S. A.* **2018**, *115* (20), 5241–5246. <https://doi.org/10.1073/pnas.1801796115>.
- (61) Wang, Q. Cancer Predisposition Genes: Molecular Mechanisms and Clinical Impact on Personalized Cancer Care: Examples of Lynch and HBOC Syndromes. *Acta Pharmacol. Sin.* **2016**, *37* (2), 143–149. <https://doi.org/10.1038/aps.2015.89>.
- (62) Hanahan, D.; Weinberg, R. A. Hallmarks of Cancer: The next Generation. *Cell* **2011**, *144* (5), 646–674. <https://doi.org/10.1016/j.cell.2011.02.013>.
- (63) Muenst, S. *et al.* The Immune System and Cancer Evasion Strategies: Therapeutic Concepts. *J. Intern. Med.* **2016**, *279* (6), 541–562. <https://doi.org/10.1111/joim.12470>.
- (64) Monjazeb, A. M. *et al.* J. Immunoediting and Antigen Loss: Overcoming the Achilles Heel of Immunotherapy with Antigen Non-Specific Therapies. *Front. Oncol.* **2013**, *3* (JUL), 197. <https://doi.org/10.3389/fonc.2013.00197>.
- (65) O’Donnell, J. S.; Teng, M. W. L.; Smyth, M. J. Cancer Immunoediting and Resistance to T Cell-Based Immunotherapy. *Nat. Rev. Clin. Oncol.* **2019**, *16* (3), 151–167. <https://doi.org/10.1038/s41571-018-0142-8>.
- (66) Durgeau, A.; Virk, Y.; Cognac, S.; Mami-Chouaib, F. Recent Advances in Targeting CD8 T-Cell Immunity for More Effective Cancer Immunotherapy. *Front. Immunol.* **2018**, *9* (JAN), 14. <https://doi.org/10.3389/fimmu.2018.00014>.
- (67) Baxevanis, C. N.; Perez, S. A. Cancer Dormancy: A Regulatory Role for Endogenous Immunity in Establishing and Maintaining the Tumor Dormant State. *Vaccines* **2015**, *3* (3), 597–619. <https://doi.org/10.3390/vaccines3030597>.
- (68) Mahnke, Y. D.; Schwendemann, J.; Beckhove, P.; Schirmacher, V. Maintenance of Long-Term Tumour-Specific T-Cell Memory by Residual Dormant Tumour Cells. *Immunology* **2005**, *115* (3), 325–336. <https://doi.org/10.1111/j.1365-2567.2005.02163.x>.
- (69) Leone, P.; Shin, E.-C.; Perosa, F.; Vacca, A.; Dammacco, F.; Racanelli, V. MHC Class I Antigen Processing and Presenting Machinery: Organization, Function, and Defects in Tumor Cells. *JNCI: Journal of the National Cancer Institute* **2013**, *105* (16), 1172–1187. <https://doi.org/10.1093/jnci/djt184>.
- (70) Garrido, F.; Aptsiauri, N.; Doorduijn, E. M.; Garcia Lora, A. M.; van Hall, T. The Urgent Need to Recover MHC Class I in Cancers for Effective Immunotherapy. *Curr. Opin. Immunol.* **2016**, *39*, 44–51. <https://doi.org/10.1016/j.coi.2015.12.007>.
- (71) Campoli, M.; Ferrone, S. HLA Antigen Changes in Malignant Cells: Epigenetic Mechanisms and Biologic Significance. *Oncogene* **2008**, *27* (45), 5869–5885. <https://doi.org/10.1038/onc.2008.273>.



- (72) Töpfer, K. *et al.* Tumor Evasion from T Cell Surveillance. *J Biomed. Biotechnol.* **2011**, 2011 (1), 1–19. <https://doi.org/10.1155/2011/918471>.
- (73) Khong, H. T.; Restifo, N. P. Natural Selection of Tumor Variants in the Generation of “Tumor Escape” Phenotypes. *Nat. Immunol.* **2002**, 3 (11), 999–1005. <https://doi.org/10.1038/ni1102-999>.
- (74) Petrova, V.; Annicchiarico-Petruzzelli, M.; Melino, G.; Amelio, I. The Hypoxic Tumour Microenvironment. *Oncogenesis* **2018**, 7 (1), 10. <https://doi.org/10.1038/s41389-017-0011-9>.
- (75) Liu, H. *et al.* Role of NKG2D and Its Ligands in Cancer Immunotherapy. *Am. J. Cancer Res.* **2019**, 9 (10), 2064–2078.
- (76) De Andrade, L. F. *et al.* Antibody-Mediated Inhibition of MICA and MICB Shedding Promotes NK Cell-Driven Tumor Immunity. *Science* **2018**, 359 (6383), 1537–1542. <https://doi.org/10.1126/science.aao0505>.
- (77) Vasievich, E. A.; Huang, L. The Suppressive Tumor Microenvironment: A Challenge in Cancer Immunotherapy. *Mol. Pharm.* **2011**, 8 (3), 635–641. <https://doi.org/10.1021/mp1004228>.
- (78) Labani-Motlagh, A.; Ashja-Mahdavi, M.; Loskog, A. The Tumor Microenvironment: A Milieu Hindering and Obstructing Antitumor Immune Responses. *Front. Immunol.* **2020**, 11 (MAY), 940. <https://doi.org/10.3389/fimmu.2020.00940>.
- (79) Timosenko, E.; Hadjinicolaou, A. V.; Cerundolo, V. Modulation of Cancer-Specific Immune Responses by Amino Acid Degrading Enzymes. *Immunotherapy* **2016**, 9 (1), 83–97. <https://doi.org/10.2217/imt-2016-0118>.
- (80) Ren, D. *et al.* Predictive Biomarkers and Mechanisms Underlying Resistance to PD1/PD-L1 Blockade Cancer Immunotherapy. *Mol. Cancer* **2020**, 19 (1), 19. <https://doi.org/10.1186/s12943-020-1144-6>.
- (81) Yu, L.; Chen, X.; Sun, X.; Wang, L.; Chen, S. The Glycolytic Switch in Tumors: How Many Players Are Involved? *J. Cancer* **2017**, 8 (17), 3430–3440. <https://doi.org/10.7150/jca.21125>.
- (82) De la Cruz-López, K. G.; Castro-Muñoz, L. J.; Reyes-Hernández, D. O.; García-Carrancá, A.; Manzo-Merino, J. Lactate in the Regulation of Tumor Microenvironment and Therapeutic Approaches. *Front. Oncol.* **2019**, 9 (NOV), 1143. <https://doi.org/10.3389/fonc.2019.01143>.
- (83) Efremova, M.; Finotello, F.; Rieder, D.; Trajanoski, Z. Neoantigens Generated by Individual Mutations and Their Role in Cancer Immunity and Immunotherapy. *Front. Immunol.* **2017**, 8 (NOV), 1679. <https://doi.org/10.3389/fimmu.2017.01679>.
- (84) Kruger, S. *et al.* Advances in Cancer Immunotherapy 2019 – Latest Trends. *J. Exp. Clin. Cancer Res.* **2019**, 38 (1), 268. <https://doi.org/10.1186/s13046-019-1266-0>.
- (85) Hoption Cann, S. A.; van Netten, J. P.; van Netten, C. Dr William Coley and Tumour Regression: A Place in History or in the Future. *Postgrad. Med. J.* **2003**, 79 (938), 672–680.
- (86) McCarthy, E. F. The Toxins of William B. Coley and the Treatment of Bone and Soft-Tissue Sarcomas. *Iowa Orthop. J.* **2006**, 26, 154–158.

- (87) Starnes, C. O. Coley's Toxins in Perspective. *Nature* **1992**, 357 (6373), 11–12. <https://doi.org/10.1038/357011a0>.
- (88) Dunn, G. P.; Old, L. J.; Schreiber, R. D. The Immunobiology of Cancer Immunosurveillance and Immunoediting. *Immunity* **2004**, 21 (2), 137–148. <https://doi.org/10.1016/j.immuni.2004.07.017>.
- (89) Miller, J. F. A. P. The Discovery of Thymus Function and of Thymus-Derived Lymphocytes. *Immunol. Rev.* **2002**, 185 (1), 7–14. <https://doi.org/10.1034/j.1600-065X.2002.18502.x>.
- (90) Steinman, R. M.; Cohn, Z. A. Identification of a Novel Cell Type in Peripheral Lymphoid Organs of Mice. I. Morphology, Quantitation, Tissue Distribution. *J. Exp. Med.* **1973**, 137 (5), 1142–1162. <https://doi.org/10.1084/jem.137.5.1142>.
- (91) Asmana Ningrum, R. Human Interferon Alpha-2b: A Therapeutic Protein for Cancer Treatment. *Scientifica* **2014**, 2014, 970315. <https://doi.org/10.1155/2014/970315>.
- (92) Alva, A. *et al.* Contemporary Experience with High-Dose Interleukin-2 Therapy and Impact on Survival in Patients with Metastatic Melanoma and Metastatic Renal Cell Carcinoma. *Cancer Immunol. Immunother.* **2016**, 65 (12), 1533–1544. <https://doi.org/10.1007/s00262-016-1910-x>.
- (93) Rider, P.; Carmi, Y.; Cohen, I. Biologics for Targeting Inflammatory Cytokines, Clinical Uses, and Limitations. *Int. J. Cell Biol.* **2016**, 2016 (1), 9259646. <https://doi.org/10.1155/2016/9259646>.
- (94) Guo, Z. S. The 2018 Nobel Prize in Medicine Goes to Cancer Immunotherapy (Editorial for BMC Cancer). *BMC cancer* **2018**, 18 (1), 1086. <https://doi.org/10.1186/s12885-018-5020-3>.
- (95) Wei, S. C.; Duffy, C. R.; Allison, J. P. Fundamental Mechanisms of Immune Checkpoint Blockade Therapy. *Cancer Discov.* **2018**, 8 (9), 1069–1086. <https://doi.org/10.1158/2159-8290.CD-18-0367>.
- (96) Wilky, B. A. Immune Checkpoint Inhibitors: The Linchpins of Modern Immunotherapy. *Immunol. Rev.* **2019**, 290 (1), 6–23. <https://doi.org/10.1111/imr.12766>.
- (97) Vaddepally, R. K.; Kharel, P.; Pandey, R.; Garje, R.; Chandra, A. B. Review of Indications of FDA-Approved Immune Checkpoint Inhibitors per NCCN Guidelines with the Level of Evidence. *Cancers* **2020**, 12 (3), 738. <https://doi.org/10.3390/cancers12030738>.
- (98) Buchbinder, E. I.; Desai, A. CTLA-4 and PD-1 Pathways: Similarities, Differences, and Implications of Their Inhibition. *Am. J. Clin. Oncol.* **2016**, 39 (1), 98–106. <https://doi.org/10.1097/COC.000000000000239>.
- (99) Alsaab, H. O. *et al.* PD-1 and PD-L1 Checkpoint Signaling Inhibition for Cancer Immunotherapy: Mechanism, Combinations, and Clinical Outcome. *Front. Pharmacol.* **2017**, 8 (AUG), 561. <https://doi.org/10.3389/fphar.2017.00561>.
- (100) Marzec, M. *et al.* Oncogenic Kinase NPM/ALK Induces through STAT3 Expression of Immunosuppressive Protein CD274 (PD-L1, B7-H1). *Proc. Natl. Acad. Sci. U. S. A.* **2008**, 105 (52), 20852–20857. <https://doi.org/10.1073/pnas.0810958105>.

- (101) Cai, J.; Wang, D.; Zhang, G.; Guo, X. The Role Of PD-1/PD-L1 Axis In Treg Development And Function: Implications For Cancer Immunotherapy. *OncoTargets Ther.* **2019**, *12*, 8437–8445. <https://doi.org/10.2147/OTT.S221340>.
- (102) Guan, H. *et al.* PD-L1 Is a Critical Mediator of Regulatory B Cells and T Cells in Invasive Breast Cancer. *Sci. Rep.* **2016**, *6* (1), 35651. <https://doi.org/10.1038/srep35651>.
- (103) Rotte, A. Combination of CTLA-4 and PD-1 Blockers for Treatment of Cancer. *J. Exp. Clin. Cancer Res.* **2019**, *38* (1), 255. <https://doi.org/10.1186/s13046-019-1259-z>.
- (104) Akinleye, A.; Rasool, Z. Immune Checkpoint Inhibitors of PD-L1 as Cancer Therapeutics. *J. Hematol. Oncol.* **2019**, *12* (1), 92. <https://doi.org/10.1186/s13045-019-0779-5>.
- (105) Qin, S. *et al.* Novel Immune Checkpoint Targets: Moving beyond PD-1 and CTLA-4. *Mol. Cancer* **2019**, *18* (1), 1–14. <https://doi.org/10.1186/s12943-019-1091-2>.
- (106) Sugimoto, H. *et al.* Crystal Structure of Human Indoleamine 2,3-Dioxygenase: Catalytic Mechanism of O<sub>2</sub> Incorporation by a Heme-Containing Dioxygenase. *Proc. Natl. Acad. Sci. U. S. A.* **2006**, *103* (8), 2611–2616. <https://doi.org/10.1073/pnas.0508996103>.
- (107) Zakharia, Y. *et al.* Updates on Phase 1b/2 Trial of the Indoleamine 2,3-Dioxygenase Pathway (IDO) Inhibitor Indoximod plus Checkpoint Inhibitors for the Treatment of Unresectable Stage 3 or 4 Melanoma. *J. Clin. Oncol.* **2016**, *34* (15), 3075. [https://doi.org/10.1200/JCO.2016.34.15\\_suppl.3075](https://doi.org/10.1200/JCO.2016.34.15_suppl.3075).
- (108) Gibney, G. T. *et al.* Phase 1/2 Study of Epacadostat in Combination with Ipilimumab in Patients with Unresectable or Metastatic Melanoma. *J. Immunother. Cancer* **2019**, *7* (1), 80. <https://doi.org/10.1186/s40425-019-0562-8>.
- (109) Marhelava, K.; Pilch, Z.; Bajor, M.; Graczyk-Jarzynka, A.; Zagozdzon, R. Targeting Negative and Positive Immune Checkpoints with Monoclonal Antibodies in Therapy of Cancer. *Cancers* **2019**, *11* (11), 1–21. <https://doi.org/10.3390/cancers11111756>.
- (110) Aspeslagh, S. *et al.* Rationale for Anti-OX40 Cancer Immunotherapy. *Eur. J. Cancer* **2016**, *52*, 50–66. <https://doi.org/10.1016/j.ejca.2015.08.021>.
- (111) Murphy, K. A. *et al.* An In Vivo Immunotherapy Screen of Costimulatory Molecules Identifies Fc-OX40L as a Potent Reagent for the Treatment of Established Murine Gliomas. *Clin. Cancer Res.* **2012**, *18* (17), 4657–4668. <https://doi.org/10.1158/1078-0432.CCR-12-0990>
- (112) Fromm, G. *et al.* Agonist Redirected Checkpoint, PD1-Fc-OX40L, for Cancer Immunotherapy. *J. Immunother. Cancer* **2018**, *6* (1), 1–16. <https://doi.org/10.1186/s40425-018-0454-3>.
- (113) Curti, B. D. *et al.* OX40 Is a Potent Immune-Stimulating Target in Late-Stage Cancer Patients. *Cancer Res.* **2013**, *73* (24), 7189–7198. <https://doi.org/10.1158/0008-5472.CAN-12-4174>.
- (114) Marin-Acevedo, J. A. *et al.* Next Generation of Immune Checkpoint Therapy in Cancer: New Developments and Challenges. *J. Hematol. Oncol.* **2018**, *11* (1), 1–20. <https://doi.org/10.1186/s13045-018-0582-8>.
- (115) Lim, Y. T. Vaccine Adjuvant Materials for Cancer Immunotherapy and Control of Infectious Disease. *Clin. Exp. Vaccine Res.* **2015**, *4* (1), 54–58. <https://doi.org/10.7774/cevr.2015.4.1.54>.

- (116) Vacchelli, E. *et al.* Trial Watch: FDA-Approved Toll-like Receptor Agonists for Cancer Therapy. *Oncoimmunology* **2012**, *1* (6), 894–907. <https://doi.org/10.4161/onci.20931>.
- (117) Bubna, A. Imiquimod - Its Role in the Treatment of Cutaneous Malignancies. *Indian J. Pharmacol.* **2015**, *47* (4), 354. <https://doi.org/10.4103/0253-7613.161249>.
- (118) Hernandez, A. *et al.* The Role of MyD88- and TRIF-Dependent Signaling in Monophosphoryl Lipid A-Induced Expansion and Recruitment of Innate Immunocytes. *J. Leukoc. Biol.* **2016**, *100* (6), 1311–1322. <https://doi.org/10.1189/jlb.1A0216-072R>.
- (119) Groves, M. J. Pharmaceutical Characterization of Mycobacterium Bovis Bacillus Calmette-Guerin (BCG) Vaccine Used for the Treatment of Superficial Bladder Cancer. *J. Pharm. Sci.* **1993**, *82* (6), 555–562. <https://doi.org/10.1002/jps.2600820602>.
- (120) Urban-Wojciuk, Z. *et al.* The Role of TLRs in Anti-Cancer Immunity and Tumor Rejection. *Front. Immunol.* **2019**, *10* (OCT), 2388. <https://doi.org/10.3389/fimmu.2019.02388>.
- (121) Sultan, H. *et al.* Poly-IC Enhances the Effectiveness of Cancer Immunotherapy by Promoting T Cell Tumor Infiltration. *J. Immunother. Cancer* **2020**, *8* (2), e001224. <https://doi.org/10.1136/jitc-2020-001224>.
- (122) Li, J.; Yang, F.; Wei, F.; Ren, X. The Role of Toll-like Receptor 4 in Tumor Microenvironment. *Oncotarget* **2017**, *8* (39), 66656–66667. <https://doi.org/10.18632/oncotarget.19105>.
- (123) Castaño-Rodríguez, N.; Kaakoush, N. O.; Mitchell, H. M. Pattern-Recognition Receptors and Gastric Cancer. *Front. Immunol.* **2014**, *5* (JUL), 336. <https://doi.org/10.3389/fimmu.2014.00336>.
- (124) Sato-Kaneko, F. *et al.* Combination Immunotherapy with TLR Agonists and Checkpoint Inhibitors Suppresses Head and Neck Cancer. *JCI insight* **2017**, *2* (18), e93397. <https://doi.org/10.1172/jci.insight.93397>.
- (125) Shi, J.; Kantoff, P. W.; Wooster, R.; Farokhzad, O. C. Cancer Nanomedicine: Progress, Challenges and Opportunities. *Nat. Rev. Cancer* **2017**, *17* (1), 20–37. <https://doi.org/10.1038/nrc.2016.108>.
- (126) Patra, J. K. *et al.* Nano Based Drug Delivery Systems: Recent Developments and Future Prospects. *J. Nanobiotechnology* **2018**, *16* (1), 71. <https://doi.org/10.1186/s12951-018-0392-8>.
- (127) Hobbs, S. K. *et al.* Regulation of Transport Pathways in Tumor Vessels: Role of Tumor Type and Microenvironment. *Proc. Natl. Acad. Sci. U.S.A.* **1998**, *95* (8), 4607–4612. <https://doi.org/10.1073/pnas.95.8.4607>.
- (128) Matsumura, Y.; Maeda, H. A New Concept for Macromolecular Therapeutics in Cancer Chemotherapy: Mechanism of Tumoritropic Accumulation of Proteins and the Antitumor Agent Smancs. *Cancer Res.* **1986**, *46* (12), 6387–6392.
- (129) Chauhan, V. P.; Stylianopoulos, T.; Boucher, Y.; Jain, R. K. Delivery of Molecular and Nanoscale Medicine to Tumors: Transport Barriers and Strategies. *Annu. Rev. Chem. Biomol. Eng.* **2011**, *2* (1), 281–298. <https://doi.org/10.1146/annurev-chembioeng-061010-114300>.

- (130) Longmire, M.; Choyke, P. L.; Kobayashi, H. Clearance Properties of Nano-Sized Particles and Molecules as Imaging Agents: Considerations and Caveats. *Nanomedicine* **2008**, *3* (5), 703–717. <https://doi.org/10.2217/17435889.3.5.703>.
- (131) Rizvi, S. A. A.; Saleh, A. M. Applications of Nanoparticle Systems in Drug Delivery Technology. *Saudi Pharm J.* **2018**, *26* (1), 64–70. <https://doi.org/10.1016/j.jsps.2017.10.012>.
- (132) Nag, O. K.; Delehanty, J. B. Active Cellular and Subcellular Targeting of Nanoparticles for Drug Delivery. *Pharmaceutics* **2019**, *11* (10), 543. <https://doi.org/10.3390/pharmaceutics11100543>.
- (133) Yu, B.; Tai, H. C.; Xue, W.; Lee, L. J.; Lee, R. J. Receptor-Targeted Nanocarriers for Therapeutic Delivery to Cancer. *Mol. Membr. Biol.* **2010**, *27* (7), 286–298. <https://doi.org/10.3109/09687688.2010.521200>.
- (134) Yao, Q.; Kou, L.; Tu, Y.; Zhu, L. MMP-Responsive ‘Smart’ Drug Delivery and Tumor Targeting. *Trends Pharmacol. Sci.* **2018**, *39* (8), 766–781. <https://doi.org/10.1016/j.tips.2018.06.003>.
- (135) Wang, X.; Wang, B.; Zhang, Q. Anti-Tumor Targeted Drug Delivery Systems Mediated by Aminopeptidase N/CD13. *Acta Pharm. Sin. B* **2011**, *1* (2), 80–83. <https://doi.org/10.1016/j.apsb.2011.06.002>.
- (136) Schneider, E.; Hunke, S. ATP-Binding-Cassette (ABC) Transport Systems: Functional and Structural Aspects of the ATP-Hydrolyzing Subunits/Domains. *FEMS Microbiol. Rev.* **1998**, *22* (1), 1–20. <https://doi.org/10.1111/j.1574-6976.1998.tb00358.x>.
- (137) Leslie, E. M.; Deeley, R. G.; Cole, S. P. C. Multidrug Resistance Proteins: Role of P-Glycoprotein, MRP1, MRP2, and BCRP (ABCG2) in Tissue Defense. *Toxicol. Appl. Pharmacol.* **2005**, *204* (3), 216–237. <https://doi.org/10.1016/j.taap.2004.10.012>.
- (138) Pham, S. H.; Choi, Y.; Choi, J. Stimuli-Responsive Nanomaterials for Application in Antitumor Therapy and Drug Delivery. *Pharmaceutics* **2020**, *12* (7), 630. <https://doi.org/10.3390/pharmaceutics12070630>.
- (139) Warburg, O. Über Den Stoffwechsel Der Carcinomzelle. *Naturwissenschaften* **1924**, *12* (50), 1131–1137. <https://doi.org/10.1007/BF01504608>.
- (140) Binauld, S.; Stenzel, M. H. Acid-Degradable Polymers for Drug Delivery: A Decade of Innovation. *Chem. Commun.* **2013**, *49* (21), 2082–2102. <https://doi.org/10.1039/C2CC36589H>.
- (141) Bareford, L. M.; Swaan, P. W. Endocytic Mechanisms for Targeted Drug Delivery. *Adv. Drug Deliv. Rev.* **2007**, *59* (8), 748–758. <https://doi.org/10.1016/j.addr.2007.06.008>.
- (142) Hu, Y.-B.; Dammer, E. B.; Ren, R.-J.; Wang, G. The Endosomal-Lysosomal System: From Acidification and Cargo Sorting to Neurodegeneration. *Transl. Neurodegener.* **2015**, *4* (1), 18. <https://doi.org/10.1186/s40035-015-0041-1>.
- (143) Laude, A. J.; Prior, I. A. Plasma Membrane Microdomains: Organization, Function and Trafficking. *Mol. Membr. Biol.* **2004**, *21* (3), 193–205. <https://doi.org/10.1080/09687680410001700517>.

- (144) Farshbaf, M. *et al.* Significant Role of Cationic Polymers in Drug Delivery Systems. *Artif. Cells Nanomed. Biotechnol.* **2018**, *46* (8), 1872–1891. <https://doi.org/10.1080/21691401.2017.1395344>.
- (145) Shen, Z.; Nieh, M.-P.; Li, Y. Decorating Nanoparticle Surface for Targeted Drug Delivery: Opportunities and Challenges. *Polymers* **2016**, *8* (3). <https://doi.org/10.3390/polym8030083>.
- (146) Bus, T.; Traeger, A.; Schubert, U. S. The Great Escape: How Cationic Polyplexes Overcome the Endosomal Barrier. *J. Mater. Chem. B* **2018**, *6* (43), 6904–6918. <https://doi.org/10.1039/C8TB00967H>.
- (147) Chen, J. *et al.* Cationic Nanoparticles Induce Nanoscale Disruption in Living Cell Plasma Membranes. *J. Phys. Chem. B* **2009**, *113* (32), 11179–11185. <https://doi.org/10.1021/jp9033936>.
- (148) Ma, J.; Goryaynov, A.; Sarma, A.; Yang, W. Self-Regulated Viscous Channel in the Nuclear Pore Complex. *Proc. Natl. Acad. Sci. U.S.A.* **2012**, *109* (19), 7326–7331. <https://doi.org/10.1073/pnas.1201724109>.
- (149) Pouton, C. W.; Wagstaff, K. M.; Roth, D. M.; Moseley, G. W.; Jans, D. A. Targeted Delivery to the Nucleus. *Adv. Drug Deliv. Rev.* **2007**, *59* (8), 698–717. <https://doi.org/10.1016/j.addr.2007.06.010>.
- (150) Parodi, A. *et al.* Enabling Cytoplasmic Delivery and Organelle Targeting by Surface Modification of Nanocarriers. *Nanomedicine* **2015**, *10* (12), 1923–1940. <https://doi.org/10.2217/nnm.15.39>.
- (151) D'Souza, G. G. M.; Cheng, S.-M.; Boddapati, S. v; Horobin, R. W.; Weissig, V. Nanocarrier-Assisted Sub-Cellular Targeting to the Site of Mitochondria Improves the pro-Apoptotic Activity of Paclitaxel. *J. Drug Target* **2008**, *16* (7), 578–585. <https://doi.org/10.1080/10611860802228855>.
- (152) Sneh-Edri, H.; Likhtenshtein, D.; Stepensky, D. Intracellular Targeting of PLGA Nanoparticles Encapsulating Antigenic Peptide to the Endoplasmic Reticulum of Dendritic Cells and Its Effect on Antigen Cross-Presentation in Vitro. *Mol. Pharm.* **2011**, *8* (4), 1266–1275. <https://doi.org/10.1021/mp200198c>.
- (153) Anselmo, A. C.; Mitragotri, S. A Review of Clinical Translation of Inorganic Nanoparticles. *AAPS J.* **2015**, *17* (5), 1041–1054. <https://doi.org/10.1208/s12248-015-9780-2>.
- (154) Revia, R. A.; Zhang, M. Magnetite Nanoparticles for Cancer Diagnosis, Treatment, and Treatment Monitoring: Recent Advances. *Mater. Today* **2016**, *19* (3), 157–168. <https://doi.org/10.1016/j.mattod.2015.08.022>.
- (155) Sun, S. *et al.* Monodisperse MFe<sub>2</sub>O<sub>4</sub> (M = Fe, Co, Mn) Nanoparticles. *J. Am. Chem. Soc.* **2004**, *126* (1), 273–279. <https://doi.org/10.1021/ja0380852>.
- (156) Wan, J.; Cai, W.; Meng, X.; Liu, E. Monodisperse Water-Soluble Magnetite Nanoparticles Prepared by Polyol Process for High-Performance Magnetic Resonance Imaging. *Chem. Commun.* **2007**, *1* (47), 5004–5006. <https://doi.org/10.1039/B712795B>.

- (157) Lee, Y. *et al.* Large-Scale Synthesis of Uniform and Crystalline Magnetite Nanoparticles Using Reverse Micelles as Nanoreactors under Reflux Conditions. *Adv. Funct. Mater.* **2005**, *15* (3), 503–509. <https://doi.org/10.1002/adfm.200400187>.
- (158) Bharde, A. *et al.* Bacterial Aerobic Synthesis of Nanocrystalline Magnetite. *J. Am. Chem. Soc.* **2005**, *127* (26), 9326–9327. <https://doi.org/10.1021/ja0508469>.
- (159) Daou, T. J. *et al.* Hydrothermal Synthesis of Monodisperse Magnetite Nanoparticles. *Chem. Mater.* **2006**, *18* (18), 4399–4404. <https://doi.org/10.1021/cm060805r>.
- (160) Yazdani, F.; Seddigh, M. Magnetite Nanoparticles Synthesized by Co-Precipitation Method: The Effects of Various Iron Anions on Specifications. *Mater. Chem. Phys.* **2016**, *184* (1), 318–323. <https://doi.org/10.1016/j.matchemphys.2016.09.058>.
- (161) Wahajuddin, M.; Arora, S. Superparamagnetic Iron Oxide Nanoparticles: Magnetic Nanoplatforms as Drug Carriers. *Int. J. Nanomedicine* **2012**, *7* (1), 3445–3471. <https://doi.org/10.2147/IJN.S30320>.
- (162) Jose, J. *et al.* Magnetic Nanoparticles for Hyperthermia in Cancer Treatment: An Emerging Tool. *Environ. Sci. Pollut. Res.* **2020**, *27* (16), 19214–19225. <https://doi.org/10.1007/s11356-019-07231-2>.
- (163) López-Lázaro, M. Dual Role of Hydrogen Peroxide in Cancer: Possible Relevance to Cancer Chemoprevention and Therapy. *Cancer Lett.* **2007**, *252* (1), 1–8. <https://doi.org/10.1016/j.canlet.2006.10.029>.
- (164) Yang, W. S.; Stockwell, B. R. Ferroptosis: Death by Lipid Peroxidation. *Trends Cell Biol.* **2016**, *26* (3), 165–176. <https://doi.org/10.1016/j.tcb.2015.10.014>.
- (165) Barb, W. G.; Baxendale, J. H.; George, P.; Hargrave, K. R. Reactions of Ferrous and Ferric Ions with Hydrogen Peroxide. Part I.—The Ferrous Ion Reaction. *J. Chem. Soc. Faraday Trans.* **1951**, *47* (1), 462–500. <https://doi.org/10.1039/TF9514700462>.
- (166) Ruiz-de-Angulo, A. *et al.* Chemically Programmed Vaccines: Iron Catalysis in Nanoparticles Enhances Combination Immunotherapy and Immunotherapy-Promoted Tumor Ferroptosis. *iScience* **2020**, *23* (9), 101499. <https://doi.org/10.1016/j.isci.2020.101499>.
- (167) Maxwell, T. *et al.* Chapter 15 - Quantum Dots. In *Micro and Nano Technologies*; Chung, E. J., Leon, L., Rinaldi, C. B. T.-N. for B. A., Eds.; Elsevier, 2020; pp 243–265. <https://doi.org/10.1016/B978-0-12-816662-8.00015-1>.
- (168) Ma, Y.; Zhang, Y.; Yu, W. W. Near Infrared Emitting Quantum Dots: Synthesis, Luminescence Properties and Applications. *J. Mater. Chem. C* **2019**, *7* (44), 13662–13679. <https://doi.org/10.1039/C9TC04065J>.
- (169) Winnik, F. M.; Maysinger, D. Quantum Dot Cytotoxicity and Ways To Reduce It. *Acc. Chem. Res.* **2013**, *46* (3), 672–680. <https://doi.org/10.1021/ar3000585>.
- (170) Soo Choi, H. *et al.* Renal Clearance of Quantum Dots. *Nat. Biotechnol.* **2007**, *25* (10), 1165–1170. <https://doi.org/10.1038/nbt1340>.
- (171) Liu, W. *et al.* Compact Cysteine-Coated CdSe(ZnCdS) Quantum Dots for in Vivo Applications. *J. Am. Chem. Soc.* **2007**, *129* (47), 14530–14531. <https://doi.org/10.1021/ja073790m>.

- (172) Asik, D.; Yagci, M. B.; Demir Duman, F.; Yagci Acar, H. One Step Emission Tunable Synthesis of PEG Coated Ag<sub>2</sub>S NIR Quantum Dots and the Development of Receptor Targeted Drug Delivery Vehicles Thereof. *J. Mater. Chem. B* **2016**, *4* (11), 1941–1950. <https://doi.org/10.1039/C5TB02599K>.
- (173) Tong, S.; Hou, S.; Ren, B.; Zheng, Z.; Bao, G. Self-Assembly of Phospholipid–PEG Coating on Nanoparticles through Dual Solvent Exchange. *Nano Lett.* **2011**, *11* (9), 3720–3726. <https://doi.org/10.1021/nl201978c>.
- (174) Mulvaney, P.; Liz-Marzán, L. M.; Giersig, M.; Ung, T. Silica Encapsulation of Quantum Dots and Metal Clusters. *J. Mater. Chem.* **2000**, *10* (6), 1259–1270. <https://doi.org/10.1039/B000136H>.
- (175) Gerion, D. *et al.* Synthesis and Properties of Biocompatible Water-Soluble Silica-Coated CdSe/ZnS Semiconductor Quantum Dots. *J. Phys. Chem. B* **2001**, *105* (37), 8861–8871. <https://doi.org/10.1021/jp0105488>.
- (176) Pandey, V. *et al.* Nitrogen Donor Ligand for Capping ZnS Quantum Dots: A Quantum Chemical and Toxicological Insight. *RSC Adv.* **2019**, *9* (49), 28510–28524. <https://doi.org/10.1039/C9RA05651C>.
- (177) Fischer, H. C.; Liu, L.; Pang, K. S.; Chan, W. C. W. Pharmacokinetics of Nanoscale Quantum Dots: In Vivo Distribution, Sequestration, and Clearance in the Rat. *Adv. Funct. Mater.* **2006**, *16* (10), 1299–1305. <https://doi.org/10.1002/adfm.200500529>.
- (178) Gao, X.; Cui, Y.; Levenson, R. M.; Chung, L. W. K.; Nie, S. In Vivo Cancer Targeting and Imaging with Semiconductor Quantum Dots. *Nat. Biotechnol.* **2004**, *22* (8), 969–976. <https://doi.org/10.1038/nbt994>.
- (179) Lee, K.-S.; El-Sayed, M. A. Gold and Silver Nanoparticles in Sensing and Imaging: Sensitivity of Plasmon Response to Size, Shape, and Metal Composition. *J. Phys. Chem. B* **2006**, *110* (39), 19220–19225. <https://doi.org/10.1021/jp062536y>.
- (180) Hainfeld, J. F. *et al.* Micro-CT Enables Microlocalisation and Quantification of Her2-Targeted Gold Nanoparticles within Tumour Regions. *Br. J. Radiol.* **2011**, *84* (1002), 526–533. <https://doi.org/10.1259/bjr/42612922>.
- (181) Xu, L.; Wang, Y.-Y.; Huang, J.; Chen, C.-Y.; Wang, Z.-X.; Xie, H. Silver Nanoparticles: Synthesis, Medical Applications and Biosafety. *Theranostics* **2020**, *10* (20), 8996–9031. <https://doi.org/10.7150/thno.45413>.
- (182) Es-haghi, A. Putative Mechanism for Anticancer Properties of Ag–PP (NPs) Extract. *IET Nanobiotechnol.* **2019**, *13* (6), 617–620(3).
- (183) Chakraborty, B. *et al.* Immunomodulatory Properties of Silver Nanoparticles Contribute to Anticancer Strategy for Murine Fibrosarcoma. *Cell. Mol. Immunol.* **2016**, *13* (2), 191–205. <https://doi.org/10.1038/cmi.2015.05>.
- (184) Vallet-Regi, M.; Rámila, A.; del Real, R. P.; Pérez-Pariente, J. A New Property of MCM-41: Drug Delivery System. *Chem. Mater.* **2001**, *13* (2), 308–311. <https://doi.org/10.1021/cm0011559>.



- (185) Barczak, M. Functionalization of Mesoporous Silica Surface with Carboxylic Groups by Meldrum's Acid and Its Application for Sorption of Proteins. *J. Porous Mater.* **2019**, *26* (1), 291–300. <https://doi.org/10.1007/s10934-018-0655-7>.
- (186) Kim, S.; Park, S.; Han, S.; Han, Y.; Park, J. Silanol-Rich Ordered Mesoporous Silica Modified Thiol Group for Enhanced Recovery Performance of Au(III) in Acidic Leachate Solution. *Chem. Eng. J.* **2018**, *351* (1), 1027–1037. <https://doi.org/10.1016/j.cej.2018.06.136>.
- (187) Alswieleh, A. M. Modification of Mesoporous Silica Surface by Immobilization of Functional Groups for Controlled Drug Release. *J. Chem.* **2020**, *2020* (1), 9176257. <https://doi.org/10.1155/2020/9176257>.
- (188) Lu, J. *et al.* Nano-Enabled Pancreas Cancer Immunotherapy Using Immunogenic Cell Death and Reversing Immunosuppression. *Nat. Commun.* **2017**, *8* (1), 1811. <https://doi.org/10.1038/s41467-017-01651-9>.
- (189) Iijima, S. Helical Microtubules of Graphitic Carbon. *Nature* **1991**, *354* (6348), 56–58. <https://doi.org/10.1038/354056a0>.
- (190) Saifuddin, N. M.; Raziah, A. Z.; Junizah, A. R. Carbon Nanotubes: A Review on Structure and Their Interaction with Proteins. *J. Chem.* **2012**, *2013* (1), 1–18. <https://doi.org/10.1155/2013/676815>.
- (191) Ani, M. H. *et al.* Critical Review on the Contributions of Chemical and Physical Factors toward the Nucleation and Growth of Large-Area Graphene. *J. Mater. Sci.* **2018**, *53* (10), 7095–7111. <https://doi.org/10.1007/s10853-018-1994-0>.
- (192) Raffa, V. *et al.* Can the Properties of Carbon Nanotubes Influence Their Internalization by Living Cells? *Carbon* **2008**, *46* (12), 1600–1610. <https://doi.org/10.1016/j.carbon.2008.06.053>.
- (193) Ferrari, R.; Sponchioni, M.; Morbidelli, M.; Moscatelli, D. Polymer Nanoparticles for the Intravenous Delivery of Anticancer Drugs: The Checkpoints on the Road from the Synthesis to Clinical Translation. *Nanoscale* **2018**, *10* (48), 22701–22719. <https://doi.org/10.1039/C8NR05933K>.
- (194) El-Say, K. M.; El-Sawy, H. S. Polymeric Nanoparticles: Promising Platform for Drug Delivery. *Int. J. Pharm.* **2017**, *528* (1), 675–691. <https://doi.org/10.1016/j.ijpharm.2017.06.052>.
- (195) Cheng, R.; Meng, F.; Deng, C.; Klok, H.-A.; Zhong, Z. Dual and Multi-Stimuli Responsive Polymeric Nanoparticles for Programmed Site-Specific Drug Delivery. *Biomaterials* **2013**, *34* (14), 3647–3657. <https://doi.org/10.1016/j.biomaterials.2013.01.084>.
- (196) Sung, Y. K.; Kim, S. W. Recent Advances in Polymeric Drug Delivery Systems. *Biomater. Res.* **2020**, *24* (1), 12. <https://doi.org/10.1186/s40824-020-00190-7>.
- (197) Thambi, T.; Park, J. H.; Lee, D. S. Stimuli-Responsive Polymersomes for Cancer Therapy. *Biomater. Sci.* **2016**, *4* (1), 55–69. <https://doi.org/10.1039/C5BM00268K>.
- (198) Rideau, E.; Dimova, R.; Schwille, P.; Wurm, F. R.; Landfester, K. Liposomes and Polymersomes: A Comparative Review towards Cell Mimicking. *Chem. Soc. Rev.* **2018**, *47* (23), 8572–8610. <https://doi.org/10.1039/C8CS00162F>.

- (199) Lale, S. V.; Kumar, A.; Prasad, S.; Bharti, A. C.; Koul, V. Folic Acid and Trastuzumab Functionalized Redox Responsive Polymersomes for Intracellular Doxorubicin Delivery in Breast Cancer. *Biomacromolecules* **2015**, *16* (6), 1736–1752. <https://doi.org/10.1021/acs.biomac.5b00244>.
- (200) Olusanya, T. O. B.; Haj Ahmad, R. R.; Ibegbu, D. M.; Smith, J. R.; Elkordy, A. A. Liposomal Drug Delivery Systems and Anticancer Drugs. *Molecules (Basel, Switzerland)* **2018**, *23* (4), 907. <https://doi.org/10.3390/molecules23040907>.
- (201) Anderson, M.; Omri, A. The Effect of Different Lipid Components on the In Vitro Stability and Release Kinetics of Liposome Formulations. *Drug Deliv.* **2004**, *11* (1), 33–39. <https://doi.org/10.1080/10717540490265243>.
- (202) Carrión, F. J.; De La Maza, A.; Parra, J. L. The Influence of Ionic Strength and Lipid Bilayer Charge on the Stability of Liposomes. *J. Colloid. Interface Sci.* **1994**, *164* (1), 78–87. <https://doi.org/10.1006/jcis.1994.1145>.
- (203) Bi, H. *et al.* Current Developments in Drug Delivery with Thermosensitive Liposomes. *Asian J. Pharm. Sci.* **2019**, *14* (4), 365–379. <https://doi.org/10.1016/j.ajps.2018.07.006>.
- (204) Allison, A. C.; Gregoriadis, G. Liposomes as Immunological Adjuvants. *Nature* **1974**, *252* (5480), 252. <https://doi.org/10.1038/252252a0>.
- (205) Kedar, U.; Phutane, P.; Shidhaye, S.; Kadam, V. Advances in Polymeric Micelles for Drug Delivery and Tumor Targeting. *Nanomed.: Nanotechnol. Biol. Med.* **2010**, *6* (6), 714–729. <https://doi.org/10.1016/j.nano.2010.05.005>.
- (206) Lu, Y.; Zhang, E.; Yang, J.; Cao, Z. Strategies to Improve Micelle Stability for Drug Delivery. *Nano Res.* **2018**, *11* (10), 4985–4998. <https://doi.org/10.1007/s12274-018-2152-3>.
- (207) Talelli, M. *et al.* Core-Crosslinked Polymeric Micelles: Principles, Preparation, Biomedical Applications and Clinical Translation. *Nano Today* **2015**, *10* (1), 93–117. <https://doi.org/10.1016/j.nantod.2015.01.005>.
- (208) Osorno, L. L. *et al.* Review of Contemporary Self-Assembled Systems for the Controlled Delivery of Therapeutics in Medicine. *Nanomaterials* **2021**, *11* (2), 278. <https://doi.org/10.3390/nano11020278>.
- (209) Anselmo, A. C.; Mitragotri, S. Nanoparticles in the Clinic: An Update. *Bioeng. Transl. Med.* **2019**, *4* (3), e10143. <https://doi.org/10.1002/btm2.10143>.
- (210) Astruc, D.; Boisselier, E.; Ornelas, C. Dendrimers Designed for Functions: From Physical, Photophysical, and Supramolecular Properties to Applications in Sensing, Catalysis, Molecular Electronics, Photonics, and Nanomedicine. *Chem. Rev.* **2010**, *110* (4), 1857–1959. <https://doi.org/10.1021/cr900327d>.
- (211) Xu, L.; Zolotarskaya, O. Y.; Yeudall, W. A.; Yang, H. Click Hybridization of Immune Cells and Polyamidoamine Dendrimers. *Adv. Healthc. Mater.* **2014**, *3* (9), 1430–1438. <https://doi.org/10.1002/adhm.201300515>.
- (212) Harms, M.; Müller-Goymann, C. C. Solid Lipid Nanoparticles for Drug Delivery. *J. Drug Deliv. Sci. Technol.* **2011**, *21* (1), 89–99. [https://doi.org/10.1016/S1773-2247\(11\)50008-5](https://doi.org/10.1016/S1773-2247(11)50008-5).

- (213) Hua, S.; de Matos, M. B. C.; Metselaar, J. M.; Storm, G. Current Trends and Challenges in the Clinical Translation of Nanoparticulate Nanomedicines: Pathways for Translational Development and Commercialization. *Front. Pharmacol.* **2018**, *9* (JUL), 790. <https://doi.org/10.3389/fphar.2018.00790>.
- (214) Blanco, E.; Shen, H.; Ferrari, M. Principles of Nanoparticle Design for Overcoming Biological Barriers to Drug Delivery. *Nat. Biotechnol.* **2015**, *33* (9), 941–951. <https://doi.org/10.1038/nbt.3330>.
- (215) Suk, J. S.; Xu, Q.; Kim, N.; Hanes, J.; Ensign, L. M. PEGylation as a Strategy for Improving Nanoparticle-Based Drug and Gene Delivery. *Adv. Drug Deliv. Rev.* **2016**, *99* (1), 28–51. <https://doi.org/10.1016/j.addr.2015.09.012>.
- (216) Mori, A.; Klibanov, A. L.; Torchilin, V. P.; Huang, L. Influence of the Steric Barrier Activity of Amphipathic Poly(Ethyleneglycol) and Ganglioside GM1 on the Circulation Time of Liposomes and on the Target Binding of Immunoliposomes in Vivo. *FEBS Lett.* **1991**, *284* (2), 263–266. [https://doi.org/10.1016/0014-5793\(91\)80699-4](https://doi.org/10.1016/0014-5793(91)80699-4).
- (217) Su, Y. *et al.* The Accelerated Blood Clearance Phenomenon of PEGylated Nanoemulsion upon Cross Administration with Nanoemulsions Modified with Polyglycerin. *Asian J. Pharm. Sci.* **2018**, *13* (1), 44–53. <https://doi.org/10.1016/j.ajps.2017.07.003>.
- (218) Ishihara, T. *et al.* Evasion of the Accelerated Blood Clearance Phenomenon by Coating of Nanoparticles with Various Hydrophilic Polymers. *Biomacromolecules* **2010**, *11* (10), 2700–2706. <https://doi.org/10.1021/bm100754e>.
- (219) Ishihara, T. *et al.* Accelerated Blood Clearance Phenomenon Upon Repeated Injection of PEG-Modified PLA-Nanoparticles. *Pharm. Res.* **2009**, *26* (10), 2270–2279. <https://doi.org/10.1007/s11095-009-9943-x>.
- (220) Pastore, M. N.; Kalia, Y. N.; Horstmann, M.; Roberts, M. S. Transdermal Patches: History, Development and Pharmacology. *Br. J. Pharmacol.* **2015**, *172* (9), 2179–2209. <https://doi.org/10.1111/bph.13059>.
- (221) Pouillot, A.; Dayan, N.; Polla, A. S.; Polla, L. L.; Polla, B. S. The Stratum Corneum: A Double Paradox. *J. Cosmet. Dermatol.* **2008**, *7* (2), 143–148. <https://doi.org/10.1111/j.1473-2165.2008.00379.x>.
- (222) Moreci, R. S.; Lechler, T. Epidermal Structure and Differentiation. *Curr. Biol.* **2020**, *30* (4), 144–149. <https://doi.org/10.1016/j.cub.2020.01.004>.
- (223) Wong, R.; Geyer, S.; Weninger, W.; Guimberteau, J.-C.; Wong, J. K. The Dynamic Anatomy and Patterning of Skin. *Exp. Dermatol.* **2016**, *25* (2), 92–98. <https://doi.org/10.1111/exd.12832>.
- (224) Weng, T. *et al.* Regeneration of Skin Appendages and Nerves: Current Status and Further Challenges. *J. Transl. Med.* **2020**, *18* (1), 53. <https://doi.org/10.1186/s12967-020-02248-5>.
- (225) Larrañeta, E.; Lutton, R. E. M.; Woolfson, A. D.; Donnelly, R. F. Microneedle Arrays as Transdermal and Intradermal Drug Delivery Systems: Materials Science, Manufacture and Commercial Development. *Mater. Sci. Eng. R Rep.* **2016**, *104*, 1–32. <https://doi.org/10.1016/j.mser.2016.03.001>.

- (226) Quaresma, J. A. S. Organization of the Skin Immune System and Compartmentalized Immune Responses in Infectious Diseases. *Clin. Microbiol. Rev.* **2019**, *32* (4), e00034-18. <https://doi.org/10.1128/CMR.00034-18>.
- (227) Yang, J.; Liu, X.; Fu, Y.; Song, Y. Recent Advances of Microneedles for Biomedical Applications: Drug Delivery and Beyond. *Acta Pharm. Sin. B* **2019**, *9* (3), 469–483. <https://doi.org/10.1016/j.apsb.2019.03.007>.
- (228) Kim, Y.-C.; Park, J.-H.; Prausnitz, M. R. Microneedles for Drug and Vaccine Delivery. *Adv. Drug Deliv. Rev.* **2012**, *64* (14), 1547–1568. <https://doi.org/10.1016/j.addr.2012.04.005>.
- (229) Saurer, E. M.; Flessner, R. M.; Sullivan, S. P.; Prausnitz, M. R.; Lynn, D. M. Layer-by-Layer Assembly of DNA- and Protein-Containing Films on Microneedles for Drug Delivery to the Skin. *Biomacromolecules* **2010**, *11* (11), 3136–3143. <https://doi.org/10.1021/bm1009443>.
- (230) He, X.; Sun, J.; Zhuang, J.; Xu, H.; Liu, Y.; Wu, D. Microneedle System for Transdermal Drug and Vaccine Delivery: Devices, Safety, and Prospects. *Dose-Response* **2019**, *17* (4), 1–18. <https://doi.org/10.1177/1559325819878585>.
- (231) Waghule, T. *et al.* Microneedles: A Smart Approach and Increasing Potential for Transdermal Drug Delivery System. *Biomed. Pharmacother.* **2019**, *109*, 1249–1258. <https://doi.org/10.1016/j.biopha.2018.10.078>.
- (232) Bolton, C. J. W. *et al.* Hollow Silicon Microneedle Fabrication Using Advanced Plasma Etch Technologies for Applications in Transdermal Drug Delivery. *Lab Chip* **2020**, *20* (15), 2788–2795. <https://doi.org/10.1039/D0LC00567C>.
- (233) Makvandi, P. *et al.* Engineering Microneedle Patches for Improved Penetration: Analysis, Skin Models and Factors Affecting Needle Insertion. *Nanomicro Lett.* **2021**, *13* (1), 93. <https://doi.org/10.1007/s40820-021-00611-9>.
- (234) Han, M. *et al.* A Novel Fabrication Process for Out-of-Plane Microneedle Sheets of Biocompatible Polymer. *J. Micromech. Microeng.* **2007**, *17* (6), 1184–1191. <https://doi.org/10.1088/0960-1317/17/6/012>.
- (235) Luangveera, W. *et al.* Fabrication and Characterization of Novel Microneedles Made of a Polystyrene Solution. *J. Mech. Behav. Biomed. Mater.* **2015**, *50* (1), 77–81. <https://doi.org/10.1016/j.jmbbm.2015.06.009>.
- (236) Moon, S. J.; Lee, S. S.; Lee, H. S.; Kwon, T. H. Fabrication of Microneedle Array Using LIGA and Hot Embossing Process. *Microsyst. Technol.* **2005**, *11* (4), 311–318. <https://doi.org/10.1007/s00542-004-0446-8>.
- (237) Donnelly, R. F. *et al.* Hydrogel-Forming Microneedle Arrays for Enhanced Transdermal Drug Delivery. *Adv. Funct. Mater.* **2012**, *22* (23), 4879–4890. <https://doi.org/10.1002/adfm.201200864>.
- (238) Yang, S. *et al.* Phase-Transition Microneedle Patches for Efficient and Accurate Transdermal Delivery of Insulin. *Adv. Funct. Mat.* **2015**, *25* (29), 4633–4641. <https://doi.org/10.1002/adfm.201500554>.
- (239) Yang, S. *et al.* A Scalable Fabrication Process of Polymer Microneedles. *Int. J. Nanomedicine* **2012**, *7* (1), 1415–1422. <https://doi.org/10.2147/IJN.S28511>.

- (240) Ye, Y.; Yu, J.; Wen, D.; Kahkoska, A. R.; Gu, Z. Polymeric Microneedles for Transdermal Protein Delivery. *Adv. Drug Deliv. Rev.* **2018**, *127* (1), 106–118. <https://doi.org/10.1016/j.addr.2018.01.015>.
- (241) Juster, H.; van der Aar, B.; de Brouwer, H. A Review on Microfabrication of Thermoplastic Polymer-Based Microneedle Arrays. *Polym. Eng. Sci.* **2019**, *59* (5), 877–890. <https://doi.org/10.1002/pen.25078>.
- (242) Han, M. *et al.* Improvement in Antigen-Delivery Using Fabrication of a Grooves-Embedded Microneedle Array. *Sens. Actuators B Chem.* **2009**, *137* (1), 274–280. <https://doi.org/10.1016/j.snb.2008.11.017>.
- (243) Sammoura, F.; Kang, J.; Heo, Y.-M.; Jung, T.; Lin, L. Polymeric Microneedle Fabrication Using a Microinjection Molding Technique. *Microsyst. Technol* **2007**, *13* (5), 517–522. <https://doi.org/10.1007/s00542-006-0204-1>.
- (244) Lippmann, J. M.; Geiger, E. J.; Pisano, A. P. Polymer Investment Molding: Method for Fabricating Hollow, Microscale Parts. *Sens. Actuator A Phys.* **2007**, *134* (1), 2–10. <https://doi.org/10.1016/j.sna.2006.05.009>.
- (245) Vecchione, R. *et al.* Electro-Drawn Drug-Loaded Biodegradable Polymer Microneedles as a Viable Route to Hypodermic Injection. *Adv. Funct. Mater.* **2014**, *24* (23), 3515–3523. <https://doi.org/10.1002/adfm.201303679>.
- (246) Lee, K.; Jung, H. Drawing Lithography for Microneedles: A Review of Fundamentals and Biomedical Applications. *Biomaterials* **2012**, *33* (30), 7309–7326. <https://doi.org/10.1016/j.biomaterials.2012.06.065>.
- (247) Kim, J. D.; Kim, M.; Yang, H.; Lee, K.; Jung, H. Droplet-Born Air Blowing: Novel Dissolving Microneedle Fabrication. *J. Control. Release* **2013**, *170* (3), 430–436. <https://doi.org/10.1016/j.jconrel.2013.05.026>.
- (248) Ruggiero, F. *et al.* Electro-Drawn Polymer Microneedle Arrays with Controlled Shape and Dimension. *Sens. Actuator B Chem.* **2018**, *255* (1), 1553–1560. <https://doi.org/10.1016/j.snb.2017.08.165>.
- (249) Economidou, S. N.; Lamprou, D. A.; Douroumis, D. 3D Printing Applications for Transdermal Drug Delivery. *Int. J. Pharm.* **2018**, *544* (2), 415–424. <https://doi.org/10.1016/j.ijpharm.2018.01.031>.
- (250) Allen, E. A. *et al.* Dissolvable Microneedle Fabrication Using Piezoelectric Dispensing Technology. *Int. J. Pharm.* **2016**, *500* (1), 1–10. <https://doi.org/10.1016/j.ijpharm.2015.12.052>.
- (251) Boehm, R. D. *et al.* Indirect Rapid Prototyping of Antibacterial Acid Anhydride Copolymer Microneedles. *Biofabrication* **2012**, *4* (1), 11002. <https://doi.org/10.1088/1758-5082/4/1/011002>.
- (252) Kirby, A. J. Method of Producing a Microneedle or Microimplant. WO2006/018642, 2006.
- (253) Luzuriaga, M. A.; Berry, D. R.; Reagan, J. C.; Smaldone, R. A.; Gassensmith, J. J. Biodegradable 3D Printed Polymer Microneedles for Transdermal Drug Delivery. *Lab Chip* **2018**, *18* (8), 1223–1230. <https://doi.org/10.1039/C8LC00098K>.

- (254) Ye, Y. *et al.* Synergistic Transcutaneous Immunotherapy Enhances Antitumor Immune Responses through Delivery of Checkpoint Inhibitors. *ACS Nano* **2016**, *10* (9), 8956–8963. <https://doi.org/10.1021/acsnano.6b04989>.
- (255) Wang, C.; Ye, Y.; Hochu, G. M.; Sadeghifar, H.; Gu, Z. Enhanced Cancer Immunotherapy by Microneedle Patch-Assisted Delivery of Anti-PD1 Antibody. *Nano Lett.* **2016**, *16* (4), 2334–2340. <https://doi.org/10.1021/acs.nanolett.5b05030>.
- (256) Kim, H. *et al.* Biodegradable Microneedle Patch Delivering Antigenic Peptide–Hyaluronate Conjugate for Cancer Immunotherapy. *ACS Biomater. Sci. Eng.* **2019**, *5* (10), 5150–5158. <https://doi.org/10.1021/acsbiomaterials.9b00961>.
- (257) Duong, H. T. T. *et al.* Highly Potent Intradermal Vaccination by an Array of Dissolving Microneedle Polypeptide Cocktails for Cancer Immunotherapy. *J. Mater. Chem. B* **2020**, *8* (6), 1171–1181. <https://doi.org/10.1039/C9TB02175B>.
- (258) Lan, X. *et al.* Microneedles Loaded with Anti-PD-1–Cisplatin Nanoparticles for Synergistic Cancer Immuno-Chemotherapy. *Nanoscale* **2020**, *12* (36), 18885–18898. <https://doi.org/10.1039/D0NR04213G>.
- (259) Duong, H. T. T. *et al.* Smart Vaccine Delivery Based on Microneedle Arrays Decorated with Ultra-PH-Responsive Copolymers for Cancer Immunotherapy. *Biomaterials* **2018**, *185* (1), 13–24. <https://doi.org/10.1016/j.biomaterials.2018.09.008>.
- (260) Zeng, Q.; Gammon, J. M.; Tostanoski, L. H.; Chiu, Y.-C.; Jewell, C. M. In Vivo Expansion of Melanoma-Specific T Cells Using Microneedle Arrays Coated with Immune-Polyelectrolyte Multilayers. *ACS Biomater. Sci. Eng.* **2017**, *3* (2), 195–205. <https://doi.org/10.1021/acsbiomaterials.6b00414>.
- (261) Demuth, P. C.; Moon, J. J.; Suh, H.; Hammond, P. T.; Irvine, D. J. Releasable Layer-by-Layer Assembly of Stabilized Lipid Nanocapsules on Microneedles for Enhanced Transcutaneous Vaccine Delivery. *ACS Nano* **2012**, *6* (9), 8041–8051. <https://doi.org/10.1021/nn302639r>.
- (262) Exner, A. A.; Saidel, G. M. Drug-Eluting Polymer Implants in Cancer Therapy. *Expert Opin. Drug Deliv.* **2008**, *5* (7), 775–788. <https://doi.org/10.1517/17425247.5.7.775>.
- (263) Wait, S. D.; Prabhu, R. S.; Burri, S. H.; Atkins, T. G.; Asher, A. L. Polymeric Drug Delivery for the Treatment of Glioblastoma. *Neuro-Oncol.* **2015**, *17* (2), 9–23. <https://doi.org/10.1093/neuonc/nou360>.
- (264) Talebian, S. *et al.* Biopolymers for Antitumor Implantable Drug Delivery Systems: Recent Advances and Future Outlook. *Adv. Mater.* **2018**, *30* (31), 1706665. <https://doi.org/10.1002/adma.201706665>.
- (265) Stewart, S. A.; Domínguez-Robles, J.; Donnelly, R. F.; Larrañeta, E. Implantable Polymeric Drug Delivery Devices: Classification, Manufacture, Materials, and Clinical Applications. *Polymers* **2018**, *10* (12), 1379–1403. <https://doi.org/10.3390/polym10121379>.
- (266) Seib, F. P.; Kaplan, D. L. Doxorubicin-Loaded Silk Films: Drug-Silk Interactions and in Vivo Performance in Human Orthotopic Breast Cancer. *Biomaterials* **2012**, *33* (33), 8442–8450. <https://doi.org/10.1016/j.biomaterials.2012.08.004>.

- (267) Wolinsky, J. B.; Colson, Y. L.; Grinstaff, M. W. Local Drug Delivery Strategies for Cancer Treatment: Gels, Nanoparticles, Polymeric Films, Rods, and Wafers. *J. Control. Release* **2012**, *159* (1), 14–26. <https://doi.org/10.1016/j.jconrel.2011.11.031>.
- (268) Fleming, A. B.; Saltzman, W. M. Pharmacokinetics of the Carmustine Implant. *Clinical Pharmacokinetics* **2002**, *41* (6), 403–419. <https://doi.org/10.2165/00003088-200241060-00002>.
- (269) Lesniak, M. S.; Upadhyay, U.; Goodwin, R.; Tyler, B.; Brem, H. Local Delivery of Doxorubicin for the Treatment of Malignant Brain Tumors in Rats. *Anticancer Res.* **2005**, *25* (6B), 3825–3831.
- (270) Walter, K. A. *et al.* Taxol Delivered from a Biodegradable Polymer Implant against Experimental Malignant Glioma. *Cancer Res.* **1994**, *54* (8), 2207.
- (271) Ashby, L. S.; Smith, K. A.; Stea, B. Gliadel Wafer Implantation Combined with Standard Radiotherapy and Concurrent Followed by Adjuvant Temozolomide for Treatment of Newly Diagnosed High-Grade Glioma: A Systematic Literature Review. *World J. Surg. Oncol* **2016**, *14* (1), 225. <https://doi.org/10.1186/s12957-016-0975-5>.
- (272) Thakur, R. R. S.; McMillan, H. L.; Jones, D. S. Solvent Induced Phase Inversion-Based in Situ Forming Controlled Release Drug Delivery Implants. *J. Control. Release* **2014**, *176* (1), 8–23. <https://doi.org/10.1016/j.jconrel.2013.12.020>.
- (273) Huang, H.; Qi, X.; Chen, Y.; Wu, Z. Thermo-Sensitive Hydrogels for Delivering Biotherapeutic Molecules: A Review. *Saudi Pharm. J.* **2019**, *27* (7), 990–999. <https://doi.org/10.1016/j.jsps.2019.08.001>.
- (274) Ruel-Gariépy, E. *et al.* Thermosensitive Chitosan-Based Hydrogel for the Local Delivery of Paclitaxel. *Eur. J. Pharm. Biopharm.* **2004**, *57* (1), 53–63. [https://doi.org/10.1016/S0939-6411\(03\)00095-X](https://doi.org/10.1016/S0939-6411(03)00095-X).
- (275) Gok, B. *et al.* Adjuvant Treatment with Locally Delivered OncoGel Delays the Onset of Paresis after Surgical Resection of Experimental Spinal Column Metastasis. *Neurosurgery* **2009**, *65* (1), 193–200. <https://doi.org/10.1227/01.NEU.0000345948.54008.82>.
- (276) Zentner, G. M. *et al.* Biodegradable Block Copolymers for Delivery of Proteins and Water-Insoluble Drugs. *J. Control. Release* **2001**, *72* (1), 203–215. [https://doi.org/10.1016/S0168-3659\(01\)00276-0](https://doi.org/10.1016/S0168-3659(01)00276-0).
- (277) Garg, T.; Rath, G.; Goyal, A. K. Biomaterials-Based Nanofiber Scaffold: Targeted and Controlled Carrier for Cell and Drug Delivery. *J. Drug Target.* **2015**, *23* (3), 202–221. <https://doi.org/10.3109/1061186X.2014.992899>.
- (278) Chen, Y.; Hou, Z.; Liu, B.; Huang, S.; Li, C.; Lin, J. DOX-Cu9S5@mSiO<sub>2</sub>-PG Composite Fibers for Orthotopic Synergistic Chemo- and Photothermal Tumor Therapy. *Dalton Transactions* **2015**, *44* (7), 3118–3127. <https://doi.org/10.1039/C4DT03113J>.
- (279) Yi, H.-G. *et al.* A 3D-Printed Local Drug Delivery Patch for Pancreatic Cancer Growth Suppression. *J. Control. Release* **2016**, *238* (1), 231–241. <https://doi.org/10.1016/j.jconrel.2016.06.015>.

- (280) Gurman, P.; Miranda, O. R.; Clayton, K.; Rosen, Y.; Elman, N. M. Clinical Applications of Biomedical Microdevices for Controlled Drug Delivery. *Mayo Clin. Proc.* **2015**, *90* (1), 93–108. <https://doi.org/10.1016/j.mayocp.2014.10.003>.
- (281) Altuna, A. *et al.* Menendez de la Prida, L. SU-8 Based Microprobes for Simultaneous Neural Depth Recording and Drug Delivery in the Brain. *Lab Chip* **2013**, *13* (7), 1422–1430. <https://doi.org/10.1039/C3LC41364K>.
- (282) Elstad, N. L.; Fowers, K. D. OncoGel (ReGel/Paclitaxel) — Clinical Applications for a Novel Paclitaxel Delivery System. *Adv. Drug Deliv. Rev.* **2009**, *61* (10), 785–794. <https://doi.org/10.1016/j.addr.2009.04.010>.
- (283) Perry, J.; Chambers, A.; Spithoff, K.; Laperriere, N. Gliadel Wafers in the Treatment of Malignant Glioma: A Systematic Rev. *Curr. Oncol. (Toronto, Ont.)* **2007**, *14* (5), 189–194. <https://doi.org/10.3747/co.2007.147>.
- (284) Djavan, B. *et al.* Analysis of Testosterone Suppression in Men Receiving Histrelin, a Novel GnRH Agonist for the Treatment of Prostate Cancer. *Can. J. Urol.* **2010**, *17* (1), 5265–5271.
- (285) Stephan, S. B. *et al.* Biopolymer Implants Enhance the Efficacy of Adoptive T-Cell Therapy. *Nat. Biotechnol.* **2015**, *33* (1), 97–101. <https://doi.org/10.1038/nbt.3104>.
- (286) Conde, J.; Oliva, N.; Zhang, Y.; Artzi, N. Local Triple-Combination Therapy Results in Tumour Regression and Prevents Recurrence in a Colon Cancer Model. *Nat. Mater.* **2016**, *15* (10), 1128–1138. <https://doi.org/10.1038/nmat4707>.
- (287) Trujillo, S. *et al.* Engineered Full-Length Fibronectin–Hyaluronic Acid Hydrogels for Stem Cell Engineering. *Adv. Healthc. Mater.* **2020**, *9* (21), 2000989. <https://doi.org/https://doi.org/10.1002/adhm.202000989>.
- (288) Takikawa, O.; Kuroiwa, T.; Yamazaki, F.; Kido, R. Mechanism of Interferon- $\gamma$  Action. Characterization of Indoleamine 2,3-Dioxygenase in Cultured Human Cells Induced by Interferon - $\gamma$  and Evaluation of the Enzyme-Mediated Tryptophan Degradation in Its Anticellular Activity. *J. Biol. Chem.* **1988**, *263* (4), 2041–2048.
- (289) Yue, E. W. *et al.* Discovery of Potent Competitive Inhibitors of Indoleamine 2,3-Dioxygenase with in Vivo Pharmacodynamic Activity and Efficacy in a Mouse Melanoma Model. *J. Med. Chem.* **2009**, *52* (23), 7364–7367. <https://doi.org/10.1021/jm900518f>.
- (290) Cobaleda-Siles, M. *et al.* An Iron Oxide Nanocarrier for DsRNA to Target Lymph Nodes and Strongly Activate Cells of the Immune System. *Small* **2014**, *10* (24), 5054–5067. <https://doi.org/10.1002/sml.201401353>.
- (291) Cicco, S. R. *et al.* Biosilica from Living Diatoms: Investigations on Biocompatibility of Bare and Chemically Modified *Thalassiosira weissflogii* Silica Shells. *Bioengineering (Basel, Switzerland)* **2016**, *3* (4), 35. <https://doi.org/10.3390/bioengineering3040035>.
- (292) Sahoo, Y. *et al.* Aqueous Ferrofluid of Magnetite Nanoparticles: Fluorescence Labeling and Magnetophoretic Control. *J. Phys. Chem. B* **2005**, *109* (9), 3879–3885. <https://doi.org/10.1021/jp045402y>.
- (293) Basotra, M.; Singh, S. K.; Gulati, M. Development and Validation of a Simple and Sensitive Spectrometric Method for Estimation of Cisplatin Hydrochloride in Tablet Dosage Forms:



Application to Dissolution Studies. *ISRN Anal. Chem.* **2013**, *13*, 1–8.  
<https://doi.org/10.1155/2013/936254>.

- (294) Mattheolabakis, G.; Milane, L.; Singh, A.; Amiji, M. M. Hyaluronic Acid Targeting of CD44 for Cancer Therapy: From Receptor Biology to Nanomedicine. *J. Drug Target.* **2015**, *23* (7–8), 605–618. <https://doi.org/10.3109/1061186X.2015.1052072>
- (295) Solis, M. A.; Chen, Y.-H.; Wong, T. Y.; Bittencourt, V. Z.; Lin, Y.-C.; Huang, L. L. H. Hyaluronan Regulates Cell Behavior: A Potential Niche Matrix for Stem Cells. *Biochem. Res. Int.* **2012**, *2012*, 346972. <https://doi.org/10.1155/2012/346972>
- (296) Lee, S. Y.; Kang, M. S.; Jeong, W. Y.; Han, D.-W.; Kim, K. S. Hyaluronic Acid-Based Theranostic Nanomedicines for Targeted Cancer Therapy. *Cancers* . 2020.  
<https://doi.org/10.3390/cancers12040940>.
- (297) Schanté, C. E.; Zuber, G.; Herlin, C.; Vandamme, T. F. Chemical Modifications of Hyaluronic Acid for the Synthesis of Derivatives for a Broad Range of Biomedical Applications. *Carbohydr. Polym.* **2011**, *85* (3), 469–489.  
<https://doi.org/https://doi.org/10.1016/j.carbpol.2011.03.019>.
- (298) Bulpitt, P.; Aeschlimann, D. New Strategy for Chemical Modification of Hyaluronic Acid: Preparation of Functionalized Derivatives and Their Use in the Formation of Novel Biocompatible Hydrogels. *J. Biomed. Mater.* **1999**, *47* (2), 152–169.  
[https://doi.org/10.1002/\(SICI\)1097-4636\(199911\)47:2<152::AID-JBM5>3.0.CO;2-I](https://doi.org/10.1002/(SICI)1097-4636(199911)47:2<152::AID-JBM5>3.0.CO;2-I).
- (299) Xue, Y. *et al.* Stimulus-Cleavable Chemistry in the Field of Controlled Drug Delivery. *Chem. Soc. Rev.* **2021**, *50* (8), 4872–4931. <https://doi.org/10.1039/D0CS01061H>.
- (300) Wei, Y.; Zhang, L.; Xu, X. Noncovalent Interaction-Assisted Drug Delivery System with Highly Efficient Uptake and Release of Paclitaxel for Anticancer Therapy. *Int. J. Nanomedicine* **2017**, *12*, 7039–7051. <https://doi.org/10.2147/IJN.S144322>.
- (301) Kuo, J. W.; Swann, D. A.; Prestwich, G. D. Chemical Modification of Hyaluronic Acid by Carbodiimides. *Bioconjugate Chem.* **1991**, *2* (4), 232–241.  
<https://doi.org/10.1021/bc00010a007>.
- (302) Fields, G. B.; Stawikowski, M. Introduction to Peptide Synthesis. *Curr. Protoc. Protein Sci.* **2002**, *69* (1), 1801. <https://doi.org/10.1002/0471140864.ps1801s26>.
- (303) Madison, S. A.; Carnali, J. O. PH Optimization of Amidation via Carbodiimides. *Ind. Eng. Chem. Res.* **2013**, *52* (38), 13547–13555. <https://doi.org/10.1021/ie401724m>.
- (304) Leiro, V.; Parreira, P.; Freitas, S. C.; Martins, M. C. L.; Pêgo, A. P. Chapter 2 - Conjugation Chemistry Principles and Surface Functionalization of Nanomaterials. In *Micro and Nano Technologies*; Sarmiento, B., das Neves, J. B. T., Eds.; Elsevier, 2018; pp 35–66.
- (305) Wickramathilaka, M. P.; Tao, B. Y. Characterization of Covalent Crosslinking Strategies for Synthesizing DNA-Based Bioconjugates. *J. Biol. Eng.* **2019**, *13* (1), 63.  
<https://doi.org/10.1186/s13036-019-0191-2>.
- (306) Luo, Y.; Prestwich, G. D. Synthesis and Selective Cytotoxicity of a Hyaluronic Acid–Antitumor Bioconjugate. *Bioconjug. Chem.* **1999**, *10* (5), 755–763. <https://doi.org/10.1021/bc9900338>.

- (307) Xin, D.; Wang, Y.; Xiang, J. The Use of Amino Acid Linkers in the Conjugation of Paclitaxel with Hyaluronic Acid as Drug Delivery System: Synthesis, Self-Assembled Property, Drug Release, and In Vitro Efficiency. *Pharm. Res.* **2010**, *27* (2), 380–389. <https://doi.org/10.1007/s11095-009-9997-9>.
- (308) Ganesh, S.; Iyer, A. K.; Morrissey, D. v; Amiji, M. M. Hyaluronic Acid Based Self-Assembling Nanosystems for CD44 Target Mediated siRNA Delivery to Solid Tumors. *Biomaterials* **2013**, *34* (13), 3489–3502. <https://doi.org/10.1016/j.biomaterials.2013.01.077>.
- (309) Morton, R. C.; Mangroo, D.; Gerber, G. E. A Novel Method of Complete Activation by Carbonyldiimidazole: Application to Ester Synthesis. *Can. J. Chem.* **1988**, *66* (7), 1701–1705. <https://doi.org/10.1139/v88-275>.
- (310) Vaidyanathan, R.; Kalthod, V. G.; Ngo, D. P.; Manley, J. M.; Lapekas, S. P. Amidations Using N,N'-Carbonyldiimidazole: Remarkable Rate Enhancement by Carbon Dioxide. *J. Org. Chem.* **2004**, *69* (7), 2565–2568. <https://doi.org/10.1021/jo049949k>.
- (311) Bellini, D.; Topai, A. WO 00/01733, 2000.
- (312) D'Este, M.; Alini, M.; Eglin, D. Single Step Synthesis and Characterization of Thermoresponsive Hyaluronan Hydrogels. *Carbohydr. Polym.* **2012**, *90* (3), 1378–1385. <https://doi.org/https://doi.org/10.1016/j.carbpol.2012.07.007>.
- (313) Dahl, L. B.; Laurent, T. C.; Smedsrød, B. Preparation of Biologically Intact Radioiodinated Hyaluronan of High Specific Radioactivity: Coupling of <sup>125</sup>I-Tyramine-Cellobiose to Amino Groups after Partial N-Deacetylation. *Anal. Biochem.* **1988**, *175* (2), 397–407. [https://doi.org/https://doi.org/10.1016/0003-2697\(88\)90563-5](https://doi.org/https://doi.org/10.1016/0003-2697(88)90563-5).
- (314) Wada, T.; Chirachanchai, S.; Izawa, N.; Inaki, Y.; Takemoto, K. Synthesis and Properties of Hyaluronic Acid Conjugated Nucleic Acid Analogs—1: Synthesis of Deacetylhyaluronan and Introduction of Nucleic Acid Bases. *J. Bioact. Compat. Polym.* **1994**, *9* (4), 429–447. <https://doi.org/10.1177/088391159400900405>.
- (315) Crescenzi, V.; Francescangeli, A.; Renier, D.; Bellini, D. New Cross-Linked and Sulfated Derivatives of Partially Deacetylated Hyaluronan: Synthesis and Preliminary Characterization. *Biopolymers* **2002**, *64* (2), 86–94. <https://doi.org/https://doi.org/10.1002/bip.10131>.
- (316) Kim, K.; Choi, H.; Choi, E. S.; Park, M.-H.; Ryu, J.-H. Hyaluronic Acid-Coated Nanomedicine for Targeted Cancer Therapy. *Pharmaceutics* **2019**, *11* (7), 301. <https://doi.org/10.3390/pharmaceutics11070301>.
- (317) Han, H. S. *et al.* Bioreducible Shell-Cross-Linked Hyaluronic Acid Nanoparticles for Tumor-Targeted Drug Delivery. *Biomacromolecules* **2015**, *16* (2), 447–456. <https://doi.org/10.1021/bm5017755>.
- (318) Thomas, A. P.; Palanikumar, L.; Jeena, M. T.; Kim, K.; Ryu, J.-H. Cancer-Mitochondria-Targeted Photodynamic Therapy with Supramolecular Assembly of HA and a Water Soluble NIR Cyanine Dye. *Chem. Sci.* **2017**, *8* (12), 8351–8356. <https://doi.org/10.1039/C7SC03169F>.
- (319) Liu, H. *et al.* Double-Layered Hyaluronic Acid/Stearic Acid-Modified Polyethyleneimine Nanoparticles Encapsulating (–)-Gossypol: A Nanocarrier for Chiral Anticancer Drugs. *J. Mater. Chem. B* **2014**, *2* (32), 5238–5248. <https://doi.org/10.1039/C4TB00539B>.

- (320) Soleymani, M.; Velashjerdi, M.; Shaterabadi, Z.; Barati, A. One-Pot Preparation of Hyaluronic Acid-coated Iron Oxide Nanoparticles for Magnetic Hyperthermia Therapy and Targeting CD44-Overexpressing Cancer Cells. *Carbohydr. Polym.* **2020**, *237* (1), 116130. <https://doi.org/https://doi.org/10.1016/j.carbpol.2020.116130>.
- (321) Liu, Y. *et al.* Dual PH-Responsive Multifunctional Nanoparticles for Targeted Treatment of Breast Cancer by Combining Immunotherapy and Chemotherapy. *Acta Biomater.* **2018**, *66* (1), 310–324. <https://doi.org/https://doi.org/10.1016/j.actbio.2017.11.010>.
- (322) Alamgeer, M. *et al.* A Phase IIa Study of HA-Irinotecan, Formulation of Hyaluronic Acid and Irinotecan Targeting CD44 in Extensive-Stage Small Cell Lung Cancer. *Invest. New Drugs* **2018**, *36* (2), 288–298. <https://doi.org/10.1007/s10637-017-0555-8>.
- (323) Yoon, H. Y. *et al.* Tumor-Targeting Hyaluronic Acid Nanoparticles for Photodynamic Imaging and Therapy. *Biomaterials* **2012**, *33* (15), 3980–3989. <https://doi.org/10.1016/j.biomaterials.2012.02.016>.
- (324) El-Dakdouki, M. H. *et al.* Assessing the in Vivo Efficacy of Doxorubicin Loaded Hyaluronan Nanoparticles. *ACS Appl. Mater. Interfaces* **2014**, *6* (1), 697–705. <https://doi.org/10.1021/am404946v>.
- (325) Pan, D. C. *et al.* Hyaluronic Acid–Doxorubicin Nanoparticles for Targeted Treatment of Colorectal Cancer. *Bioeng. Transl. Med.* **2020**, *1* (1), 10166. <https://doi.org/10.1002/btm2.10166>.
- (326) Ponnuraj, K.; Jedrzejewski, M. J. Mechanism of Hyaluronan Binding and Degradation: Structure of Streptococcus Pneumoniae Hyaluronate Lyase in Complex with Hyaluronic Acid Disaccharide at 1.7 Å Resolution<sup>11</sup>Edited by I. Wilson. *J. Mol. Biol.* **2000**, *299* (4), 885–895. <https://doi.org/10.1006/jmbi.2000.3817>.
- (327) McAtee, C. O.; Barycki, J. J.; Simpson, M. A. Emerging Roles for Hyaluronidase in Cancer Metastasis and Therapy. *Adv. Cancer Res.* **2014**, *123* (1), 1–34. <https://doi.org/10.1016/B978-0-12-800092-2.00001-0>.
- (328) Linker, A.; Meyer, K.; Weissmann, B. Enzymatic Formation of Monosaccharides from Hyaluronate. *J. Biol. Chem.* **1955**, *213* (1), 237–248.
- (329) Stern, R.; Jedrzejewski M. J. Hyaluronidases: Their Genomics, Structures, and Mechanisms of Action. *Chem. Rev.* **2006**, *106* (3), 818–839. <https://doi.org/10.1021/cr050247k>.
- (330) Zhang, L. *et al.* Hyaluronidase Activity of Human Hyal1 Requires Active Site Acidic and Tyrosine Residues. *Int. J. Biol. Chem.* **2009**, *284* (14), 9433–9442. <https://doi.org/10.1074/jbc.M900210200>.
- (331) Liu, D. *et al.* Expression of Hyaluronidase by Tumor Cells Induces Angiogenesis in Vivo. *Proc. Natl. Acad. Sci. U.S.A.* **1996**, *93* (15), 7832 LP – 7837. <https://doi.org/10.1073/pnas.93.15.7832>.
- (332) Liu, N. *et al.* Hyaluronan Synthase 3 Overexpression Promotes the Growth of TSU Prostate Cancer Cells<sup>1</sup>. *Cancer Res.* **2001**, *61* (13), 5207–5214.

- (333) Tavianatou, A. G. *et al.* Hyaluronan: Molecular Size-Dependent Signaling and Biological Functions in Inflammation and Cancer. *FEBS J.* **2019**, *286* (15), 2883–2908. <https://doi.org/https://doi.org/10.1111/febs.14777>.
- (334) Liu, M.; Tolg, C.; Turley, E. Dissecting the Dual Nature of Hyaluronan in the Tumor Microenvironment. *Front. Immunol.* **2019**, *10*. <https://doi.org/10.3389/fimmu.2019.00947>.
- (335) Botzki, A. *et al.* L-Ascorbic Acid 6-Hexadecanoate, a Potent Hyaluronidase Inhibitor: X-RAY STRUCTURE AND MOLECULAR MODELING OF ENZYME-INHIBITOR COMPLEXES\*. *J. Biol. Chem.* **2004**, *279* (44), 45990–45997. <https://doi.org/10.1074/jbc.M406146200>.
- (336) Isoyama, T. *et al.* Differential Selectivity of Hyaluronidase Inhibitors toward Acidic and Basic Hyaluronidases. *Glycobiology* **2006**, *16* (1), 11–21. <https://doi.org/10.1093/glycob/cwj036>.
- (337) Hornyák, L. *et al.* The Role of Indoleamine-2,3-Dioxygenase in Cancer Development, Diagnostics, and Therapy. *Front. Immunol.* **2018**, *9* (155), 1–8. <https://doi.org/10.3389/fimmu.2018.00151>.
- (338) Badawy, A. A.-B. Kynurenine Pathway of Tryptophan Metabolism: Regulatory and Functional Aspects. *Int. J. Tryptophan Res.* **2017**, *10* (1), 1–20. <https://doi.org/10.1177/1178646917691938>.
- (339) Muller, A. J. *et al.* Inhibition of Indoleamine 2,3-Dioxygenase, an Immunoregulatory Target of the Cancer Suppression Gene Bin1, Potentiates Cancer Chemotherapy. *Nat. Med.* **2005**, *11* (3), 312–319. <https://doi.org/10.1038/nm1196>.
- (340) Cady, S. G.; Sono, M. 1-Methyl-DL-Tryptophan, Beta-(3-Benzofuranyl)-DL-Alanine (the Oxygen Analog of Tryptophan), and Beta-[3-Benzo(b)Thienyl]-DL-Alanine (the Sulfur Analog of Tryptophan) Are Competitive Inhibitors for Indoleamine 2,3-Dioxygenase. *Arch. Biochem. Biophys.* **1991**, *291* (2), 326–333. [https://doi.org/10.1016/0003-9861\(91\)90142-6](https://doi.org/10.1016/0003-9861(91)90142-6).
- (341) Moon, Y. W.; Hajjar, J.; Hwu, P.; Naing, A. Targeting the Indoleamine 2,3-Dioxygenase Pathway in Cancer. *J. Immunother. Cancer* **2015**, *3* (1), 51. <https://doi.org/10.1186/s40425-015-0094-9>.
- (342) Tang, K.; Wu, Y.-H.; Song, Y.; Yu, B. Indoleamine 2,3-Dioxygenase 1 (IDO1) Inhibitors in Clinical Trials for Cancer Immunotherapy. *J. Hematol. Oncol.* **2021**, *14* (1), 68. <https://doi.org/10.1186/s13045-021-01080-8>.
- (343) Coletti, A. *et al.* Advances in Indoleamine 2,3-Dioxygenase 1 Medicinal Chemistry. *Med. Chem. Commun.* **2017**, *8* (7), 1378–1392. <https://doi.org/10.1039/C7MD00109F>.
- (344) Lewis-Ballester, A. *et al.* Structural Insights into Substrate and Inhibitor Binding Sites in Human Indoleamine 2,3-Dioxygenase 1. *Nat. Commun.* **2017**, *8* (1), 1693. <https://doi.org/10.1038/s41467-017-01725-8>.
- (345) Jiang, S. *et al.* Computational Study on New Natural Compound Inhibitors of Indoleamine 2,3-Dioxygenase 1. *Aging* **2020**, *12* (12), 11349–11363. <https://doi.org/10.18632/aging.103113>.
- (346) Ye, Z.; Yue, L.; Shi, J.; Shao, M.; Wu, T. Role of IDO and TDO in Cancers and Related Diseases and the Therapeutic Implications. *J. Cancer* **2019**, *10* (12), 2771–2782. <https://doi.org/10.7150/jca.31727>.

- (347) Madau, M.; Le Cerf, D.; Dulong, V.; Picton, L. Hyaluronic Acid Functionalization with Jeffamine® M2005: A Comparison of the Thermo-Responsiveness Properties of the Hydrogel Obtained through Two Different Synthesis Routes. *Gels* . 2021. <https://doi.org/10.3390/gels7030088>.
- (348) Sahoo, S.; Chung, C.; Khetan, S.; Burdick, J. A. Hydrolytically Degradable Hyaluronic Acid Hydrogels with Controlled Temporal Structures. *Biomacromolecules* **2008**, *9* (4), 1088–1092. <https://doi.org/10.1021/bm800051m>.
- (349) Anderson, G. W.; Paul, R. N,N'-CARBONYLDIIMIDAZOLE, A NEW REAGENT FOR PEPTIDE SYNTHESIS. *J. Am. Chem. Soc.* **1958**, *80* (16), 4423. <https://doi.org/10.1021/ja01549a078>.
- (350) Picotti, F. *et al.* Hyaluronic Acid Lipoate: Synthesis and Physicochemical Properties. *Carbohydr. Polym.* **2013**, *93* (1), 273–278. <https://doi.org/10.1016/j.carbpol.2012.04.009>.
- (351) Coradini, D. *et al.* Hyaluronic Acid as Drug Delivery for Sodium Butyrate: Improvement of the Anti-Proliferative Activity on a Breast-Cancer Cell Line. *Int. J. Cancer* **1999**, *81* (3), 411–416. [https://doi.org/10.1002/\(SICI\)1097-0215\(19990505\)81:3<411::AID-IJC15>3.0.CO;2-F](https://doi.org/10.1002/(SICI)1097-0215(19990505)81:3<411::AID-IJC15>3.0.CO;2-F).
- (352) Potenzzone, R.; Hopfinger, A. J. Conformational Analysis of Glycosaminoglycans. III. Conformational Properties of Hyaluronic Acid and Sodium Hyaluronate. *Polym. J.* **1978**, *10* (2), 181–199. <https://doi.org/10.1295/polymj.10.181>.
- (353) Snetkov, P.; Zakharova, K.; Morozkina, S.; Olekhovich, R.; Uspenskaya, M. Hyaluronic Acid: The Influence of Molecular Weight on Structural, Physical, Physico-Chemical, and Degradable Properties of Biopolymer. *Polymers* . 2020. <https://doi.org/10.3390/polym12081800>.
- (354) Mero, A.; Campisi, M. Hyaluronic Acid Bioconjugates for the Delivery of Bioactive Molecules. *Polymers* . 2014, pp 346–369. <https://doi.org/10.3390/polym6020346>.
- (355) Choi, K. Y. *et al.* Self-Assembled Hyaluronic Acid Nanoparticles as a Potential Drug Carrier for Cancer Therapy: Synthesis, Characterization, and in Vivo Biodistribution. *J. Mater. Chem.* **2009**, *19* (24), 4102–4107. <https://doi.org/10.1039/B900456D>.
- (356) Luo, Y.; Bernshaw, N. J.; Lu, Z.-R.; Kopecek, J.; Prestwich, G. D. Targeted Delivery of Doxorubicin by HEMA Copolymer-Hyaluronan Bioconjugates. *Pharm. Res.* **2002**, *19* (4), 396–402. <https://doi.org/10.1023/A:1015170907274>.
- (357) Som, A.; Bloch, S.; Ippolito, J. E.; Achilefu, S. Acidic Extracellular PH of Tumors Induces Octamer-Binding Transcription Factor 4 Expression in Murine Fibroblasts in Vitro and in Vivo. *Sci. Rep.* **2016**, *6* (1), 27803. <https://doi.org/10.1038/srep27803>.
- (358) Fennelly, C.; Amaravadi, R. K. Lysosomal Biology in Cancer BT - Lysosomes: Methods and Protocols; Öllinger, K., Appelqvist, H., Eds.; Springer New York: New York, NY, 2017; pp 293–308. [https://doi.org/10.1007/978-1-4939-6934-0\\_19](https://doi.org/10.1007/978-1-4939-6934-0_19).
- (359) Zhu, C. *et al.* Purification and Characterization of Hyaluronate Lyase from *Arthrobacter Globiformis* A152. *Appl. Biochem. Biotechnol.* **2017**, *182* (1), 216–228. <https://doi.org/10.1007/s12010-016-2321-3>.

- (360) Tokita, Y.; Okamoto, A. Degradation of Hyaluronic Acid—Kinetic Study and Thermodynamics. *Eur. Polym. J.* **1996**, *32* (8), 1011–1014. [https://doi.org/10.1016/0014-3057\(96\)00019-5](https://doi.org/10.1016/0014-3057(96)00019-5).
- (361) Sun, Y.; Frenkel-Pinter, M.; Liotta, C. L.; Grover, M. A. The PH Dependent Mechanisms of Non-Enzymatic Peptide Bond Cleavage Reactions. *Phys. Chem. Chem. Phys.* **2020**, *22* (1), 107–113. <https://doi.org/10.1039/C9CP05240B>.
- (362) Prestwich, G. D. *et al.* Controlled Chemical Modification of Hyaluronic Acid: Synthesis, Applications, and Biodegradation of Hydrazide Derivatives. *J. Control. Release* **1998**, *53* (1), 93–103. [https://doi.org/10.1016/S0168-3659\(97\)00242-3](https://doi.org/10.1016/S0168-3659(97)00242-3).
- (363) Senbanjo, L. T.; Chellaiah, M. A. CD44: A Multifunctional Cell Surface Adhesion Receptor Is a Regulator of Progression and Metastasis of Cancer Cells. *Front. Cell Dev. Biol.* **2017**, *5*. <https://doi.org/10.3389/fcell.2017.00018>.
- (364) Chen, C.; Zhao, S.; Karnad, A.; Freeman, J. W. The Biology and Role of CD44 in Cancer Progression: Therapeutic Implications. *J. Hematol. Oncol.* **2018**, *11* (1), 64. <https://doi.org/10.1186/s13045-018-0605-5>.
- (365) Yang, M. *et al.* Increased Expression of Surface CD44 in Hypoxia-DCs Skews Helper T Cells toward a Th2 Polarization. *Sci. Rep.* **2015**, *5* (1), 13674. <https://doi.org/10.1038/srep13674>.
- (366) Misra, S.; Hascall, V. C.; Markwald, R. R.; Ghatak, S. Interactions between Hyaluronan and Its Receptors (CD44, RHAMM) Regulate the Activities of Inflammation and Cancer. *Front. Immunol.* **2015**, *6*. <https://doi.org/10.3389/fimmu.2015.00201>.
- (367) LoPresti, C.; Lomas, H.; Massignani, M.; Smart, T.; Battaglia, G. Polymersomes: Nature Inspired Nanometer Sized Compartments. *J. Mater. Chem.* **2009**, *19* (22), 3576–3590. <https://doi.org/10.1039/B818869F>.
- (368) Kim, J. H.; Moon, M. J.; Kim, D. Y.; Heo, S. H.; Jeong, Y. Y. Hyaluronic Acid-Based Nanomaterials for Cancer Therapy. *Polymers (Basel)*. **2018**, *10* (10), 1133. <https://doi.org/10.3390/polym10101133>.
- (369) Bermudez, H.; Brannan, A. K.; Hammer, D. A.; Bates, F. S.; Discher, D. E. Molecular Weight Dependence of Polymersome Membrane Structure, Elasticity, and Stability. *Macromolecules* **2002**, *35* (21), 8203–8208. <https://doi.org/10.1021/ma020669l>.
- (370) Xu, Z.; Wang, Y.; Zhang, L.; Huang, L. Nanoparticle-Delivered Transforming Growth Factor- $\beta$  siRNA Enhances Vaccination against Advanced Melanoma by Modifying Tumor Microenvironment. *ACS Nano* **2014**, *8* (4), 3636–3645. <https://doi.org/10.1021/nn500216y>.
- (371) Duan, H. *et al.* Hyaluronic-Acid-Presenting Self-Assembled Nanoparticles Transform a Hyaluronidase HYAL1 Substrate into an Efficient and Selective Inhibitor. *Angew. Chem. Int. Ed.* **2020**, *59* (32), 13591–13596. <https://doi.org/10.1002/anie.202005212>.
- (372) Ansari, M. O.; Ahmad, Md. F.; Shadab, G. G. H. A.; Siddique, H. R. Superparamagnetic Iron Oxide Nanoparticles Based Cancer Theranostics: A Double Edge Sword to Fight against Cancer. *J. Drug Deliv. Sci. Technol.* **2018**, *45* (1), 177–183. <https://doi.org/https://doi.org/10.1016/j.jddst.2018.03.017>.

- (373) Dulińska-Litewka, J. *et al.* Superparamagnetic Iron Oxide Nanoparticles—Current and Prospective Medical Applications. *Materials* **2019**, *12* (4), 617. <https://doi.org/10.3390/ma12040617>.
- (374) Chen, Z. *et al.* Dual Enzyme-like Activities of Iron Oxide Nanoparticles and Their Implication for Diminishing Cytotoxicity. *ACS Nano* **2012**, *6* (5), 4001–4012. <https://doi.org/10.1021/nn300291r>.
- (375) Zanganeh, S. *et al.* Iron Oxide Nanoparticles Inhibit Tumour Growth by Inducing Pro-Inflammatory Macrophage Polarization in Tumour Tissues. *Nat. Nanotechnol.* **2016**, *11* (11), 986–994. <https://doi.org/10.1038/nnano.2016.168>.
- (376) Kelland, L. The Resurgence of Platinum-Based Cancer Chemotherapy. *Nat. Rev. Cancer* **2007**, *7* (8), 573–584. <https://doi.org/10.1038/nrc2167>.
- (377) Dasari, S.; Bernard Tchounwou, P. Cisplatin in Cancer Therapy: Molecular Mechanisms of Action. *Eur. J. Pharmacol.* **2014**, *740* (1), 364–378. <https://doi.org/10.1016/j.ejphar.2014.07.025>.
- (378) Siddik, Z. H. Cisplatin: Mode of Cytotoxic Action and Molecular Basis of Resistance. *Oncogene* **2003**, *22* (47), 7265–7279. <https://doi.org/10.1038/sj.onc.1206933>.
- (379) Johnstone, T. C.; Suntharalingam, K.; Lippard, S. J. The Next Generation of Platinum Drugs: Targeted Pt(II) Agents, Nanoparticle Delivery, and Pt(IV) Prodrugs. *Chem. Rev.* **2016**, *116* (5), 3436–3486. <https://doi.org/10.1021/acs.chemrev.5b00597>.
- (380) Ishida, S.; Lee, J.; Thiele, D. J.; Herskowitz, I. Uptake of the Anticancer Drug Cisplatin Mediated by the Copper Transporter Ctr1 in Yeast and Mammals. *Proc. Natl. Acad. Sci. U.S.A.* **2002**, *99* (22), 14298–14302. <https://doi.org/10.1073/pnas.162491399>.
- (381) Awuah, S. G.; Zheng, Y.-R.; Bruno, P. M.; Hemann, M. T.; Lippard, S. J. A Pt(IV) Pro-Drug Preferentially Targets Indoleamine-2,3-Dioxygenase, Providing Enhanced Ovarian Cancer Immuno-Chemotherapy. *J. Am. Chem. Soc.* **2015**, *137* (47), 14854–14857. <https://doi.org/10.1021/jacs.5b10182>.
- (382) De Biasi, A. R.; Villena-Vargas, J.; Adusumilli, P. S. Cisplatin-Induced Antitumor Immunomodulation: A Review of Preclinical and Clinical Evidence. *Clin. Cancer Res.* **2014**, *20* (21), 5384–5391. <https://doi.org/10.1158/1078-0432.CCR-14-1298>.
- (383) Hato, S. v; Khong, A.; de Vries, I. J. M.; Lesterhuis, W. J. Molecular Pathways: The Immunogenic Effects of Platinum-Based Chemotherapeutics. *Clin. Cancer Res.* **2014**, *20* (11), 2831–2837. <https://doi.org/10.1158/1078-0432.CCR-13-3141>.
- (384) Englinger, B. *et al.* Metal Drugs and the Anticancer Immune Response. *Chem. Rev.* **2019**, *119* (2), 1519–1624. <https://doi.org/10.1021/acs.chemrev.8b00396>.
- (385) Wong, D. Y. Q.; Yeo, C. H. F.; Ang, W. H. Immuno-Chemotherapeutic Platinum(IV) Prodrugs of Cisplatin as Multimodal Anticancer Agents. *Angew. Chem. Int. Ed.* **2014**, *53* (26), 6752–6756. <https://doi.org/10.1002/anie.201402879>.
- (386) Ragni, R.; Cicco, S.; Vona, D.; Leone, G.; Farinola, G. M. Biosilica from Diatoms Microalgae: Smart Materials from Bio-Medicine to Photonics. *J. Mater. Res.* **2017**, *32* (2), 279–291. <https://doi.org/10.1557/jmr.2016.459>.

- (387) Wang, J.-K.; Seibert, M. Prospects for Commercial Production of Diatoms. *Biotechnol. Biofuels* **2017**, *10* (1), 16. <https://doi.org/10.1186/s13068-017-0699-y>.
- (388) Falciatore, A.; Bowler, C. Revealing the Molecular Secrets of Marine Diatoms. *Annu. Rev. Plant Biol.* **2002**, *53* (1), 109–130. <https://doi.org/10.1146/annurev.arplant.53.091701.153921>.
- (389) Falciatore, A.; Jaubert, M.; Bouly, J. P.; Bailleul, B.; Mock, T. Diatom Molecular Research Comes of Age: Model Species for Studying Phytoplankton Biology and Diversity. *Plant Cell* **2020**, *32* (3), 547–572. <https://doi.org/10.1105/tpc.19.00158>.
- (390) Jiang, W. *et al.* Purification of Biosilica from Living Diatoms by a Two-Step Acid Cleaning and Baking Method *J. Appl. Phycol.* **2014**, *26* (3), 1511–1518. <https://doi.org/10.1007/s10811-013-0192-3>.
- (391) Maher, S.; Kumeria, T.; Aw, M. S.; Losic, D. Diatom Silica for Biomedical Applications: Recent Progress and Advances. *Adv. Healthc. Mater.* **2018**, *7* (19), 1800552. <https://doi.org/10.1002/adhm.201800552>.
- (392) Uthappa, U. T. *et al.* Nature Engineered Diatom Biosilica as Drug Delivery Systems. *J. Control. Release* **2018**, *281* (1), 70–83. <https://doi.org/10.1016/j.jconrel.2018.05.013>.
- (393) Mishra, M.; Arukha, A. P.; Bashir, T.; Yadav, D.; Prasad, G. B. K. S. All New Faces of Diatoms: Potential Source of Nanomaterials and Beyond. *Front. Microbiol.* **2017**, *8* (JUL), 1–8. <https://doi.org/10.3389/fmicb.2017.01239>.
- (394) Terracciano, M.; de Stefano, L.; Rea, I. Diatoms Green Nanotechnology for Biosilica-Based Drug Delivery Systems. *Pharmaceutics* **2018**, *10* (4), 1–15. <https://doi.org/10.3390/pharmaceutics10040242>.
- (395) Rea, I. *et al.* Diatomite Biosilica Nanocarriers for SiRNA Transport inside Cancer Cells. *Biochim. Biophys. Acta Gen. Subj.* **2014**, *1840* (12), 3393–3403. <https://doi.org/10.1016/j.bbagen.2014.09.009>.
- (396) Hildebrand, M. *et al.* Nanoscale Control of Silica Morphology and Three-Dimensional Structure during Diatom Cell Wall Formation. *J. Mater. Res.* **2006**, *21* (10), 2689–2698. <https://doi.org/10.1557/jmr.2006.0333>.
- (397) Delasoie, J.; Rossier, J.; Haeni, L.; Rothen-Rutishauser, B.; Zobi, F. Slow-Targeted Release of a Ruthenium Anticancer Agent from Vitamin B12 Functionalized Marine Diatom Microalgae. *Dalton Trans.* **2018**, *47* (48), 17221–17232. <https://doi.org/10.1039/c8dt02914h>.
- (398) Delalat, B. *et al.* Targeted Drug Delivery Using Genetically Engineered Diatom Biosilica. *Nat. Commun.* **2015**, *6* (8791), 1–11. <https://doi.org/10.1038/ncomms9791>.
- (399) Boussif, O. *et al.* Versatile Vector for Gene and Oligonucleotide Transfer into Cells in Culture and in Vivo: Polyethylenimine. *Proc. Natl. Acad. Sci. U.S.A.* **1995**, *92* (16), 7297. <https://doi.org/10.1073/pnas.92.16.7297>.
- (400) Lin, X.; Xiao, Z.; Chen, T.; Liang, S. H.; Guo, H. Glucose Metabolism on Tumor Plasticity, Diagnosis, and Treatment. *Front. Oncol.* **2020**, *10* (MAR), 317. <https://doi.org/10.3389/fonc.2020.00317>.



- (401) Gao, Y.; Huang, X.; Zhu, Y.; Lv, Z. A Brief Review of Monoclonal Antibody Technology and Its Representative Applications in Immunoassays. *J. Immunoass. Immunochem.* **2018**, *39* (4), 351–364. <https://doi.org/10.1080/15321819.2018.1515775>.
- (402) Darvin, P.; Toor, S. M.; Sasidharan Nair, V.; Elkord, E. Immune Checkpoint Inhibitors: Recent Progress and Potential Biomarkers. *Exp. Mol. Med.* **2018**, *50* (12), 1–11. <https://doi.org/10.1038/s12276-018-0191-1>.
- (403) Yao, H.; Jiang, F.; Lu, A.; Zhang, G. Methods to Design and Synthesize Antibody-Drug Conjugates (ADCs). *Int. J. Mol. Sci.* **2016**, *17* (2), 194. <https://doi.org/10.3390/ijms17020194>.
- (404) Agarwal, P.; Bertozzi, C. R. Site-Specific Antibody-Drug Conjugates: The Nexus of Bioorthogonal Chemistry, Protein Engineering, and Drug Development. *Bioconjugate Chem.* **2015**, *26* (2), 176–192. <https://doi.org/10.1021/bc5004982>.
- (405) Josephy, P. D.; Eling, T.; Mason, R. P. The Horseradish Peroxidase-Catalyzed Oxidation of 3,5,3',5'-Tetramethylbenzidine. Free Radical and Charge-Transfer Complex Intermediates. *Int. J. Biol. Chem.* **1982**, *257* (7), 3669–3675. [https://doi.org/10.1016/S0021-9258\(18\)34832-4](https://doi.org/10.1016/S0021-9258(18)34832-4).
- (406) Choi, K. Y. *et al.* Self-Assembled Hyaluronic Acid Nanoparticles for Active Tumor Targeting. *Biomaterials* **2010**, *31* (1), 106–114. <https://doi.org/https://doi.org/10.1016/j.biomaterials.2009.09.030>.
- (407) Lee, H.; Lee, K.; Park, T. G. Hyaluronic Acid–Paclitaxel Conjugate Micelles: Synthesis, Characterization, and Antitumor Activity. *Bioconjug. Chem.* **2008**, *19* (6), 1319–1325. <https://doi.org/10.1021/bc8000485>.
- (408) Cadete, A. *et al.* D. Self-Assembled Hyaluronan Nanocapsules for the Intracellular Delivery of Anticancer Drugs. *Sci. Rep.* **2019**, *9* (1), 11565. <https://doi.org/10.1038/s41598-019-47995-8>.
- (409) Zhang, Y. *et al.* Self-Stabilized Hyaluronate Nanogel for Intracellular Codelivery of Doxorubicin and Cisplatin to Osteosarcoma. *Adv. Sci.* **2018**, *5* (5), 1700821. <https://doi.org/10.1002/advs.201700821>.
- (410) Ren, Q. *et al.* Enzyme and PH Dual-Responsive Hyaluronic Acid Nanoparticles Mediated Combination of Photodynamic Therapy and Chemotherapy. *Int. J. Biol. Macromol.* **2019**, *130*, 845–852. <https://doi.org/10.1016/j.ijbiomac.2019.03.030>.
- (411) Beaven, G. H.; Holiday, E. R. Ultraviolet Absorption Spectra of Proteins and Amino Acids. In *Advances in Protein Chemistry*; Anson, M. L., Bailey, K., Edsall, J. T., Eds.; Academic Press, 1952; Vol. 7, pp 319–386. [https://doi.org/10.1016/S0065-3233\(08\)60022-4](https://doi.org/10.1016/S0065-3233(08)60022-4).
- (412) Halake, K.; Lee, J. Functional Hyaluronic Acid Conjugates Based on Natural Polyphenols Exhibit Antioxidant, Adhesive, Gelation, and Self-Healing Properties. *J. Ind. Eng. Chem.* **2017**, *54*, 44–51. <https://doi.org/10.1016/j.jiec.2017.04.018>.
- (413) Catalán, J. The First UV Absorption Band of L-Tryptophan Is Not Due to Two Simultaneous Orthogonal Electronic Transitions Differing in the Dipole Moment. *Phys. Chem. Chem. Phys.* **2016**, *18* (22), 15170–15176. <https://doi.org/10.1039/C6CP00790B>.

- (414) Starmans, L. W. E. *et al.* Iron Oxide Nanoparticle-Micelles (ION-Micelles) for Sensitive (Molecular) Magnetic Particle Imaging and Magnetic Resonance Imaging. *PLoS One* **2013**, *8* (2), e57335.
- (415) Ma, S. *et al.* Fabricating Nanoparticles Co-Loaded with Survivin siRNA and Pt(IV) Prodrug for the Treatment of Platinum-Resistant Lung Cancer. *Int. J. Pharm.* **2021**, *601*, 120577. <https://doi.org/10.1016/j.ijpharm.2021.120577>.
- (416) Dhar, S.; Gu, F. X.; Langer, R.; Farokhzad, O. C.; Lippard, S. J. Targeted Delivery of Cisplatin to Prostate Cancer Cells by Aptamer Functionalized Pt(IV) Prodrug-PLGA-PEG Nanoparticles. *Proc. Natl. Acad. Sci.* **2008**, *105* (45), 17356–17361. <https://doi.org/10.1073/pnas.0809154105>.
- (417) Awuah, S. G.; Zheng, Y.-R.; Bruno, P. M.; Hemann, M. T.; Lippard, S. J. A Pt(IV) Pro-Drug Preferentially Targets Indoleamine-2,3-Dioxygenase, Providing Enhanced Ovarian Cancer Immuno-Chemotherapy. *J. Am. Chem. Soc.* **2015**, *137* (47), 14854–14857. <https://doi.org/10.1021/jacs.5b10182>.
- (418) Hou, X.; Zaks, T.; Langer, R.; Dong, Y. Lipid Nanoparticles for mRNA Delivery. *Nat. Rev. Mater.* **2021**, *6* (12), 1078–1094. <https://doi.org/10.1038/s41578-021-00358-0>.
- (419) Chen, W.; Yan, W.; Huang, L. A Simple but Effective Cancer Vaccine Consisting of an Antigen and a Cationic Lipid. *Cancer Immunol. Immunother.* **2008**, *57* (4), 517–530. <https://doi.org/10.1007/s00262-007-0390-4>.
- (420) Bianchi, F.; Pretto, S.; Tagliabue, E.; Balsari, A.; Sfondrini, L. Exploiting Poly(I:C) to Induce Cancer Cell Apoptosis. *Cancer Biol. Ther.* **2017**, *18* (10), 747–756. <https://doi.org/10.1080/15384047.2017.1373220>.
- (421) Di, S. *et al.* Combined Adjuvant of Poly I:C Improves Antitumor Effects of CAR-T Cells. *Front. Oncol.* **2019**, *9* (APR), 241. <https://doi.org/10.3389/fonc.2019.00241>.
- (422) Colapicchioni, V. *et al.* Killing Cancer Cells Using Nanotechnology: Novel Poly(I:C) Loaded Liposome-Silica Hybrid Nanoparticles. *J. Mater. Chem. B* **2015**, *3* (37), 7408–7416. <https://doi.org/10.1039/C5TB01383F>.
- (423) Dacoba, T. G. *et al.* Arginine-Based Poly(I:C)-Loaded Nanocomplexes for the Polarization of Macrophages Toward M1-Antitumoral Effectors. *Front. Immunol.* **2020**, *11*. <https://doi.org/10.3389/fimmu.2020.01412>.
- (424) Xu, L. *et al.* Indocyanine Green and Poly I:C Containing Thermo-Responsive Liposomes Used in Immune-Photothermal Therapy Prevent Cancer Growth and Metastasis. *J. Immunother. Cancer* **2019**, *7* (1), 220. <https://doi.org/10.1186/s40425-019-0702-1>.
- (425) Fang, L. *et al.* Light-Controllable Charge-Reversal Nanoparticles with Polyinosinic-Polycytidylic Acid for Enhancing Immunotherapy of Triple Negative Breast Cancer. *Acta Pharm. Sin. B* **2022**, *12* (1), 353–363. <https://doi.org/10.1016/j.apsb.2021.06.006>.
- (426) Pazur, J. H.; Kleppe, K. The Oxidation of Glucose and Related Compounds by Glucose Oxidase from *Aspergillus Niger*\*. *Biochemistry* **1964**, *3* (4), 578–583. <https://doi.org/10.1021/bi00892a018>.

- (427) Sulpizi, M.; Gageot, M.-P.; Sprik, M. The Silica–Water Interface: How the Silanols Determine the Surface Acidity and Modulate the Water Properties. *J. Chem. Theory Comput.* **2012**, *8* (3), 1037–1047. <https://doi.org/10.1021/ct2007154>.
- (428) von Harpe, A.; Petersen, H.; Li, Y.; Kissel, T. Characterization of Commercially Available and Synthesized Polyethylenimines for Gene Delivery. *J. Control. Release* **2000**, *69* (2), 309–322. [https://doi.org/10.1016/S0168-3659\(00\)00317-5](https://doi.org/10.1016/S0168-3659(00)00317-5).
- (429) Huo, M.; Wang, L.; Chen, Y.; Shi, J. Tumor-Selective Catalytic Nanomedicine by Nanocatalyst Delivery. *Nat. Commun.* **2017**, *8* (1), 357. <https://doi.org/10.1038/s41467-017-00424-8>.
- (430) Ke, W. *et al.* Therapeutic Polymersome Nanoreactors with Tumor-Specific Activable Cascade Reactions for Cooperative Cancer Therapy. *ACS Nano* **2019**, *13* (2), 2357–2369. <https://doi.org/10.1021/acsnano.8b09082>.
- (431) Zhang, T. *et al.* Glucose Oxidase and Polydopamine Functionalized Iron Oxide Nanoparticles: Combination of the Photothermal Effect and Reactive Oxygen Species Generation for Dual-Modality Selective Cancer Therapy. *J. Mater. Chem. B* **2019**, *7* (13), 2190–2200. <https://doi.org/10.1039/C8TB03320J>.
- (432) Wang, X.; Teng, F.; Kong, L.; Yu, J. PD-L1 Expression in Human Cancers and Its Association with Clinical Outcomes. *Onco Targets Ther.* **2016**, *9*, 5023–5039. <https://doi.org/10.2147/OTT.S105862>.
- (433) Davis, A. A.; Patel, V. G. The Role of PD-L1 Expression as a Predictive Biomarker: An Analysis of All US Food and Drug Administration (FDA) Approvals of Immune Checkpoint Inhibitors. *J. Immunother. Cancer* **2019**, *7* (1), 278. <https://doi.org/10.1186/s40425-019-0768-9>.
- (434) Boyle, A. J. *et al.* The Effect of Metal-Chelating Polymers (MCPs) for <sup>111</sup>In Complexed via the Streptavidin-Biotin System to Trastuzumab Fab Fragments on Tumor and Normal Tissue Distribution in Mice. *Pharm. Res.* **2013**, *30* (1), 104–116. <https://doi.org/10.1007/s11095-012-0853-y>.
- (435) McCall, M. J.; Diril, H.; Meares, C. F. Simplified Method for Conjugating Macrocyclic Bifunctional Chelating Agents to Antibodies via 2-Iminoethanol. *Bioconjug. Chem.* **1990**, *1* (3), 222–226. <https://doi.org/10.1021/bc00003a007>.
- (436) Nair, D. P. *et al.* The Thiol-Michael Addition Click Reaction: A Powerful and Widely Used Tool in Materials Chemistry. *Chem. Mater.* **2014**, *26* (1), 724–744. <https://doi.org/10.1021/cm402180t>.
- (437) Yang, D.; Kroe-Barrett, R.; Singh, S.; Laue, T. IgG Charge: Practical and Biological Implications. *Antibodies*. 2019. <https://doi.org/10.3390/antib8010024>.
- (438) Squire, K. J. *et al.* Photonic Crystal-Enhanced Fluorescence Imaging Immunoassay for Cardiovascular Disease Biomarker Screening with Machine Learning Analysis. *Sensors Actuators B Chem.* **2019**, *290*, 118–124. <https://doi.org/10.1016/j.snb.2019.03.102>.
- (439) Ren, F.; Campbell, J.; Wang, X.; Rorrer, G. L.; Wang, A. X. Enhancing Surface Plasmon Resonances of Metallic Nanoparticles by Diatom Biosilica. *Opt. Express* **2013**, *21* (13), 15308–15313. <https://doi.org/10.1364/OE.21.015308>.

- (440) Rea, I. *et al.* Bioengineered Silicon Diatoms: Adding Photonic Features to a Nanostructured Semiconductive Material for Biomolecular Sensing. *Nanoscale Res. Lett.* **2016**, *11* (1), 405. <https://doi.org/10.1186/s11671-016-1624-1>.
- (441) Quaresma, J. A. S. Organization of the Skin Immune System and Compartmentalized Immune Responses in Infectious Diseases. *Clin. Microbiol. Rev.* **2019**, *32* (4), e00034-18. <https://doi.org/10.1128/CMR.00034-18>.
- (442) Fehres, C. M.; Garcia-Vallejo, J. J.; Unger, W. W. J.; van Kooyk, Y. Skin-Resident Antigen-Presenting Cells: Instruction Manual for Vaccine Development. *Front. Immunol.* **2013**, *4* (JUN), 1–8. <https://doi.org/10.3389/fimmu.2013.00157>.
- (443) Arora, A.; Prausnitz, M. R.; Mitragotri, S. Micro-Scale Devices for Transdermal Drug Delivery. *Int. J. Pharm.* **2008**, *364* (2), 227–236. <https://doi.org/10.1016/j.ijpharm.2008.08.032>.
- (444) Francis, D. M.; Thomas, S. N. Progress and Opportunities for Enhancing the Delivery and Efficacy of Checkpoint Inhibitors for Cancer Immunotherapy. *Adv. Drug Deliv. Rev.* **2017**, *114* (1), 33–42. <https://doi.org/10.1016/j.addr.2017.04.011>.
- (445) Alkilani, A. Z.; McCrudden, M. T. C.; Donnelly, R. F. Transdermal Drug Delivery: Innovative Pharmaceutical Developments Based on Disruption of the Barrier Properties of the Stratum Corneum. *Pharmaceutics* **2015**, *7* (4), 438–470. <https://doi.org/10.3390/pharmaceutics7040438>.
- (446) Indermun, S. *et al.* Current Advances in the Fabrication of Microneedles for Transdermal Delivery. *J. Control. Release* **2014**, *185* (1), 130–138. <https://doi.org/10.1016/j.jconrel.2014.04.052>.
- (447) Hong, X. *et al.* Dissolving and Biodegradable Microneedle Technologies for Transdermal Sustained Delivery of Drug and Vaccine. *Drug Des. Devel. Ther.* **2013**, *7* (1), 945–952. <https://doi.org/10.2147/DDDT.S44401>.
- (448) Liu, T.; Luo, G.; Xing, M. Biomedical Applications of Polymeric Microneedles for Transdermal Therapeutic Delivery and Diagnosis: Current Status and Future Perspectives. *Adv. Ther.* **2020**, *3* (9), 1900140. <https://doi.org/10.1002/adtp.201900140>.
- (449) Hao, Y. *et al.* Near-Infrared Responsive PEGylated Gold Nanorod and Doxorubicin Loaded Dissolvable Hyaluronic Acid Microneedles for Human Epidermoid Cancer Therapy. *Adv. Ther.* **2018**, *1* (2), 1800008. <https://doi.org/10.1002/adtp.201800008>.
- (450) Juster, H.; van der Aar, B.; de Brouwer, H. A Review on Microfabrication of Thermoplastic Polymer-Based Microneedle Arrays. *Polym. Eng. Sci.* **2019**, *59* (5), 877–890. <https://doi.org/10.1002/pen.25078>.
- (451) Nejad, H. R.; Sadeqi, A.; Kiaee, G.; Sonkusale, S. Low-Cost and Cleanroom-Free Fabrication of Microneedles. *Microsyst. Nanoeng.* **2018**, *4* (1), 17073. <https://doi.org/10.1038/micronano.2017.73>.
- (452) Yang, P. *et al.* Construction of a Core-Shell Microneedle System to Achieve Targeted Co-Delivery of Checkpoint Inhibitors for Melanoma Immunotherapy. *Acta Biomater.* **2020**, *104* (1), 147–157. <https://doi.org/10.1016/j.actbio.2019.12.037>.

- (453) Chen, S.-X. *et al.* Construction of Microneedle-Assisted Co-Delivery Platform and Its Combining Photodynamic/Immunotherapy. *J. Control. Release* **2020**, *324* (1), 218–227. <https://doi.org/10.1016/j.jconrel.2020.05.006>.
- (454) Adu-Berchie, K.; Mooney, D. J. Biomaterials as Local Niches for Immunomodulation. *Acc. Chem. Res.* **2020**, *53* (9), 1749–1760. <https://doi.org/10.1021/acs.accounts.0c00341>.
- (455) Chew, S. A.; Danti, S. Biomaterial-Based Implantable Devices for Cancer Therapy. *Adv. Healthc. Mater.* **2017**, *6* (2), 1600766. <https://doi.org/10.1002/adhm.201600766>.
- (456) Fung, L. K.; Saltzman, W. M. Polymeric Implants for Cancer Chemotherapy. *Adv. Drug Deliv. Rev.* **1997**, *26* (2), 209–230. [https://doi.org/10.1016/S0169-409X\(97\)00036-7](https://doi.org/10.1016/S0169-409X(97)00036-7).
- (457) Brem, H.; Gabikian, P. Biodegradable Polymer Implants to Treat Brain Tumors. *J. Control. Release* **2001**, *74* (1), 63–67. [https://doi.org/10.1016/S0168-3659\(01\)00311-X](https://doi.org/10.1016/S0168-3659(01)00311-X).
- (458) Phuengkham, H.; Song, C.; Um, S. H.; Lim, Y. T. Implantable Synthetic Immune Niche for Spatiotemporal Modulation of Tumor-Derived Immunosuppression and Systemic Antitumor Immunity: Postoperative Immunotherapy. *Adv. Mater.* **2018**, *30* (18), 1706719. <https://doi.org/10.1002/adma.201706719>.
- (459) Park, C. G. *et al.* Extended Release of Perioperative Immunotherapy Prevents Tumor Recurrence and Eliminates Metastases. *Sci. Transl. Med.* **2018**, *10* (433), 1–14. <https://doi.org/10.1126/scitranslmed.aar1916>.
- (460) Kwee, B. J. *et al.* Treating Ischemia via Recruitment of Antigen-Specific T Cells. *Sci. Adv.* **2022**, *5* (7), eaav6313. <https://doi.org/10.1126/sciadv.aav6313>.
- (461) Wei, J. C. J. *et al.* Allometric Scaling of Skin Thickness, Elasticity, Viscoelasticity to Mass for Micro-Medical Device Translation: From Mice, Rats, Rabbits, Pigs to Humans. *Sci. Rep.* **2017**, *7* (1), 15885. <https://doi.org/10.1038/s41598-017-15830-7>
- (462) Chen, M.-C.; Ling, M.-H.; Lai, K.-Y.; Pramudityo, E. Chitosan Microneedle Patches for Sustained Transdermal Delivery of Macromolecules. *Biomacromolecules* **2012**, *13* (12), 4022–4031. <https://doi.org/10.1021/bm301293d>.
- (463) Larrañeta, E.; Moore, J.; Vicente-Pérez, E. M.; González-Vázquez, P.; Lutton, R.; Woolfson, A. D.; Donnelly, R. F. A Proposed Model Membrane and Test Method for Microneedle Insertion Studies. *Int. J. Pharm.* **2014**, *472* (1), 65–73. <https://doi.org/10.1016/j.ijpharm.2014.05.042>.
- (464) Moronkeji, K.; Todd, S.; Dawidowska, I.; Barrett, S. D.; Akhtar, R. The Role of Subcutaneous Tissue Stiffness on Microneedle Performance in a Representative in Vitro Model of Skin. *J. Control. Release* **2017**, *265*, 102–112. <https://doi.org/10.1016/j.jconrel.2016.11.004>.
- (465) van der Maaden, K.; Sekerdag, E.; Jiskoot, W.; Bouwstra, J. Impact-Insertion Applicator Improves Reliability of Skin Penetration by Solid Microneedle Arrays. *AAPS J.* **2014**, *16* (4), 681–684. <https://doi.org/10.1208/s12248-014-9606-7>.
- (466) Makvandi, P. *et al.* Engineering Microneedle Patches for Improved Penetration: Analysis, Skin Models and Factors Affecting Needle Insertion. *Nano-Micro Lett.* **2021**, *13* (1), 93. <https://doi.org/10.1007/s40820-021-00611-9>.

- (467) Rodgers, A. M. *et al.* Design and Characterisation of a Dissolving Microneedle Patch for Intradermal Vaccination with Heat-Inactivated Bacteria: A Proof of Concept Study. *Int. J. Pharm.* **2018**, *549* (1), 87–95. <https://doi.org/10.1016/j.ijpharm.2018.07.049>.
- (468) Nasiri, M. I. *et al.* Nanoemulsion-Based Dissolving Microneedle Arrays for Enhanced Intradermal and Transdermal Delivery. *Drug Deliv. Transl. Res.* **2022**, *12* (4), 881–896. <https://doi.org/10.1007/s13346-021-01107-0>.
- (469) Ling, M.-H.; Chen, M.-C. Dissolving Polymer Microneedle Patches for Rapid and Efficient Transdermal Delivery of Insulin to Diabetic Rats. *Acta Biomater.* **2013**, *9* (11), 8952–8961. <https://doi.org/10.1016/j.actbio.2013.06.029>.
- (470) Krause, M. O.; Oliver, J. H. Natural Widths of Atomic K and L Levels, K $\alpha$  X-ray Lines and Several KLL Auger Lines. *J. Phys. Chem. Ref. Data* **1979**, *8* (2), 329–338. <https://doi.org/10.1063/1.555595>.
- (471) Merino, M.; Zalba, S.; Garrido, M. J. Immunoliposomes in Clinical Oncology: State of the Art and Future Perspectives. *J. Control. Release* **2018**, *275* (1), 162–176. <https://doi.org/10.1016/j.jconrel.2018.02.015>.
- (472) Bachmann, M. F.; Jennings, G. T. Vaccine Delivery: A Matter of Size, Geometry, Kinetics and Molecular Patterns. *Nat. Rev. Immunol.* **2010**, *10* (11), 787–796. <https://doi.org/10.1038/nri2868>.
- (473) Schudel, A.; Francis, D. M.; Thomas, S. N. Material Design for Lymph Node Drug Delivery. *Nat. Rev. Mater.* **2019**, *4* (6), 415–428. <https://doi.org/10.1038/s41578-019-0110-7>.
- (474) Jung, J. H.; Jin, S. G. Microneedle for Transdermal Drug Delivery: Current Trends and Fabrication. *J. Pharm. Investig.* **2021**, *51* (5), 503–517. <https://doi.org/10.1007/s40005-021-00512-4>.
- (475) Sokolowska, M. *et al.* Low Molecular Weight Hyaluronan Activates Cytosolic Phospholipase A $2\alpha$  and Eicosanoid Production in Monocytes and Macrophages. *J. Biol. Chem.* **2014**, *289* (7), 4470–4488. <https://doi.org/10.1074/jbc.M113.515106>.
- (476) Kumar, S. *et al.* Discovery of Indoximod Prodrugs and Characterization of Clinical Candidate NLG802. *Eur. J. Med. Chem.* **2020**, *198* (1), 112373. <https://doi.org/10.1016/j.ejmech.2020.112373>.
- (477) Matin, A.; Streete, I. M.; Jamie, I. M.; Truscott, R. J. W.; Jamie, J. F. A Fluorescence-Based Assay for Indoleamine 2,3-Dioxygenase. *Anal. Biochem.* **2006**, *349* (1), 96–102. <https://doi.org/10.1016/j.ab.2005.10.039>.
- (478) Löb, S. *et al.* IDO1 and IDO2 Are Expressed in Human Tumors: Levo- but Not Dextro-1-Methyl Tryptophan Inhibits Tryptophan Catabolism. *Cancer Immunol. Immunother.* **2009**, *58* (1), 153–157. <https://doi.org/10.1007/s00262-008-0513-6>.
- (479) Liu, M. *et al.* Targeting the IDO1 Pathway in Cancer: From Bench to Bedside. *J. Hematol. Oncol.* **2018**, *11* (1), 100. <https://doi.org/10.1186/s13045-018-0644-y>.
- (480) Espinosa, A. *et al.* Duality of Iron Oxide Nanoparticles in Cancer Therapy: Amplification of Heating Efficiency by Magnetic Hyperthermia and Photothermal Bimodal Treatment. *ACS Nano* **2016**, *10* (2), 2436–2446. <https://doi.org/10.1021/acsnano.5b07249>.

- (481) Bocanegra Gondan, A. I. *et al.* Effective Cancer Immunotherapy in Mice by PolyIC-Imiquimod Complexes and Engineered Magnetic Nanoparticles. *Biomaterials* **2018**, *170*, 95–115. <https://doi.org/10.1016/j.biomaterials.2018.04.003>.
- (482) Fu, L.-H.; Qi, C.; Lin, J.; Huang, P. Catalytic Chemistry of Glucose Oxidase in Cancer Diagnosis and Treatment. *Chem. Soc. Rev.* **2018**, *47* (17), 6454–6472. <https://doi.org/10.1039/C7CS00891K>.
- (483) Zaric, M. *et al.* Skin Dendritic Cell Targeting via Microneedle Arrays Laden with Antigen-Encapsulated Poly-d,l-Lactide-Co-Glycolide Nanoparticles Induces Efficient Antitumor and Antiviral Immune Responses. *ACS Nano* **2013**, *7* (3), 2042–2055. <https://doi.org/10.1021/nn304235j>.
- (484) Lee, J. *et al.* Flexible, Sticky, and Biodegradable Wireless Device for Drug Delivery to Brain Tumors. *Nat. Commun.* **2019**, *10* (1), 5205. <https://doi.org/10.1038/s41467-019-13198-y>.
- (485) Donnelly, R. F. *et al.* Optical Coherence Tomography Is a Valuable Tool in the Study of the Effects of Microneedle Geometry on Skin Penetration Characteristics and In-Skin Dissolution. *J. Control. Release* **2010**, *147* (3), 333–341. <https://doi.org/10.1016/j.jconrel.2010.08.008>.
- (486) Wainwright, D. A. *et al.* IDO Expression in Brain Tumors Increases the Recruitment of Regulatory T Cells and Negatively Impacts Survival. *Clin. Cancer Res.* **2012**, *18* (22), 6110–6121. <https://doi.org/10.1158/1078-0432.CCR-12-2130>.
- (487) Munn, D. H. *et al.* Inhibition of T Cell Proliferation by Macrophage Tryptophan Catabolism. *J. Exp. Med.* **1999**, *189* (9), 1363–1372. <https://doi.org/10.1084/jem.189.9.1363>.